AD NUMBER: AD0910454

LIMITATION CHANGES

TO:

Approved for public release; distribution is unlimited.

FROM:

Distribution authorized to U.S. Government agencies only; Administrative/Operational Use; Feb 1973. Other requests shall be referred to Space and Missile Systems Organization, Los Angeles, CA 90045.

AUTHORITY

SAMSO ltr dtd 17 Jun 1977

SAMSO TR 73-65, Vol III

Final Report

SYSTEM 621B USER EQUIPMENT DEFINITION AND EXPERIMENTS PROGRAM

TASK VI – PHASE II

Volume III – Test Data And Analyses
Part 2

Grumman Aerospace Corporation

Technical Report SAMSO TR 73-65, Vol. III
April 1973

Space and Missile Systems Organization
Air Force Systems Command
Los Angeles, California 90045

ERRATA

for Technical Report SAMSO TR 73-65 Volume III, Part 2

1. Page 7-20, top of page, second line now reads; "At a received signal...".
   Should read; "At received signal...".

2. Page 7-20, second paragraph, fourth line now reads; "...plots of Section 9.".
   Should read; "...plots of Section 9, e.g., Figures 9-9 and 9-10.".

3. Page 9-5, para. 9-2, second paragraph, ninth line now reads; "...and plus a determination...".
   Should read; "...and in addition a determination...".

4. Page 9-25, Figure 9-18, change to; "Figure 9-17".

5. Page 9-61/62, last paragraph, ninth line now reads; "...reduces the standard derivation of...".
   Should read; "...reduces the standard deviation of...".

6. Page 9-79, para. 9.8.1, fourth line from bottom now reads; "...due to antenna proximity to ground and loss) between...".
   Should read; "...due to antenna proximity to ground) and loss between...".

7. Page 9-100, line preceding Equation 21 now reads; "...terms of the grazing angle, and the...".
   Should read; "...terms of the grazing angle, ψ and the...".

8. Page 9-109/100, third line now reads; "Note that when $D = n\tau, \ldots$".
   Should read; "Note that when $D = n\lambda, \ldots$".

9. Page 10-17, last line of first paragraph now reads; "...the low velocities in those axis.".
   Should read; "...the low velocities in those axes.".

10. Page 10-19, third paragraph, last line now reads; "Run 02 near touchdown.".
    Should read; "Run 04 near touchdown.".

SAMSO TR 73-65, Vol III

Final Report

SYSTEM 621B USER EQUIPMENT DEFINITION AND EXPERIMENTS PROGRAM

TASK VI – PHASE II

Volume III – Test Data And Analyses
Part 2

Prepared by

Grumman Aerospace Corporation
Bethpage, New York 11714

For

Space and Missile Systems Organization
Air Force Systems Command
Los Angeles, California 90045

April 1973

FOREWORD

This report dated 11 April 1973, contains the findings of a program titled "System 621B User Equipment Definition and Experiments Program, Phase II Field Test". The work was accomplished by Grumman Aerospace Corporation (GAC), Grumman Data Systems Corp. (GDSC), both of Bethpage, N.Y. and the Hazeltine Corporation (HC) at Greenlawn, N.Y. and complies with all the requirements of Contract Number F04701-71-C-0176. In addition to the receivers which were designed and built under this contract, the Air Force provided an additional receiver designed and built by the Magnavox Research Laboratory (MRL) of Torrance, California which was also flight tested.

System 621B is a concept for a global satellite - based precision navigation system designed to meet the requirements of land, sea and air military forces in an advantageous cost effective manner. One of the most important elements in this system is the user receiver. This report summarizes a series of flight and ground tests conducted at the White Sands Missile Range to evaluate the performance of a four-channel receiver in typical flight and field environments in order to solidify confidence in the predicted performance of System 621B receivers.

The report is published in three (3) volumes and bears the Air Force report number SAMSO-TR 73-65. Volume I is an Executive Summary, presenting in concise form a description of the program, the ground and flight equipment and an overview of the test results. Volume II contains the detailed program history, equipment description and data processing approach. Volume III contains a detailed presentation of the data taken during the program and a discussion of the results and conclusions to be drawn therefrom.

Grumman wishes to acknowledge the assistance of Lt. Col. V.L. Denninger, Program Manager, and Capt. D. Wilson, of the Air Force Space and Missile System Organization and of Messrs. W. Melton, F. Butterfield, T. Connor, A. Gillogly, W. Feess, Dr. J. Clifford, and Dr. L. Hagerman, of the Aerospace Corporation.

This report was prepared by Messrs. J. Courtney, R. Laho, I. Kadar, P. Richards, M. Moore, M. Neglia, I. Shulman, E. Graber, L. Pangburn, R. Latham, E. Burke of Grumman, R. Regis of Hazeltine, and B. Glazer of Magnavox.

John J. Courtney, Jr.
621B Director

Edward Z. Gray, Director
Special Projects

Publication approval of this technical report does not constitute Air Force approval of the report's findings or conclusions. It is published only for exchange and stimulation of ideas.

Valentine L. Denninger, Lt. Col., USAF
Program Manager
System 621B

ABSTRACT

System 621B is a concept for a global satellite-based precision navigation system designed to meet the requirements of land, sea and air military forces in an advantageous cost effective manner. One of the most important elements in this system is the user receiver. This report summarizes a series of flight and ground tests conducted at the White Sands Missile Range to evaluate the performance of a four-channel receiver in typical flight and field environments in order to solidify confidence in the predicted performance of System 621B receivers.

TABLE OF CONTENTS

For Volume III Part 1

TABLE OF CONTENTS

For Volume III, Part 2

TABLE OF CONTENTS (CONT)

For Volume III, Part 2

APPENDICES

LIST OF ILLUSTRATIONS

For Volume III, Part 1

LIST OF ILLUSTRATIONS (CONT)

For Volume III, Part 2

LIST OF ILLUSTRATIONS (CONT)

For Volume III, Part 2

LIST OF ILLUSTRATIONS (CONT)

For Volume III, Part 2

LIST OF ILLUSTRATIONS (CONT)

For Volume III, Part 2

LIST OF ILLUSTRATIONS (Cont)
For Volume III, Part 2

LIST OF ILLUSTRATIONS (CONT)
For Volume III, Part 2

LIST OF ILLUSTRATIONS (CONT)

For Volume III, Part 2

LIST OF TABLES

For Volume III, Part 1

LIST OF TABLES

For Volume III, Part 2

SECTION VII

ILS TESTING - FLIGHTS 25-31

7.1 INTRODUCTION

The test system was exercised in an aircraft approach and landing configuration on flights 25-31. Low approaches were accomplished on flights 25-27 where the aircraft did not descend below 100 ft AGL. On flights 28-31, the aircraft final approach was carried to touchdown which was then followed by a normal takeoff after a ground roll of a few thousand feet. The data throughout both phases of the ILS testing show great consistency. There are some important differences in the performance of the HC and MRL receivers during these tests which did not occur during testing in the area navigation configuration. These differences are analyzed in this section and related to the basic receiver design differences.

Equipment failures on flights 26 and 28 did not permit a navigation solution to be computed and therefore these flights will not be discussed in this section.

7.2 TEST CONFIGURATION

The ground system was less complex in the ILS configuration than in the area navigation configuration. This simplicity is due to the fact that the calibration receiver and the transmitters are separated by a few thousand feet instead of by 20,000 ft as in area navigation and there was no attempt to control power level at the aircraft within a few db as in area navigation. Consequently, omni antennas were used at the transmitter sites instead of shaped beam antennas, and a single omni was used to receive at the MCS site instead of the four parabolic dish antennas needed for the long ranges in the area navigation configuration.

The principal result of this configuration simplification was that there were no Spiroline cables used in the signal path, thus eliminating this variable which plagued us during area navigation testing. Moreover, because there was only a single omni antenna at the MCS calibration receiver site, there were no cable delays to account for in the navigation solution.

As shown in Figure 7-1, for area navigation the calibration receiver measurements were effectively made at the 4-way power combiner. The signals experienced equal delays from that point on into the receiver. The equal delays were computed in the navigation solution as part of the user-to-calibration receiver clock bias (B). As discussed in Section 4, the delays from the 4-way power combiner back through the cabling to the MCS dish, and over the link to the transmitter site uplink antenna had to be known.

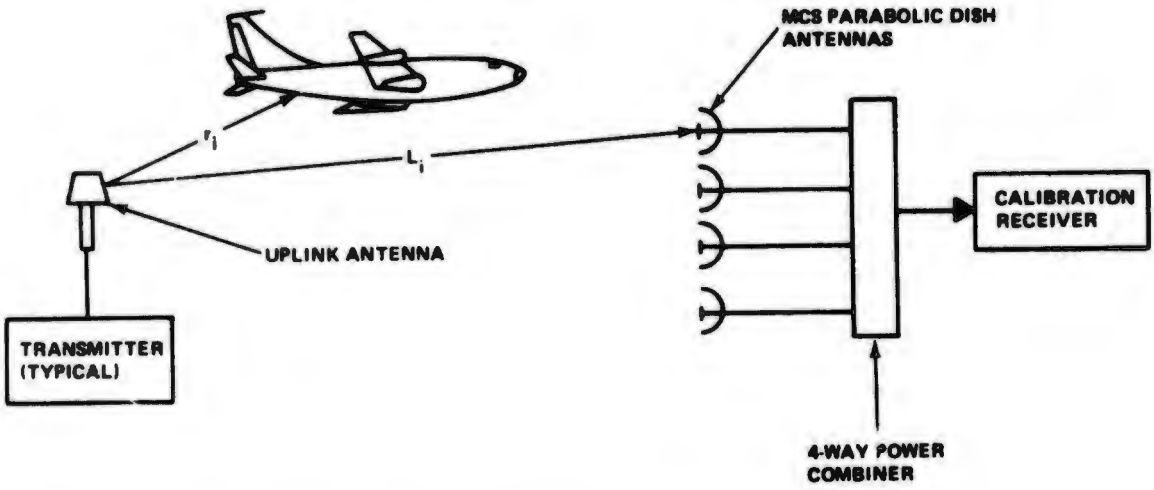

Figure 7-1 Area Navigation Configuration (Flights 17-23)

In the ILS configuration, Figure 7-2, the omni antenna at the MCS site served the same purpose as the 4-way power combiner did for area navigation. Therefore, since the calibration receiver effectively made the measurements at the omni antenna, there was no cabling to account for in the individual signal paths between transmitter and MCS sites.

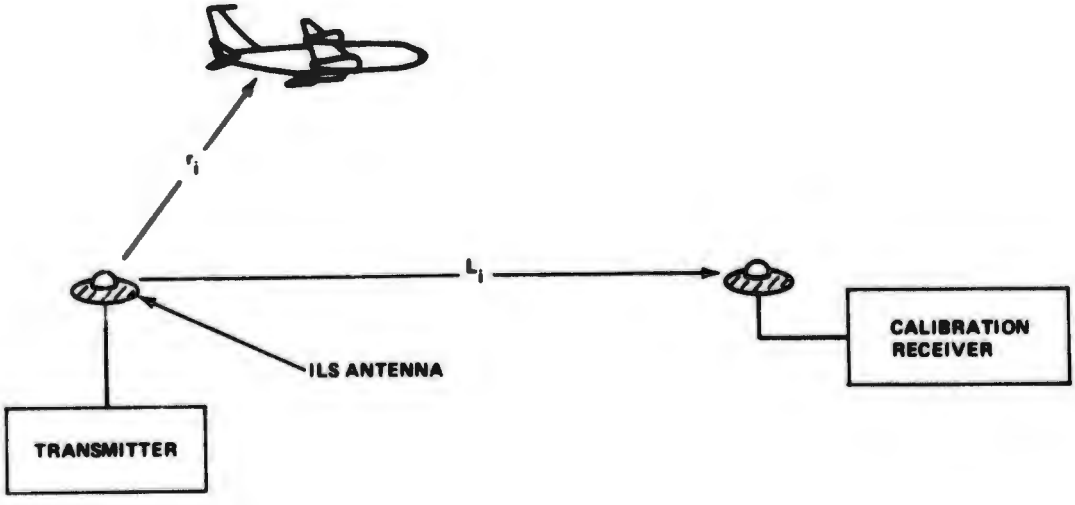

Figure 7-2 ILS Configuration (Flights 25-31)

7.2.1 Geometric Dilution of Precision (GDOP)

The primary purpose of these tests was to evaluate the system vertical position and sink rate accuracy during landing flare-out. In order to improve the test geometry relative to vertical position accuracy, one of the transmitters was suspended on a balloon at about 5000 ft altitude.

We define

$$GDOP_z = \frac{\sigma z}{\sigma m}$$

and σm is the measurement error, assumed to be the same for all channels, with no correlation between channels. This GDOP is simply a magnification of the measurement noise for an aircraft approaching and landing at the ILS test site.

Figure 7-3 is a plot of $GDOP_z$ in the YZ plane of the coordinate system used in this test. The plane is formed by the flare point and the centerline of the runway. The abscissa is Y, in 1000 ft increments, measured along the centerline of the runway. The ordinate is the GDOP. During almost all of the landings made during these tests, the receivers locked up at about 8000 ft before the flare point; note that the $GDOP_z$ at this point is approximately 40, which means that even a 1 ft measurement error would produce a 40 ft error in Z. The flare point for the normal approach and landing occurred at approximately 1000 ft before the runway threshold, touchdown was approximately 1000 ft after threshold and the aircraft was on the runway for another 5000 ft for a total from flare of about 7000 ft. At this point the $GDOP_z$ is approximately 30.

The above discussion is prefatory to an examination of the residuals between the 621B solution and the White Sands Missile Range (WSMR) trajectory. As will be seen, these residuals are extremely small in the region of small GDOP's and even in the areas of large and rapidly changing GDOP's, the accuracy is excellent.

Figure 7-4 is a time history of the z-position residual. Each of the major divisions on the abscissa represents 4 sec, during which time the aircraft travels approximately 1300 ft. Flare occurs at 20 sec. It should be noted that the error at that point is only a few feet. This test system trajectory data has been processed with an 11-state Kalman filter (see Section 3). The primary cause of the differences between the HC and MRL data is a result of multipath signals (see Subsection 7.2.4).

Another way of looking at the same effect can be seen in Figure 7-5 which shows a plot of the YZ trajectory similar to the GDOP plot of Figure 7-3. The plot of Figure 7-5 shows the error vector between the 621B solution and the WSMR BET in a plane perpendicular to the runway and passing through the runway centerline.

The flight path is scaled at 5000 ft per box, but the error vectors have a scale of 50 ft per box. As shown, the error vectors close to the flare point are very small and become larger as the aircraft passes through the large GDOP regions. The data in Figure 7-5 has not been filtered and therefore reflects the GDOP effect. Figure 7-4 shows that the GDOP effect is practically eliminated when the data is filtered.

The system accuracy is summarized in Table 7-1. Table 7-1 presents a statistical characterization (mean value, standard deviation and rms) of the residuals obtained from the trajectory comparisons. The table summarizes approximately 2000 navigation solution points obtained from five test flights. The

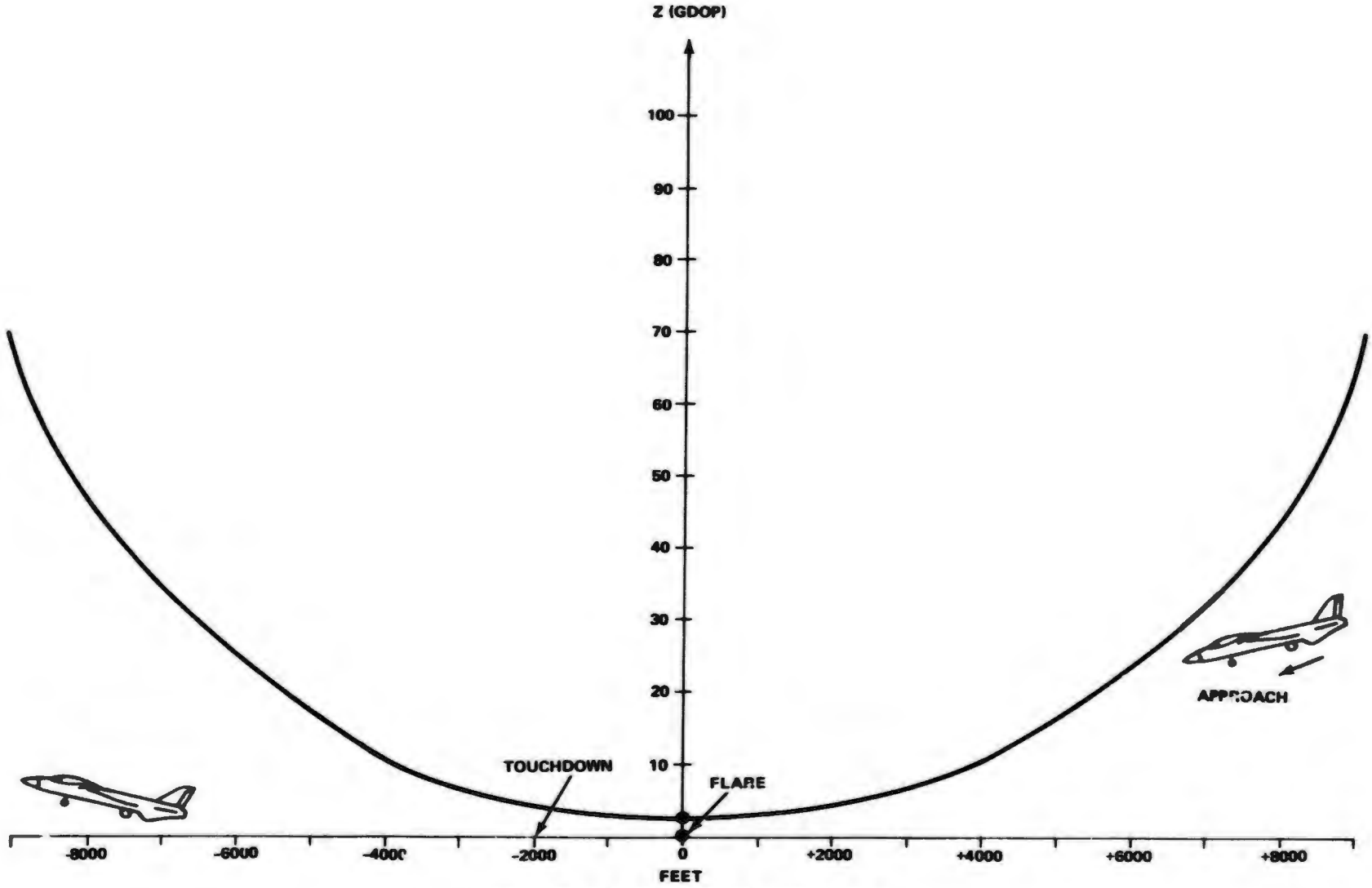

Figure 7-3 Z GDOP Contour as a Function of Position Along the ILS Y Axis

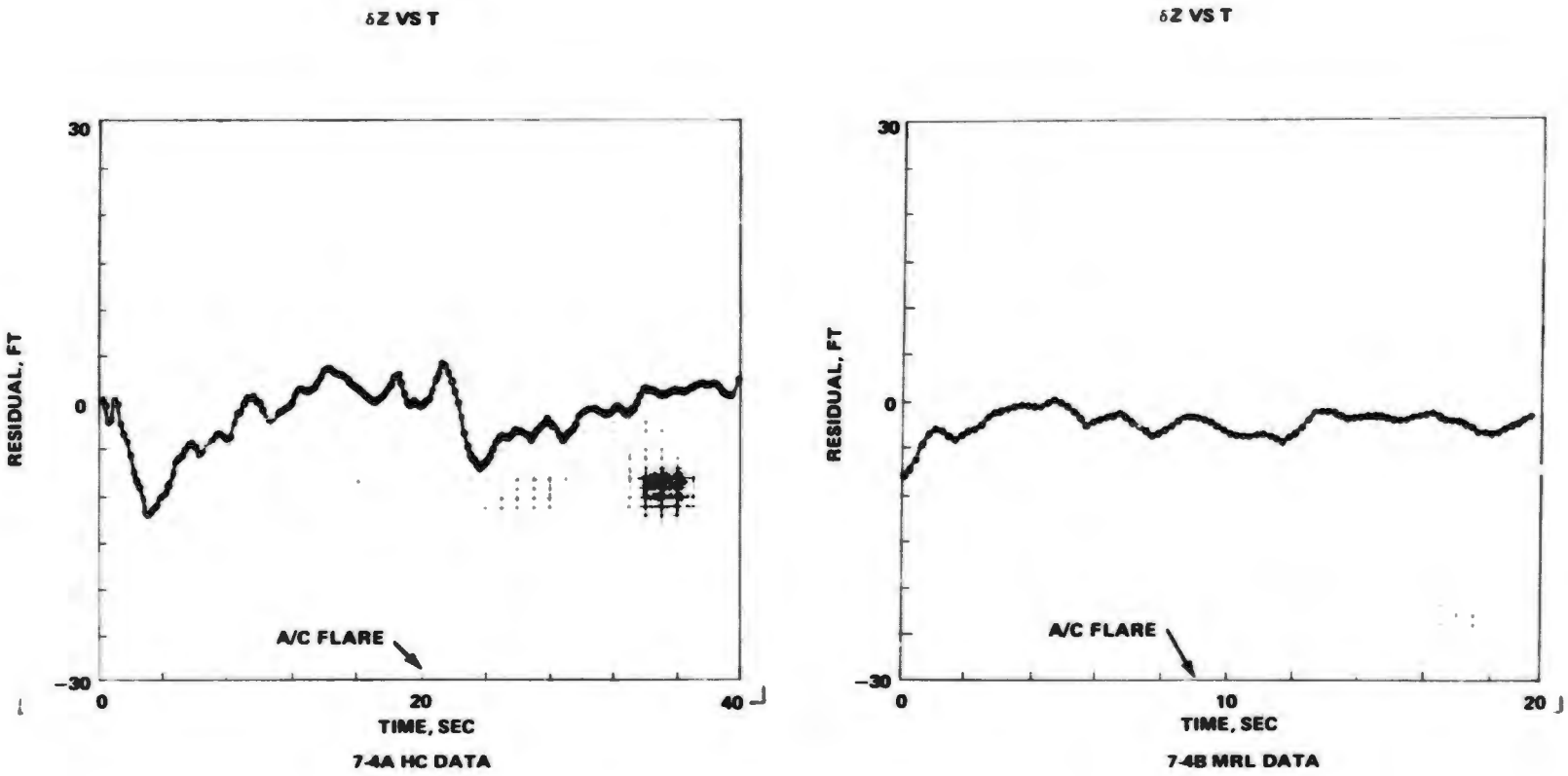

Figure 7-4 Z-Position Residual for Flight 25, Run 05

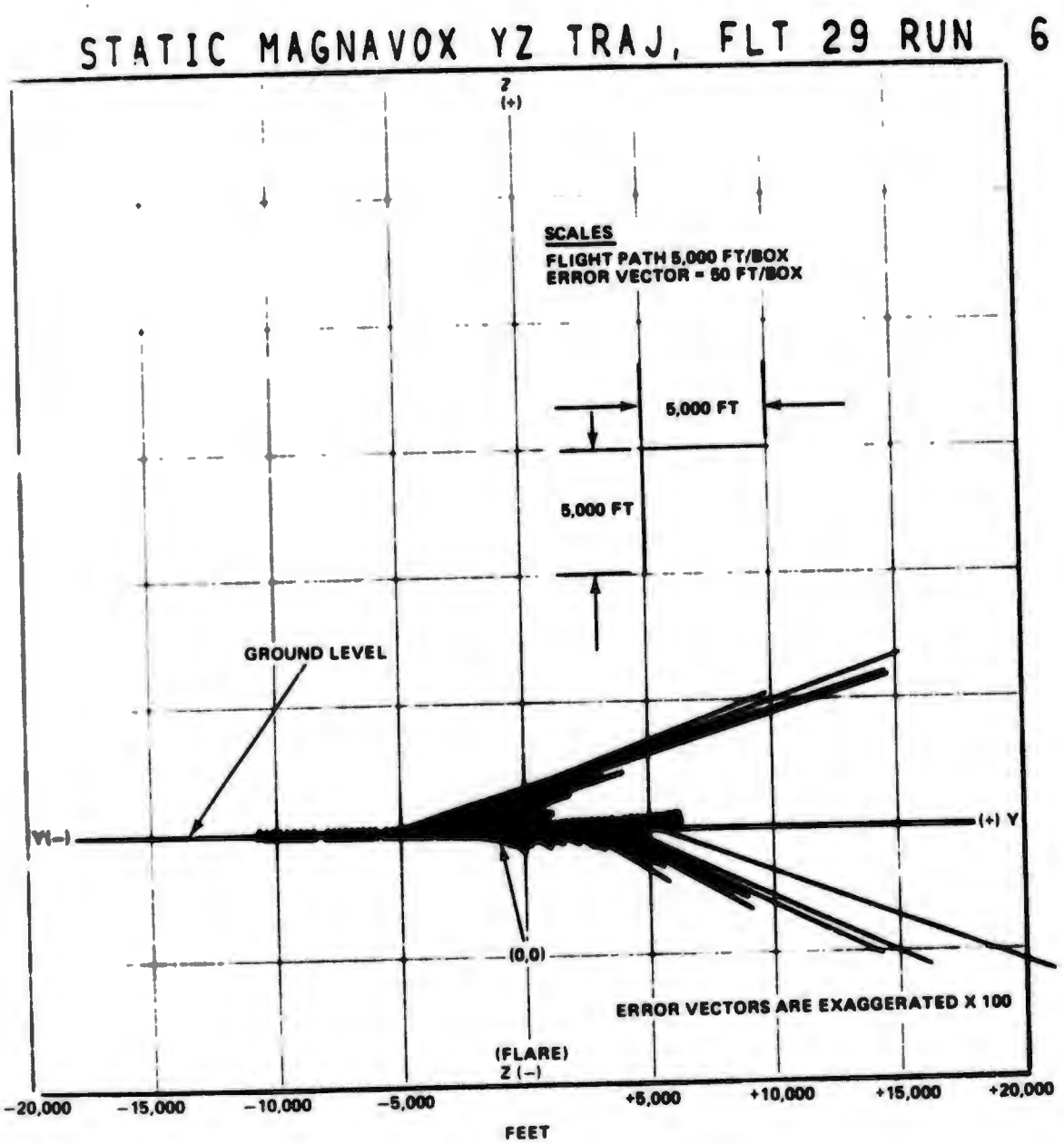

Figure 7-5 MRL Trajectory for ILS in the YZ Plane with Solution Error Vectors Overlayed

Table 7-1 ILS Navigation Accuracy

	MEAN	1σ		MEAN	1σ
X, FT			$\dot{X}$, FPS		
HC	0.3	3.3	HC	0.2	1.1
MRL	−1.1	7.3	MRL	0.2	1.4
Y, FT			$\dot{Y}$, FPS		
HC	−2.7	11.4	HC	−0.5	1.7
MRL	2.2	12.3	MRL	−0.2	2.2
Z, FT			$\dot{Z}$, FPS		
HC	−1.3	13.3	HC	−0.2	2.3
MRL	−1.3	8.3	MRL	−0.4	2.0

data are obtained from a region on the aircraft flight path from approximately 8000 ft before the nominal aircraft flare point to approximately 7000 ft beyond the runway threshold at the approach end. This region requires the most accurate vertical navigation information and corresponds to a position on the approach path where the aircraft is approximately 300 ft above ground to a position where the aircraft is braking on the runway.

Figure 7-6 is another presentation of the same data showing the percentage of the data points which are less than a particular value of a residual; 80% of the data points fall below the 9 ft error bound. This affirms the high accuracy of the system in this mode and its suitability for instrument landing.

Until now, this discussion has been concerned primarily with Z position and velocity, quantities which are very important in ILS; however, the errors in X and Y are also interesting and will be discussed after examining the X and Y GDOP's. Both of these parameters behave similar to the Z GDOP but their magnitudes are far different. For example, the X GDOP at 5000 ft from the flare point is only 9; the Y GDOP at this same point is 125.

The effect of this great difference in X and Y GDOP's is illustrated in Figures 7-7 and 7-8. These figures are plots of the static position errors for the HC and MRL receivers in the X Y plane. As can be seen, the great majority of points are clustered about the origin, but the scattering is primarily along the Y axis due to the large Y GDOP's. By utilizing a Kalman filter this effect can be minimized as shown in Figure 7-4.

7.2.2 Signal Dynamic Effects

During the planning for the ILS testing, it was recognized that, because the transmitters were located close to the flight path, appreciable signal dynamics could be generated.

To determine the magnitude of this potential problem, a computer simulation of the response of a linearized model of the Hazeltine carrier loop tracking performance in the presence of signal dynamics along the aircraft trajectory was performed. Since the loop parameters vary with signal level, the simulation program was implemented to include signal strength as a variable. The HC receiver carrier tracking loop open loop transfer characteristics at the tracking threshold of -140 dbm is given by:

$$H(S) = \frac{S(S + \frac{1}{\tau})^2}{K_1 S^2 + K_2 S + K_3}$$

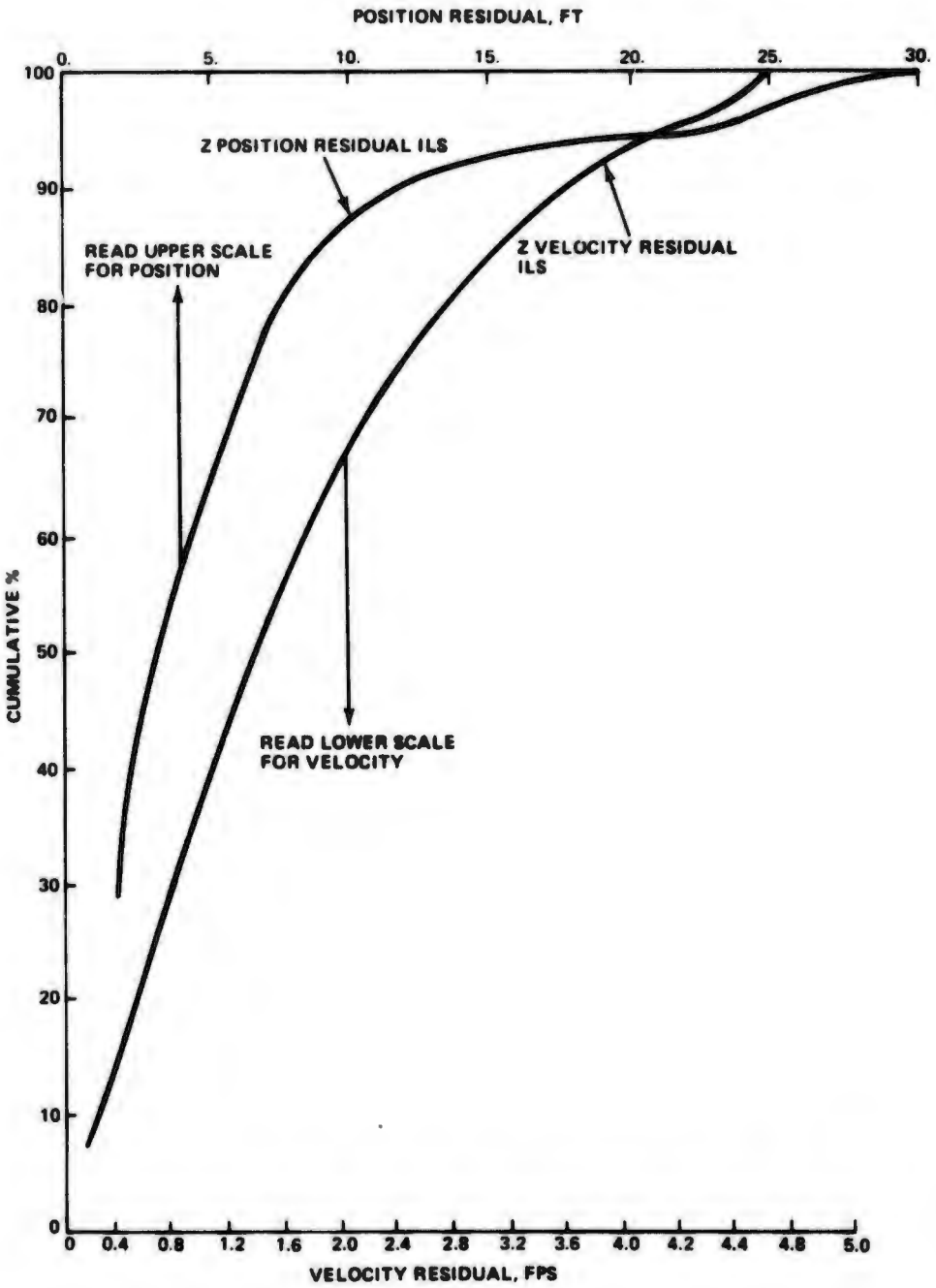

Figure 7-6 Cumulative Distribution of Total Position and Velocity Residuals for MRL During ILS Testing

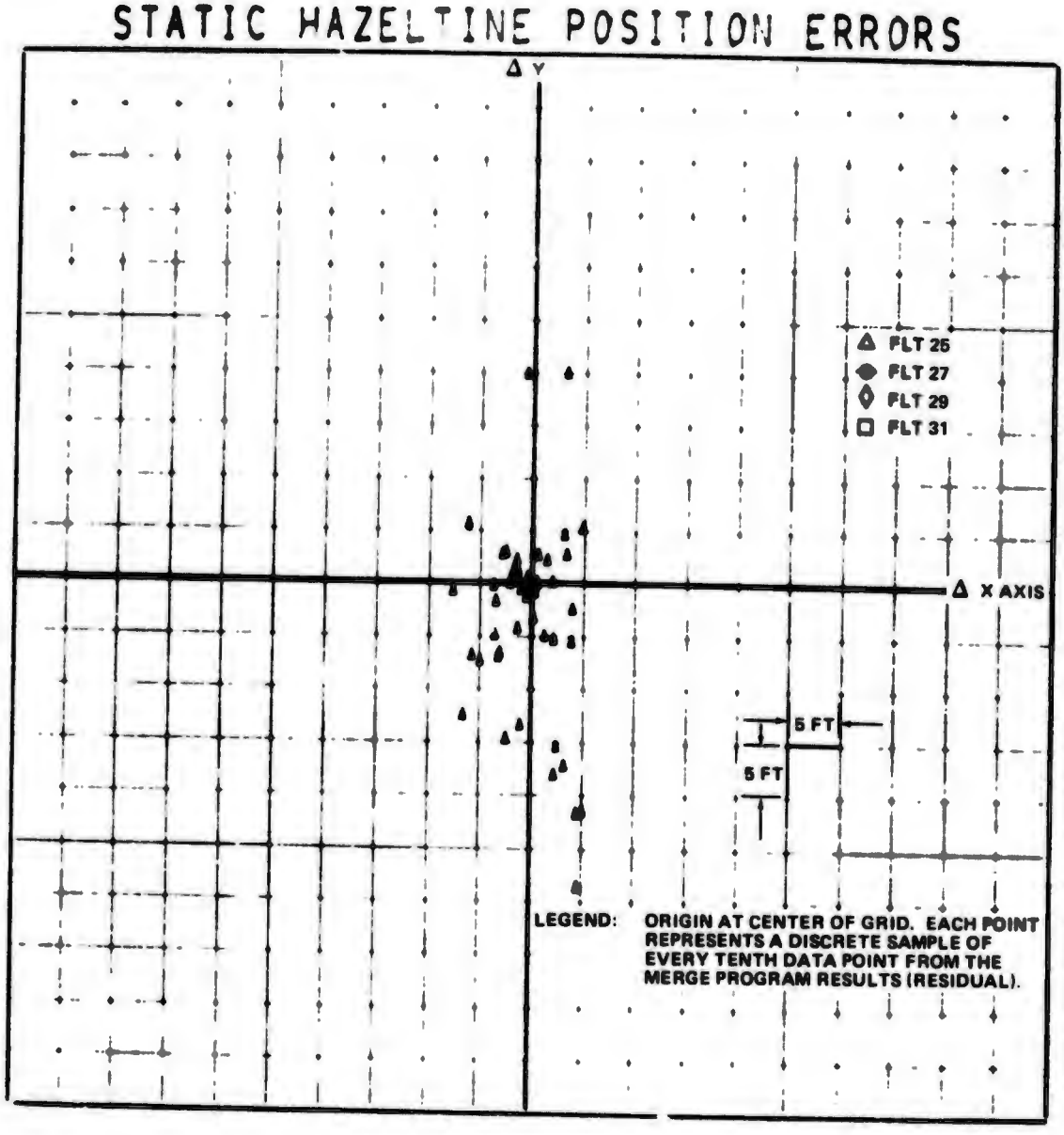

Figure 7-7 HC Horizontal Position Errors for ILS Tests

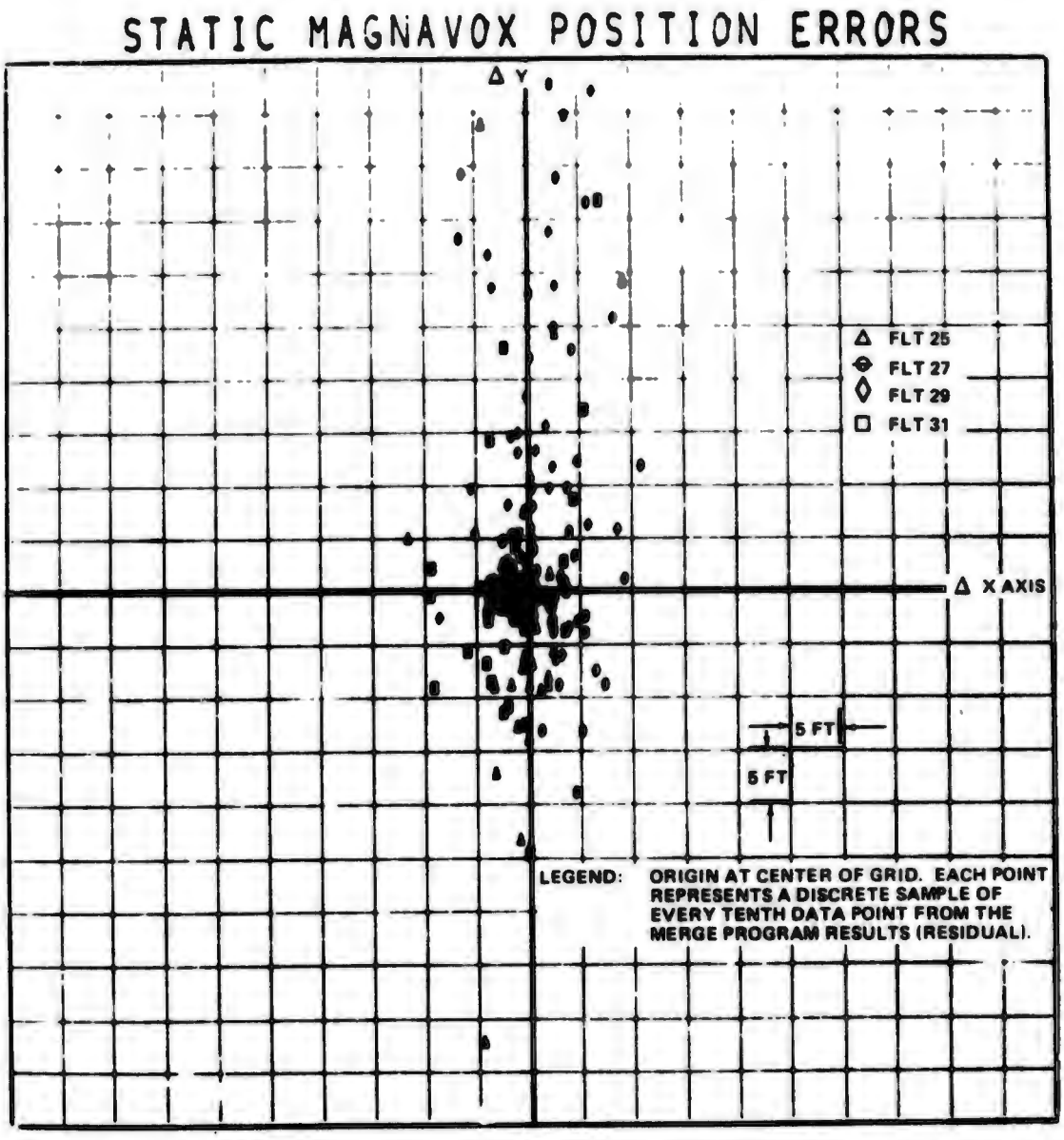

Figure 7-8 MRL Horizontal Position Errors for ILS Tests

where, at -140 dbm, $A = A_{min} = 1$, $T = 25$, $K_1 = 26.2$, $K_2 = 343.2$, $K_3 = 2248$ and the one sided loop noise bandwidth, $B_L = 10.9$ Hz. The loop gain constant, A, varies with received power as:

$$A = \begin{cases} A_{min}\, 10^{\frac{P_{received} - P_0}{20}}, & P_{received} < -115 \text{ dbm} \\ 17.8, & P_{received} > -115 \text{ dbm} \end{cases}$$

where $P_0 = -140$ dbm and $A_{min} = 1$

To evaluate the HC non-ideal third order linearized carrier tracking closed loop transfer function relating the phase error, $\phi(s)$, to a given input displacement, X(s), on a digital computer, the closed loop transfer function was expressed in terms of integrators by standard block diagram reduction techniques.

The closed loop transfer function is given by:

$$H_c(s) = \frac{s\left(s + \frac{1}{T}\right)^2}{s^3 + A(K_1 s^2 + K_2 s + K_3)} = \frac{\phi(s)}{X(s)}$$

which is shown in block diagram representation in Figure 7-9. This approach allowed the use of simple but accurate discrete integration routines in the solution of the closed loop response. The input to the simulation program consisted of a simulated time series of slant range trajectory data derived from the aircraft trajectory with respect to a particular transmitter.

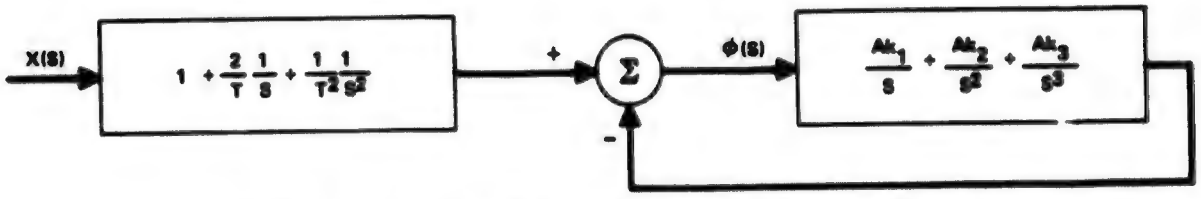

Figure 7-9 Expansion of the Closed Loop Transfer Function

We were able to evaluate the effects of relative dynamics from any one transmitter on the tracking performance of the carrier tracking loop. While the simulation was performed on the linearized equivalent mathematical model of the carrier tracking loop, the results can be related to the code tracking loop performance. With both the carrier and code loops of the same order, the simulation results may be related by the relative ratios of the one sided loop noise bandwidths. The code loop one sided noise bandwidth is 1.4 Hz, so the phase error in the code loop is related to the phase error in the carrier loop as:

$$\phi_{code} = \sqrt{\frac{B_{code}}{B_{carrier}}}\, \phi_{carrier}$$

substituting the respective bandwidths

$$\phi_{code} \simeq 0.36\, \phi_{carrier}$$

The loop phase error may be related to range rate error as:

$$\Delta\dot{R} = 0.1\,\phi_{carrier}\ ,\ \text{fps}$$

while for the code tracking loop the range error in terms of the loop phase error is given by:

$$\Delta R = 16\,\phi_{code}\ ,\ \text{ft}$$

The simulation results for the maximum tracking errors on ILS are shown in Figure 7-10. Note that the tracking errors follow the shape of the third derivative of range (jerk) along the line-of-sight (LOS) to a transmitter. The errors in both range and range rate are small. For the HC receiver the tracking errors due to relative dynamics reduce with increased signal level. The MRL tracking loop nominal noise bandwidths are equivalent to HC at -140 dbm. Therefore, the tracking performance of MRL should be comparable to the HC at -140 dbm and independent of power level. The exact MRL tracking error response due to dynamics, although not simulated, is expected to be somewhat smaller than that for the HC due to the different pole locations and ideal integrators used in the MRL digital implementation ($T = \infty$ in Figure 7-9), providing zero steady state errors to constant dynamic inputs. During the ILS flights, the maximum theoretical dynamics are given by:

$$\dddot{R}_M = \frac{48\,V_Y}{25\sqrt{5}\,r^2}\ ,\ \text{at } y = \frac{r}{2}$$

$$\ddot{R}_M = \frac{V_Y^2}{r}\ ,\ \text{at } y = 0$$

where V_Y is the horizontal component of the aircraft velocity (in the Y-direction) and r is the LOS distance to a transmitter; for the dynamics of the ILS test, the worst case values are:

$$\dddot{R}_M \simeq 13\ \text{fps}^3\ ,\quad \ddot{R}_M \simeq 62\ \text{fps}^2\ ,\quad \dot{R}_M \simeq 250\ \text{fps}$$

This analysis determined that the error induced in the range and range rate measurements from relative acceleration rate dynamics is considerably smaller than the thermal noise contribution and can thus be neglected.

7.2.3 Received Channel Signal Strengths

Just as we recognized that there would be appreciable signal dynamics in the ILS testing, we were also certain that there would be large variations in signal strengths as the aircraft passed by each of the transmitters. An analysis was performed to determine whether or not this phenomenon would adversely affect the tracking performance at the receivers.

As the aircraft approaches for a landing it passes by channel 1 about 1500 ft before the flare point. Figure 7-11 is a plot of the received signal level from channel 1 vs the Y position (position along the runway) of the aircraft.

As shown in Figure 7-11 there is peak (-110 dbm) in the channel 1 received power just before the flare point, which coincides with the analysis predictions. As the aircraft comes to the flare point, it is closest to channel 2. Figure 7-12 is a plot of the channel 2 received signal level vs the Y position of the aircraft and shows the power peaking at the flare point to about -116 dbm as expected.

The next transmitter the aircraft encounters is channel 3 about 1700 ft beyond the flare point. Figure 7-13 shows the power peaking for channel 3 as the aircraft passes by. The balloon-borne transmitter, channel 4, shows peak power at the aircraft, Figure 7-14, as the aircraft passes by the flare point.

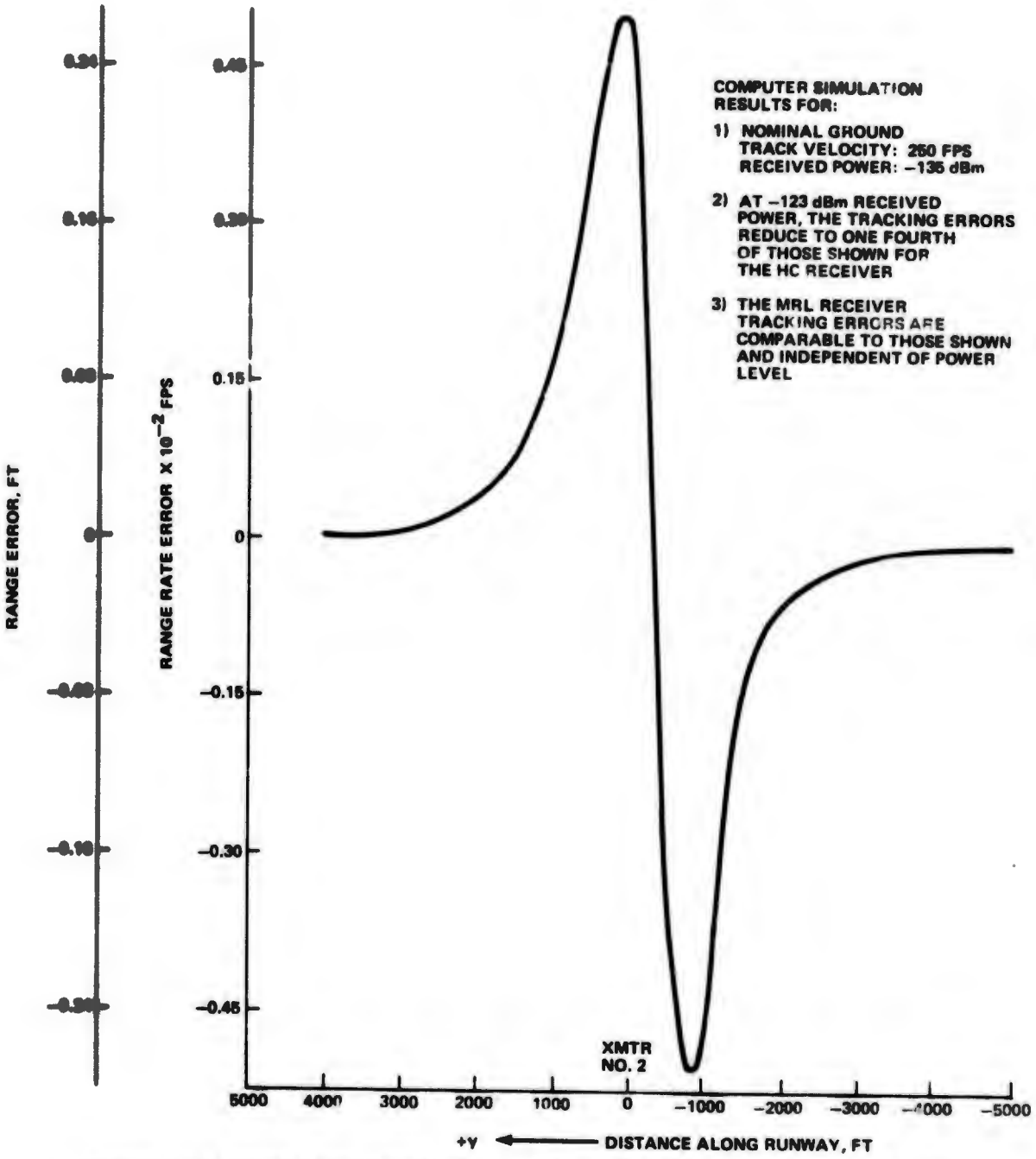

Figure 7-10 Worst Case Tracking Error From Relative Dynamics on ILS (At 135 dBm HC Loops)

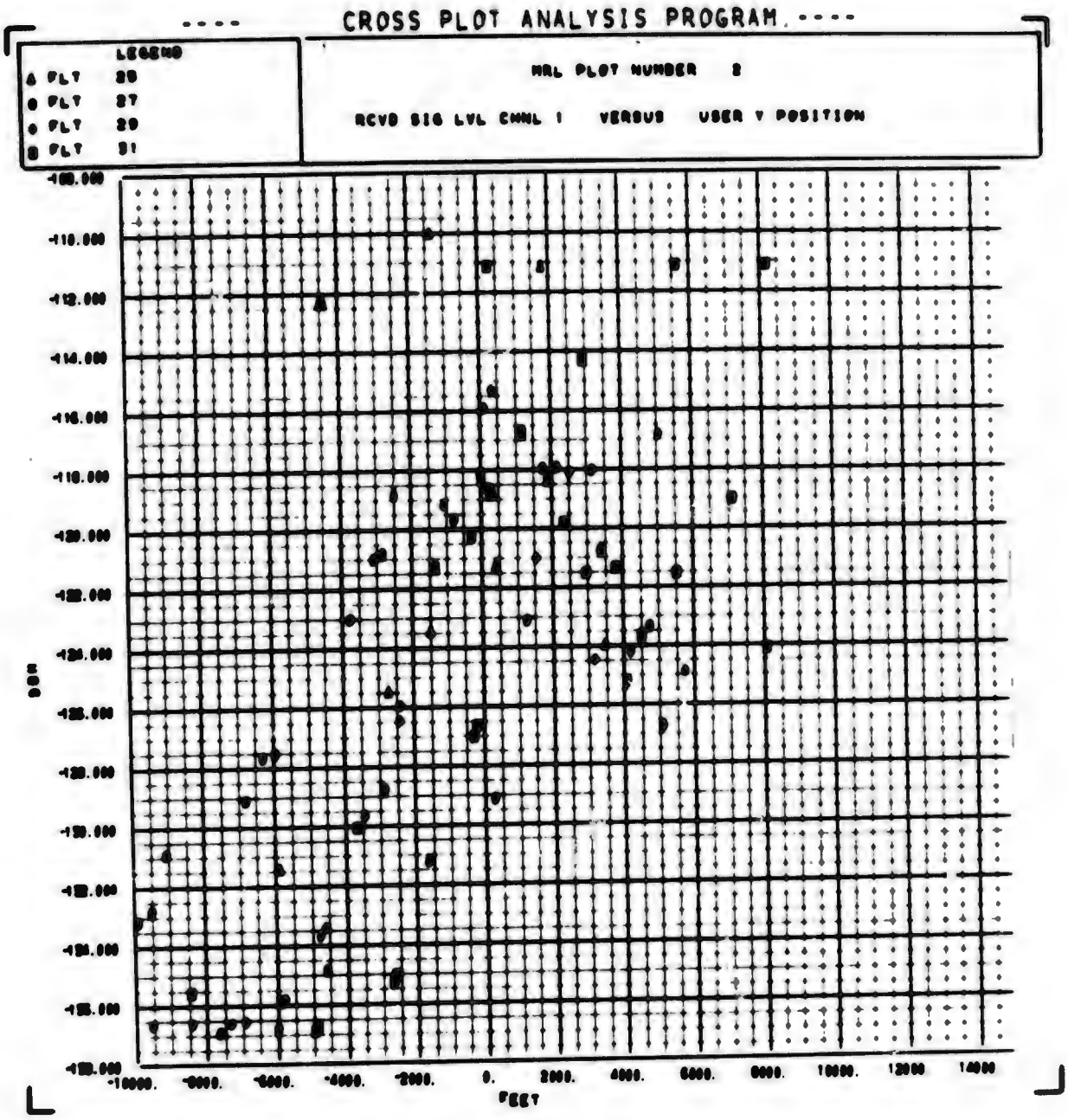

Figure 7-11 Signal Level Input to MRL Channel 1 vs Aircraft Position Along Runway Centerline

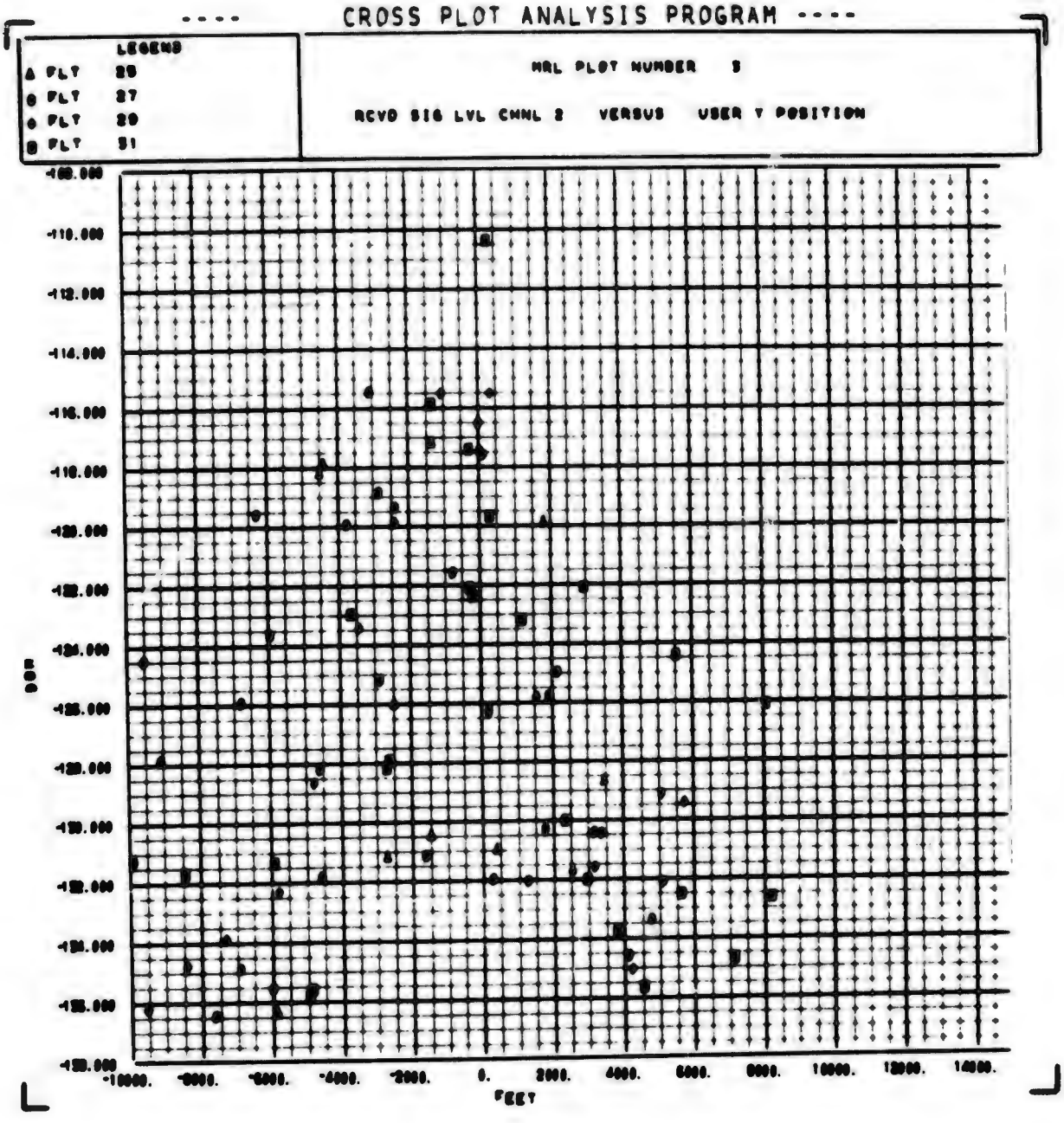

Figure 7-12 Signal Level Input to MRL Channel 2 vs Aircraft Position Along Runway Centerline

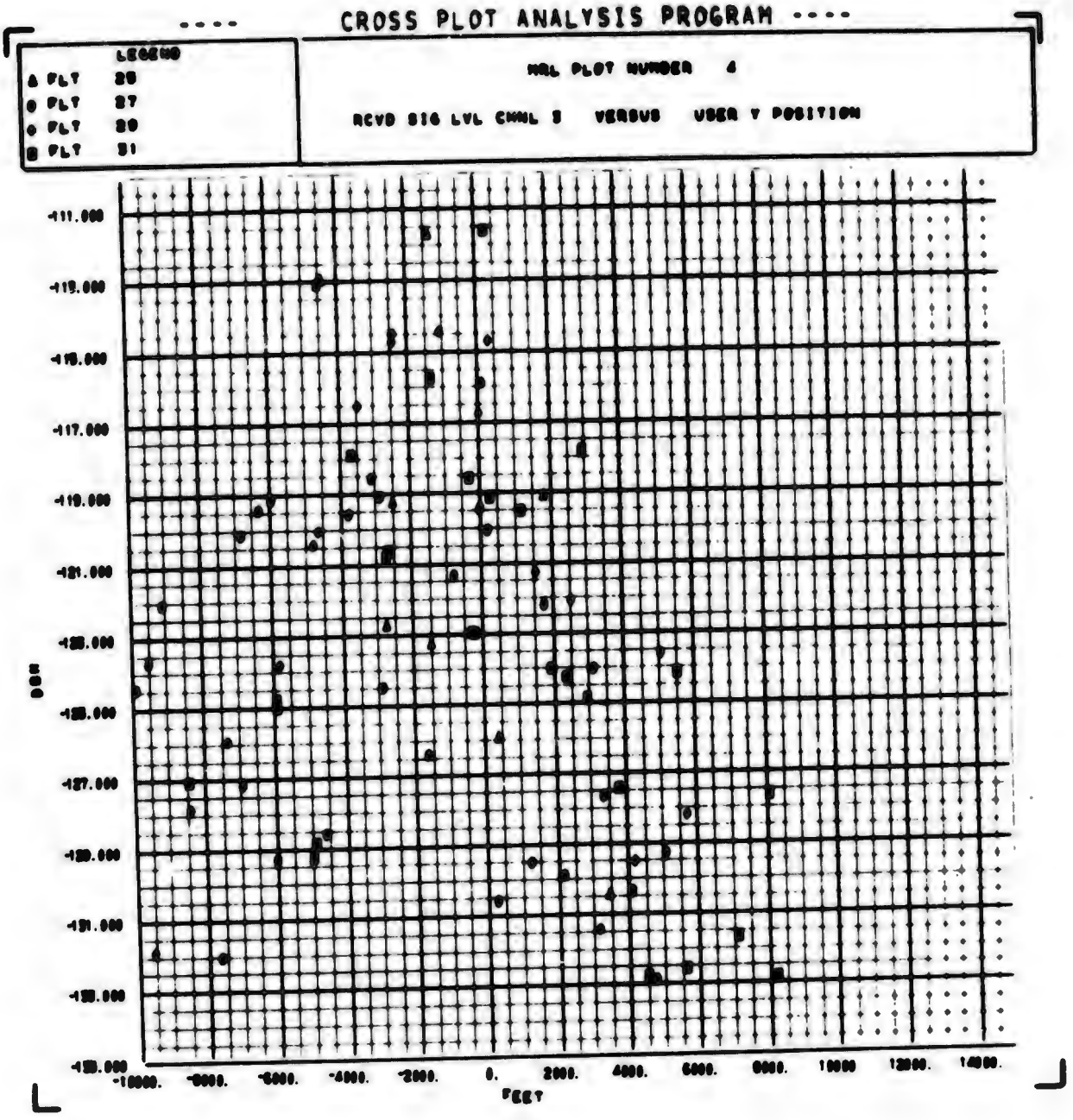

Figure 7 13 Signal Level Input to MRL Channel 3 vs Aircraft Position Along Runway Centerline

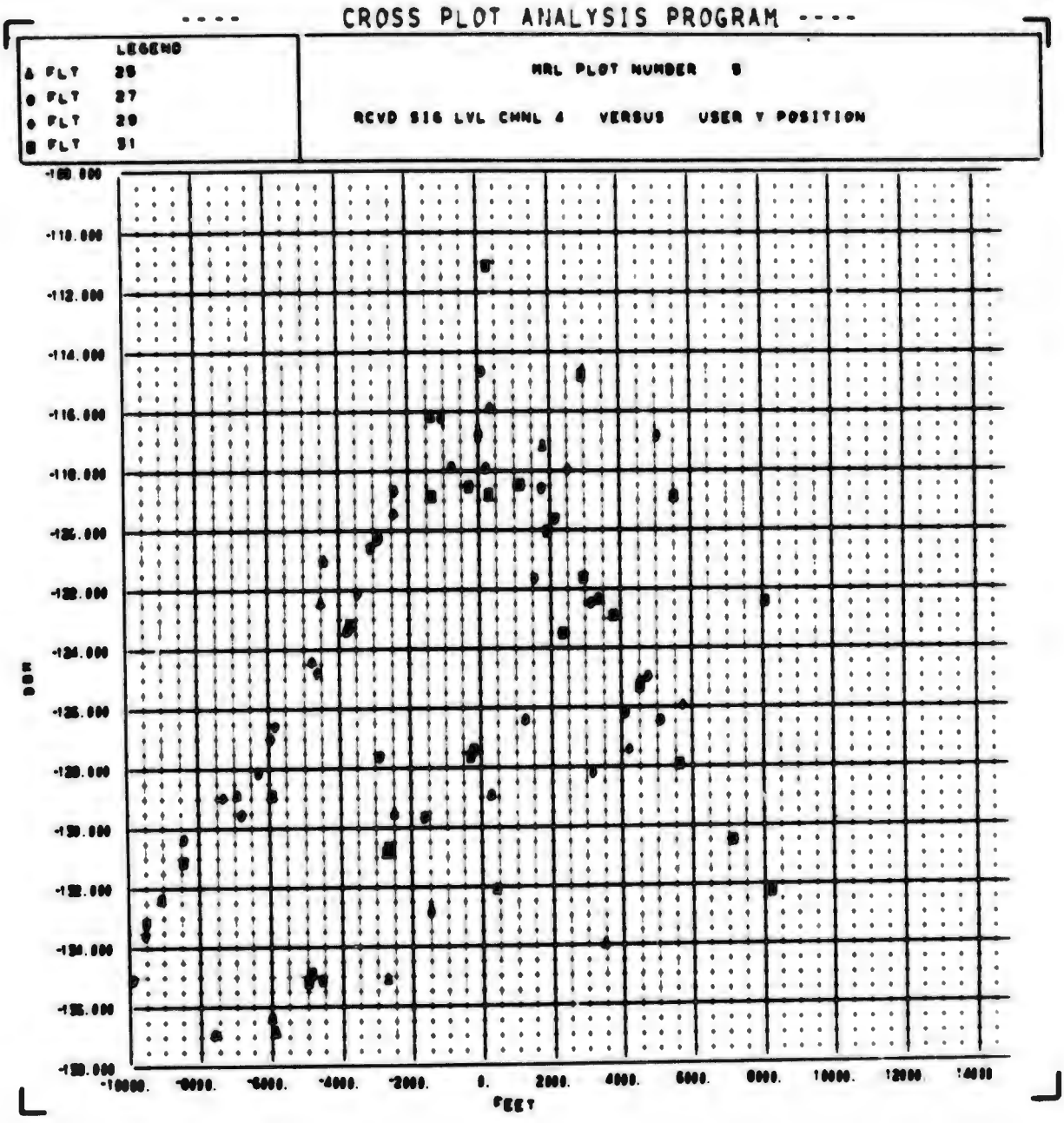

Figure 7-14 Signal Level Input to MRL Channel 4 vs Aircraft Position Along Runway Centerline

The next problem was to determine the effect of these large power variations on tracking accuracy. Figure 7-15 is a plot of the received signal level in channel 4 vs the residuals of the range differences. These residuals are generally flat indicating that the large variations in signal level had no effect on tracking accuracy.

The conclusion drawn from the analysis was that the magnitude of the received signal strengths followed the predicted signal strengths obtained by models of the ILS glide slope trajectory and the antennas. The wide variations in signal strength had no effect on the MRL receiver. Presumably the effect on the HC receiver was the same as that observed during area navigation although this could not be verified due to the presence of a multipath error discussed in the following paragraphs.

7.2.4 Multipath Environment During ILS

Multipath relections from the ground or aircraft structure cause periodic errors in both the range and range-rate measurements. A simple two-ray specular analysis of the effects of multipath on the code and carrier tracking loops has shown that a user moving with respect to the transmitters will create scintillations in multipath. Depending upon the relative geometry, the reflections can be either specular or diffuse, and will create either dominant single frequency or noise-like (multiple frequency) interference in the receiver tracking loops. To evaluate the degree to which multipath scintillations affect the measurements we determined the rate of change of delay between the direct and reflected signal paths (differential delay). The differential delay itself affects the magnitude of the error, while the rate of change of differential delay (which is a function of user's motion) times the free space wave number, called fade frequency or differential doppler, relates to the rate of scintillations (i.e. frequency) which are weighted by the tracking loop noise bandwidths.

The fade frequency is given by:

$$\Delta w = \frac{2\pi}{\lambda} \dot{d} \text{ , rad/sec}$$

where $\dot{d}$ is the rate of change of differential delay and λ is the free space wavelength of the source; $\dot{d}$ is a function of the relative geometry and user's motion.

The fade frequencies have been evaluated for the ILS flight geometry, and Δf ranges from approximately 0.1 to 0.6 Hz for transmitters 1, 2 and 3 and from approximately 1 Hz to 48 Hz for transmitter 4, which is located on a tethered balloon.

The amount of multipath rejection provided in a particular channel is a function of the relative geometry, antenna patterns, polarization effects and tracking loop noise bandwidths. Both the HC and MRL receiver tracking loop bandwidths are wider than a fraction of a Hz and therefore the multipath scintillations from transmitters 1, 2, 3 and at times from transmitter 4 should be present in the data from both receivers.

The HC receiver carrier tracking loop noise bandwidth varies with received power. The variation of loop noise bandwidth (single sided) can be expressed approximately as

$$B_L = \begin{cases} 10.9 \left[10^{\frac{P_{IN} - P_0}{20}}\right] \text{ Hz}, & P_{IN} < -115 \text{ dbm} \\ 194 \text{ Hz}, & P_{IN} > -115 \text{ dbm} \end{cases}$$

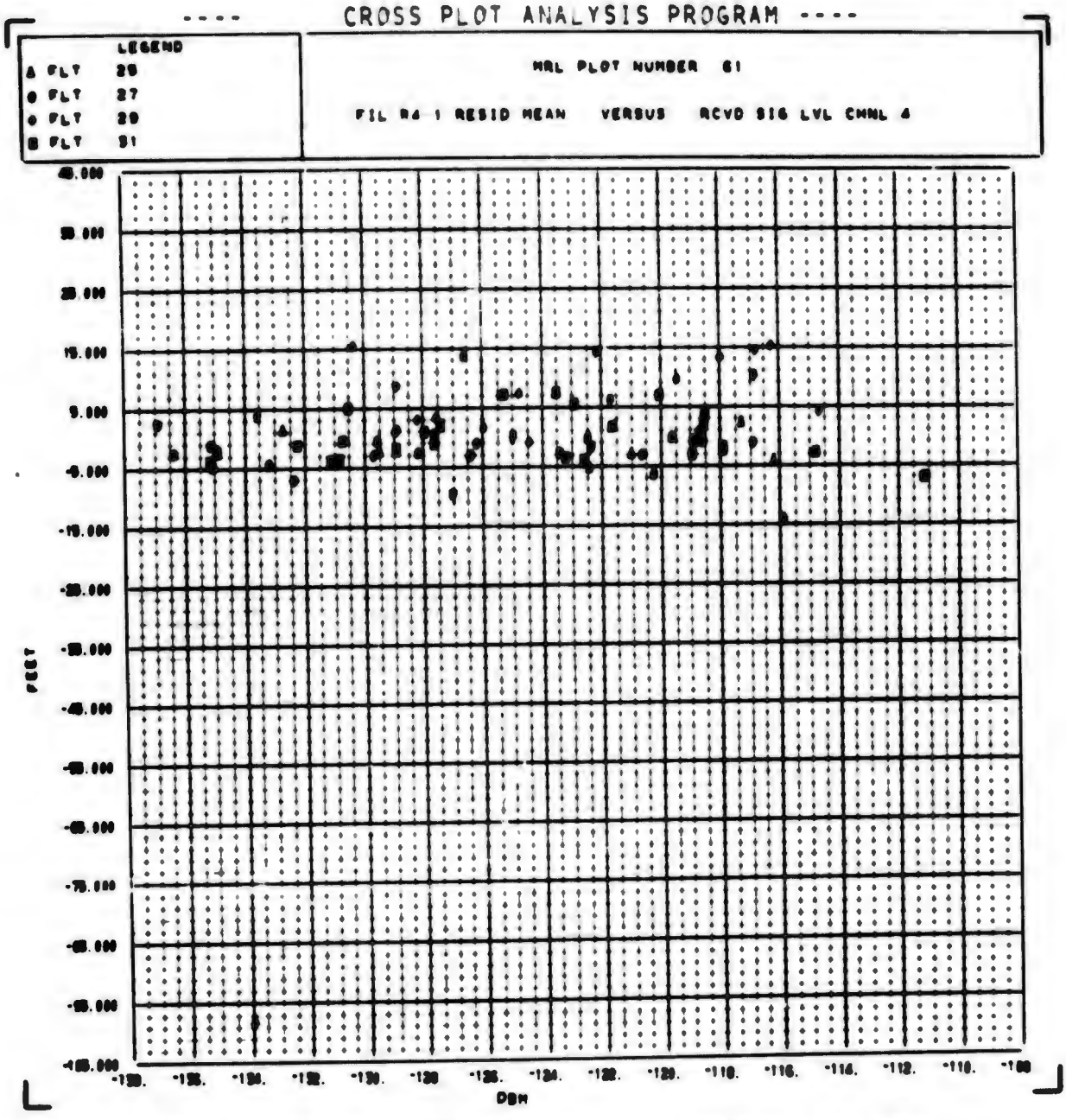

NOTE: FIL R_{4-1} RESID MEAN = [(FILTERED NAV SOLN R_4-R_1) – (WSMR BET R_4-R_1)] MEAN

Figure 7-15 Mean Error in Channel 4-1 Residual vs Channel 4 Signal Level

where P_Q = -140 dbm and P_{in} is the received power in dbm (e.g. at P_{in} = -140 dbm B_C = 10.9 Hz see Section 4). At a received signal strengths in the balloon channel of -120 to -130 dbm the HC carrier tracking loop single sided noise bandwidths are respectively 109 and 34.5 Hz which will pass the balloon transmitter-caused multipath at an average fade frequency of 24 Hz. At the same time the MRL receiver is not expected to respond to balloon caused multipath, since the MRL carrier tracking loop noise bandwidth is approximately 10 Hz (single sided) and is not a function of power level.

During the ILS flights, a cyclic variation of the Z-position residual highly correlated with the variation of the received power from the balloon transmitter (channel number 4) as a function of user Y-position was observed for the HC receiver.

A good example of this phenomena is shown in run 6 of flight 25. A plot of the static Z-position residual and the received power in channel 4 (balloon channel) as a function of user Y position, Figure 7-16, shows marked similarity to the multipath error and power plots of Section 9. As expected, this occurs only in the HC receiver data. On the same run, the channel 1 Z-position residual of both the HC and MRL receivers shows a slow cyclic variation at a rate of approximately 0.25 Hz as expected. Multipath errors are also exhibited in Z-velocity by differencing the MRL and HC static solutions (see Figure 7-17). The Z-velocity error (in the solution domain) is representative of the balloon channel (transmitter 4) measurement error which in this case is a characteristic of the transformation geometry between the two domains.

It is important to observe that the balloon channel multipath scintillation rate at times is very much above the data sampling rate of 5 sample/sec, representing a 2.5 Hz bandwidth system. Therefore, the highest frequency in the recorded data cannot exceed 2.5 Hz. The approximate frequency of Z-velocity differences between MRL and HC is in the range of 0.5 to 1 Hz, although the scintillations could have been as high as 48 Hz.

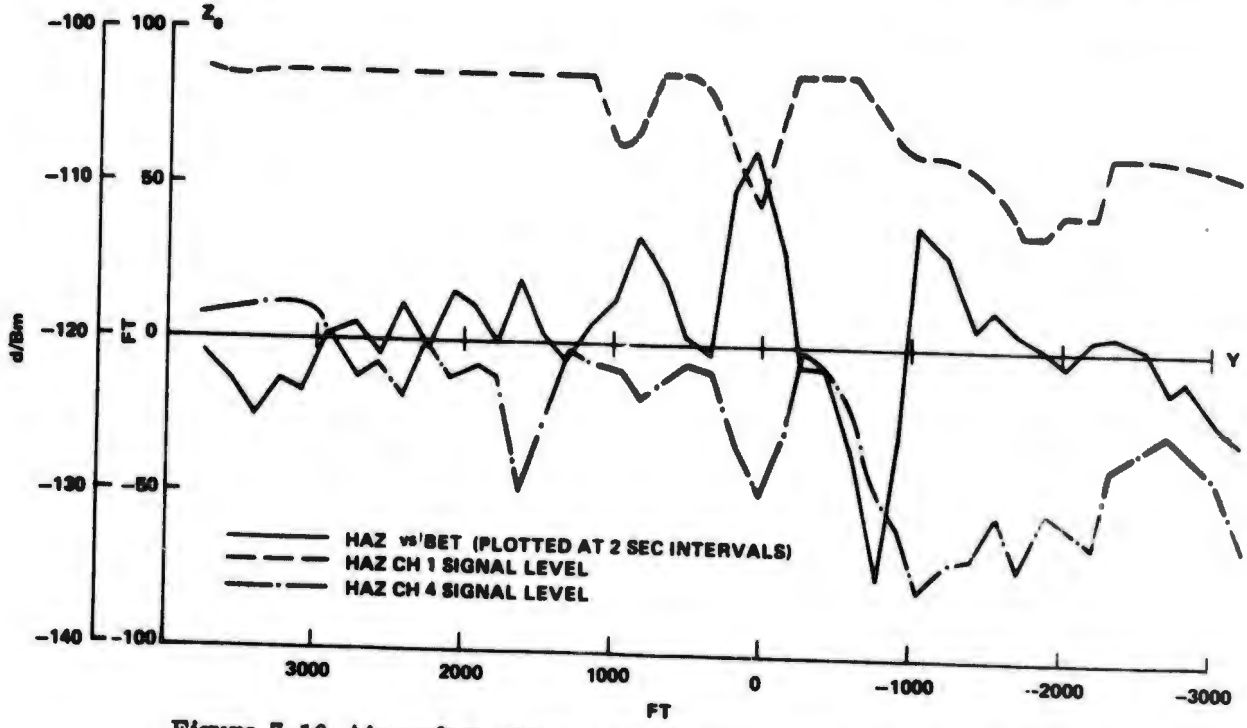

Figure 7-16 Aircraft Position Along Runway Centerline (Y Position)

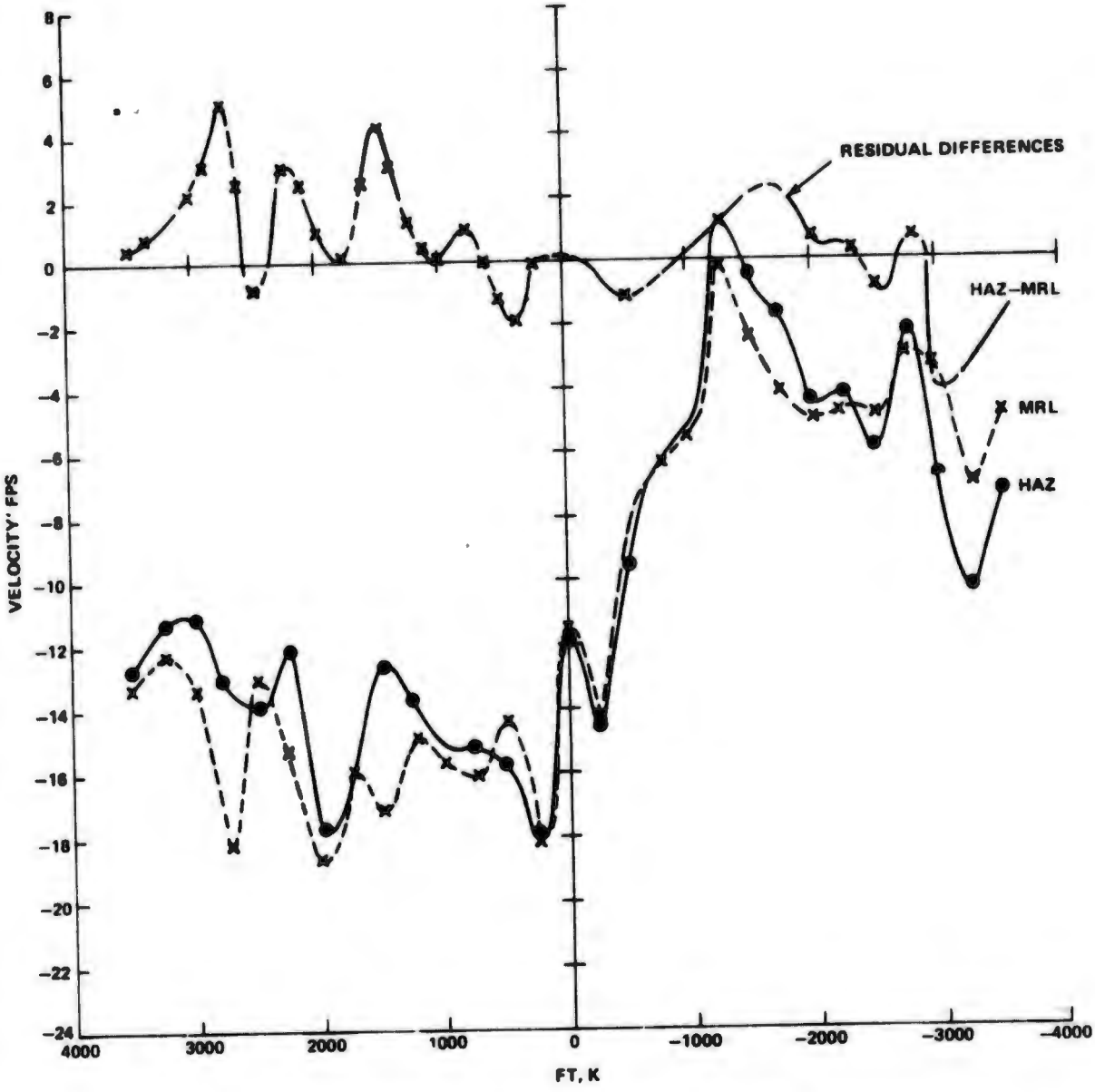

Figure 7-17 Static Solution Z - Velocity Residuals and Residual Difference Between HAZ and MRL, Flight 25 Run 6

7.3 SUMMARY

The ILS testing conclusively demonstrated the suitability of the system in an aircraft landing environment. The mean error for vertical position was about 1.5 ft and for vertical velocity less than 0.5 fps. These are representative of absolute errors with a filtered solution. This quality of system performance is more than adequate for landing and the test results indicate that the signal environment (large dynamics, large changes in power, and multipath effects) during this phase of aircraft operation do not degrade the navigation accuracy.

SECTION VIII

ANALYSIS OF EQUIPMENT FAILURES THAT OCCURRED DURING FIELD TESTING

In order to have a successful flight (obtain useful trajectory data), several hardware items must function properly and certain events must occur. A failure in some hardware components may only degrade the data, while other types of failures will result in complete loss of data or in fact prevent a flight from occurring. As a minimum the following items had to be available and operational for a successful flight:

- Airborne Equipment
  - Aircraft (NC-135) (GFE)
  - At least one airborne 621B receiver
  - Interface Unit
  - Recording System (GFE)
  - Timing System (GFE)
- Ground Equipment
  - Calibration 612B receiver
  - Data Acquisition System and Recording System
  - Timing System (GFE)
  - Four Transmitters and Antennas

In addition, for the ILS test phase a transmitter and antenna were carried aloft by a balloon (GFE).

- WSMR tracking instrumentation and reference trajectory (BET)
- Data reduction facility and software.

8.1 MISSION SUCCESS RATE

It became apparent that a high mission success rate could not be achieved simply by specifying a high predicted Mean Time Between Failure (MTBF) for the 621B receivers and transmitters, since the receivers and transmitters were only two very important items in a serial chain of equipments and operations that were required for a successful mission. Table 8-1 is a summary of 31 attempts to obtain data (flights). Note that ten flights did not yield useful data, for an indicated mission success rate

of approximately 68%. For example, two flights were aborted because of aircraft failure; on one flight no data was obtained because of balloon equipment failure and on several flights the airborne recorders failed.

8.2 HAZELTINE EQUIPMENT FIELD FAILURE ANALYSIS

The failures during field testing are treated in two categories: those which directly affected the complete success of flights and failures during ground test, routine maintenance and flight tests. The former is subdivided into the categories of receiver availability and loss of data including a tabularized analysis by flight. The latter is presented by type of failure associated with a major system component.

Table 8-2 is a summary of all equipment failures grouped in broad categories with the cause, number of flights affected, and detectability of the failure listed. These failures are not the receiver alone but rather include the equipment required to achieve good recorded data. Flights where only partial data was acceptable are included in this table.

Table 8-3 is an overall analysis and history of failures which are summarized in Table 8-2. Each failure is listed with corrective actions taken.

Trends which are indicated by this analysis show that two problems existed in the Mobile Calibration Station (MCS) receiver frequency synthesizer causing loss of data and repeated failure of the receiver. The major problem has been a marginal design on the 15 MHz board. Changes in the 15 MHz level due to aging of components, vibration, etc., may result in insufficient drive on the following multipliers causing either a spurious mode of operation or no output. The subsequent receiver failure may be indicated by loss of doppler data, inability to lock on self test or loss of lock on all channels caused by a loss of, or noisy 90, 75 or 1.125 MHz signals, respectively.

A second problem which existed in the 1.125 MHz chain which has been masked by the 15 MHz problem was detected and corrected in October. In the 1.125 MHZ multiplier chain a multiplier driven by the 15 MHz was tuned at a point which was sensitive to input level causing excessive warm-up time and possible intermittent dropping of all channels. This has been returned to a stable mode and this problem has not been observed in subsequent receiver operation.

Data losses which were a result of defective synthesizers, intermittent connectors, etc., were not always detected until printouts of the data were examined. A certain percentage of this type of failure was detected during the pre-flight checkouts by examining the serial data stream to the recorders and were corrected. However, since it was not possible to monitor the data stream during the flight and the intermittency of the problem, a large percentage of these failures were not discovered until post flight data analysis occurred. At the MCS (ground calibration receiver location) where it is possible to monitor the data stream, the test set is being modified, to permit this mode of operation during future use of the equipment.

The preceding discussion dealt with failures which directly affected the results of scheduled flights. Total failures must be examined for an indication of the operating equipment failure rate versus operating hours. Table 8-4 lists the specific failed components normally considered in a reliability predication, as well as other failures such as broken wires, retuning circuits and open/short circuits. This table covers the period January to October, 1972, during which an estimated 3000 and 6000

Table 8-1 D

Flt. No.	Date	OD No.	Flight Profiles	Data Runs	Non-Data Runs	Receiver Status (MRL, HAZ, CAL)	Recorder Status (GFE)	XMTTR Status (HC)	IU Status (GAC)	Sensors Used In BET (WSMR)	C (N
1.	3/7/72	04	A,C,Descent	0	9	CAL NO-GO	LTN-51 Recorder No-Go	Okay	A/D Converter Malfunctioned	N/A	
2.	3/21/72	04	A,C,Descent	0	6	MRL,HAZ. NO-Go*	*MRL,HAZ Recorders No-Go	Okay	Okay	N/A	
3.	3/28/72	04	A,C,Descent	11	1	MRL GO HAZ GO* CAL GO	*HAZ Recorder No-Go	Okay	Okay	Optics, Radar	
4.	4/6/72	04	A,C,Descent	9	0	MRL GO HAZ NO-GO	Okay	Okay	Okay	Optics, DOVAP, LTN-51	
5.	4/7/72	02	A,B,C,Descent	0	9	MRL GO HAZ GO CAL GO*	*CAL MAG Tape Ruined	Okay	Okay	–	
6.	4/12/72	07	A,C,D,Ascent	0	7	CAL No-Go	LTN Recorder No-Go	Okay	Okay	–	
7.	4/13/72	01	A,B',C,Descent, Orbit	4	5	CAL (No-Go Runs 5-9)	Okay	Okay	Okay	DOVAP, LTN-51	
8.	4/27/72	02	A,B',C,Descent	12	0	MRL GO HAZ GO (HAZ In MCS) CAL No-Go	Analog No-Go	Okay	Okay	Optics, DOVAP LTN-51	
9.	5/1/72	04	A,C,Descent	9	0	MRL GO HAZ NO-GO CAL GO	Okay	Okay	Okay	DOVAP, LTN-51	
10.	5/4/72	04	A,C,Descent Runs 8&9 Ran Perpendicular to A path	9	0	Okay	Okay	Okay	Okay	Optics, DOVAP, LTN-51, Radar	
11.	5/9/72	08	D,Ascent	5	1	Okay	Okay	Okay	Okay	Optics, DOVAP	
12.	5/10/72	08	C,Ascent	0	8	MRL GO CAL-No-Go HAZ GO*	*HAZ Recorder No-Go	Okay	Okay	–	
13.	5/13/72	06	Cloverleaf, 90 degree turns	8	0	MRL GO HAZ-No-Go CAL GO	Okay	Okay	Okay	Optics, DOVAP	
14.	5/17/72	03	A, B, C, Ascent	12	1	MRL GO HAZ-No-Go CAL GO	Okay	Okay	Okay	DOVAP, LTN-51	
15.	5/19/72	05	B; Clouds forced A/C to fly at 24K' MSL. (This was a deviation)	13	0	Okay	Okay	Okay	Okay	Optics, LTN-51 Radar	
16.	6/7/72	04	A/C Did Not Take-Off	0	0	–	–	–	–	–	
17.	6/14/72	06	A,B'	2	5	CAL-No-Go	Okay	Okay	Okay	DOVAP LTN-51	

*Recorder failure
–Flights resulting in no data
**Flight 16 is a misnomer, the mission was cancelled just prior to takeoff
***Flights producing good quality 621B data, but satisfying duplicate test points

Table 8-1 Detailed Flight Breakdown

ight rofiles	Data Runs	Non-Data Runs	Receiver Status (MRL, HAZ, CAL)	Recorder Status (GFE)	XMTTR Status (HC)	IU Status (GAC)	Sensors Used In BET (WSMR)	Quality of BETS (WSMR)	Test Points Fulfilled
,Descent	0	9	CAL NO-GO	LTN-51 Recorder No-Go	Okay	A/D Converter Malfunctioned	N/A	–	1,2,3,6,7
,Descent	0	6	MRL,HAZ. NO-Go*	*MRL,HAZ Recorders No-Go	Okay	Okay	N/A	–	–
,Descent	11	1	MRL GO HAZ GO* CAL GO	*HAZ Recorder No-Go	Okay	Okay	Optics, Radar	Poor- (Tgt. Uncertain)	4,9,10
,Descent	9	0	MRL GO HAZ NO-GO	Okay	Okay	Okay	Optics, DOVAP, LTN-51	Poor (Tgt. Uncertain)	•••
,C,Descent	0	9	MRL GO HAZ GO CAL GO*	*CAL MAG Tape Ruined	Okay	Okay	–	–	9•••
,D,Ascent	0	7	CAL No-Go	LTN Recorder No-Go	Okay	Okay	–	–	–
',C,Descent,	4	5	CAL (No-Go Runs 5-9)	Okay	Okay	Okay	DOVAP, LTN-51	Fair	5
',C,Descent	12	0	MRL GO HAZ GO (HAZ In MCS) CAL No-Go	Analog No-Go	Okay	Okay	Optics, DOVAP LTN-51	Good	•••
,C,Descent	9	0	MRL GO HAZ NO-GO CAL GO	Okay	Okay	Okay	DOVAP, LTN-51	Fair	14,19,20,15, 16,21,22
,Descent Runs Ran Perpen- ular to A path	9	0	Okay	Okay	Okay	Okay	Optics, DOVAP, LTN-51, Radar	Good	55,56,72,73, 57,58
Ascent	5	1	Okay	Okay	Okay	Okay	Optics, DOVAP	Poor (Low Altitude)	35,36,77,41
Ascent	0	8	MRL GO CAL-No-Go HAZ GO*	*HAZ Recorder No-Go	Okay	Okay	–	–	–
verleaf, degree turns	8	0	MRL GO HAZ-No-Go CAL GO	Okay	Okay	Okay	Optics, DOVAP	Good	76,63,61,62, 89,88
B,'C, Ascent	12	1	MRL GO HAZ-No-Go CAL GO	Okay	Okay	Okay	DOVAP, LTN-51	Fair	66,67,42,29, 30,27,33,17, 18,23,24
Clouds forced to fly at ' MSL. (This a deviation)	13	0	Okay	Okay	Okay	Okay	Optics, LTN-51 Radar	Fair	•••
Did Not ke-Off	0	0	–	–	–	–	–	–	–
'	2	5	CAL-No-Go	Okay	Okay	Okay	DOVAP LTN-51	Fair	92,93

ancelled just prior to takeoff
, but satisfying duplicate test points

Table 8-1 Detailed Flight Breakdown (Concluded)

Flt. No.	Date	OD No.	Flight Profiles	Data Runs	Non-Data Runs	Receiver Status	Recorder Status (GFE)	XMTTR Status	IU Status	Sensors Used in BET
18.	6/20/72	04	A,C	7	0	Okay	Okay	Okay	Okay	Optics, DOVA LTN-51
19.	6/22/72	04	A,Descent	7	1	Okay	Okay	Okay	Okay	Optics, DOVA LTN-51
20.	6/26/72	04	A	12	0	CAL GO MRL-No-Go (CH2) HAZ GO	Okay	Okay	Okay	Optics, DOVA LTN-51
21.	6/28/72	03	D(A/C Hit Buzzard and Aborted Mission)	0	1	–	–	–	–	–
22.	7/27/72	05	B	12	2	Okay	Okay	Okay	Okay	Optics, DOVA LTN-51
23.	8/1/72	07	D	4	5	MRL GO HAZ GO CAL (No-Go, Runs 7-9)	Okay	Okay	Okay	Optics, DOVA LTN-51
24.	8/16/72	09	ILS/Fly By	0	5	MRL GO HAZ (In MCS) GO	Okay	Okay	Okay	–
25.	8/18/72	09	ILS/Fly By	8	2	Okay	*HAZ Primary No-Go, HAZ Secondary OK	Okay	Okay	Optics
26.	8/20/72	09	ILS/Fly By	0	4	HAZ&MRL Could Not Look. CAL did lock	Okay	CH 2 No-Go	Okay	–
27.	8/25/72	09	ILS/Fly By	8	4	MRL Go Haz-No-Go	Okay	Okay	Okay	Optics
28.	8/27/72	09	ILS/Touchdown	0	12	MRL GO HAZ-No-Go CAL GO	*MRL-Recorder No-Go	Okay	Okay	–
29.	8/28/72	09	ILS/Touchdown	6	0	MRL GO HAZ-No-Go CAL GO	Okay	Okay	Okay	Optics
	8/29/72	09	ILS/Touchdown	2	1	Okay	Okay	CH 4 Battery Depleted	Okay	Optics
31.	8/30/72	09	ILS/Touchdown	7	1	MRL GO HAZ GO* CAL Power Supply Malfunctioned After Run 7	*HAZ-Recorder Malfunction (No HAZ Secondary Recorder)	Okay	Okay	Optics

NOTES:

*Recorder failure

–Flights resulting in no data

•••Flights producing good quality 621B data, but satisfying duplicate test points

Receiver Status	Recorder Status (GFE)	XMTTR Status	IU Status	Sensors Used in BET	Optimum BETS	Test Points Fulfilled
Okay	Okay	Okay	Okay	Optics, DOVAP, LTN-51	Good	•••
Okay	Okay	Okay	Okay	Optics, DOVAP, LTN-51	Good	13,26,66,69, 43,83
CAL GO MRL-No-Go (CH2) HAZ GO	Okay	Okay	Okay	Optics, DOVAP, LTN-51	Good	31,32,64
–	–	–	–	–	–	–
Okay	Okay	Okay	Okay	Optics, DOVAP, LTN-51	Poor (Bad Optics)	59,75,96,68, 100,101,38,60
MRL GO HAZ GO CAL (No-Go, Runs 7-9)	Okay	Okay	Okay	Optics, DOVAP, LTN-51	Poor (Bad Optics Low Altitude)	28,51,80
MRL GO HAZ (In MCS) GO	Okay	Okay	Okay	–	–	–
Okay	*HAZ Primary No-Go, HAZ Secondary OK	Okay	Okay	Optics	Good	1,4,5,3 (ILS)
HAZ&MRL Could Not Lock. CAL did lock	Okay	CH 2 No-Go	Okay	–	–	–
MRL Go Haz-No-Go	Okay	Okay	Okay	Optics	Poor	•••
MRL GO HAZ-No-Go CAL GO	*MRL-Recorder No-Go	Okay	Okay	–	–	–
MRL GO HAZ-No-Go CAL GO	Okay	Okay	Okay	Optics	Poor	6,7,8,9 (ILS)
Okay	Okay	CH 4 Battery Depleted	Okay	Optics	Poor	10 (ILS)
MRL GO HAZ GO* CAL Power Supply Malfunctioned After Run 7	*HAZ-Recorder Malfunction (No HAZ Secondary Recorder)	Okay	Okay	Optics	Good	11,15,16 (ILS)

b test points

hours have been accumulated on the two 621B receivers and four transmitters, respectively. Failures occurring prior to shipping the equipment to the field in January have not been considered, nor have the additional operating hours accumulated prior to field testing.

Based on the failure counts and 3000 hours operation, this receiver indicated MTBF is 40 hours as compared to a predicted 200 hours. Similarly, the transmitter indicated MTBF is 400 hours based on 6000 hours as compared to 2770 hours predicted.

Table 8-2 Summary Analysis of Flight Test Failures

Failure Category	Cause	No.	Detectable
Airborne Receiver Not Available for Flights	MCS Rcvr Synthesizer	3	N/A
	Airborne Rcvr Synthesizer	1	N/A
	Airborne Rcvr VCXO's	2	N/A
Airborne Data Failure	Failed IC	3	Yes
	Erratic Coax Pin (Probable)	1	Yes
Airborne Recorder Failure (GFE)	Unknown	5	Unknown
MCS Data Failure	Broken Wire	1	Yes
	MSC Rcvr Synthesizer	2	Yes
	Erratic Coax Pin (Probable)	2	Yes
	Noisy	1	No
Transmitter Shut Down During Flight	Battery Failure	3	Unknown

Table 8-3 Failure Analysis

	Failure	Rcvr	Flight
1.	Processor 6 (channel 3) failed to lock prior to start of first run. Determined to be an intermittent short under a board. Program connector was put in spare Processor 7 during which a wire was broken. Printout showed missing fine doppler and range.	MCS Rcvr 1	1
2.	No doppler data from Processor 2 (channel 1). Suspected erratic coax pin.	MCS Rcvr 2	2A
3.	Receiver would not lock caused by failed synthesizer. Traced to a burned resistor.	AIR Rcvr 1	4
4.	Erratic doppler data due to noisy 90 MHz from synthesizer. Recurred during last half of flight. Returned F.E.I. where 15 MHz was retuned. Both units were checked out including operation with temperature, vibration and power supply variation. The MCS receiver synthesizer was returned for bad 90 MHZ and was for low 100 MHz. The airborne receiver was used in the MCS during this cycle and two flights were lost.	MCS	6 P/07

Table 8-3 Failure Analysis (concluded)

	Failure	Rcvr	Flight
5.	Fine range bad on Processor 5 (channel 2). No cause was ever determined and suspect erratic co-ax pin.	AIR Rcvr 1	9
6.	Doppler bad on Processor 2 (channel 1). No cause was ever determined and suspect erratic co-ax.	MCS Rcvr 2	12
7.	Two flights missed for the airborne receiver when three VCXO failures occurred following transporting from the HAFB shop to the MCS for testing. All had mechanical type failures probably due to severe vibration/shock during transportation.	AIR Rcvr 1	13 & 14
8.	Doppler data erratic for 5 runs caused by noisy 90 MHz. Returned to F.E.I. for returning of 15 MHz.	MCS Rcvr 2	17
9.	Receiver dropping lock intermittently. Determined to be noisy 1.125 MHz. No loss of data on flights. Returned after flight 19 to F.E.I. where 15 MHz was retuned.	MCS Rcvr 2	18 & 19
10.	Receiver developed bad synthesizer prior to flight 24 and was returned to F.E.I. for repair. When returned to HAFB the 75 MHz was found to be erratic. F.E.I. found that the15 MHz had been mistuned and was jumping to an oscillatory mode. Airborne receiver was used in MCS and missed Flight 24.	MCS Rcvr 2	24
11.	Coarse range bad on Processor 5 (channel 2). Discovered after looking at data printouts. Was easily detected on the Test Set and should have been found during preflight for flight 26. Data loss due to failed IC chip.	AIR Rcvr 1	26,27 & 28
12.	Processor 1 (channel 1) would not lock on self test code but was ok on code A. This problem first appeared during pre-flight for 28, but cleared itself. All controls were reaching IC's but code changeover did not occur because of a failed IC chip.	AIR Rcvr 1	29
13.	The receiver developed a problem in which all channels dropped simultaneously and then reacquired at the next COP. Due to the intermittent nature of the problem, the cause could not be determined. Subsequently, excessive time was required before the receiver could achieve lock. On 9/3/72 all outputs of the synthesizer were observed and found to be normal except the 1.125 MHz which was noisy. Tuning of the 15 to 45 MHz multiplier corrected this problem. Circuit component aging caused the multiplier to be sensitive to the 15 MHz input in that it went to a spurious oscillatory mode when the 15 MHz was at a "low" amplitude. Receiver dropping lock has not been reported since tuning. A power supply failure occurred prior to run seven of flight 31, a diode had failed.	MCS Rcvr 2	20, 25 & 31

Table 8-4 Detailed Failures

Equipment	Component/Type Failure	Air	MCS	Failures
Receiver	Analog I.C.	2	1	3
	Digital I.C.	4	2	6
	Zener Diode	1	0	1
	Coil	3	0	3
	Potentiometers	2	1	3
	Varicap Diode	1	0	1
	Resistor (RC07)	1	0	1
	Capacitor (CK21)	2	0	2
	Co-ax Pins	7	4	11
	Matched Filter	0	1	1
	Shorts, opens, retuming broken wires, etc.	18	15	33
	TOTAL	41	24	65
Power Supply	Rectifier Diodes	3	2	5
	Capacitor, Alum. Electrolytic	0	1	1
	TOTAL	3	3	6
Transmitter	Balanced Modulator	N/A	N/A	1
	Power Splitter	N/A	N/A	3
	5 MHz Oscillator	N/A	N/A	5
	Power Supplies	N/A	N/A	5
	Potentiometer	N/A	N/A	1
	Broken wires, retuming, etc.	N/A	N/A	4
	TOTAL	N/A	N/A	15

8.3 DAS EQUIPMENT FAILURE

A mishap occurred at the MCS during flight 5 which prevented a 621B trajectory from being obtained. A recycled tape which had been recertified by KAFB, had been used. Post flight data analysis revealed the tape was overprinted with spurious information making it unreadable. As a result of this incident, it was decided to use only virgin tapes for all subsequent flights. A reoccurrance of this problem was not encountered during the remainder of the flight program.

8.4 MRL RECEIVER FIELD FAILURE ANALYSIS

The following has been extracted from SAMSO TR-72-213, a report generated by MRL.

The MX-450 Navigation Receiver failed during flights 2 and 20 during the field test and two additional failures occurred during bench testing. Total operating time was estimated as being 1400 hours.

8.5 PREDICTED/INDICATED MTBF

Refer to Table 8-5 for a summary of predicted/indicated MTBF for all 621B receiver and transmitter equipment used during the flight test program.

Table 8-5 Summary of Predicted/Indicated MTBF

Equipment	Predicted MTBF	Indicated MTBF
Haz. Receiver	200 hr	46 hr
Haz. Transmitter	2,770 hr	400 hr
MRL Receiver	369 hr	*350 hr

*Estimated on reported failures during 1400 hr of operation

SECTION IX

GROUND USER MULTIPATH DATA ANALYSIS

9.1 INTRODUCTION

The overall objective of the multipath test was to evaluate the sensitivity of a 621B-type receiver to multipath signals from typical ground environments. Multipath signals degrade the ranging accuracy of the receiver by creating a distortion of the modulation envelope of the total received signal. This develops an error in the receiver code tracking loop which effects the range measurement accuracy.

Establishing a valid multipath test required:

- Determination of a test geometry to simulate radiation received from a satellite
- Sufficient variety of topographical features
- Selection of test signal levels to insure that the multipath signal is above the threshold sensitivity of the receiving system.

Broadly speaking, multipath effects are created by ground reflections of signals and by signal scattering from both natural and man-made localized obstacles. Ground reflections originate from either dry or moist soil or from water and can be classified as smooth or rough. Natural localized obstacles are typified by rocks or boulders and by dense foilage. Man-made obstacles include buildings, fences, communications lines, and moving vehicles.

The severity of a multipath is measured by the relative amplitudes of the direct and reflected signals, the phase angles of the two signals, and the differential delay between the two signals. Signals exhibiting various values of these characteristics can be generated by selecting different types of reflective surfaces and by choosing various geometries for the transmitting and receiving antennas.

Four test sites were used at the White Sands Missile Range (WSMR). These typified certain classes of ground reflection environments; smooth and rough earth, small natural obstacles, and man-made obstacles. To simulate various satellite transmitter positions, elevation angles from receiver to transmitter of 5^{o}–60^{o} were included in these tests. The tests were conducted using a balloon-borne transmitter at approximately 2000 ft above ground level (AGL) for the high elevation angles, and using a transmitter antenna 10 to 20 ft above ground level for the lower angle geometries. In each case, the test configuration was sufficiently controlled to achieve an accurate measure of the differential range, effective reflecting area (first Fresnel zone) and grazing angle to permit an evaluation of the test results.

9.1.1 Relationship of the Multipath Tests to an Operational Situation

There are a number of points to be made about the characteristics of the multipath tests conducted at WSMR and the characteristics of an operational satellite situation. The WSMR tests specifically addressed situations typical of a class of ground users. These ground users are essentially motionless while making measurements from the system. Care must be used in attempting to extend these test results to other classes of users. The following paragraphs point out some important multipath characteristics not simulated in the WSMR tests which are inherent in some classes of users.

There is a difference between the ground tests and the satellite system for users making measurements while in motion. In an actual situation, the path length difference between the direct and reflected ray (differential delay) changes with time due to user motion. This causes the net received signal strength to pass through a series of maxima and minima. The rate at which the two signals "beat" against one another in this manner is called the fade frequency or differential doppler for smooth earth reflections. In a rough earth area geometry the fade frequency becomes the highest beat frequency between the direct signal and the individual components of the scattered signal, which also contains the frequency products from mixing of the scattered signal components. In this case one has to define a fading bandwidth rather than a "signal" fade frequency as in the smooth earth case (Ref. 37). Hence, in a dynamic system the range and range rate errors become a function of the interacting design of the code and carrier loops which was not simulated during the ground tests. However, since the ground multipath tests did not simulate the motion of the user relative to the signal source, the multipath range error behavior followed the code tracking loop static characteristics without any benefit from the filtering (averaging) effects of either the code or the carrier loops. Consequently, the ground multipath test results are representative of system performance under worst-case conditons.

The multipath test geometries utilized have some application for both airborne and ground users. A representative geometry of a satellite in circular equatorial synchronous orbit and an airborne user (aircraft) is given in Figure 9.1. The minimum differential delay and differential doppler for specular reflection to an aircraft (flying due north and level) at 30,000 ft AGL, with the reflecting surface being flat and tangent to the earth's surface directly below the aircraft has been evaluated. Scaling the frequency from UHF to L-band (1.6 GHz), a plot of differential delay and fade frequency are given in Figure 9.2 as a function of aircraft latitude. The range of differential delays and grazing angles of this typical satellite geometry were simulated by the ground tests. However, in the satellite-to-aircraft geometry the predominant reflections will be diffused, except when the aircraft is at high latitudes. The diffuse, reflected signals, combined in random phase under dynamic conditions, will cause random, noise-like errors in the range and range rate measurements due to the scintillation of the multipath signals. These signal characteristics are not present in the WSMR multipath tests.

In the case of a ground based user (i.e., backpack or slowly moving vehicle) the operational system multipath errors will be comparable to those measured during the ground tests, except that, the operational case will be complicated by the presence of the satellites. One would, however, expect that the multipath interference contribution from each of the four satellites would be comparable.

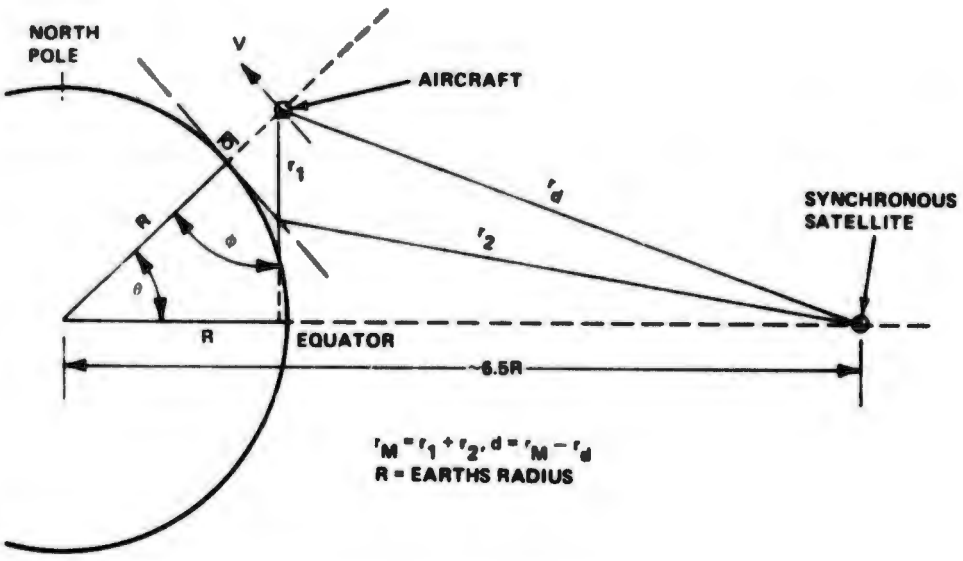

Figure 9-1 Path Geometry for Multipath Transmission

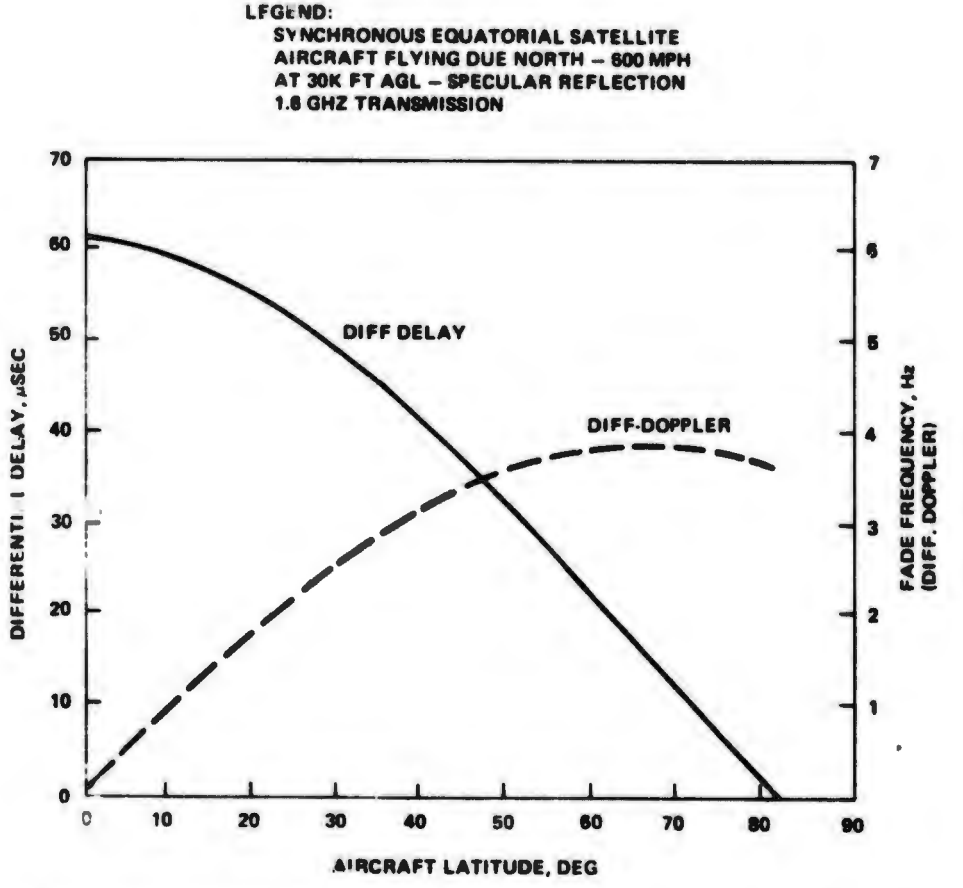

Figure 9-2 Differential-Multipath Delay and Differential-Doppler (Fade Frequency)

This could cause the effect of multipath interference to be cancelled in the pseudo-range algorithms and thus would yield smaller position errors than in the static test environment.

Each WSMR test evaluated the interference effect under unique conditions pertaining only to that geometry and surface characteristics of the indicated multipath environments. Therefore, the results from one test geometry cannot necessarily be correlated to a different one.

9.1.2 WSMR Multipath Test Sites

The test results of Tula Peak are representative of short differential delay with low grazing incidence causing specular reflection. Dead Man Canyon is characteristic of a terrain with obstructions in the line-of-sight causing signal diffractions resulting in bias-like multipath errors. The tests at Northrop Strip encompassed both high and low grazing angle geometries (diffuse, partly diffuse and partly specular reflections) both with short and long differential delays. The tests in the White Sands Dunes Area had a surface roughness characteristic, expressed in terms of the root-mean-square deviation of the terrain profile relative to a smooth curve-to-wavelength ratio, which varied from test to test. The area of signal reflections in some of these tests (e.g., test position number 5 in the Dunes Area) was localized in a region of smooth terrain although total terrain profile between the transmitting and receiving antennas was characterized to be rough. The results in this case are in agreement with a theoretical model of smooth surface reflections.

9.1.3 Multipath Test Evaluation Technique

A theoretical simulation model was developed both as a tool to check the reasonableness of the test results and as an aid in interpreting the nature of the reflections. The mathematical model of test site terrain profiles, electromagnetic propagation, antenna patterns and receiver tracking characteristics was included in the simulation program (see Section 9.8).

The simulation model is an approximation to the real world. It represents an analytical tool by which one can evaluate the measurements with respect to "known" system behavior. The mathematical simulation did not include unique peculiarities of the test site propagation path, e.g., signal diffraction by obstacles. Such conditions are difficult to model since they are a function of several uncontrolled and unknown variables. The parameter values used in the simulation program represent best available data obtained either by measurements or by empirical estimates. No attempt was made to optimize the parameters to fit the measurements. The electrical properties of the terrain were estimated based upon available measured data for similar terrain profiles and soil characteristics.

The multipath test results are categorized by site location in the discussion that follows. A feature of each discussion is the comparison of the test results to the theoretical predictions obtained from the simulation program. In these discussions the fine structure of the multipath error predicted by the simulation is magnified and the location of the measured data values (for vertical polarization only) with respect to the simulation results is indicated. Due to the sensitivity of multipath range error to antenna height for a given geometry (i.e., the sensitivity of differential delay) any error in recording the actual antenna height above the ground during the test can

cause an offset between the measured and simulated values. Furthermore, the simulation is only meant to be an approximation to the complex test conditions, geometry, and irregular surface characteristics. The fact that nevertheless the measured data points are generally in good agreement with the predicted multipath fine structure and fall well within the multipath error envelopes is consisted a remarkable verification of the validity of the mathematical model developed.

9.2 CHANNEL DELAY, DATA CALIBRATION AND DATA RECORDING

The inherent receiver interchannel delays (channel mismatch) affect the time-of-arrival measurements by introducing an unknown time delay in the measurements. Therefore, to determine the unknown receiver channel delays, the channels have to track a single known signal (see Section 2, Volume II) to allow the computation of the interchannel receiver delays (biases). The interchannel biases are then used to correct the receiver apparent time-of-arrival measurements.

The equipment configurations and test procedures used to obtain the calibration data are discussed in detail in Volume II. The important point to realize here is that the receiver is virtually acting as two receivers for the multipath test. An omni antenna, rf cabling, and an RF/IF section feed a range tracking channel which sees the entire multipath-contaminated signal. At the same time, a directional antenna (parabolic dish), rf cabling, and a second RF/IF section feed another range tracking channel which sees a signal free of multipath reflections. The common elements of these "two" receivers allow the direct comparison of the two range tracking channels and plus a determination of the effect of multipath signals on the receiver. The signal delays through each path from antennas to receiver output must be calibrated to separate these delay components from the multipath effects of interest in the receiver output data. The following paragraphs present the results of the calibration procedures.

By taking fine range differences between channels 4-1, 4-2, and 4-3 under two conditions, i.e., omni antenna connected to processors 1, 2 and 3 and the dish antenna connected to processor 4 (Condition A), and then interchanging the connections (Condition B) the following data were obtained:

	Ch(4-1)	Ch(4-2)	Ch(4-3)
Condition A, nanosec	-10	-20	-10
Condition B, nanosec	+8	-8	+9

With multipath error defined as the difference between the omni and dish channel measurements, the channel delay correction in terms of the above measurements may be expressed as:

$$\text{CHDCOR}(i) = \frac{\text{CH}(4\text{-}i)/A + \text{CH}(4\text{-}i)/B}{2} \quad , i = 1, 2, 3$$

The cable delays between the omni antenna and the receiver input terminals and the dish antenna and the receiver input terminal were measured as:

	CDO Omni	CDD Dish
Total Cable Delay	83.8, nanosec	111.2 nanosec

The multipath error, E, in nanoseconds can be expressed in terms of the measured quantities as:

$$E(i) = CH(4-i) - CDD + CDO - CHDCOR(i)$$

where CH(4-i) is the fine range difference data recorded during the multipath tests.

As an example, consider two data points taken for the "Rough Earth Balloon Test", Site Number 6:

Data Point No.	Antenna Height, ft.	Vertical Dipole CH(4-3)
1	13.5	-40
2	5	+4

The multipath error, for the above example is given by:

$$E_1 = -(-40) - 111.2 + 83.8 - \frac{-10+9}{2} = +13.1 \text{ nanosec}$$

$$E_2 = -(+4) - 111.2 + 83.8 - \frac{-10+9}{2} = -30.9 \text{ nanosec}$$

Using the above rules, all multipath data recorded during the tests were converted to multipath error, plotted as a function of test antenna heights and presented in parallel with simulation results for each test configuration.

The data recorded during the tests were taken at discrete antenna heights. The data points are thus presented in discrete rather than continuous form and no attempt should be made to connect the data points with continuous smooth curves since the sampling distance (i.e., the distance between adjacent antenna height locations) was not always sufficiently spaced to record the multipath fine structure. (Refer to simulation program in Section 9.8.)

During the smooth earth tests at Northrop Strip in four test configurations (test points 2,3,4 and 5, see Section 9.5) the pseudo range data were recorded on magnetic tape in addition to the CRT display data recorded at the other test sites. The data were recorded continuously at a rate of one sample per second. For each test point the time interval spent at every antenna height location was recorded. This allowed time slicing the tape recorded data into discrete data blocks for every antenna height and polarization. For each data block (antenna height) the mean and standard deviation was computed and plotted (see Section 9.5).

9.3 TULA PEAK MULTIPATH TEST

A multipath test was conducted on Tula Peak located on the eastern border of WSMR. Tula Peak is a hill approximately 260 ft higher than its surrounding terrain; its top has been flattened to form a plateau 200 ft square to support a radar test facility (Figure 9-3 and -4). The transmitter was set atop the plateau with its omni antenna facing down Tula Peak's east slope. The receiver was positioned in two places 1500 ft down the slope with its dish and omni antenna looking west up the Tula's east slope at the transmitter omni antenna. (Figures 9-5 and Fig. 9-6).

Figures 9-7 and -8 are the result of a geodetic survey of the Tula Peak multipath test configuration and associated land contours. Slant ranges, elevation and ground track distances were calculated for the separation between the omni antenna at the transmitter and the receiver reference channel dish feed tip which remains in a fixed position for each test*. A 6 ft diameter reference channel dish with a linearly polarized feed was utilized in all tests. The X, Y and Z position of the receiver omni antenna is reported at the ground level below the telescoping omni and dipole antenna mast because both omni and dipole receiving antennas heights were varied, as part of the test procedure, from 5 ft to 31 ft AGL. The elevation and slant range between receiving and transmitting omnis are functions of the receiving omni height above the ground (Fig. 9-7).

The ground texture in front of the receiving antennas was sandy and very dry. Small salt bushes and rocks 5 in. to 3 ft in diameter were scattered between antennas along the line of sight. A pole line suspending communication lines 22 ft above ground level ran parallel to the line-of-sight between antennas as shown in Figures 9-6 and -8. During the time data were taken, cars and trucks were kept clear of the antennas' line of sight.

9.3.1 Tula Peak Test Results

The Tula Peak configuration is representative of a slightly rough surface with a predominantly specular reflection characteristic. This is demonstrated by the multipath error curves of Figures 9-9 and -11 which follow closely the variation of the received power shown in Figures 9-10, -12 for the three polarizations considered, viz. right hand circular, horizontal and vertical. This correlation between multipath error and received power is characteristic of specular reflection.

The shape of the curves shown in Figures 9-9 to 12 are good representations of the observed receiver behavior even though the quantitative measurements forming the basis for these curves were made at discrete antenna heights and not continuously as the curves might imply. In moving the antenna from one height to another, the power level and range measurement displays were observed to insure that no peaks or nulls were missed during the test.

---

*Adjusted in a manner to reduce the reception of reflected energy.

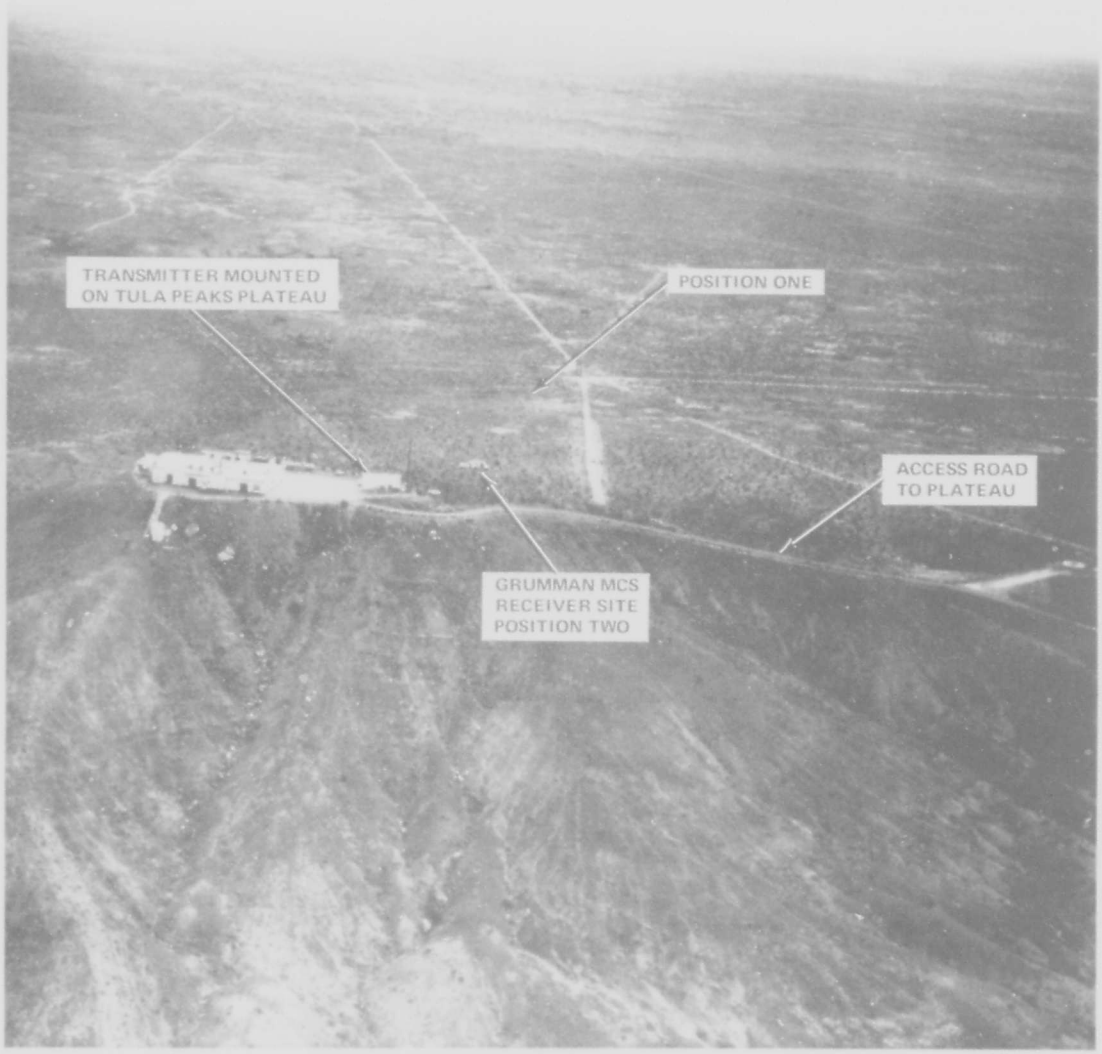

Figure 9-3 Tula Peak Looking East

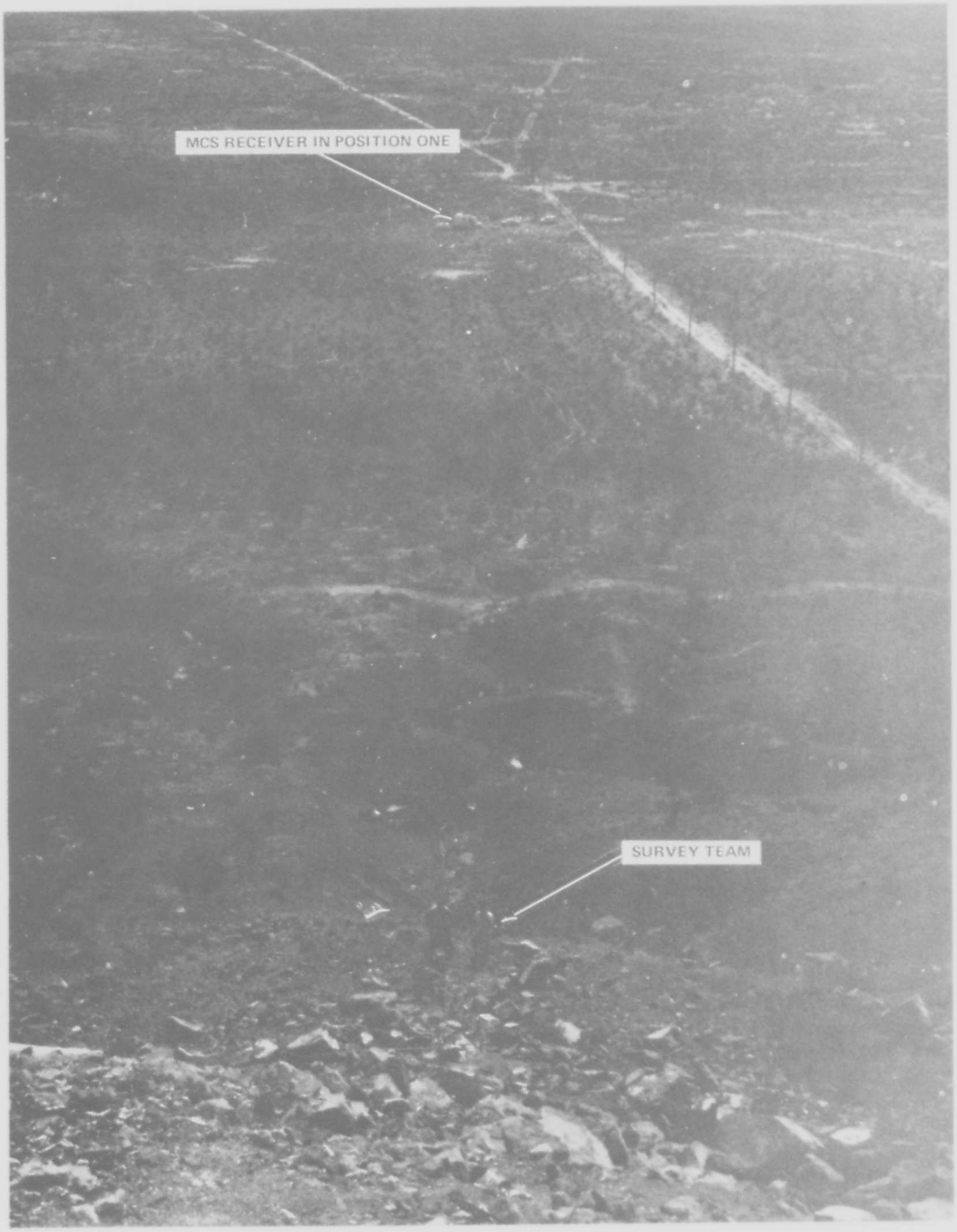

Figure 9-4 Tula Peak Multipath Test View From Transmitter to Receiver Site

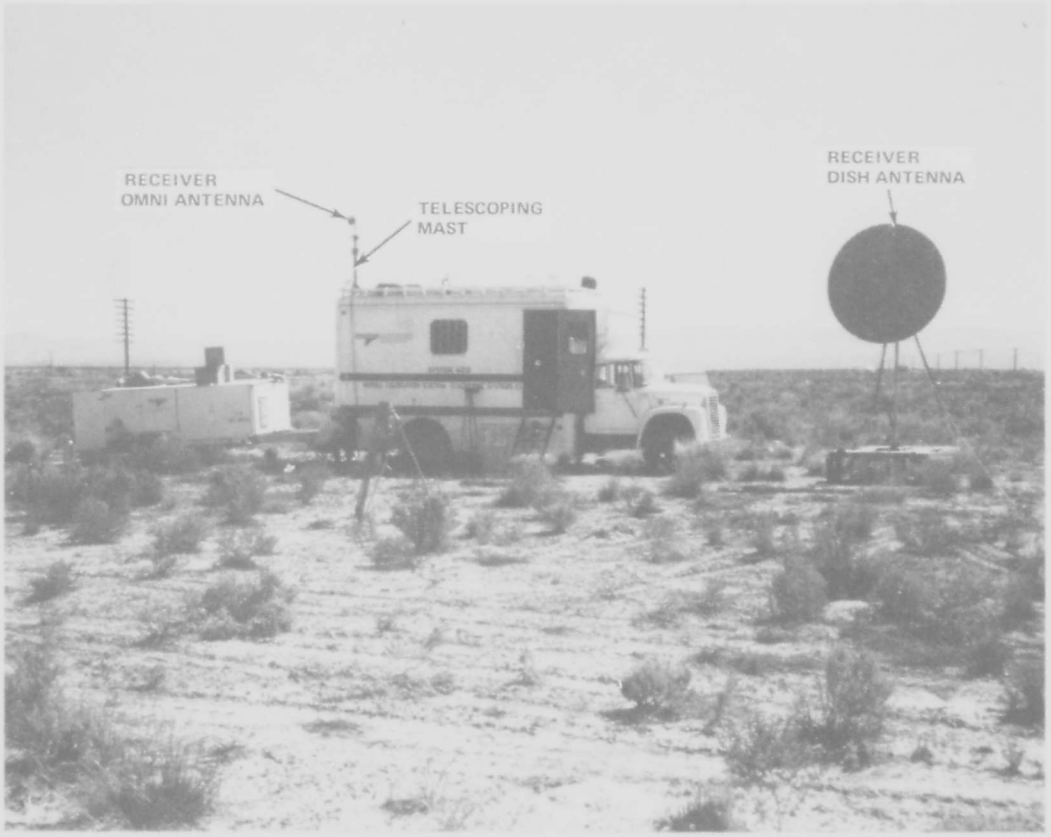

Figure 9-5 Tula Peak Multipath Test MCS Receiver Site - Position One

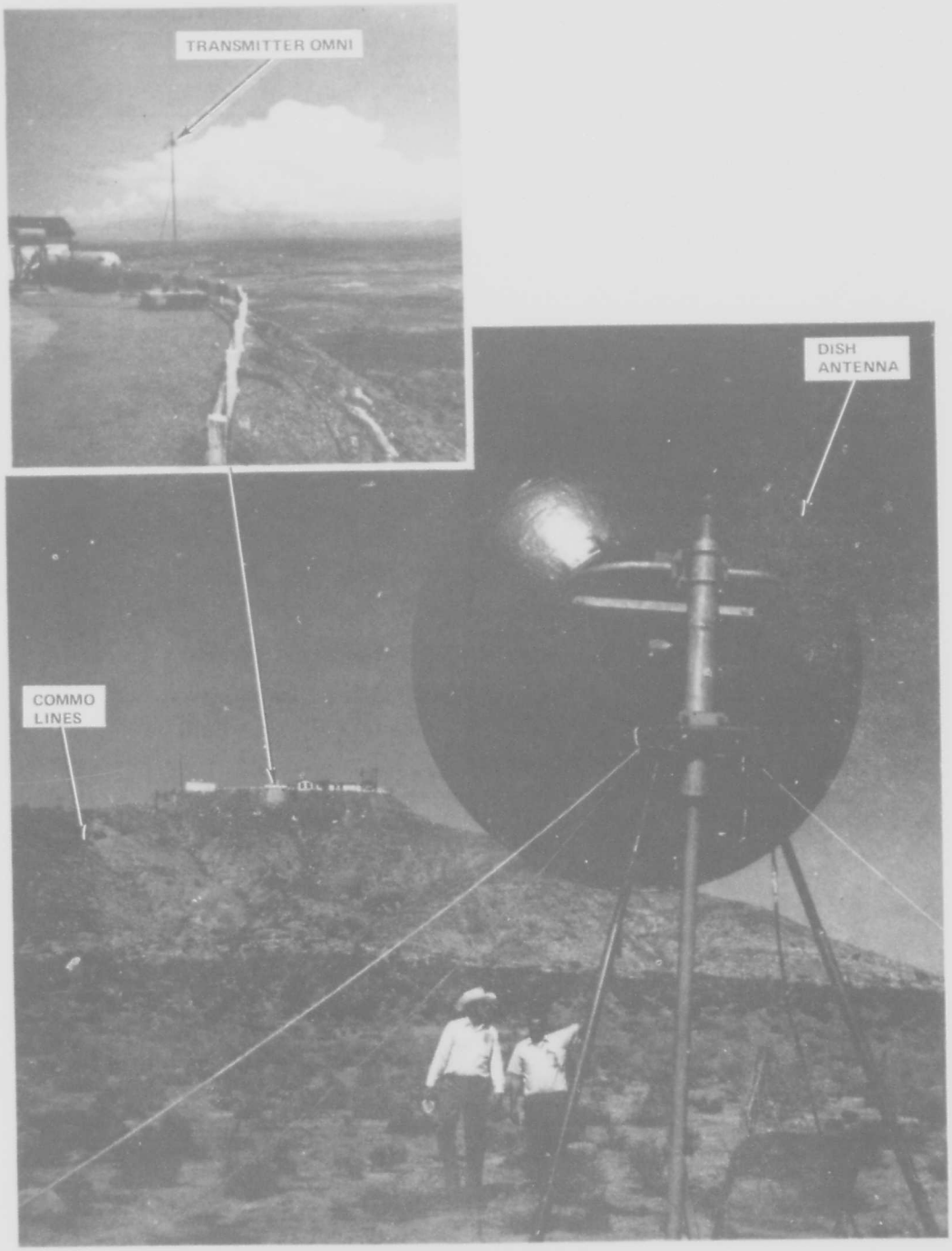

Figure 9-6 Tula Peak Multipath Test Position One

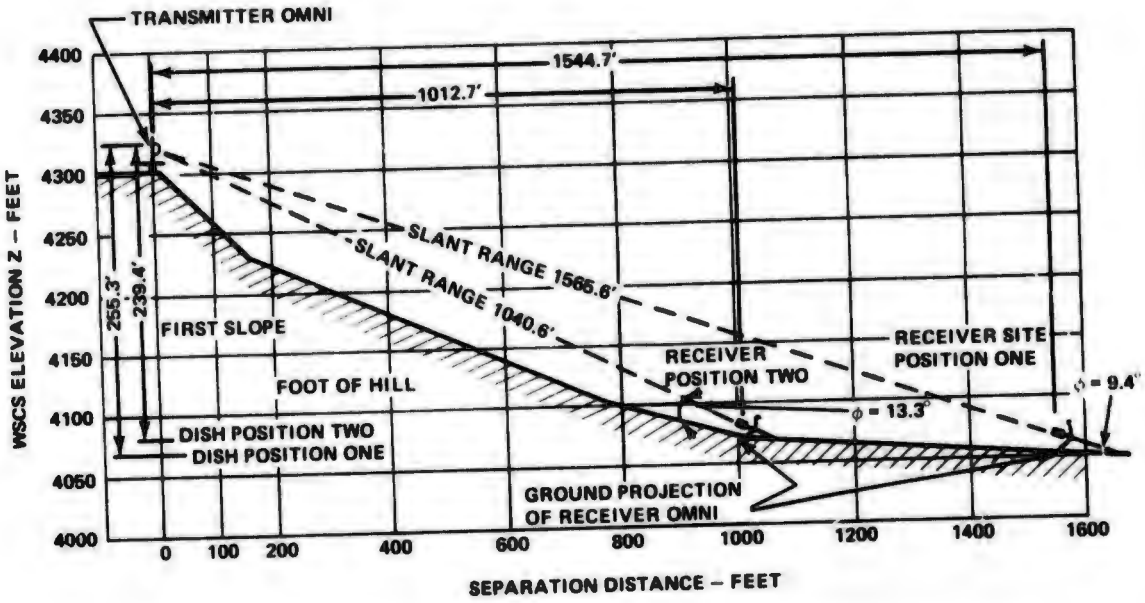

Figure 9-7 Tula Peak Multipath Test Geometry of Test Configuration

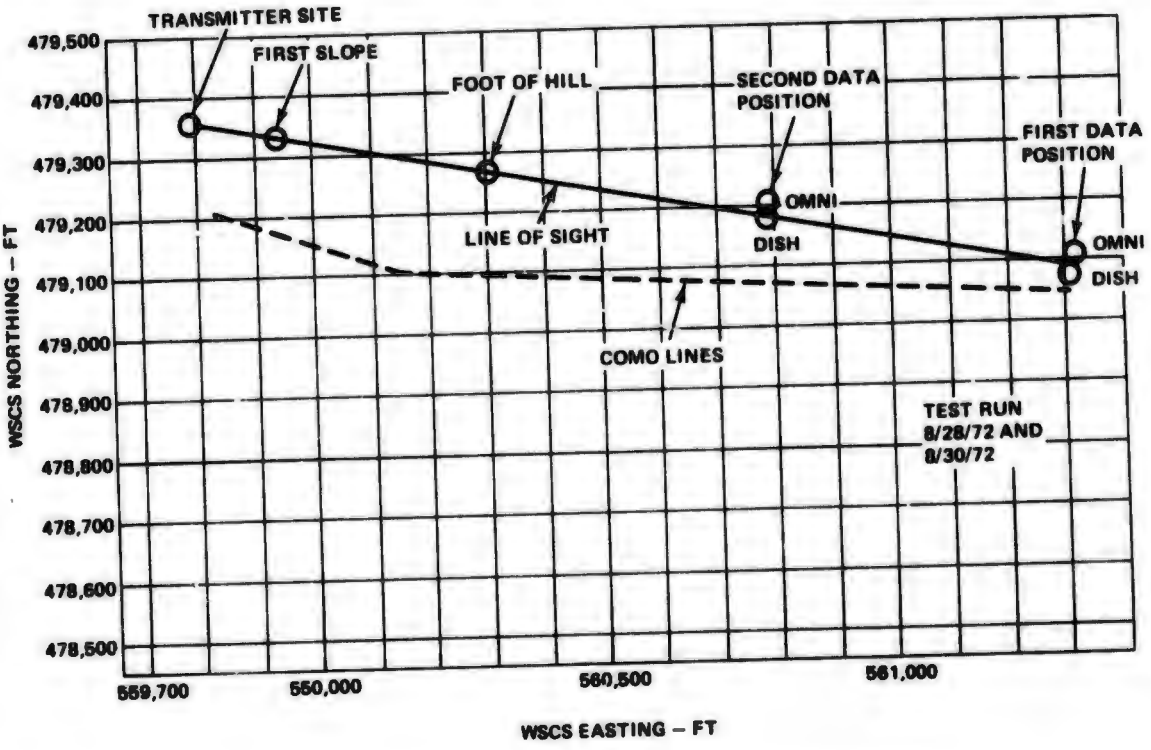

Figure 9-8 Tula Peak Multipath Test Grid Layout in WSCS

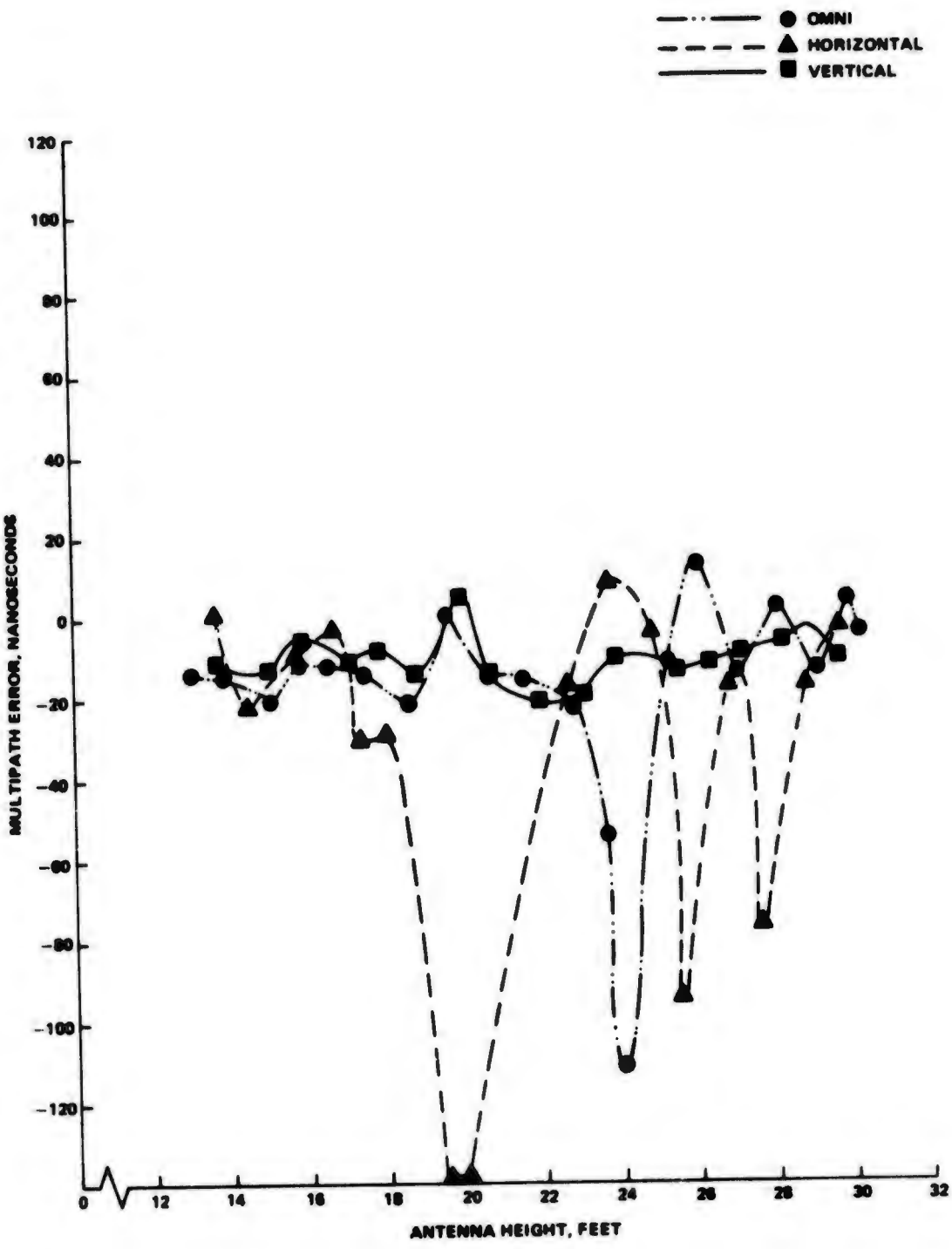

Figure 9-9 Tula Peak Site No. 1

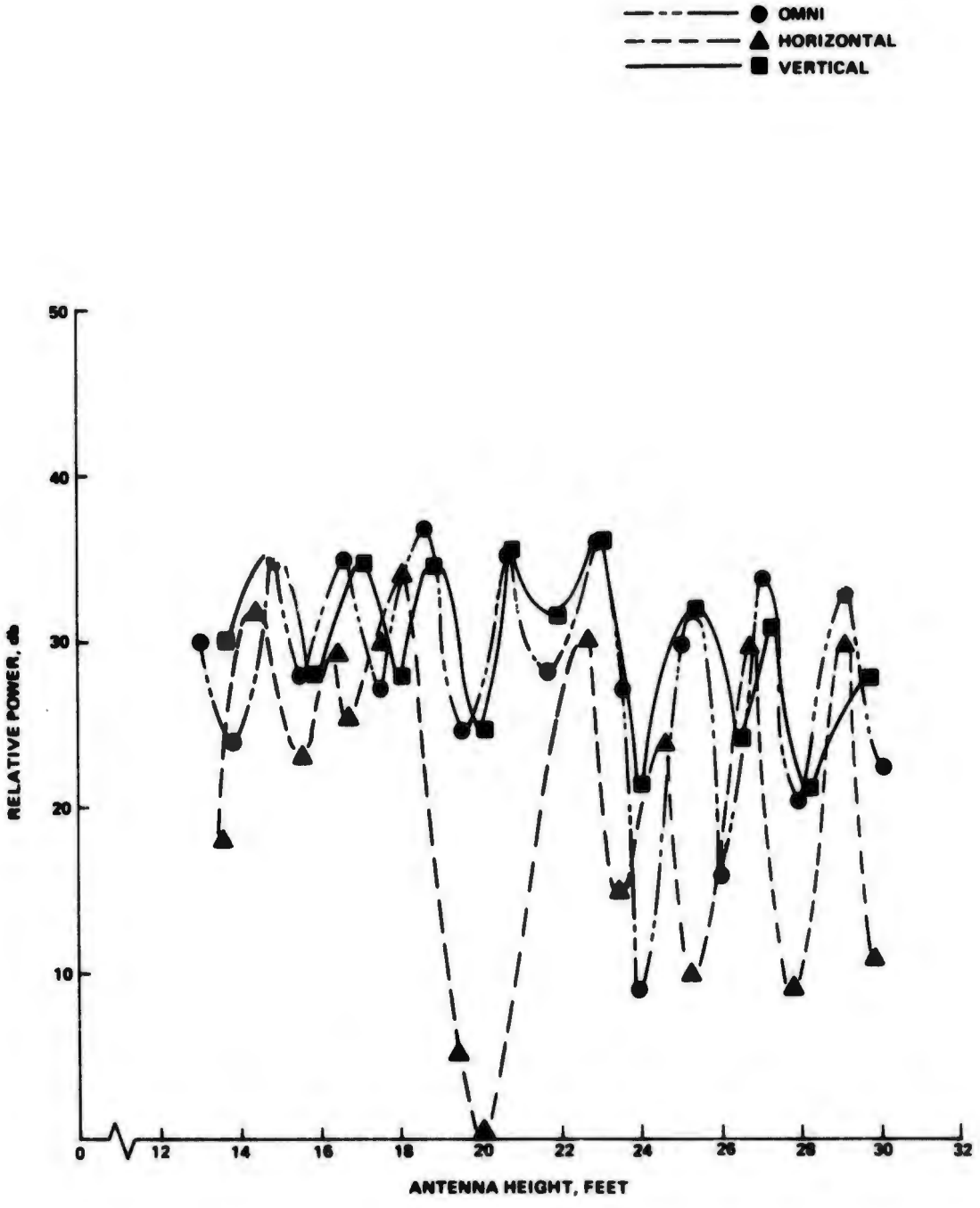

Figure 9-10 Tula Peak Site No. 1

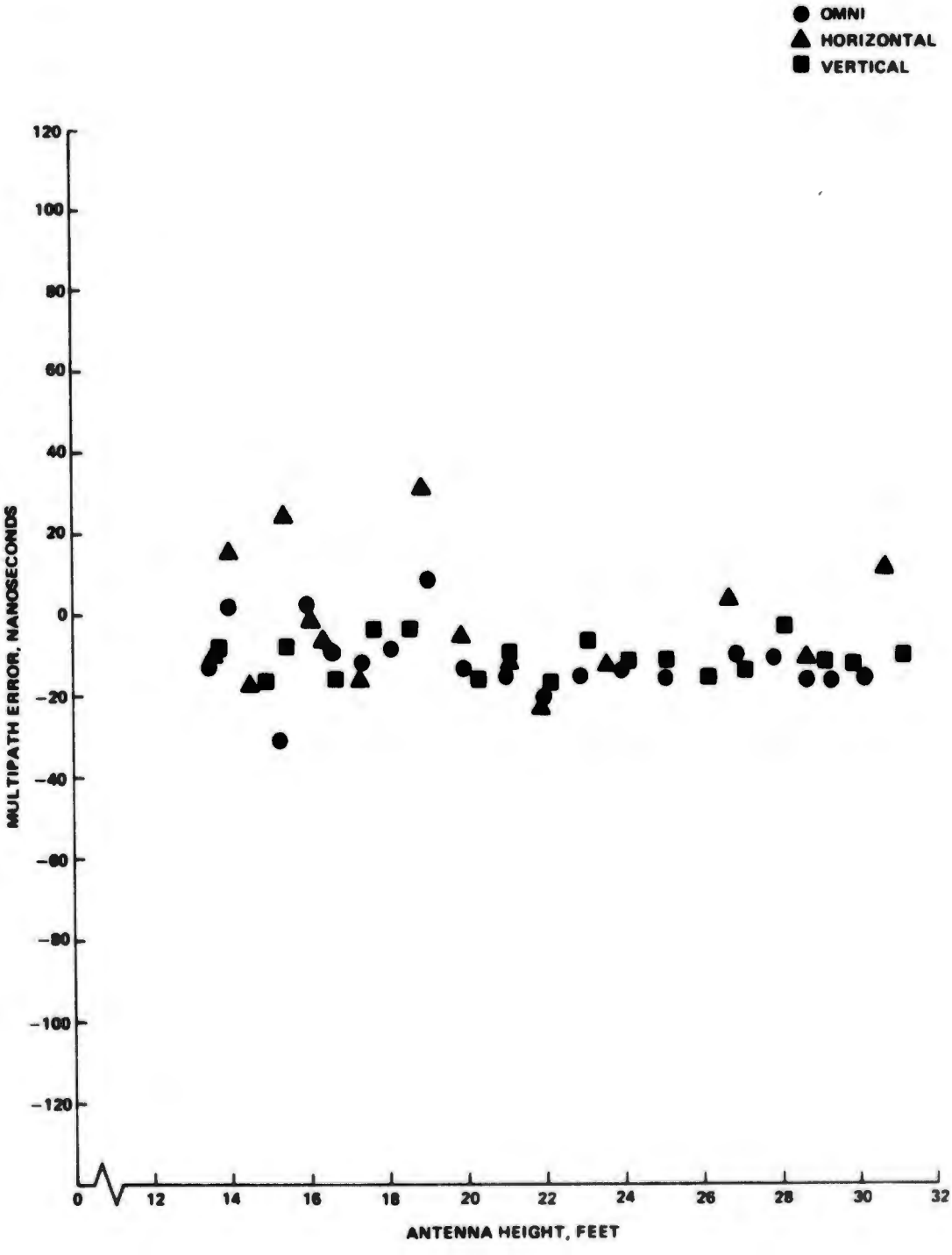

Figure 9-11 Tula Peak No. 2

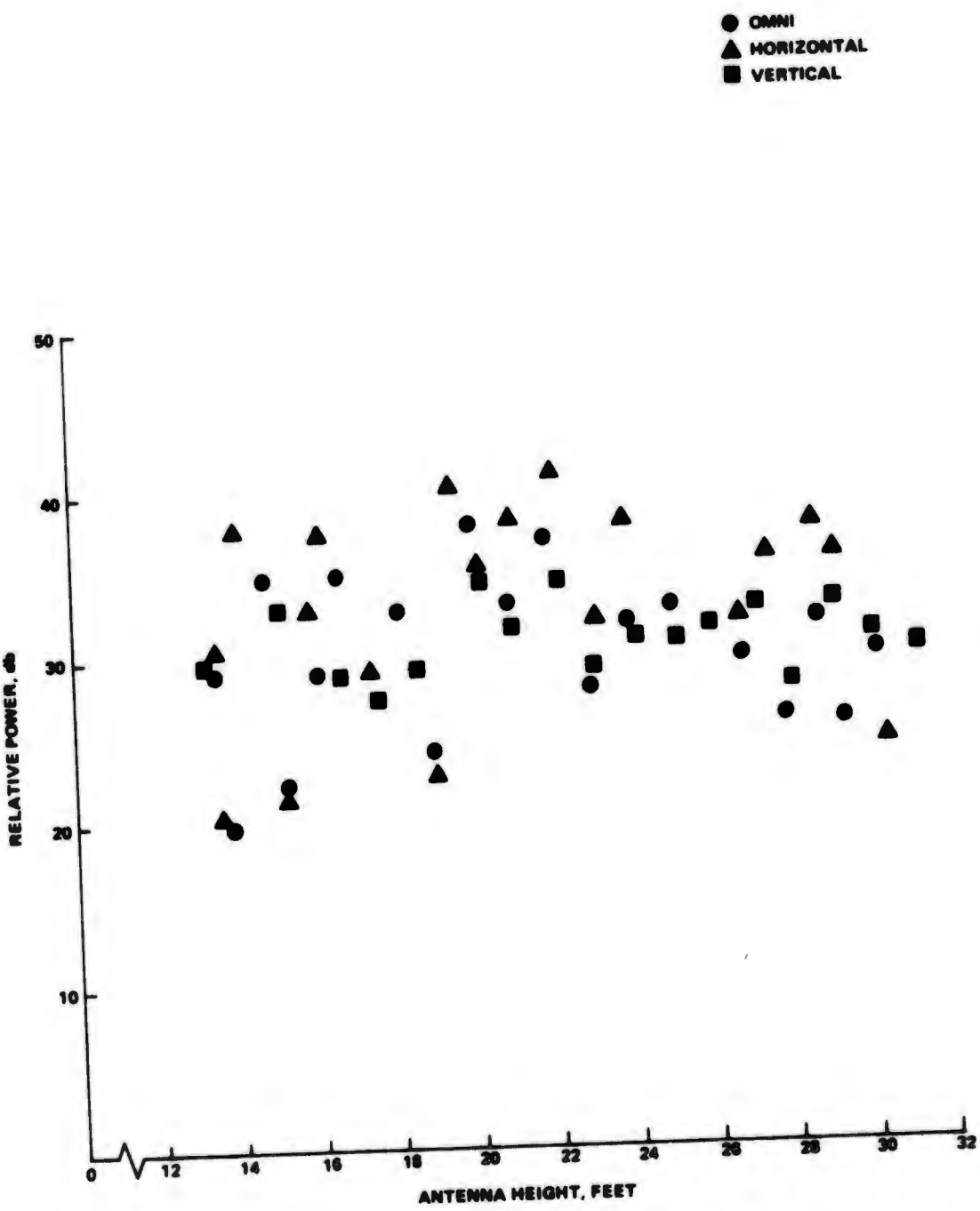

Figure 9-12 Tul a Peak No. 2

In test position No. 1, the grazing angle seems to be close to the Brewster angle for vertical polarization, computed to be approximately 14° for average ground, as indicated by the sharp dips for horizontal polarization and essentially flat profile for vertical polarization (Figure 9-10). The similar power profiles for both the horizontal and vertical polarizations at test position no. 2, Figure 9-12, indicate that this position had a grazing incidence well below the Brewster angle.

The delay lock loop implementation in the receiver used to track the coded range signal has a theoretically predictable response to multipath signals which indicates that the tracking error should not exceed 50 nanosec. (The delay lock loop multipath response is discussed later. The model predictions had been verified by laboratory bench testing before commencing the field tests, so we were quite surprised to find a region of multipath on the first day of testing which produced receiver tracking errors greater than 130 nanosec. This condition was observed (Figure 9-9) for the horizontally polarized signal at an antenna height of 19 ft 10 in. with the antenna located at position no. 1. The condition was repeatable; however, the receiver behavior was somewhat erratic. This was due to the low signal level at which the receiver was operating. A very deep signal fade, approximately 30 db, was associated with the large tracking error. This placed the signal level in the tracking loop at approximately -140 dbm, resulting in noisy range measurements.

The large multipath error can be caused by a number of phenomena not previously recognized while studying the tracking loop characteristics. Either a false lock of the receiver code tracking loop discriminator under deep fade conditions or tracking of only the reflected signals instead of the composite signal containing both direct and reflected ray components could be responsible for the large observed errors. In this case the -130 ft multipath error was due to false lock. This is shown by the substantial drop in the received power which occurred simultaneously with the tracking error (see Figure 9-10). If the large multipath error were caused by tracking the reflected signal, the received power would stay constant.

In the Tula Peak test, the signal environment results in a specular reflection signal fade condition. This is due to a combination of effects. The geometry produces a short differential delay, under 7 ft, and a low grazing incidence of approximately 12°. The effective voltage reflection coefficient magnitude for horizontal polarization is close to unity. These factors together with the antenna array effect above the ground plane cause a phase change in the reflected signal which results in the signal fade condition.

These conditions were modelled in the multipath simulation program. For the purposes of simulation the geometry of Figure 9-7 was replaced by an equivalent equally rough terrain model with antenna heights of approximately 175 ft and a separation distance of 1566 ft for position no. 1; and antenna heights of approximately 75 ft and a separation distance of 1041 ft for position no. 2. The grazing angles for this geometry are 12° for position no. 1 and 8.5° for position no. 2. The dimensions of the first Fresnel Zone (Ref. 38) (for position no. 1) centered midway between the receiving and transmitting antennas are 72 ft x 15 ft describing the dimensions of an ellipse with minor axes perpendicular to the line-of-sight between antennas. Therefore, the area of reflection is localized to a relatively smooth location along the terrain.

Figures 9-13, 13A and 9-14, 14A, show the theoretical simulation of the equivalent geometry with the measured data points superimposed, for vertical polarization conditions at the two test sites used at Tula Peak. The measured data, represented by squares on the figures, shows the actual receiver range measurement error resulting from the multipath environment. For these tests, the antenna heights were known to an accuracy of about 1 in. so the plots are an accurate representation of the true errors.

The deviation of the theoretical curves from these data is due to the difficulties of approximating the actual geometry in the mathematical model. This is in part caused by the presence of the communication lines which may cause additional reflections (see Figure 9-8) that were not taken into account in the simulation program.

9.4 DEAD MAN CANYON MULTIPATH TEST CONFIGURATION

The Dead Man Canyon multipath test was run on the west boundary of WSMR at the base of the San Andres Mountains in a gravel quarry located within Dead Man Canyon. The canyon contained small salt bush brush, a gravel pile, two water tanks, a sharp terrain drop-off resulting from the removal of soil used to construct road beds, heavy construction equipment traveling in and out such as trucks, dozers, buckets and stationary gravel processing equipment. During the multipath tests, trucks and bucket loaders passed randomly through the field of view of the 621B receiving antennas.

The receiving antennas were situated at the entrance to the quarry and not moved during the test, while the transmitter was positioned on a rise above the moving construction equipment at three separate locations. The positions of each antenna as well as all the obstacles in the antennas' field of view were surveyed and are shown in Figures 9-15 and 9-16 plotted in White Sands Cartesian System (WSCS) coordinates. Ground track and slant range distance were calculated from WSCS coordinates. The elevation of each antenna was surveyed and is reported in Figure 9-16 with the exception of the mast-mounted omni antenna at the receiver site. The elevation of the receiver omni and dipole was varied from 5 ft AGL to 31 ft AGL as part of the test procedure. The antenna coordinates (X and Y) and elevation (Z) reported in Figure 9-16 refer to point of intersection of the antenna mast with the ground. The slant range reported is from the receiver dish antenna feed tip to the transmitter omni antenna. The total distance travelled by the "direct" signal is the slant range plus 5.1 ft allowing for the distance between the feed and parabolic reflector.

Figure 9-17 is the receiver site at the entrance to the quarry and the 621B transmitter set up at position one, typical of all three transmitter sites. It should be noted that the terrain in front of the receiving antennas was rolled and packed down dry soil while the ground in front of the transmitter was covered with salt bush and chapperal type vegetation intermixed with dry soft sand and 0.5 in. to 2-ft diameter rocks. Figure 9-18 has two views of position one; from receiver to transmitter, and from transmitter to receiver. The gravel pile shown in Figure 9-18 is made up of small gravel 0.25 to 0.5-in. in diameter slightly moist from rain a few days prior to the test. Figures 9-19 and -20 show positions no. 2 and 3 respectively. The gravel processing equipment noted in Figure 9-21 was being operated during the multipath tests at all three positions.

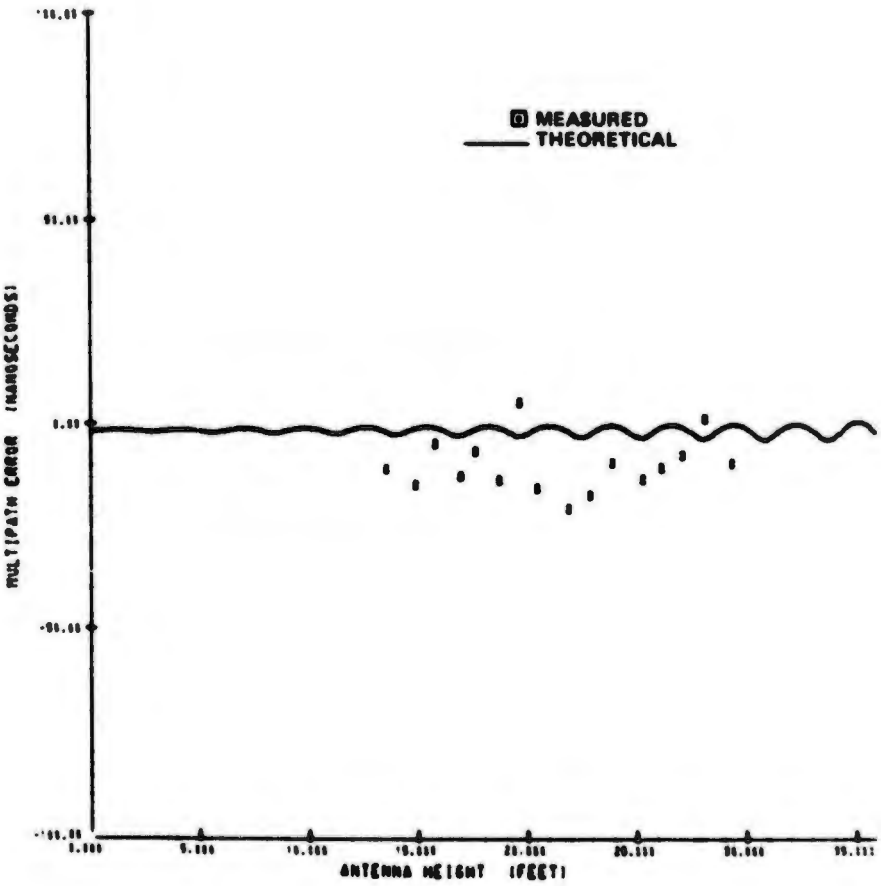

Figure 9-13 Tula Peak Site No. 1, Vertical Dipole

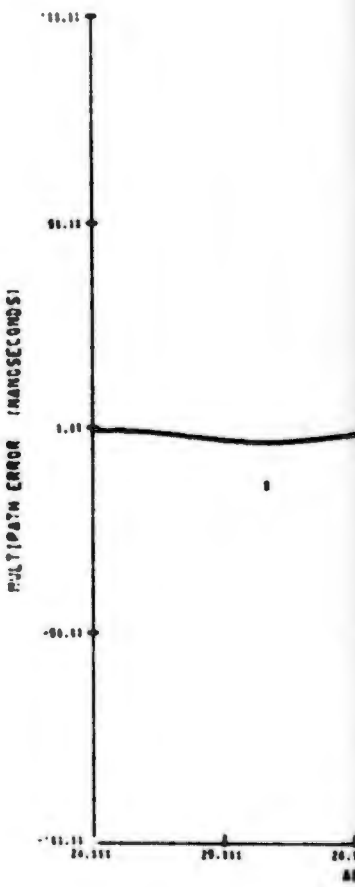

Figure 9-13A Tula

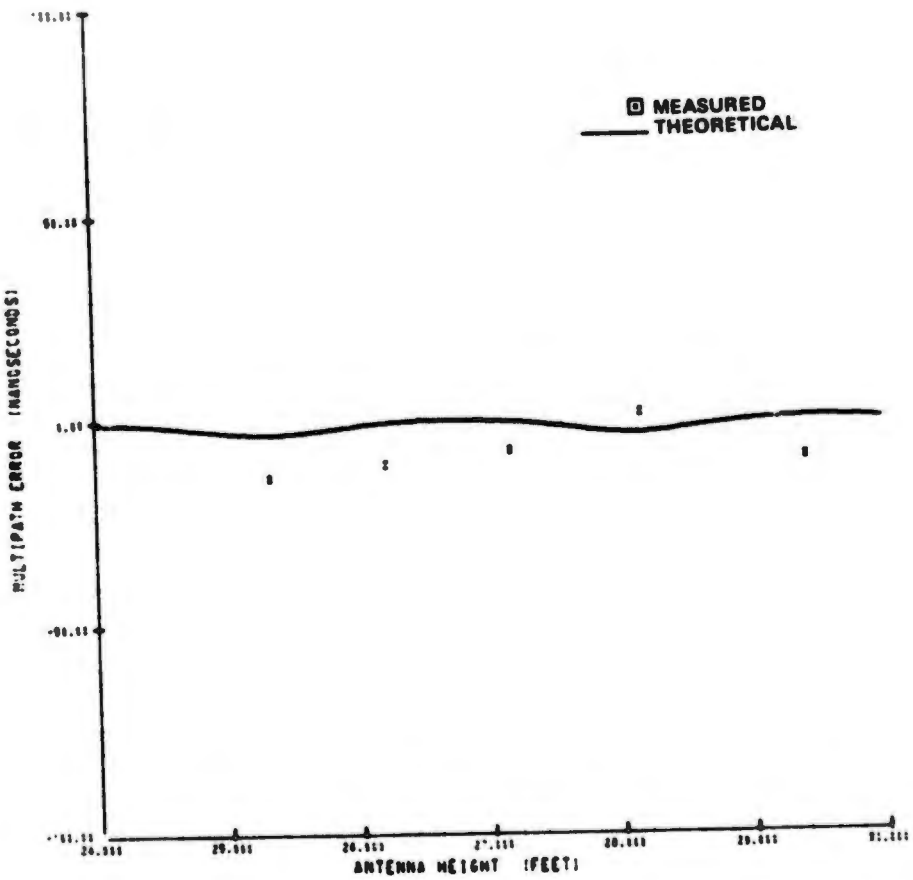

Figure 9-13A Tula Peak Site No. 1, Vertical Dipole

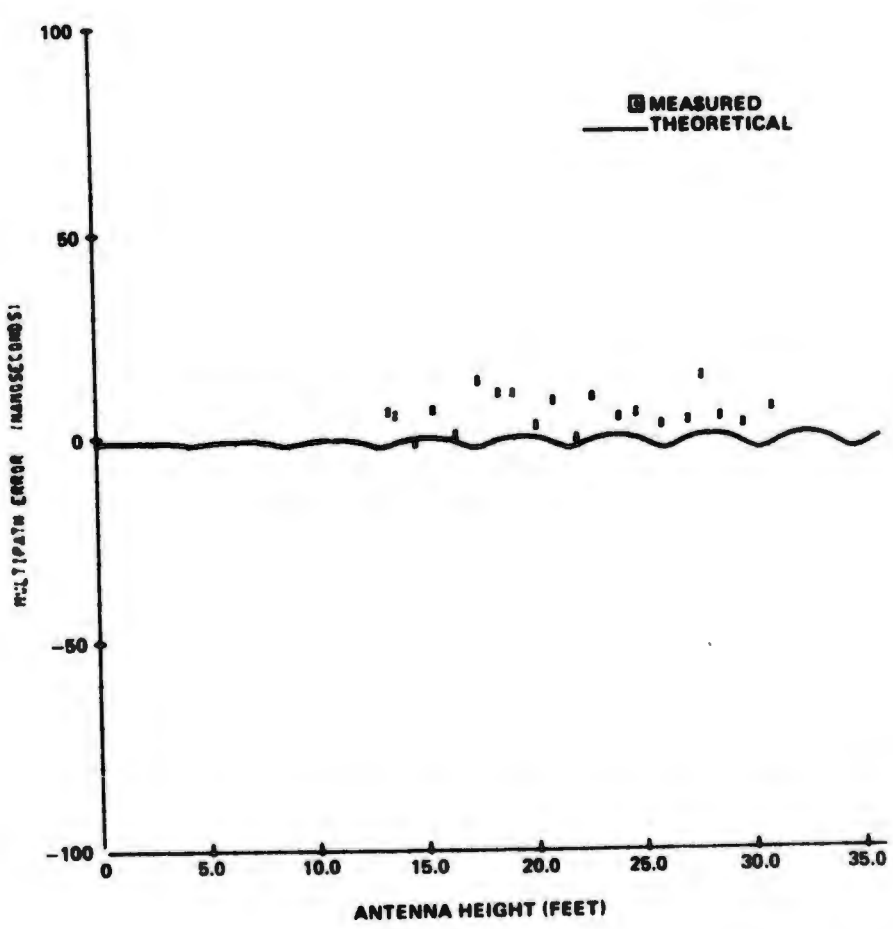

Figure 9-14 Tula Peak Site No. 2, Vertical Dipole

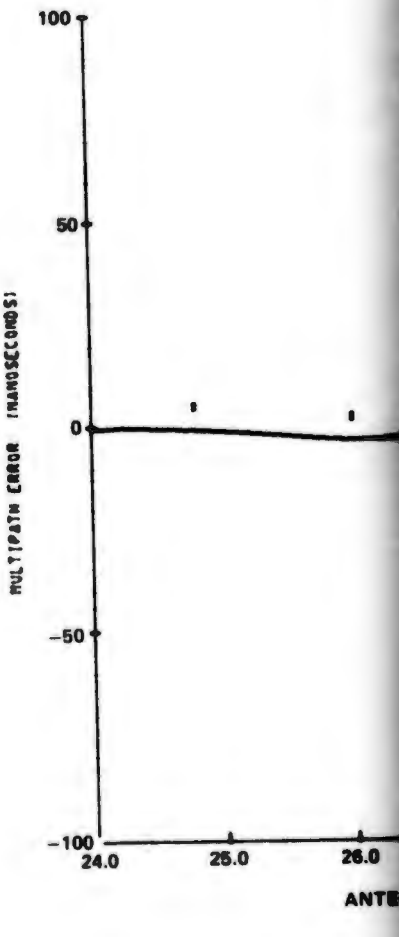

Figure 9-14A Tula P

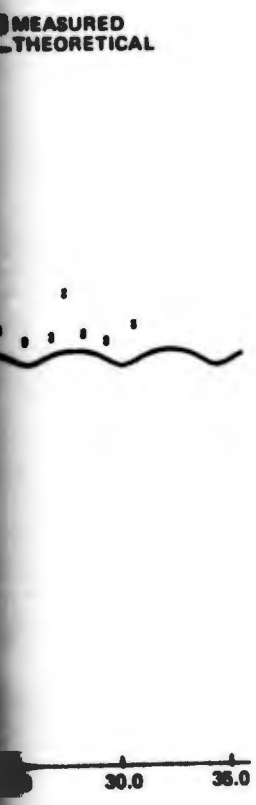

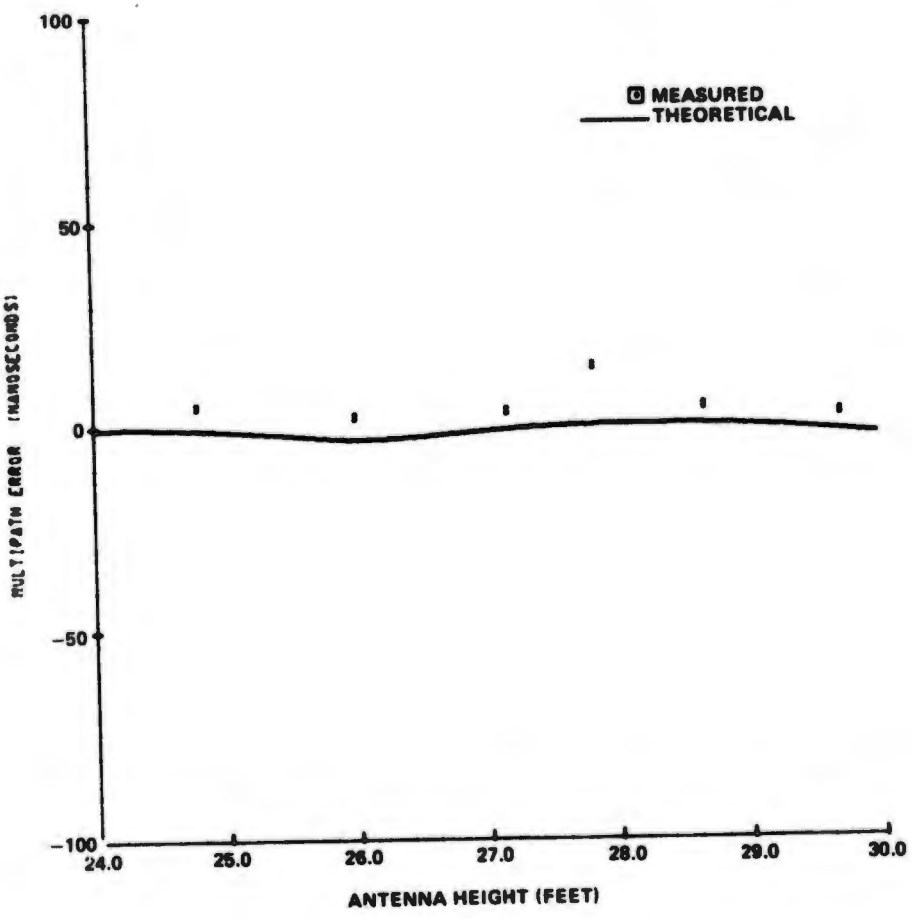

ical Dipole

Figure 9-14A Tula Peak Site No. 2, Vertical Dipole

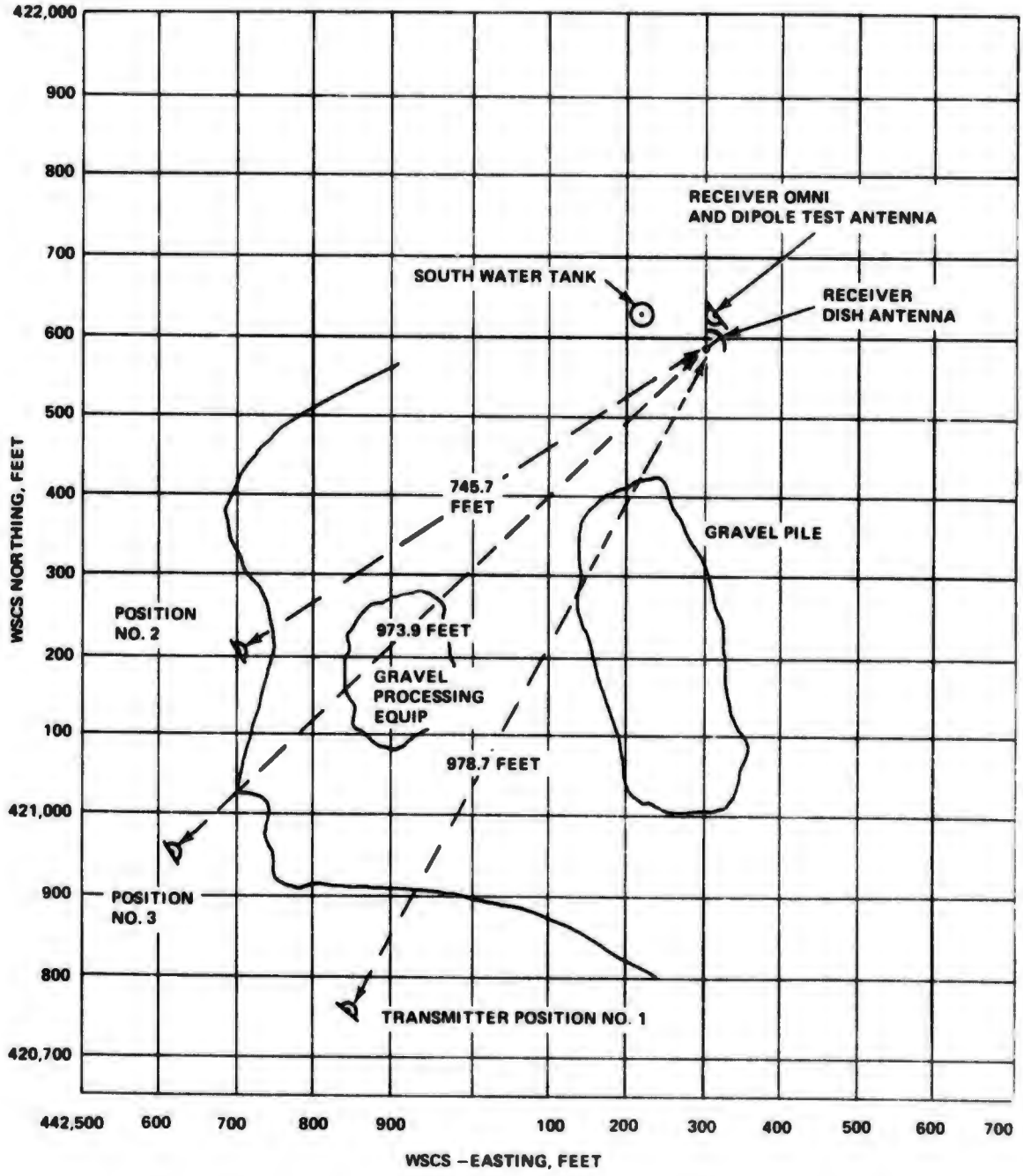

Figure 9-15 Dead Man Canyon Multipath Test Configuration

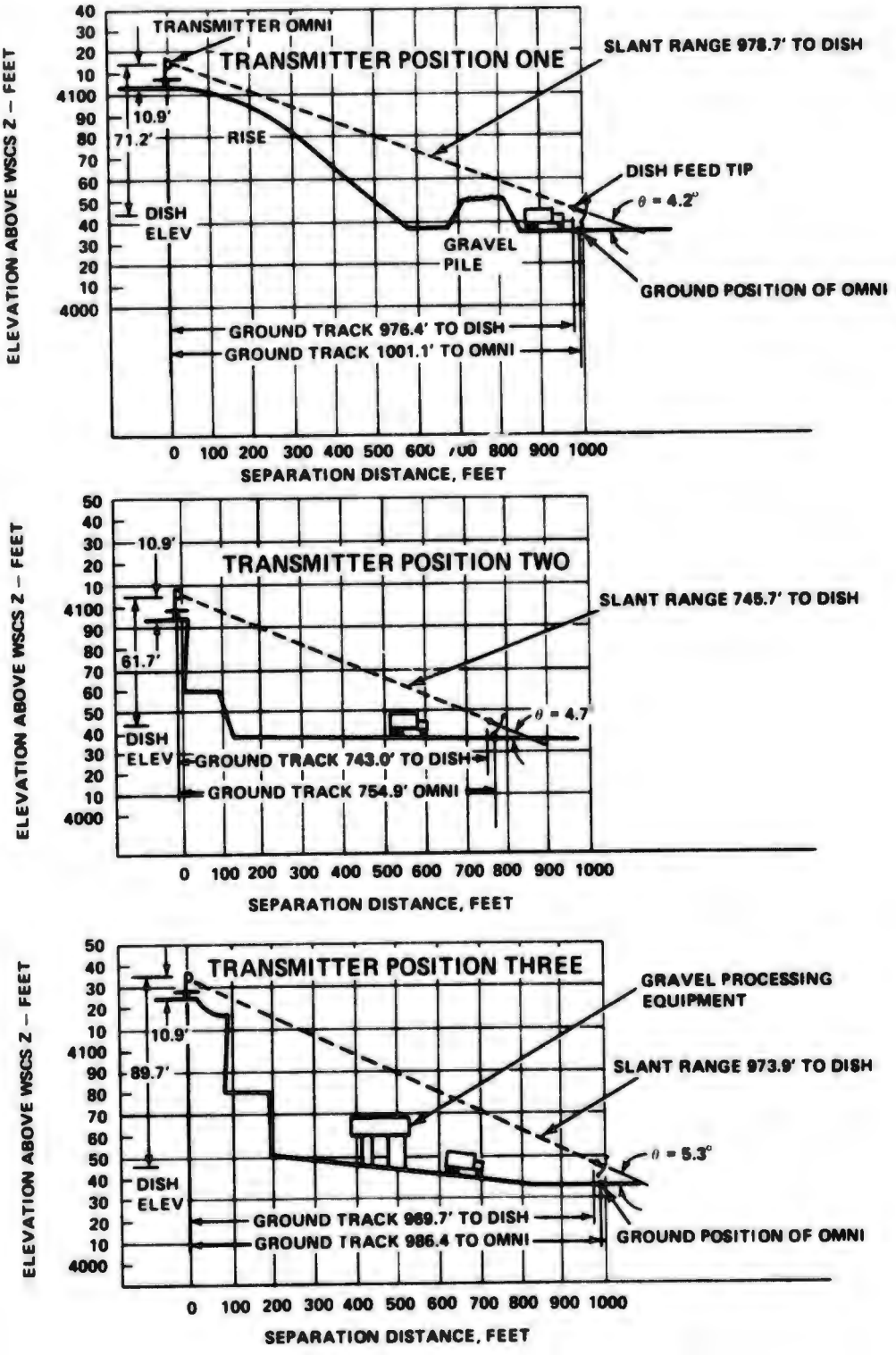

Figure 9-16 Dead Man Canyon Multipath

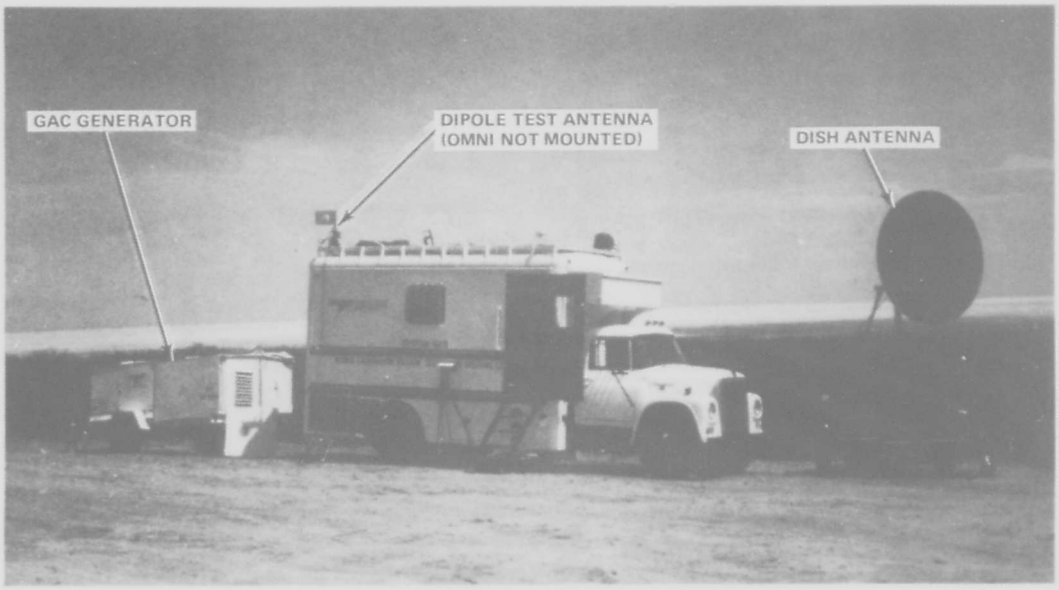

RECEIVER SITE AT ENTRANCE TO QUARRY

TRANSMITTER SITE TYPICAL
(SHOWN AT POSITION ONE)

Figure 9-18 Dead Man Canyon Multipath Test

VIEW TO RECEIVING SITE FROM TRANSMITTER POSITION NO. 1

VIEW TO TRANSMITTER FROM RECEIVER POSITION NO. 1

Figure 9-18 Dead Man Canyon Multipath Test

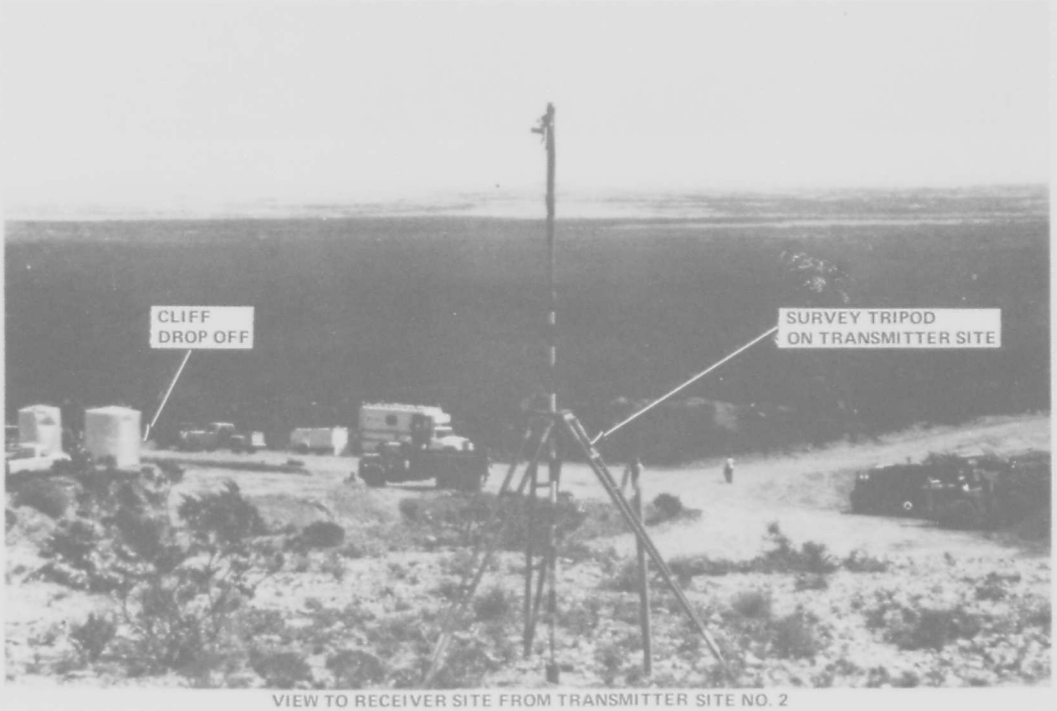

VIEW TO RECEIVER SITE FROM TRANSMITTER SITE NO. 2

VIEW TO TRANSMITTER SITE NO. 2

Figure 9-19 Dead Man Canyon Multipath Test

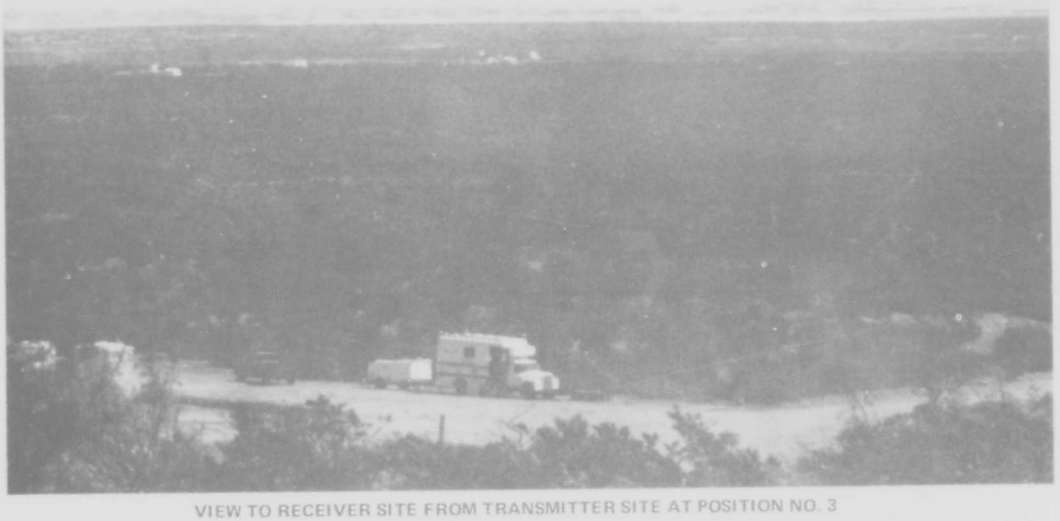

VIEW TO RECEIVER SITE FROM TRANSMITTER SITE AT POSITION NO. 3

VIEW TO TRANSMITTER SITE AT POSITION NO. 3

Figure 9-20 Dead Man Canyon Multipath Test

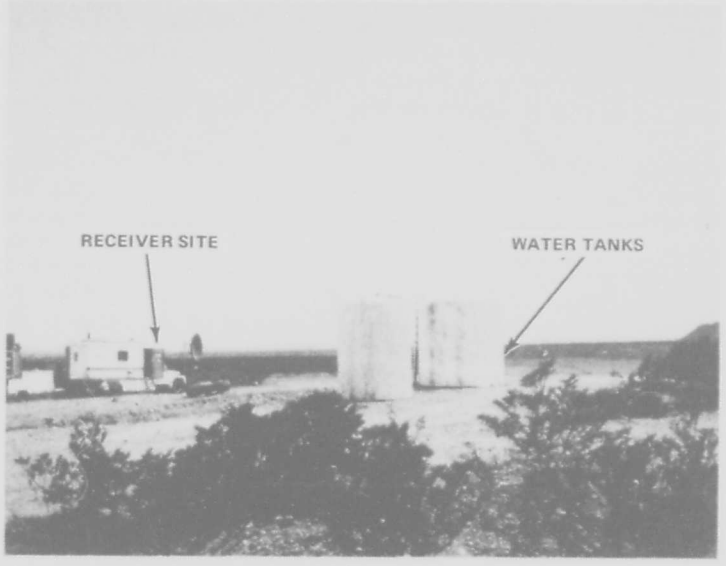

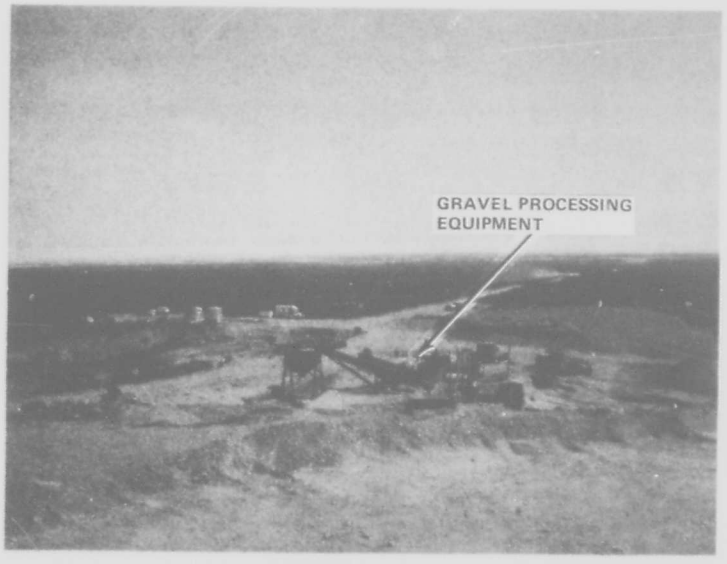

Figure 9-21 Dead Man Canyon Multipath Test

9.4.1 Test Results

Figures 9-15 and 9-16 depict the top and cross sectional views respectively of the three configuration geometries used in the Dead Man Canyon tests. In the first and third configurations, gravel pile and gravel processing equipment blocked part of the transmitted energy from reaching the receiving antennas; in the second test configuration there was no obstruction in the vicinity of the line-of-sight.

The types of obstructions shown in Figures 9-15 and 9-16 are sometimes referred to as ridges. Ridges in the vicinity of the line-of-sight between the transmitting and receiving antennas diffract part of the energy as it passes from the transmitter to the receiver. There was no ridge in the way for test position two, but positions one and three are representative of diffraction by a ridge referred to as Fresnel diffraction. In these two cases, it was confirmed that the diffracted electromagnetic field several wavelengths away from the ridge is substantially independent at polarization. This is exemplified in Figure 9-22 which shows a plot of the antenna height in feet vs the multipath error in nanosec for three different polarizations, right hand circular, horizontal, and vertical. As the antenna height was varied from about 13 ft to 31 ft, the multipath error remained within 5 ft and the three errors are practically coincidental.

Figure 9-23 is a plot of antenna height vs signal level for the same test. Again there are three curves, one for each of the three polarizations. From this figure it is clear that there is multipath present, since there are significant (5 db) signal level power variations for a particular polarization. The three curves are separated as shown in Figure 9-23, since the antenna gains for the respective polarizations are not normalized.

Test position three data, Figures 9-24 and 9-25 show a signal environment similar to position one.

In order to assess the degree of obstruction taking place (relative to free space) by the ridge, one needs to compute the ratio of the path clearance to the first Fresnel zone clearance.

The following is a simplified figure of the test set-up for positions one and three.

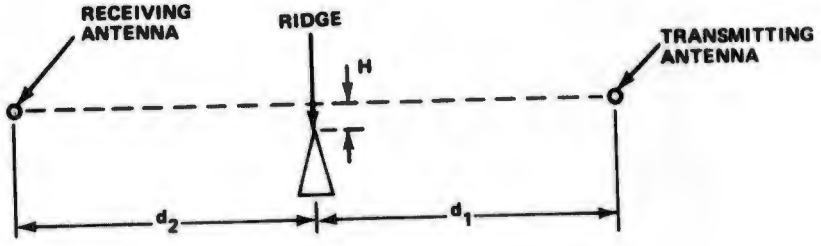

With the path clearance H between the line-of-sight of the antennas and the top of the ridge (i.e. either the gravel pile or the gravel processing equipments

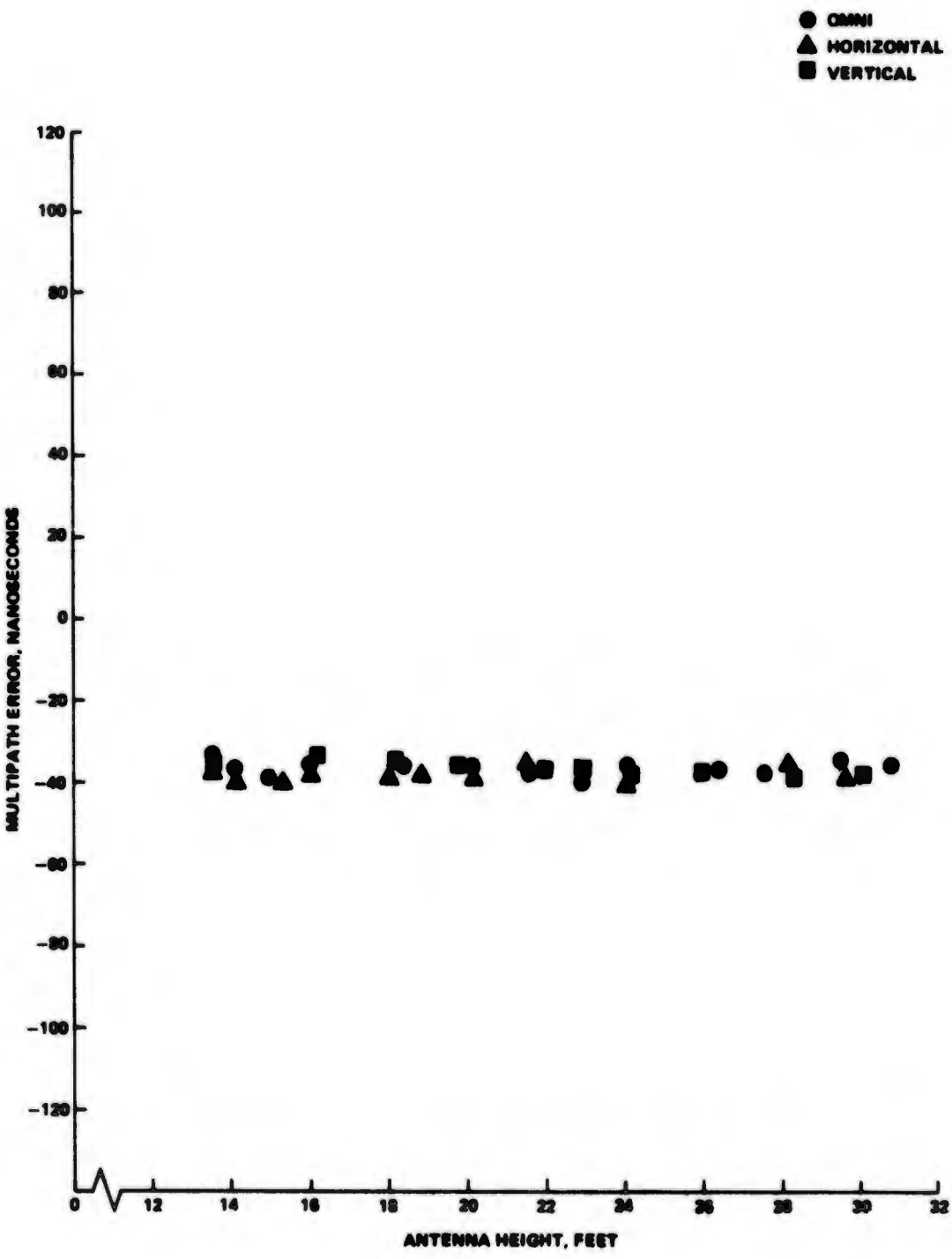

Figure 9-22 Dead Man's Canyon Site No. 1

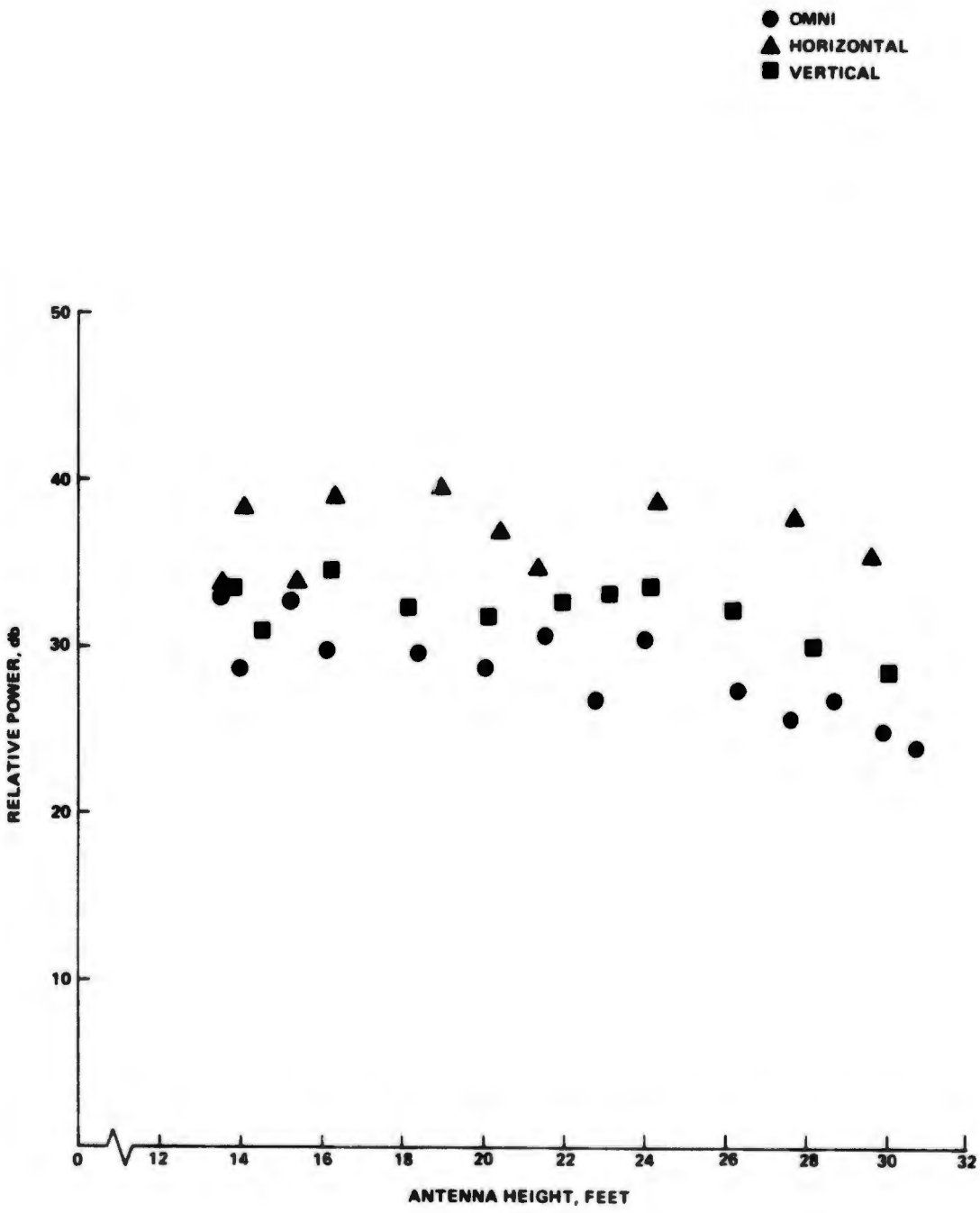

Figure 9-23 Dead Man's Canyon Site No. 1

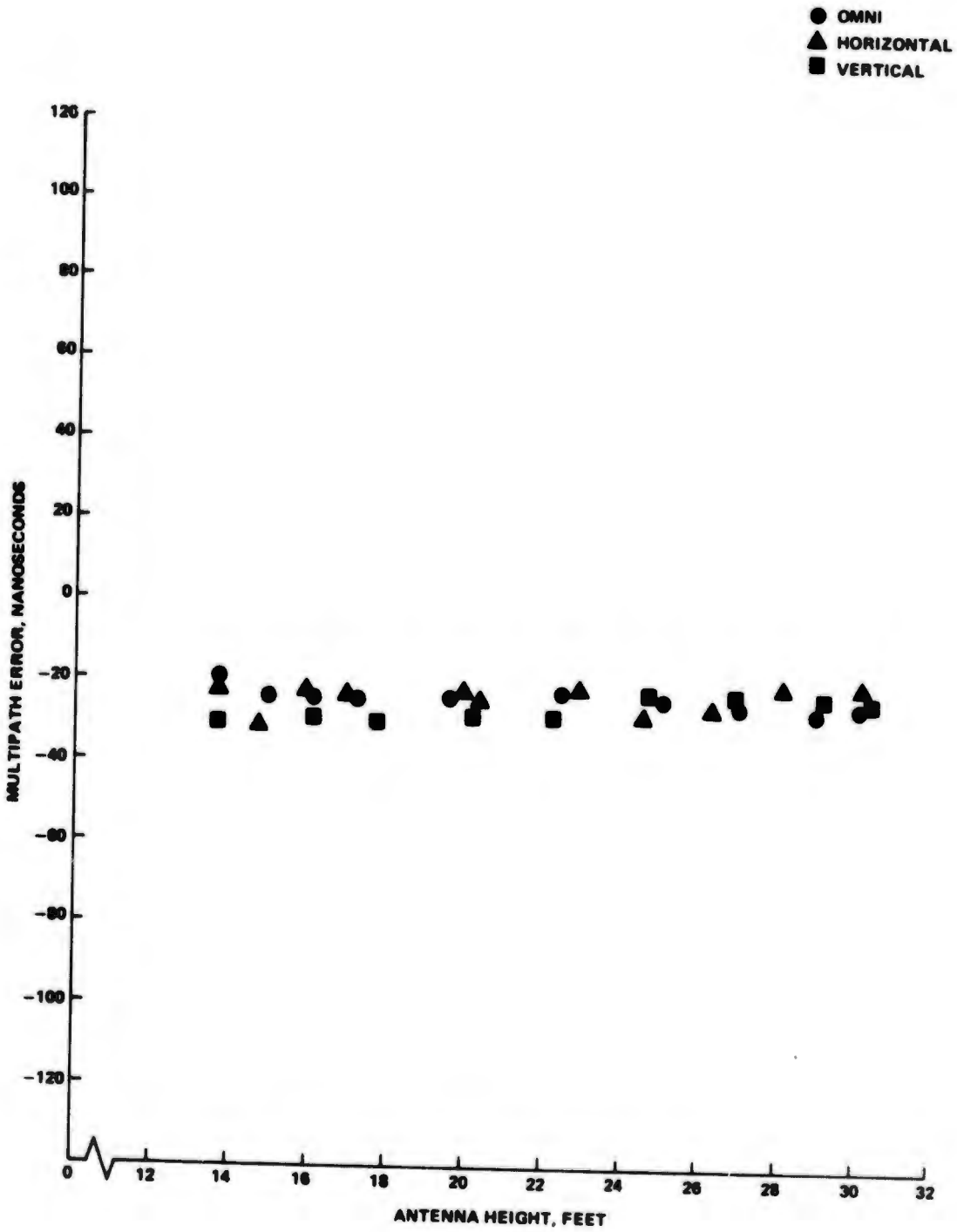

Figure 9-24 Dead Man's Canyon Site No. 3

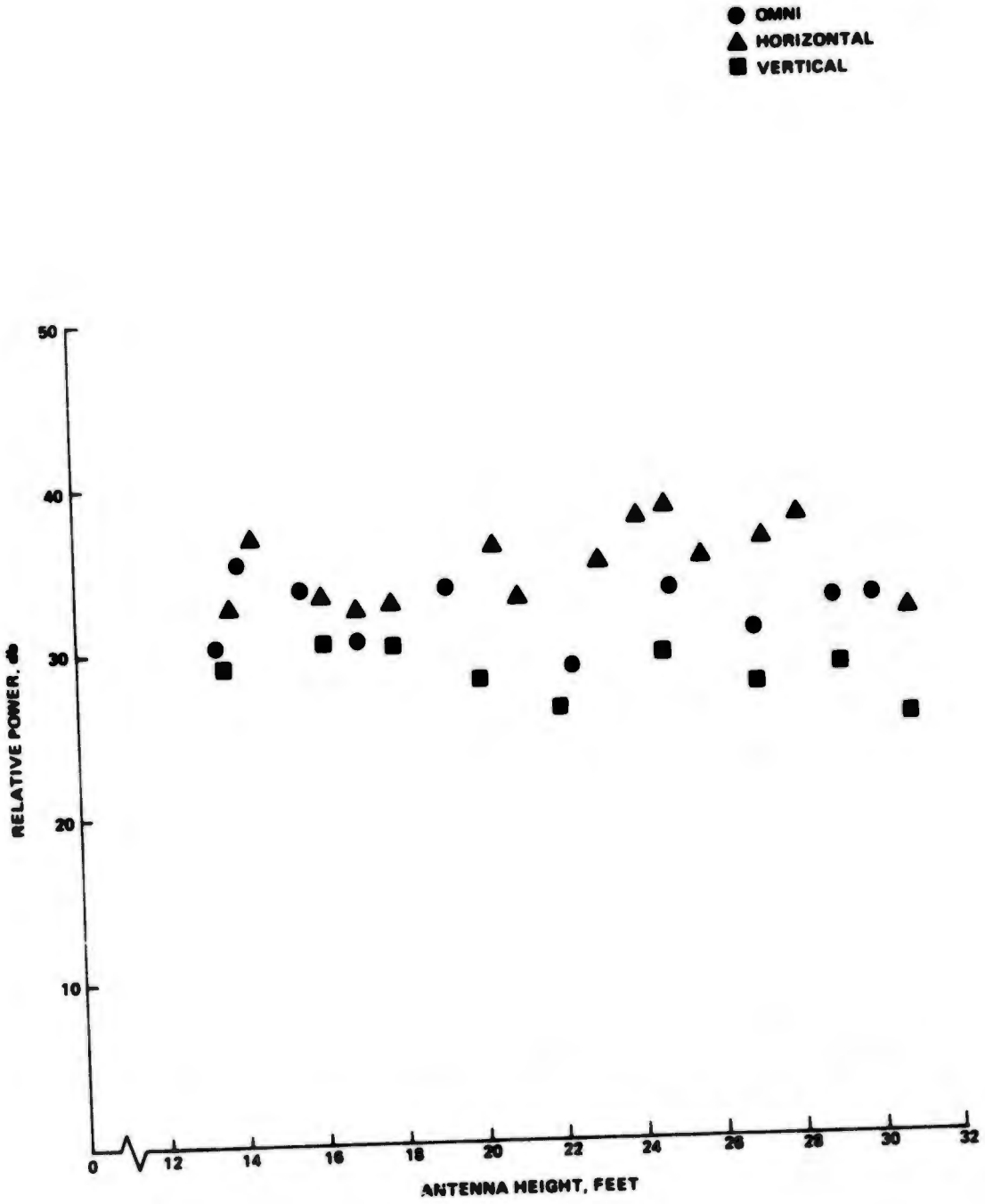

Figure 9-25 Dead Man's Canyon Site No. 3

corresponding to test configuration one and three respectively) the first Fresnel zone clearance is given by:

$$H_o = \sqrt{\frac{\lambda d_1 d_2}{d_1 + d_2}}$$

where d_1 is the distance from the transmitting antenna to the ridge, d_2 is the distance from the receiving antenna to the ridge, and λ is the wavelength for a frequency of 1575 MHz.

The ratio of the path clearance, H, to the first Fresnel zone clearance, H_o is $\frac{H}{H_o}$.

The ratios H/H_o for the range of omni antenna heights (AGL) varied from 1.75 to 3.1 for test position one and from 2.4 to 3.7 for test position three.

In test position two, the line-of-sight between antennas was clear of obstructions. In this case there is more variation between the multipath error and received signal strength data for the three polarization test conditions.

Figure 9-26 is a plot of antenna height (ft) vs multipath error (nanosec) showing a peak to peak variation of approximately 12 nanosec for site position two, as opposed to the 5 nanosec for site positions one and three.

Figure 9-27 is a plot of antenna height (ft) vs signal level (db) for site position two (no obstructions) for the three polarizations. This figure shows a smaller variation in signal level than was the case for test positions one and three.

A theoretical simulation has been made for all three of these site positions, and is explained in detail in Section 9.8. The results of this simulation are plotted in Figure 9-28 which shows antenna height (ft) vs multipath error (nanosec) for site one. The straight line parallel to the abscissa is the theoretical simulation result assuming average ground characteristics. The points below this line are the measured data for the vertical polarization case. Since the theoretical simulation does not model diffraction by obstacles, the two sets of data do not coincide. This same conclusion can be drawn from Figure 9-29 showing data for site position three.

Figures 9-30 and 9-30A are the same type of plots for position two, which was free of obstruction. Here the two data sets are somewhat closer than the diffracted cases just presented. In this case, approximations used in converting the actual geometry of the test to the level simulation geometry can account for the discrepancy. In addition, the electrical properties of the terrain were only approximated from published results of comparable terrain types and profiles. No attempt was made to optimize the simulation parameters to fit the data.

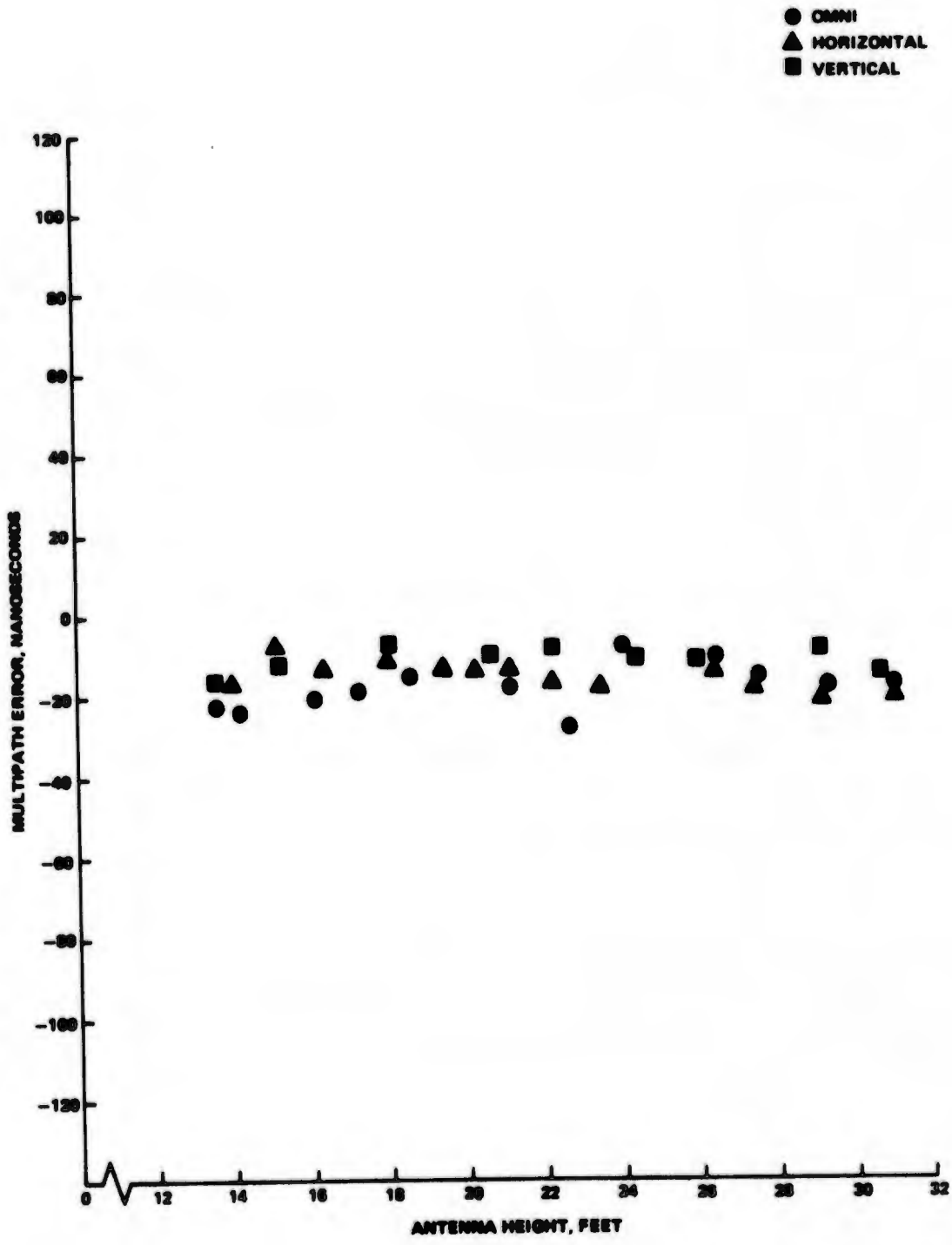

Figure 9-26 Dead Man's Canyon Site No. 2

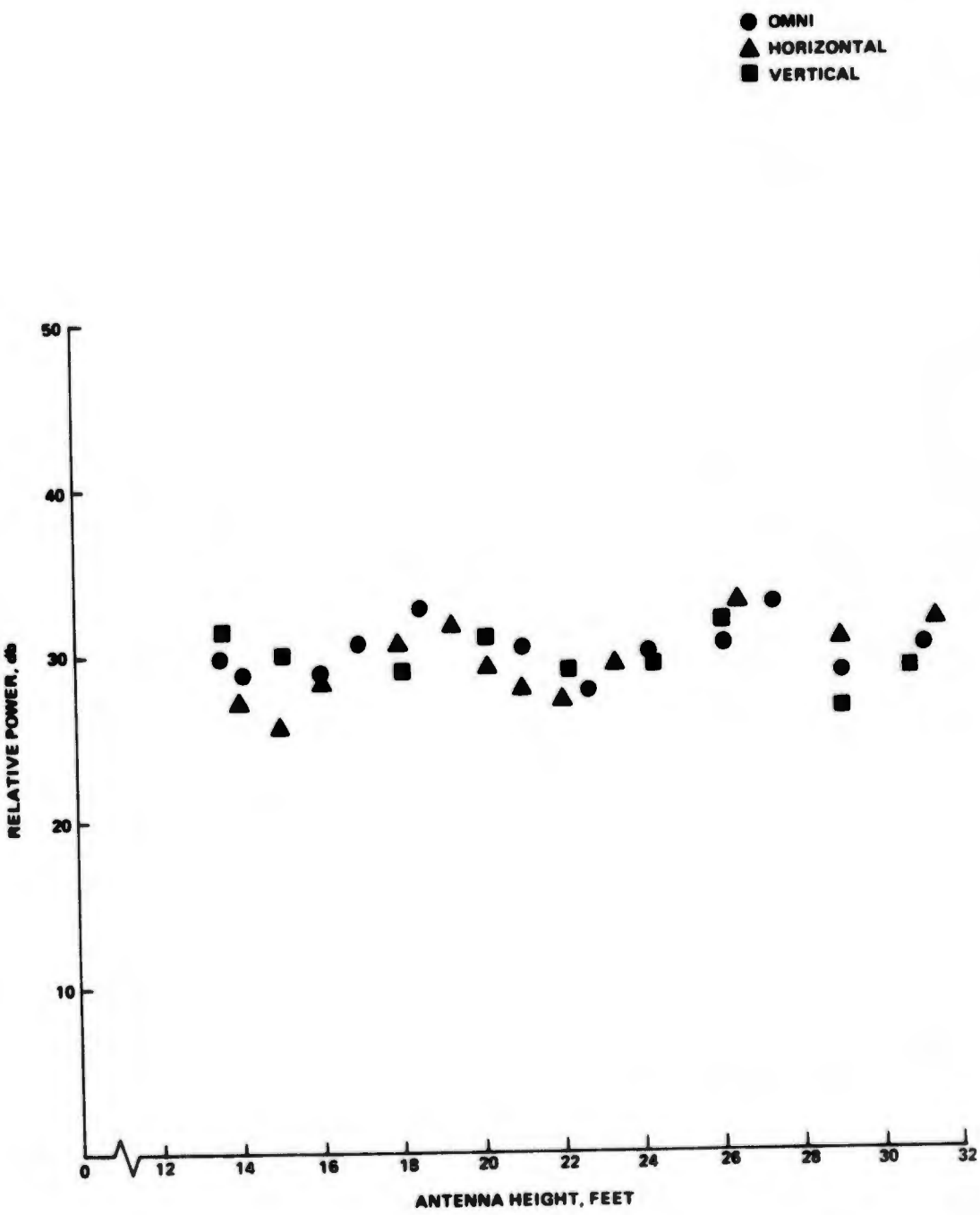

Figure 9-27 Dead Man's Canyon Site No. 2

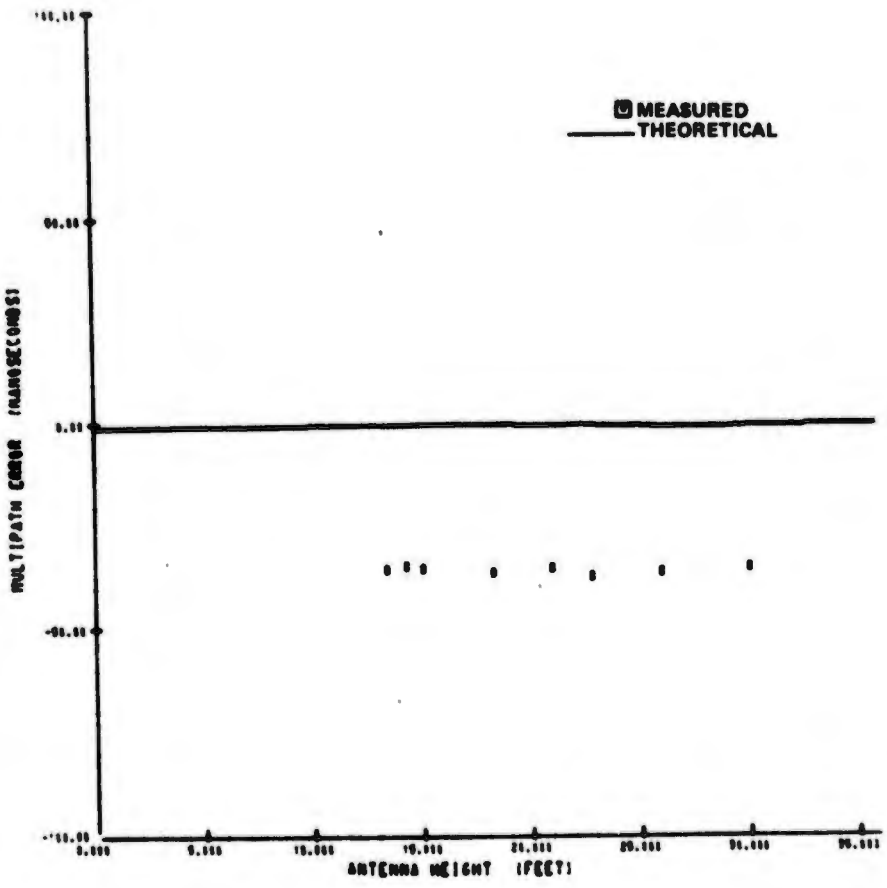

Figure 9-28 Dean Man Canyon Site No. 1 (Diffracted), Vertical Dipole

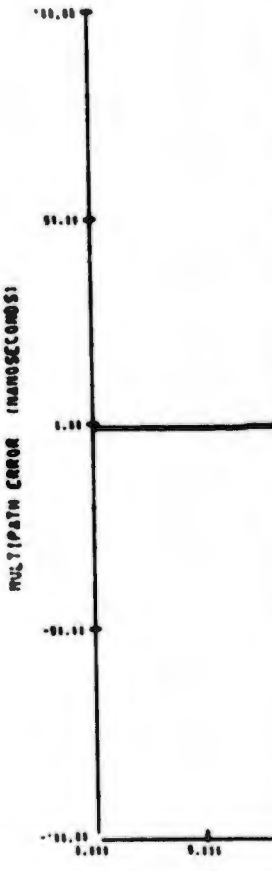

Figure 9-29 Dead Ma

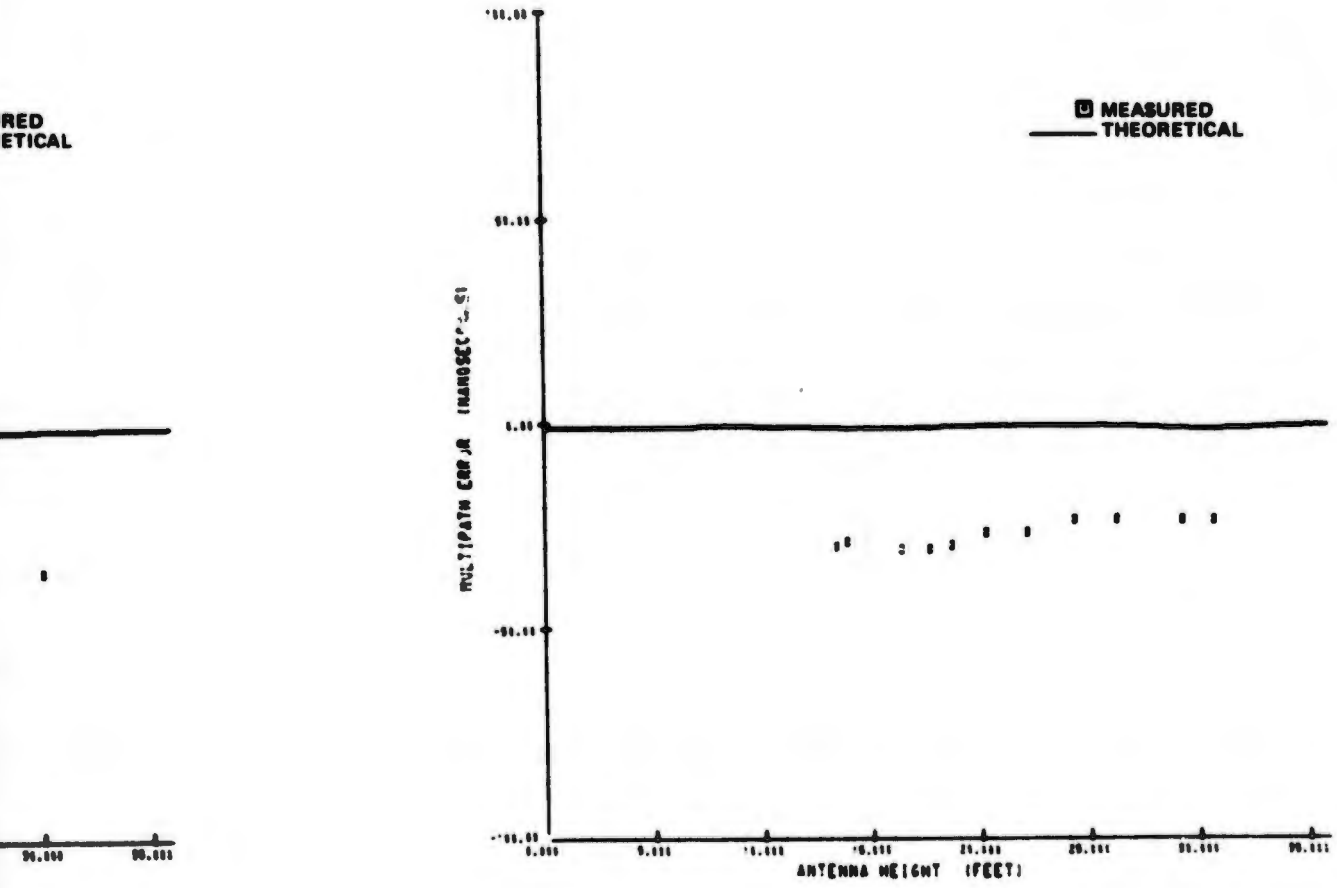

, Vertical Dipole

Figure 9-29 Dead Man Canyon Site No. 3 (Diffracted), Vertical Dipole

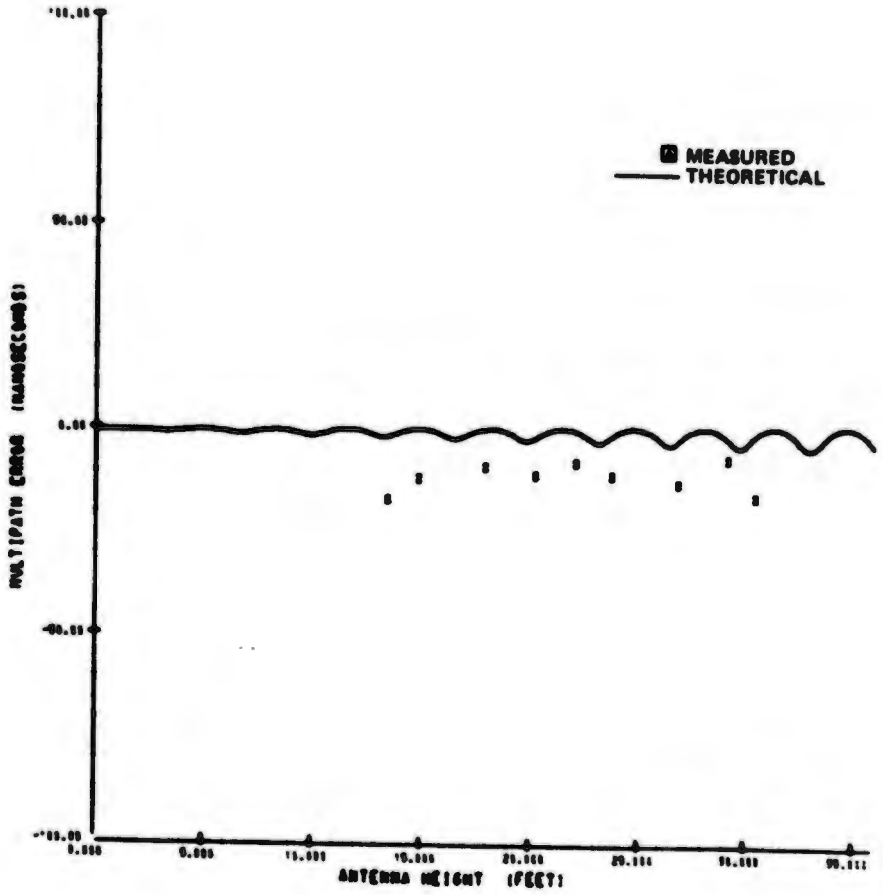

Figure 9-30 Dead Man Canyon Site No. 2

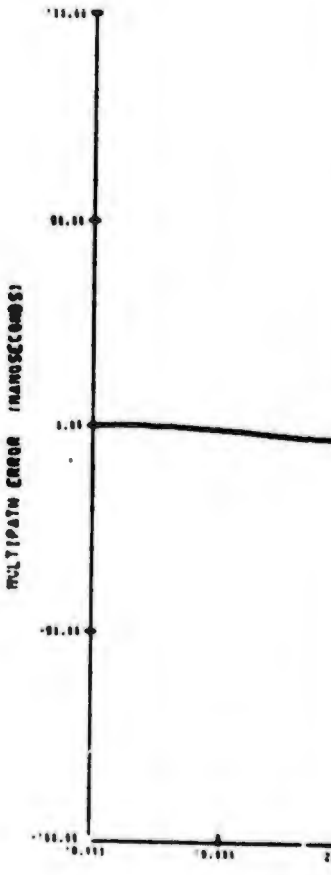

Figure 9-30A

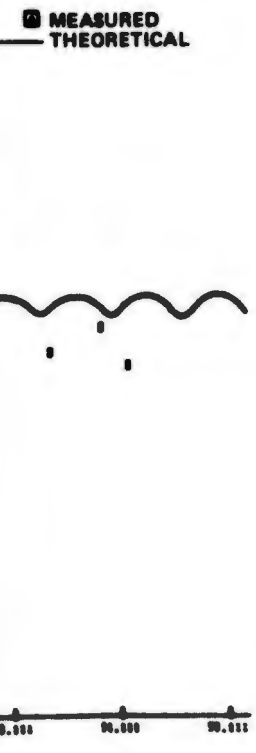

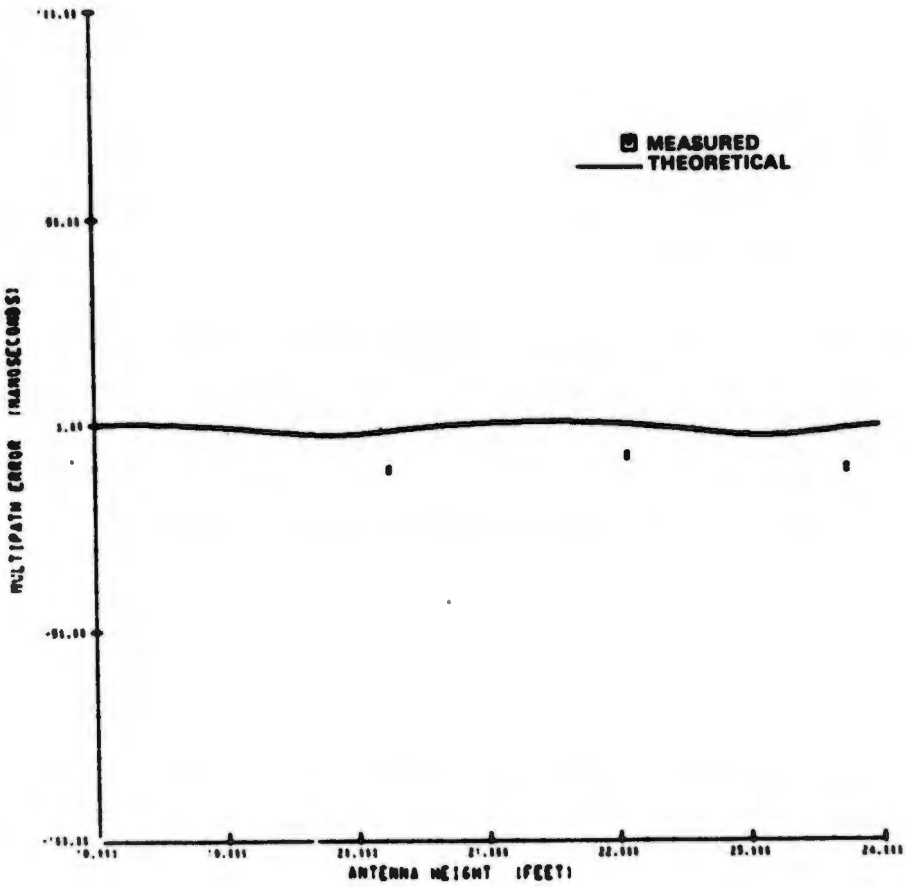

e No. 2

Figure 9-30A Dead Man Canyon Site No. 2

9.5 SMOOTH EARTH TEST AT NORTHROP STRIP

The smooth earth multipath test was conducted on the Salt Flats in the area southeast of Northrop Strip on WSMR. This test utilized a balloon-borne transmitter, the MCS and a set of receiving antennas. The balloon was launched carrying the 612B transmitter aloft to 2000 ft AGL. The position of the receiving site was moved along a constant 145° azimuth (TN) to presurveyed sites to obtain look angles of approximately 60°, 40°, 30°, 20° and 10° from receiving to transmitting antennas, Figure 9-31. The balloon was positioned nominally over survey marker BTR, but was not always directly over it because of varying wind conditions. The look angle, θ, was measured during the time data were taken on position one (60°) and was found to vary as much as 5° during the run. Data taken by geodetics on 24 Aug. 72 at position one show the mean was 59.4° with a standard deviation of 1.23° and on 25 Aug. 72 the mean was 58.3° with a standard deviation of 1.82°. The angle data show that the ground track distance and slant range varied during the test. Nominal ground track and slant ranges between receiver dish feed tip and transmitter omni are shown in Figure 9-31. On position one, 60°, the balloon transmitter drifted out to the 8° field of view of the dish antenna. An omni antenna, placed at ground level to eliminate ground reflected signals, replaced the dish antenna. Positions two through eight used the dish as shown in Figure 9-32.

An attempt was made to track the balloon transmitter with two theodolites manned by geodetic personnel standing over surveyed ground stations. Data were taken simultaneously at five-minute intervals. The resulting balloon position determined from measurements by two theodolite stations, proved to be highly variable because of the position error sensitivity to small changes in elevation angle. The tracking effort was abandoned after two attempts on 24 Aug. 72 and 25 Aug. 72 at position one. Elevation angle (θ) from receiving antenna to transmitter omni was taken with a "bubble" inclinometer at each receiver position of rough earth and smooth earth test after 25 Aug. 72.

The ground surface between receiver and transmitter antennas was extremely flat, dry, and hard consisting of gypsum, sand and a high degree of salt. The 621B ILS runway was constructed on this same type of surface and withstood the touch down of a NC-135 aircraft weighing 186,000 lb, 31 times without showing appreciable surface degradation.

Figure 9-32 shows a typical receiver transmitter configuration for smooth earth testing. During test measurements, all vehicles were kept out of the line of sight between antennas.

9.6 ROUGH EARTH TEST AT WHITE SANDS DUNE AREA

An area of sand dunes southeast of the WSMR Salt Flats was selected to run the rough earth multipath testing. Dunes ranging from 10 to 60 ft high spaced 100 to 200 ft peak-to-peak, formed the rough earth test area. The sand, salt and gypsum surface was relatively soft and granular for about 3 to 6-in. in depth. Dust storms, blowing fine sand, are common to this area (see Figure 9-33). Unlike beach sand, the dunes consist of very small grain size sand.

Sites were selected within the sand dunes to yield a 60°, 40°, 30°, look angles between the receiver and the balloon transmitter positioned at the edge of the dunes.

After the data were taken, the sites were surveyed. The results of the survey are shown in Figures 9-34 and 9-35. As in the smooth earth test, only nominal ranges

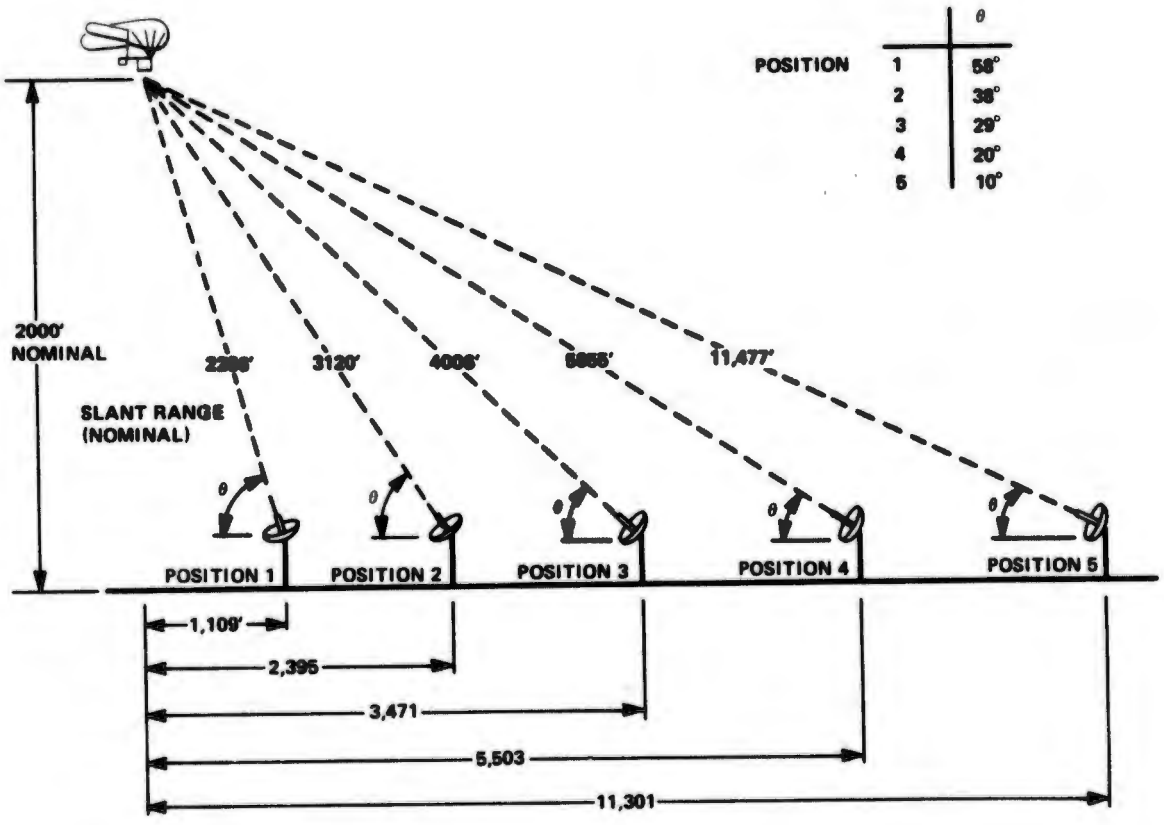

Figure 9-31 Smooth Earth Multipath Test

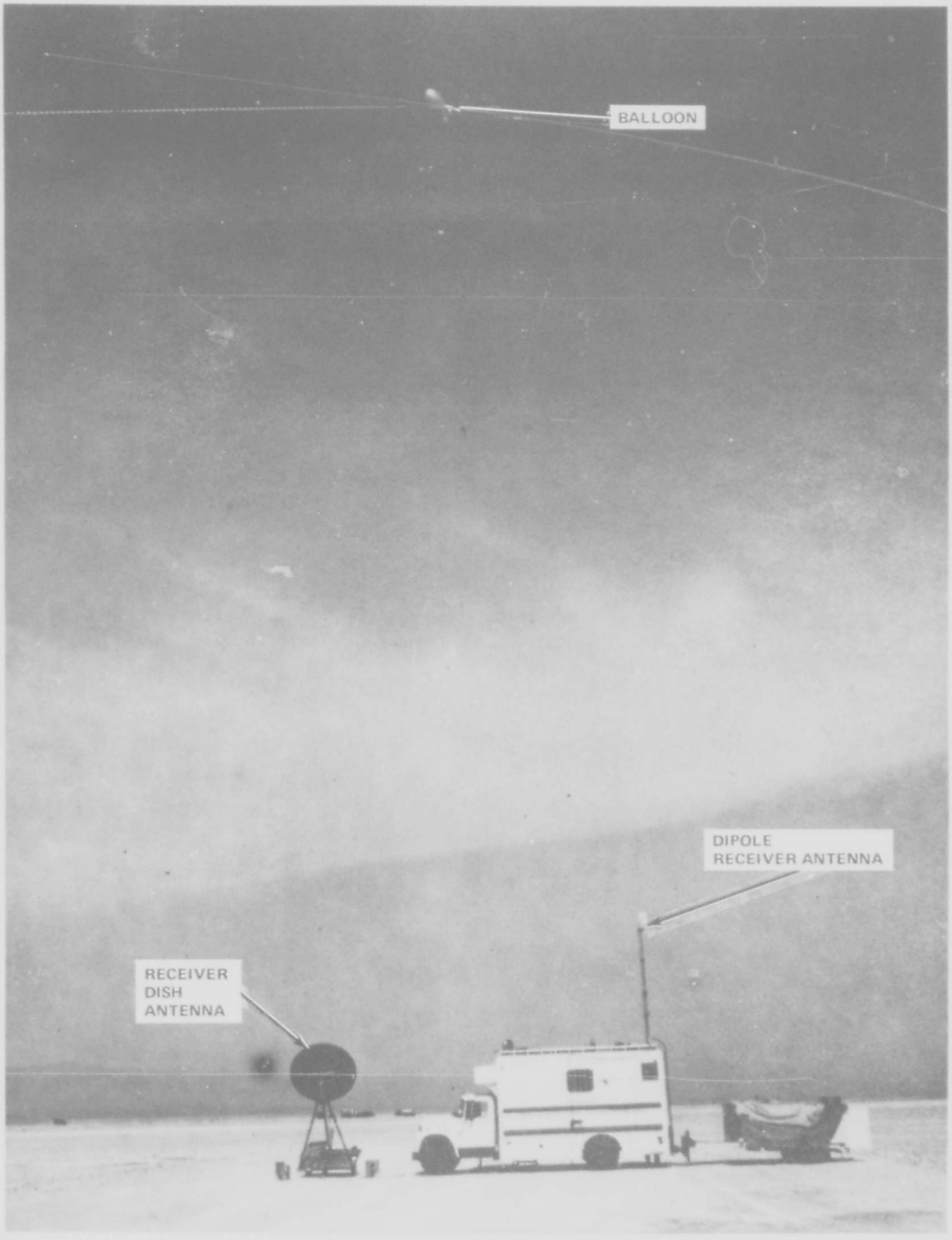

Figure 9-32 Smooth Earth Multipath Test Position 2, θ - 40°

Figure 9-33 Rough Earth Sand Dune (Typical)

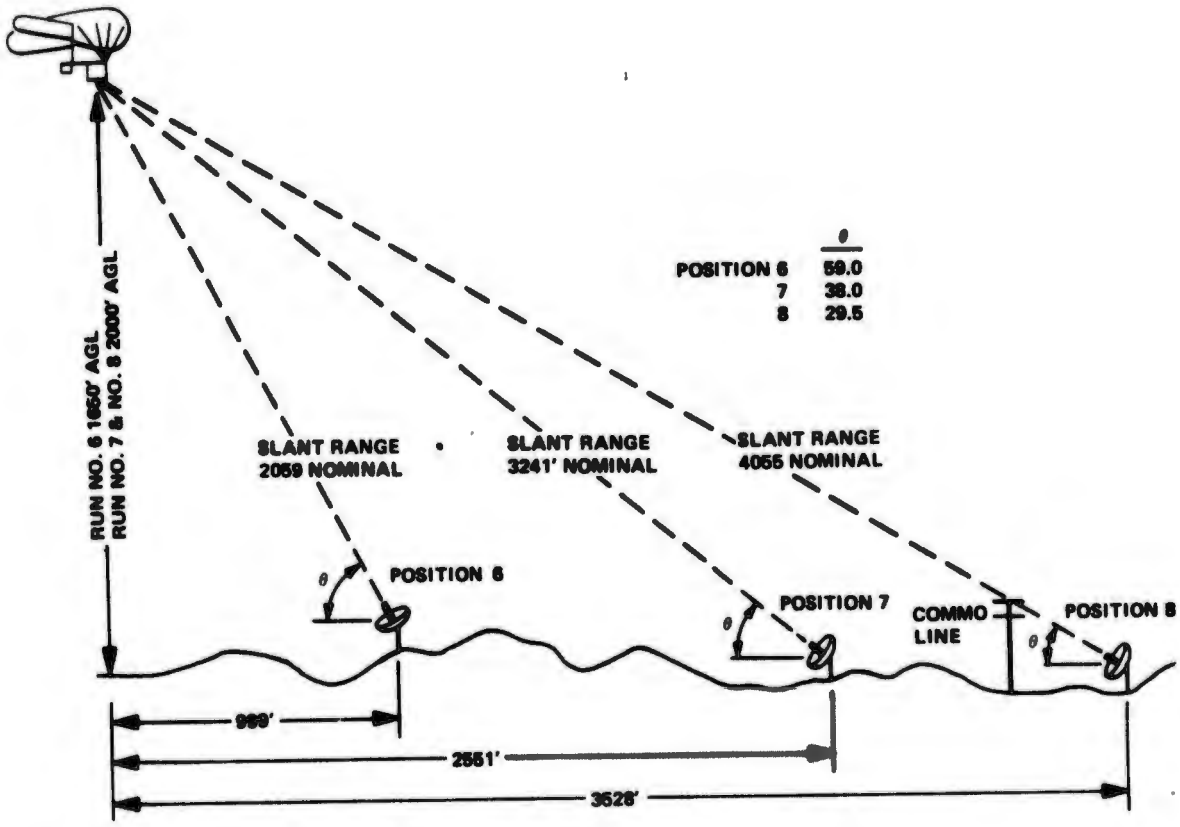

Figure 9-34 Rough Earth Multipath Test

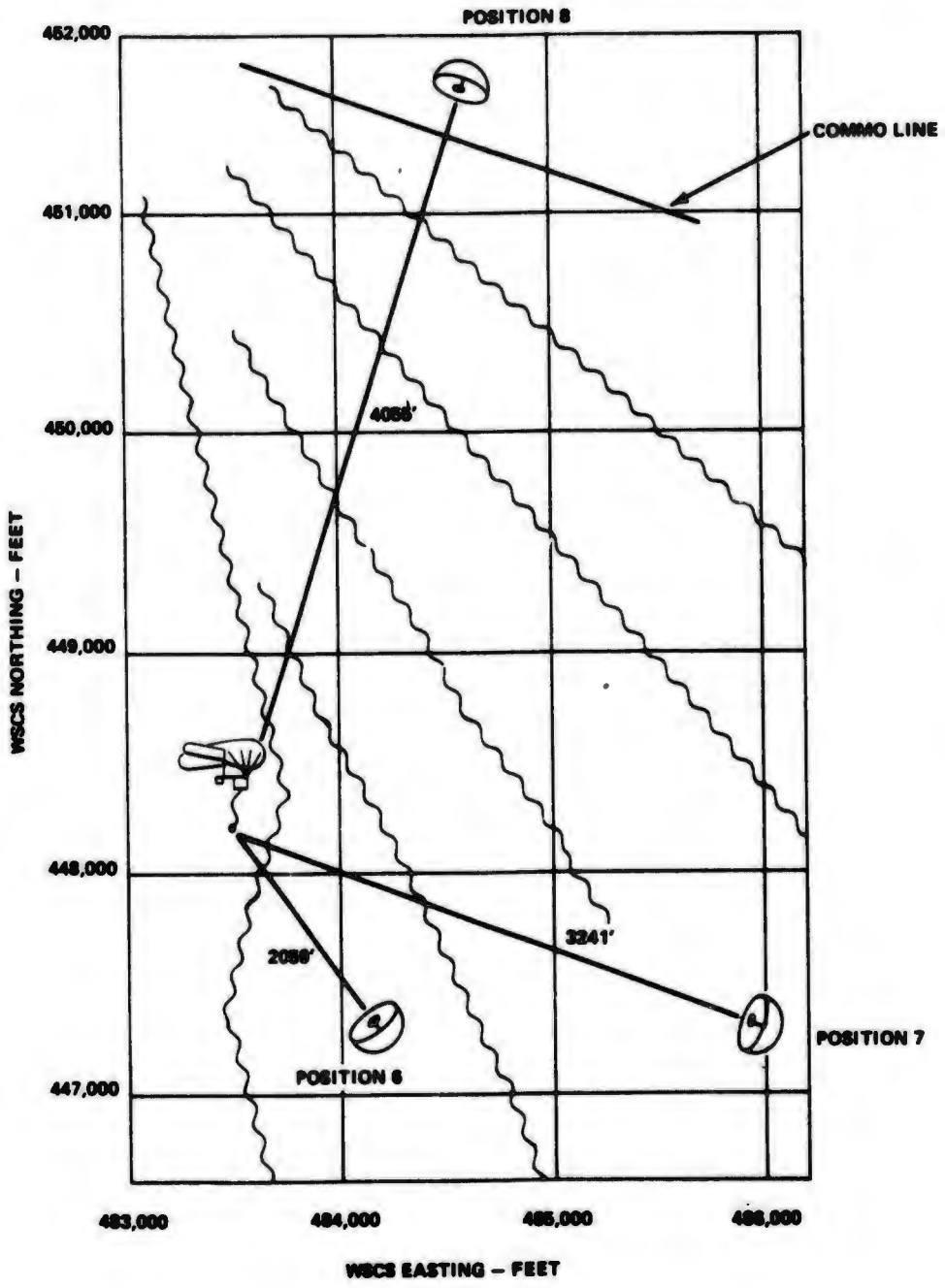

Figure 9-35 Rough Earth Multipath Test

can be reported because of balloon variation. Figure 9-36 shows the position of communication lines suspended from poles running perpendicular to the receiving antennas line of sight. These communication lines were about 24 ft AGL and 100 ft in front of the MSC.

Figure 9-37 is a tabulation of relative distances between receiving antennas and their relationship to the MCS. Each measurement was taken from a reference stake located at each site.

9.7 TEST RESULTS FOR SMOOTH AND ROUGH EARTH MULTIPATH

The theoretical envelope range tracking error as a function of multipath differential delay between the desired and interfering signals is shown in Figure 9-38 for a reflection coefficient of 1.0. Receiver ranging errors can take on any value within this envelope depending on the exact signal differential delay. Inside the theoretical envelope is drawn another smaller theoretical envelope corresponding to the test conditions at WSMR where the average reflection coefficient was 0.7. The test results for the smooth earth tests follow this prediction as shown in Figure 9-39 which is a plot of antenna height (and corresponding differential delay) vs multipath error in nanosec. Figure 9-39 contains all the data collected for smooth earth tests. The smaller theoretical envelope from Figure 9-38 has been superimposed on this figure. Since differential delay is essentially a linear function of antenna height for the tests under consideration, the abscissas of Figure 9-39 are related as indicated. The data on this figure show that the multipath errors were caused by reflections with predominately short (less than 50 ft) differential delays with an average effective voltage reflection coefficient of approximately 0.7.

The few points which fall outside of the envelope are a result of uncertainty in the true transmitter position, variations in the receiving antenna position due to wind and therefore, of uncertainty in the value of differential delay determined from the transmitter-to-receiver geometry. This uncertainty means that the measured tracking errors (ordinate) cannot be properly located on the plot of Figure 9-39. The transmitter position could not be precisely measured since, for these tests, the transmitter was carried 2000 ft above the ground by a tethered balloon which drifted slightly in the wind.

To examine the effect of balloon position variation on the multipath error one needs to compute the perturbation of differential delay, D, which directly affects the magnitude of the multipath error. The following is a simplified sketch of the test set-up.

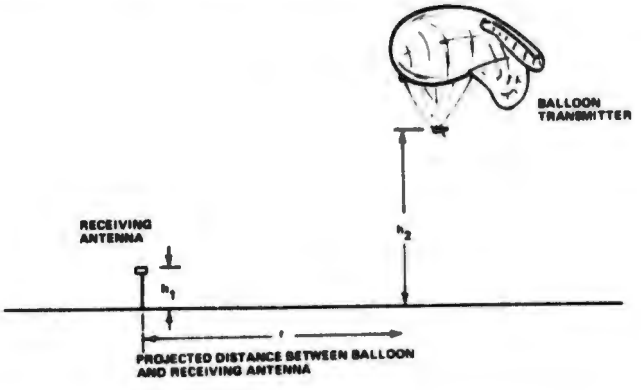

Figure 9-36 Rough Earth Multipath Test Position, No. 8, $\theta = 30^{\circ}$

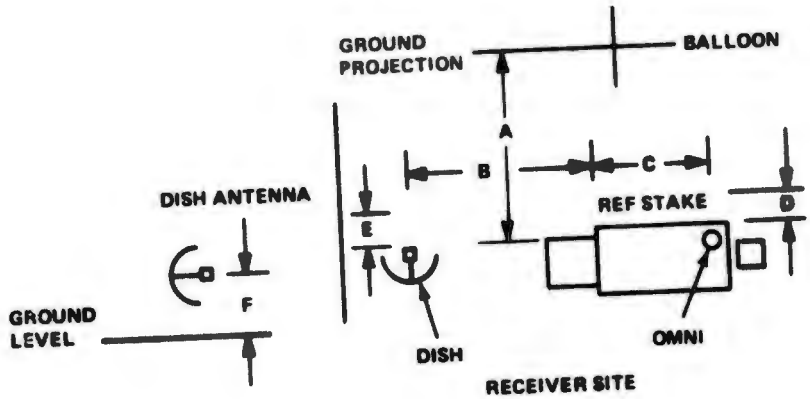

Date	PT No.	Dim. A, Feet	Dim. B, Feet	Dim. C, Feet	Dim. D, Feet	Dim. E, Feet	Dim. F, Feet	Comments
9-26-72	1, 66°	1109	9.2	9.0	17.4	0	0	Omni used on ground
10-03-72	1, 66°	1109	15.4	17.2	4.0	9.8	9.7	
10-03-72	2, 26°	2395	17.4	14.8	4.2	7.4	10.5	
10-03-72	3, 26°	3471	23.8	14.4	3.7	7.4	–	
10-03-72	4, 26°	5503	18.2	14.5	2.5	3.8	10.5	
10-04-72	5, 16°	11,391	19.9	14.5	3.8	1.9	10.4	
10-05-72	6, 66°	999	18.2	16.8	2.3	8.4	11.1	Balloon at 1000 feet
10-05-72	7, 26°	2,551	17.8	15.6	2.8	9.0	10.9	
10-05-72	8, 26.5°	3,528	20.0	15.4	3.4	7.9	11.1	

Figure 9-37 Tabulation of Test Setup Distances for Smooth and Rough Multipath Testing at Salt Flats W.S.M.R.

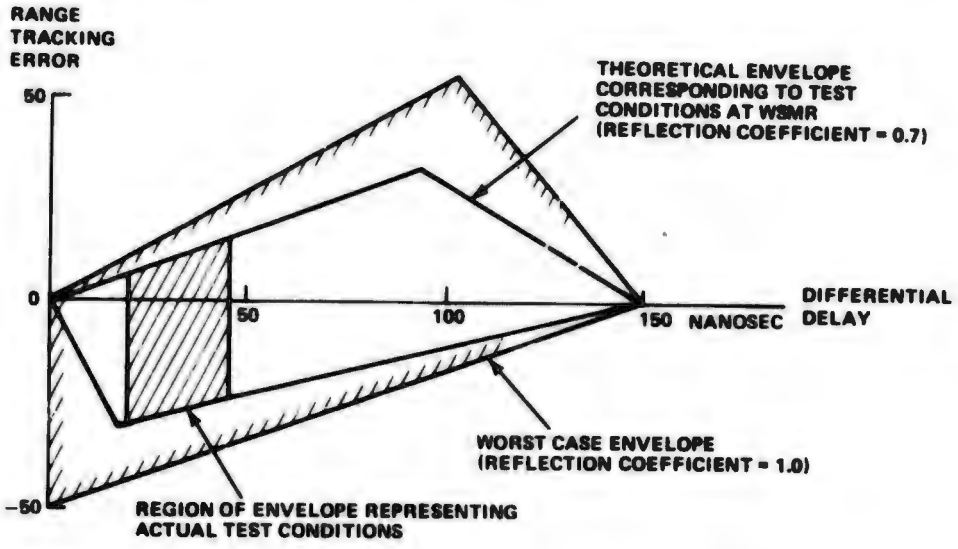

Figure 9-38 Theoretical Envelope of Range Tracking Error Caused by Signal Multipath

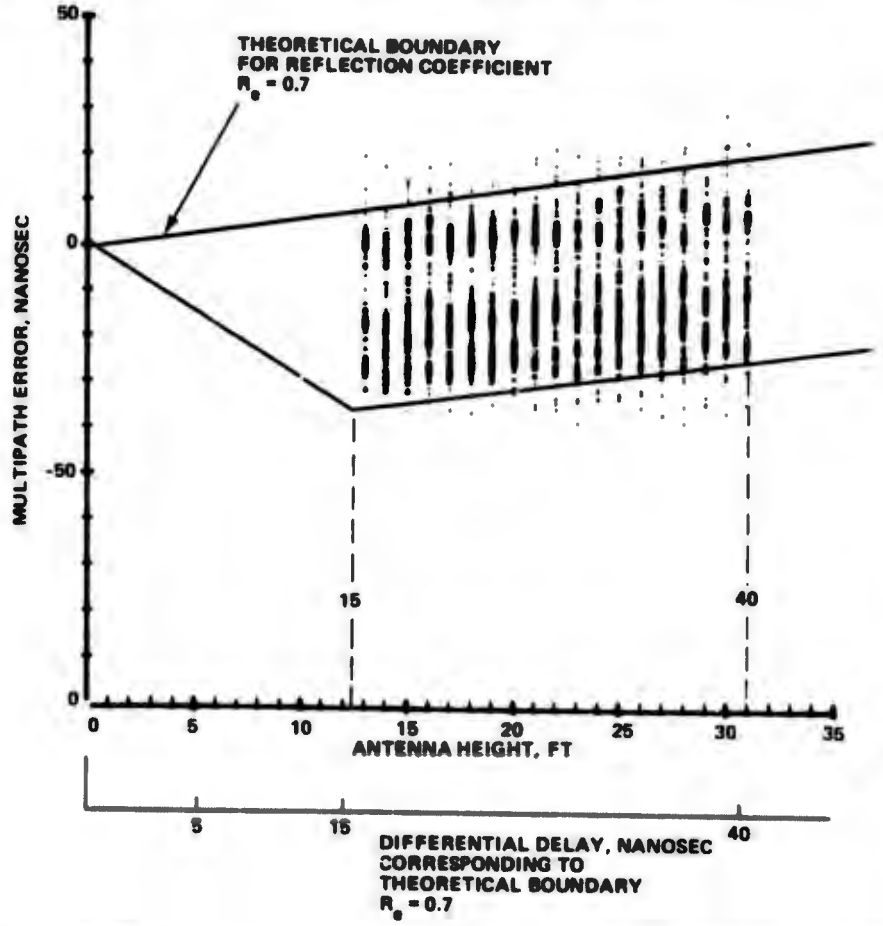

Figure 9-39 Composite Summary of Test Data for Smooth Earth Tests

The sensitivity of differential delay for the geometries of test positions two, three, four and five (smooth earth) with $h_2 \gg h_1$ and $h_2 \sim r$ is given by

$$\delta D \simeq \frac{2h_1 \delta h_2 + 2h_2 \delta h_1}{\sqrt{r^2 + h_2^2}}$$

where h_1 is the receiving antenna height (AGL), h_2 is the balloon transmitter height (AGL) and r is the projected distance between the balloon and the receiving antenna. Since for these tests, the sensitivity of δD with changes of δh_2 is approximately zero, the overall results are essentially unaffected by the uncertainty in the position of the balloon, except that the data is noisy as a result of small changes in δh_1 due to wind.

Figure 9-40 is a plot of antenna height (ft) vs multipath error (nanosec) for three polarizations, circular, horizontal, and vertical, the first of the smooth earth tests at position one, a look angle of 60°. In this case the relative motion between transmitting and receiving antennas caused by the wind also induced changes in the point of reflection, grazing angle and reflection coefficient. An examination of the relative magnitude of the reflection coefficient for horizontal and vertical polarization for this grazing angle of 60° shows a greater sensitivity of the horizontally polarized system to changes in geometry than the vertically polarized set-up. This fact is illustrated by the spread of the points for the horizontal polarization, 40 nanosec, compared to the vertical polarization spread of 20 nanosec.

Figure 9-41 is a plot of antenna height (ft) vs signal strength (db) for the same test. This figure also illustrates the sensitivity of the reflection coefficient for horizontal polarization by a large spread in received power. The peak-to-peak variation here is 20 db for horizontal vs 5 db for vertical polarization.

Figure 9-42, shows the theoretical envelope of multipath error for the smooth earth test at test position one. The multipath error vs antenna height for vertical polarization were plotted for antenna heights of 0 to 6 ft, 6 ft to 12 ft, 12 ft to 18 ft, 18 ft to 24 ft, 24 ft to 30 ft, 30 ft to 36 ft, and a composite 0 to 36 ft. Figure 9-42 is a 0 to 36 ft plot and represents the total multipath error envelope. However, all the 0 to 36 ft plots show moire patterns due to aliasing of data points within the envelope due to insufficient sampling rate. These patterns within the envelope have no consequence to the results. The measured data points are shown by "squares" superimposed on the plot of the theoretical envelope. In this case it can be seen that all the measured data falls within the theoretical envelope.

Figure 9-43 is a blown-up portion of the same data. Each increment on the abscissa (antenna height) in this figure is only 1 ft as opposed to the abscissa on Figure 9-42 where each increment is 5 ft. However, in Figure 9-43 there are no moire patterns due to aliasing of data points, and the sinusoidal curve shows the structure of the signal. Here again one can see that all the measured data points fall within the envelope of the fine structure.

Figures 9-44 and 9-45 are the same kind of plots as Figures 9-40 and 9-41 but for the second smooth earth test position two. These two figures again demonstrate, as did Figures 9-40 and 9-41, the sensitivity of the magnitude of the reflection coefficient for horizontal polarization as a function of changes in geometry.

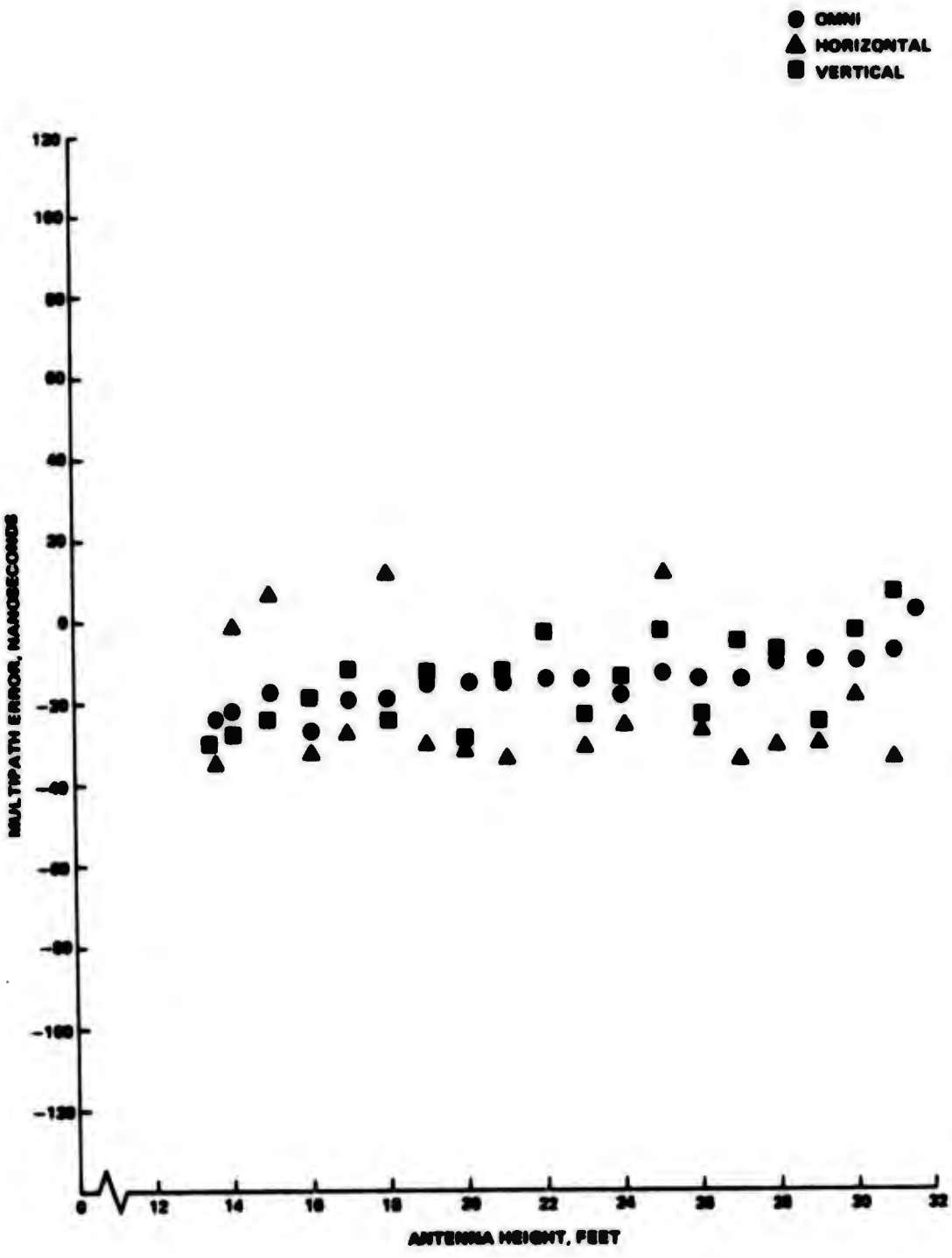

Figure 9-40 "Smooth Earth" Northrop Strip - Site No. 1

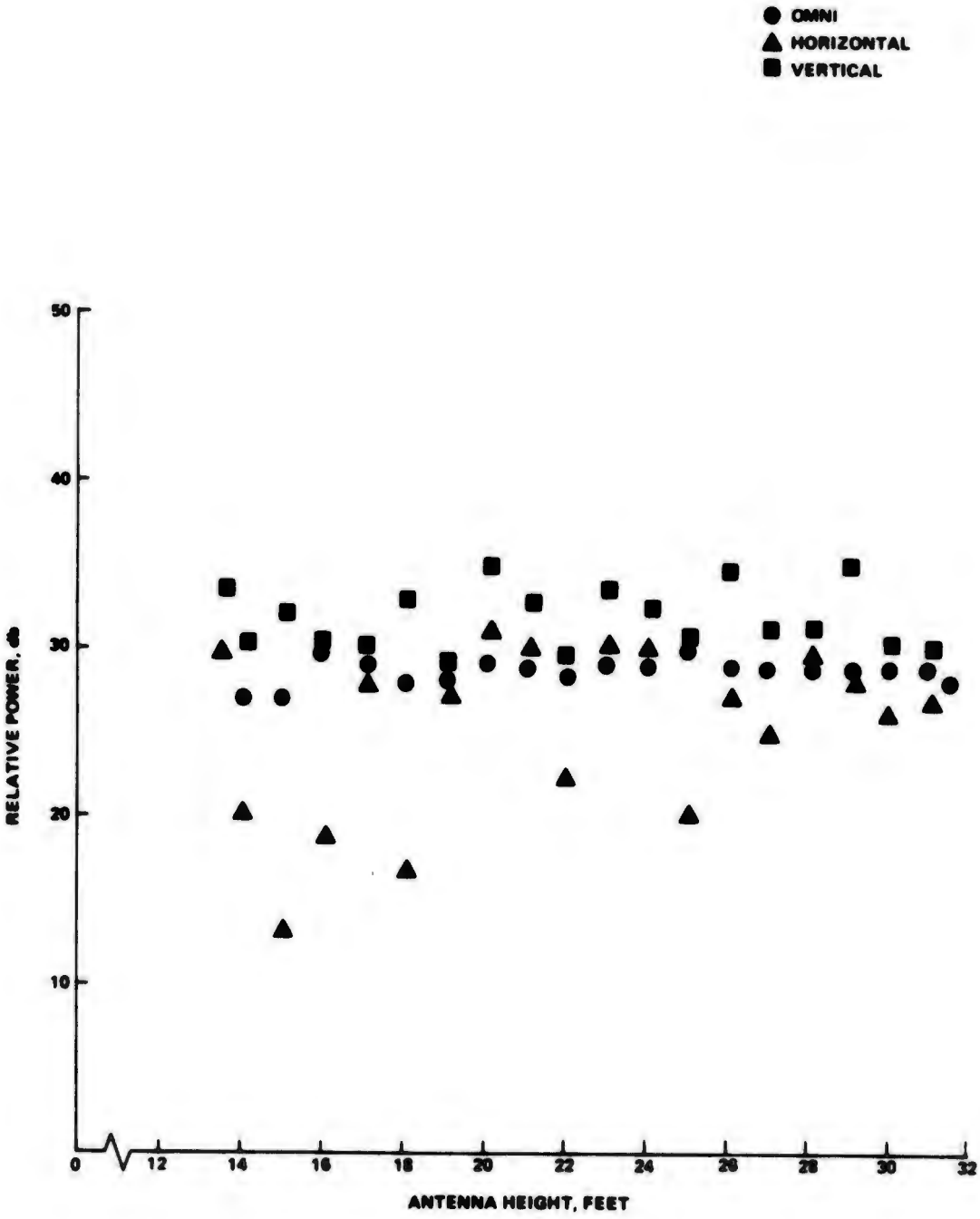

Figure 9-41 "Smooth Earth" Northrop Strip - Site No. 1

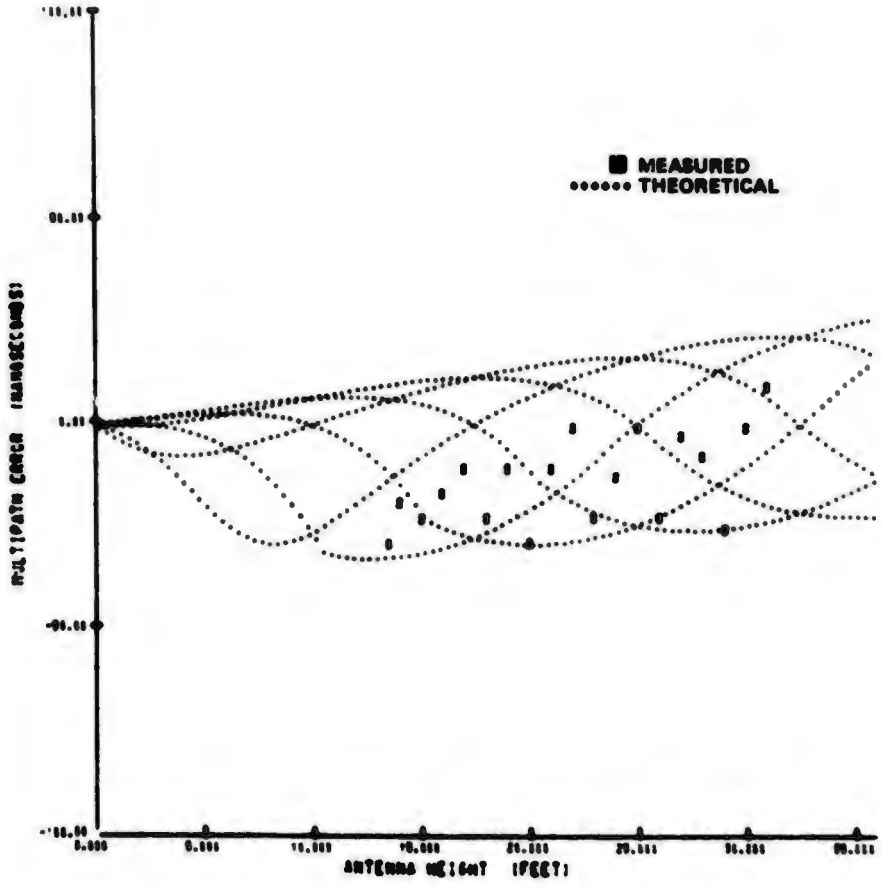

Figure 9-42 Northrop Strip Smooth Earth, Site No. 1, Vertical Dipole

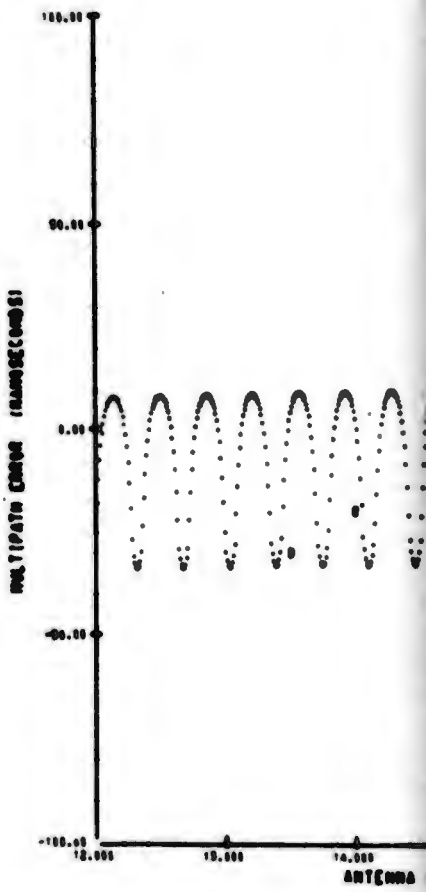

Figure 9-43 Northrop Strip Smoo

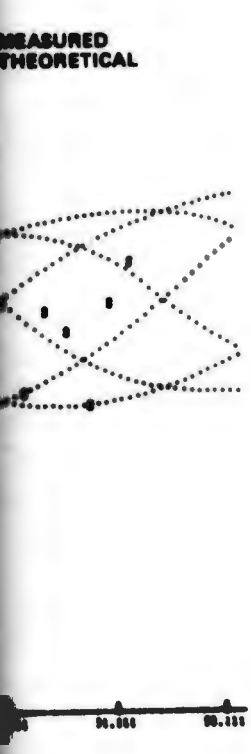

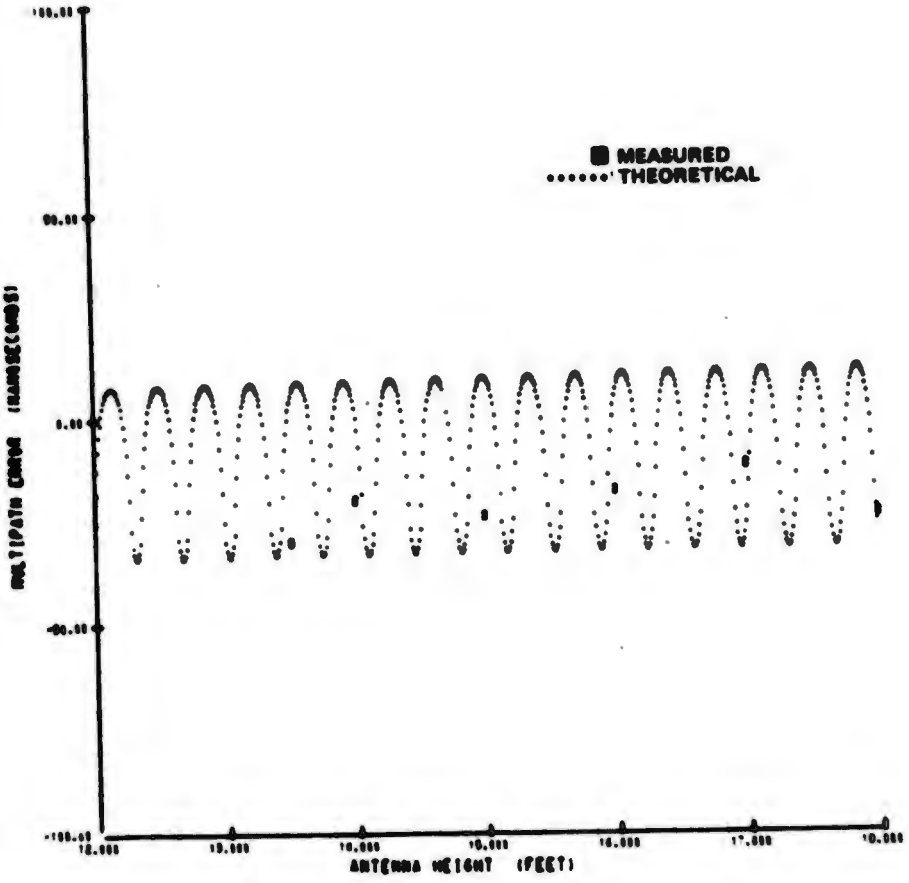

No. 1, Vertical Dipole

Figure 9-43 Northrop Strip Smooth Earth, Site No. 1, Vertical Dipole

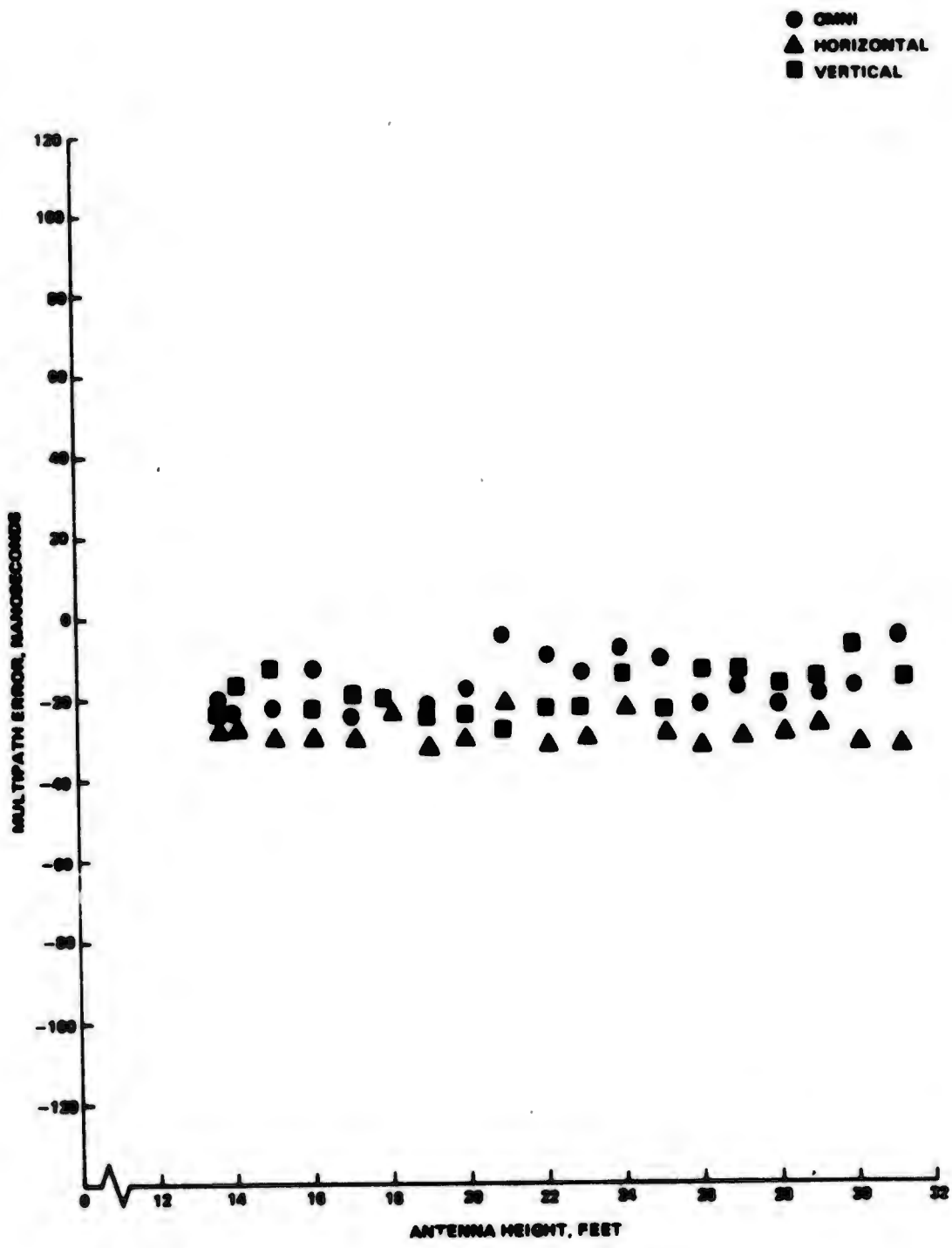

Figure 9-44 "Smooth Earth" Northrup Strip - Site No. 2

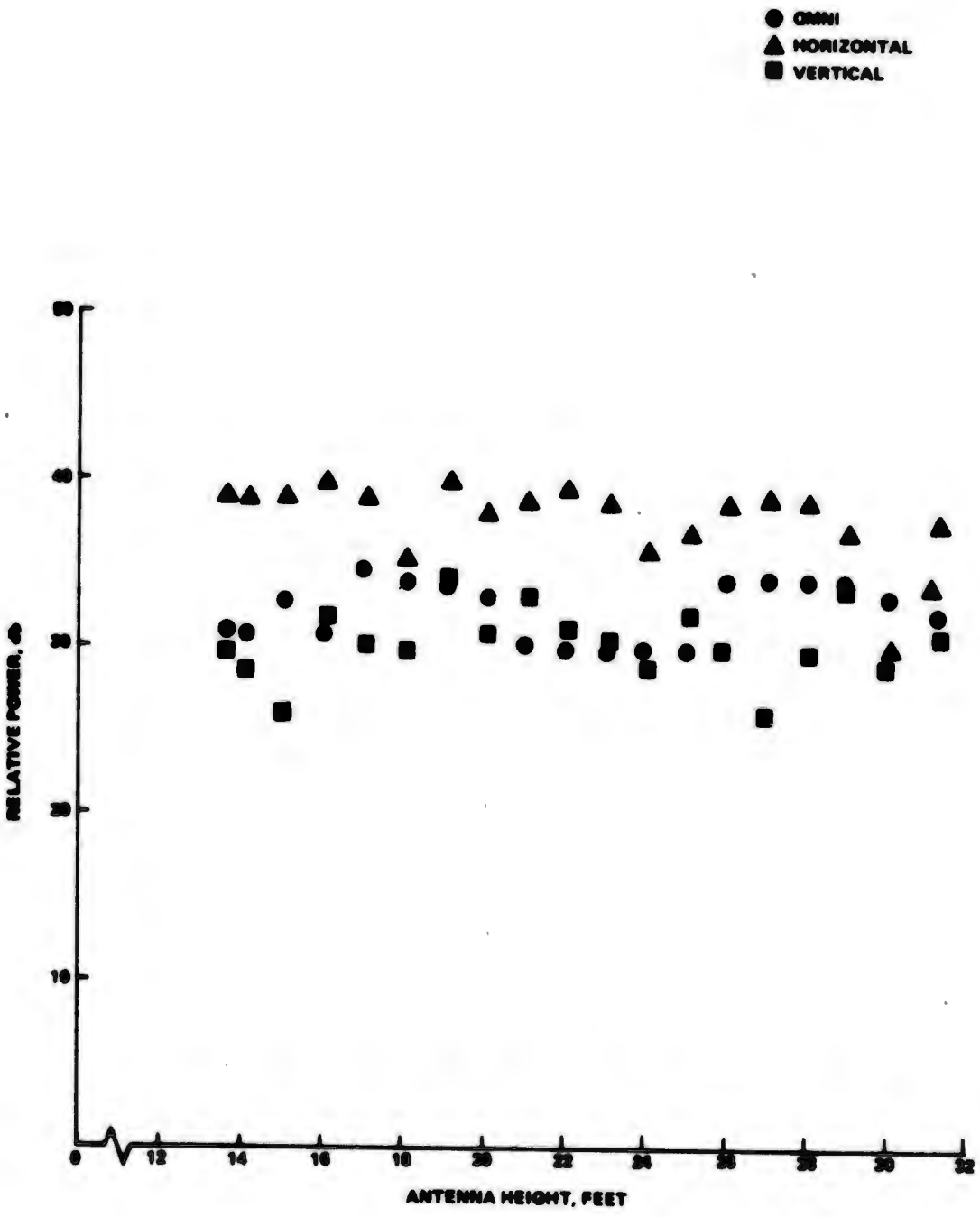

Figure 9-45 "Smooth Earth" Northrop Strip - Site No. 2

Figure 9-46 is a plot of the means (square symbol) and the standard deviations (dot symbol), for a number of measurements taken at a particular antenna height vs the multipath error in nanosec, at site position two, for a circular polarization. Figure 9-47 is for vertical polarization, and Figure 9-48 for horizontal polarization. This presentation of the data highlights the effects of wind as shown by the substantial increase in the spread of the standard deviation of multipath error for horizontal polarization. The increased noiseness of the data is a direct result of changes in differential delay and apparent electrical properties of the terrain.

The change in the standard deviation of multipath error is correlated with the wind direction and speed for a particular geometry (See Appendix B). However, the receiver noise contribution to pseudo-range error in any of the receiver channels is in the order of 0.5 ft, since the receiver power levels during the tests were in the region of -120 dbm to -110 dbm. Therefore, the noisiness of multipath data is predominantly a function of the change in the relative geometry caused by transmitting and receiving antenna relative motion. The standard deviation of multipath error becomes smaller as the elevation angle decreases. This is a direct result of the larger geometry (i.e., increase in projected distance) reducing the sensitivity of differential delay.

The data from test position three and four exhibited the same characteristics as the data from test positions one and two (See Figures 9-49 thru 9-62). In these tests however, the data shows the reduction in the noisiness of multipath error as a result of decreased look angels.

Figure 9-63 and 9-64 are a presentation of the measured data (square symbol) superimposed on the theoretical envelope with most of the measured points falling within the theoretical envelope. In general, it is not reasonable to expect that all simulated and measured values agree, and this is especially true in these tests, since no attempt was made to adjust or optimize the simulation parameters to fit the data. Discrepancies can be attributed to a number of factors. One such possibility is poor modelling of the geometry of antenna heights, terrain roughness. As an additional factor, the complex reflecting surface (which is practically impossible to model accurately) may have caused the point of reflection of a single specularly reflected signal to deviate from the theoretical model, or may have caused multiple and strong specularly reflected signals to reach the receiving antenna. These latter effects would cause a bias shift to the multipath data.

Such a shift has taken place in the data at site position five. Figures 9-65 and 9-66 are plots of antenna height vs multipath error showing the measured data as square symbols superimposed on the curves of the theoretical model. The theoretical curves are generally above the measured data points as a direct result of multipath bias shift. This effect was not modelled and the shift between the theoretical curves and measured data points is expected. The statistical summary plots, multipath error and received power versus antenna heights are given in Figures 9-67 thru 9-71. In this test the projected distance increased to 11,301 feet, approximately six times the value in site two. This increase in geometry reduces the standard derivation of multipath error by at least a factor of six is shown in Figure 9-67 by decreasing the coupling of test antenna height variation caused by wind to changes in differential delay.

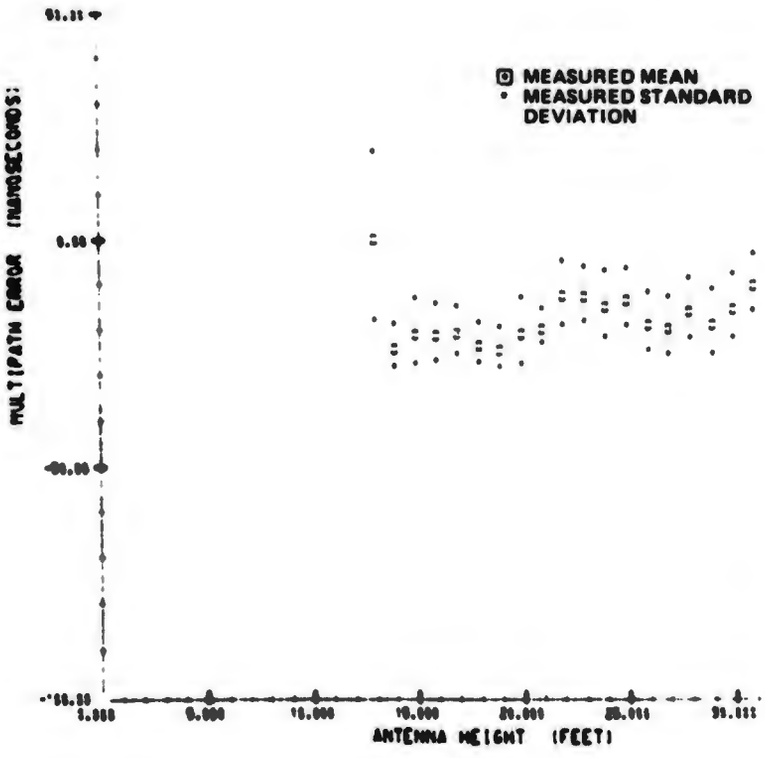

Figure 9-46 Northrop Strip Smooth Earth, Site No. 2 Omni

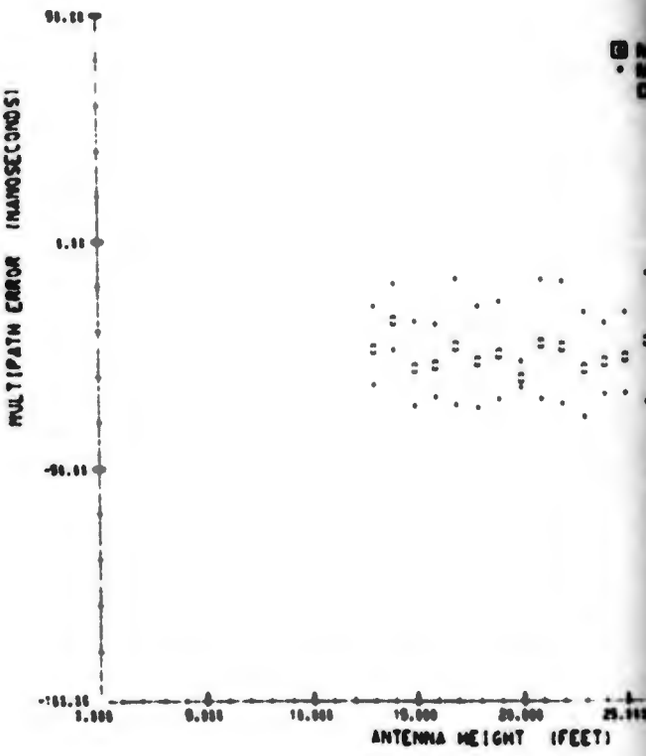

Figure 9-47 Northrop Strip Smo
Site No. 2 Vertical

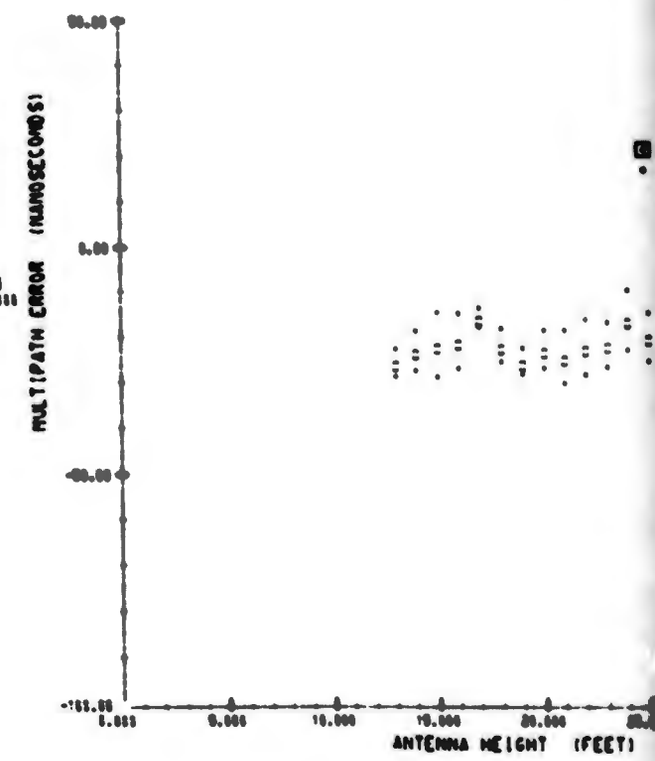

Figure 9-48 Northrop Strip Sm
Site No 2 Horizon

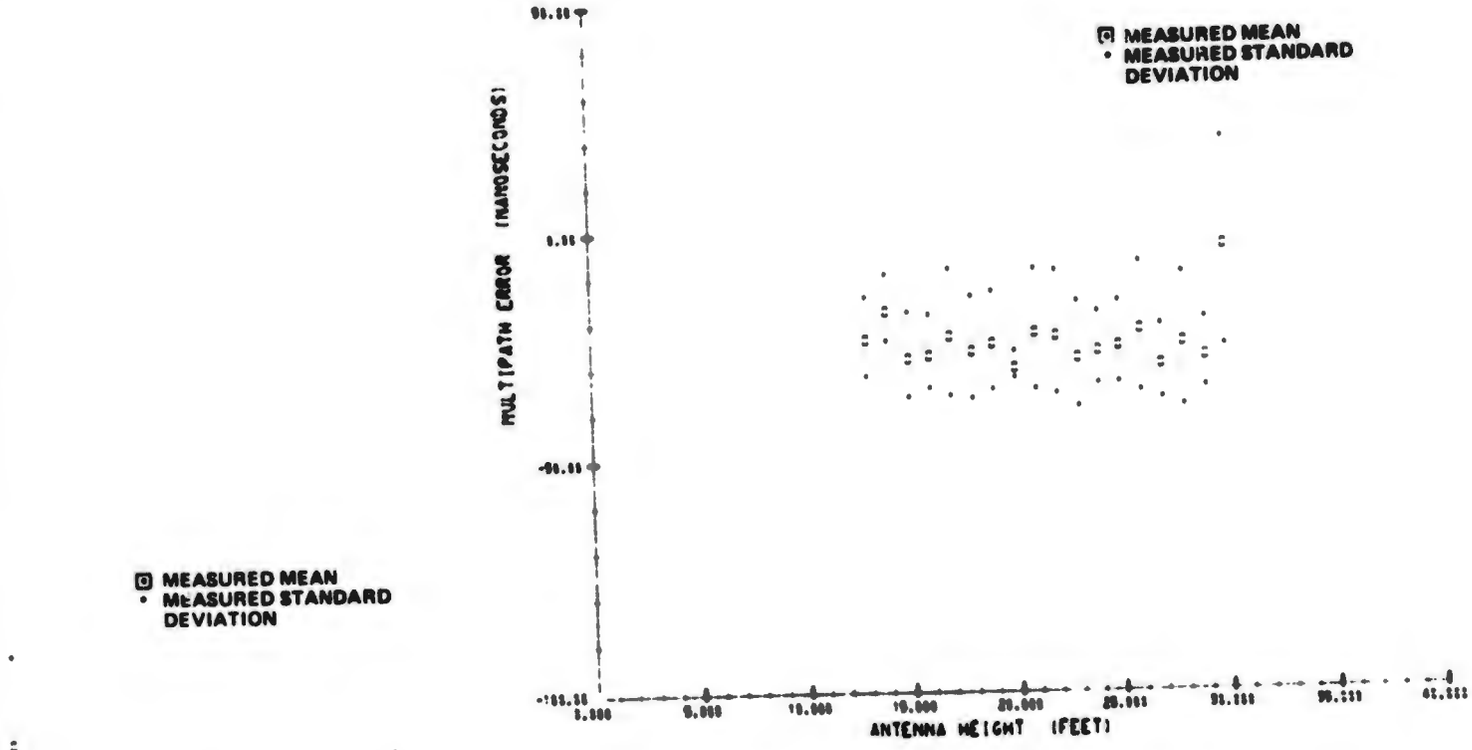

Figure 9-47 Northrop Strip Smooth Earth, Site No. 2 Vertical Dipole

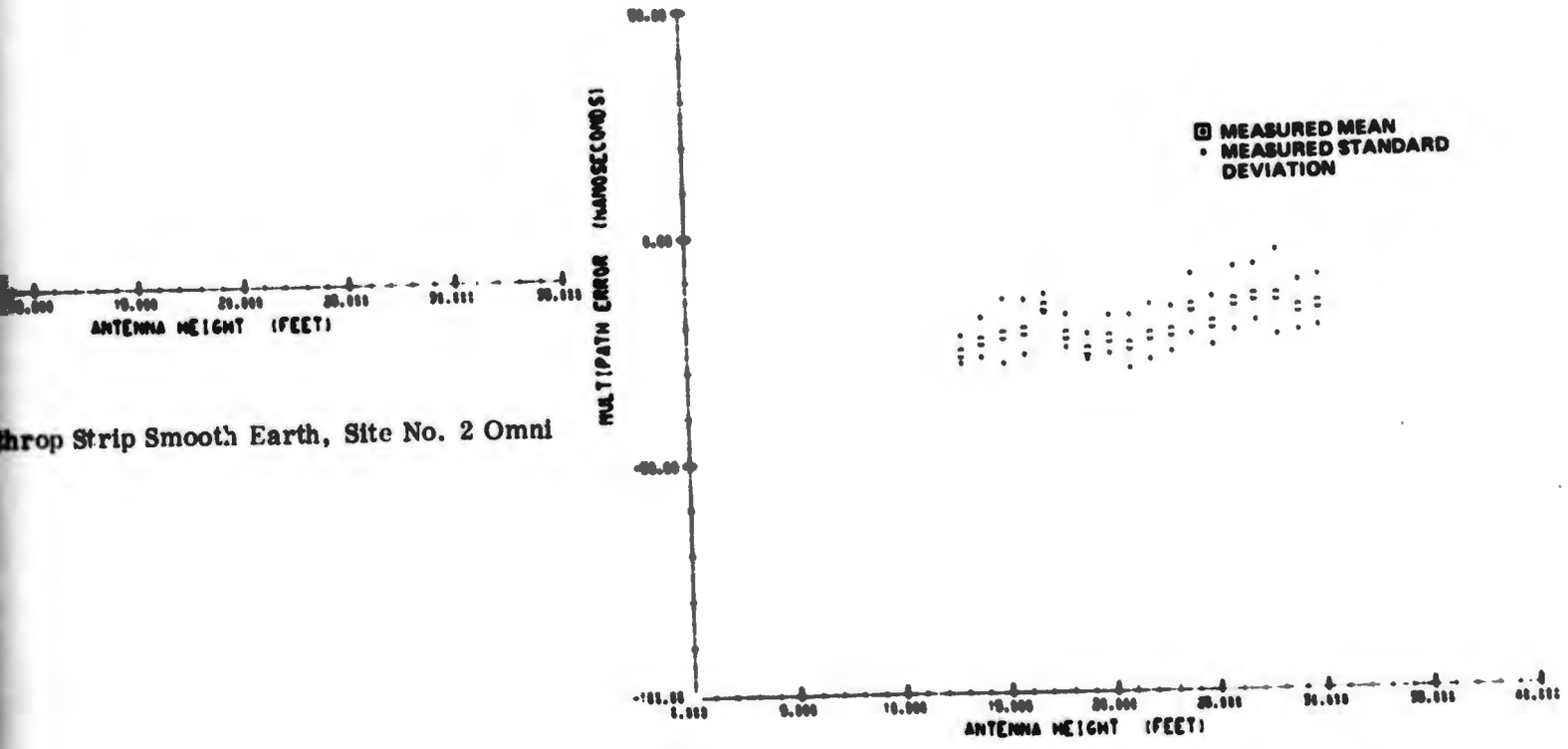

hrop Strip Smooth Earth, Site No. 2 Omni

Figure 9-48 Northrop Strip Smooth Earth, Site No 2 Horizontal Dipole

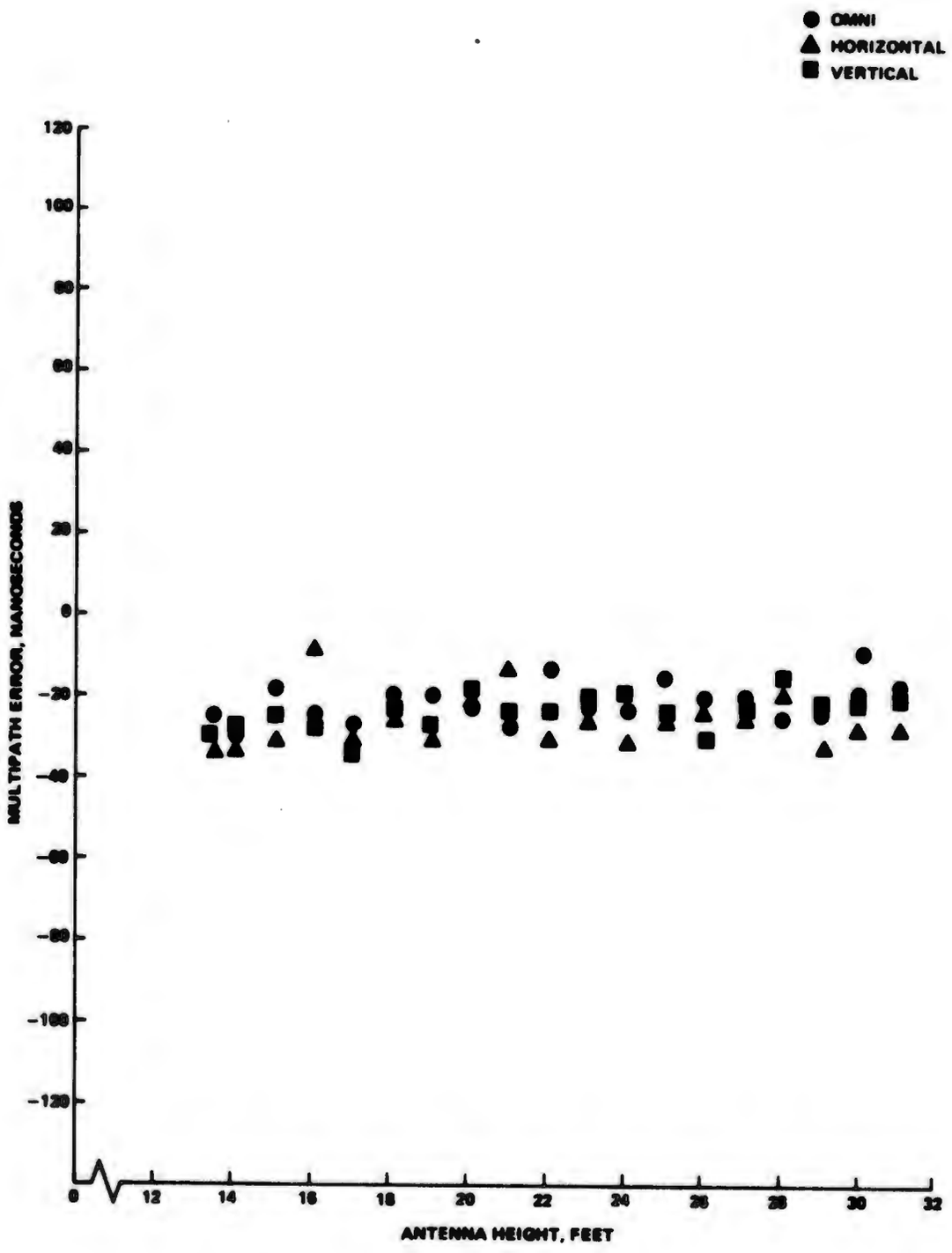

Figure 9-49 "Smooth Earth" Northrop Strip - Site No. 3

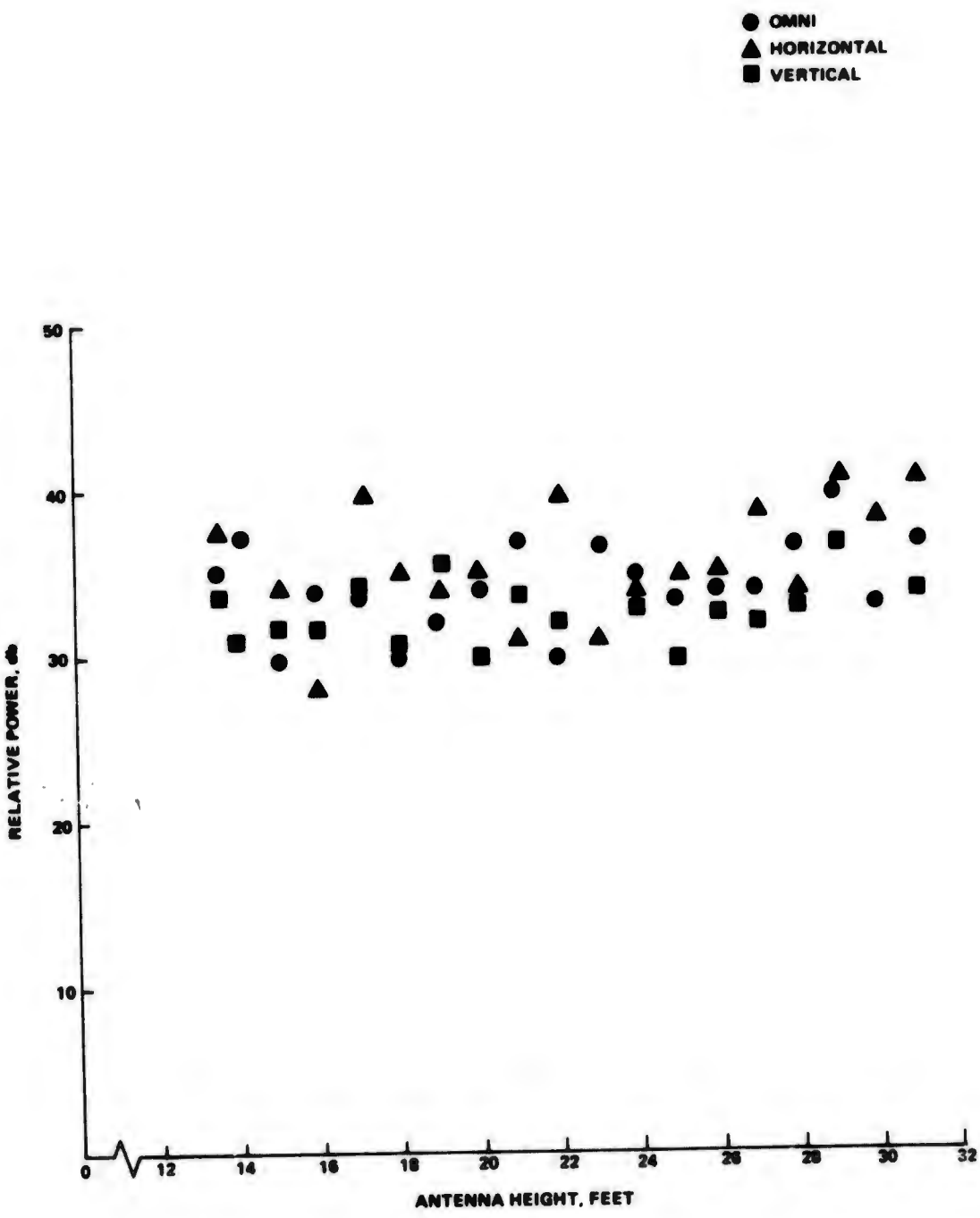

Figure 9-50A "Smooth Earth" Northrop Strip - Site No. 3

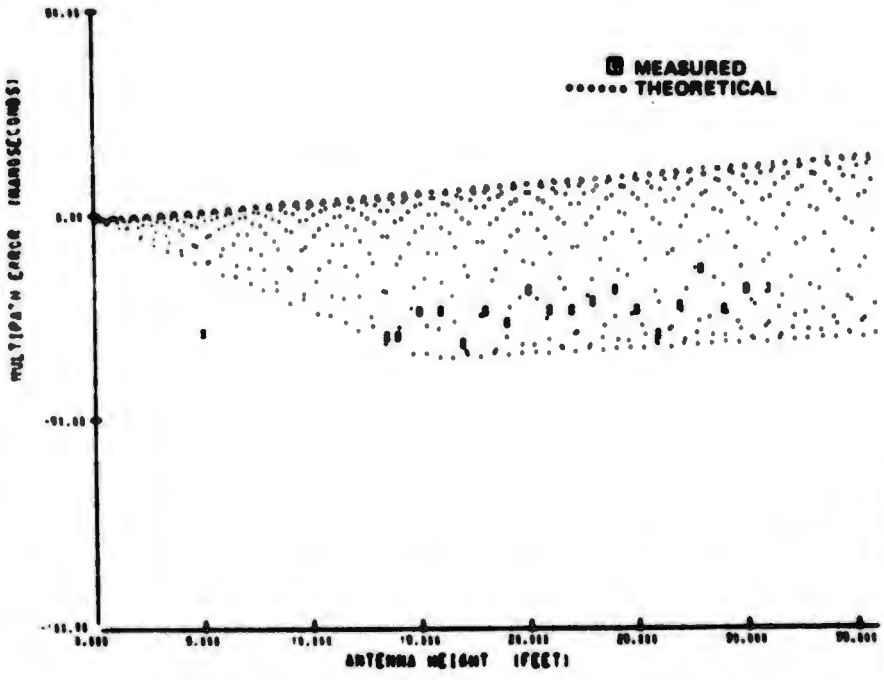

Figure 9-50 Northrop Strip Smooth Earth, Site No. 3, Vertical Dipole

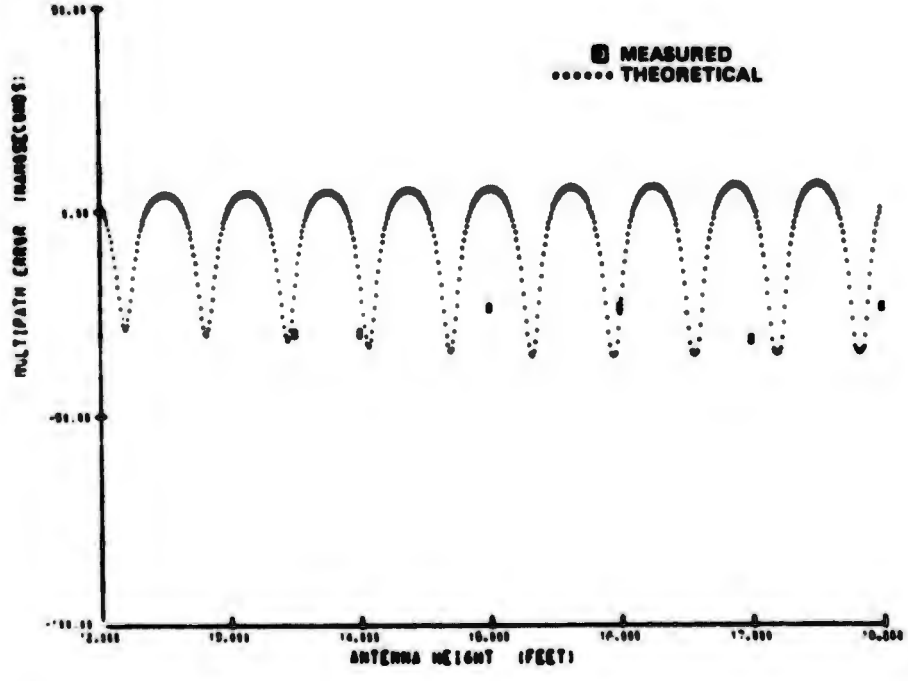

Figure 9-51 Northrop Strip Smooth Earth, Site No. 3, Vertical Dipole

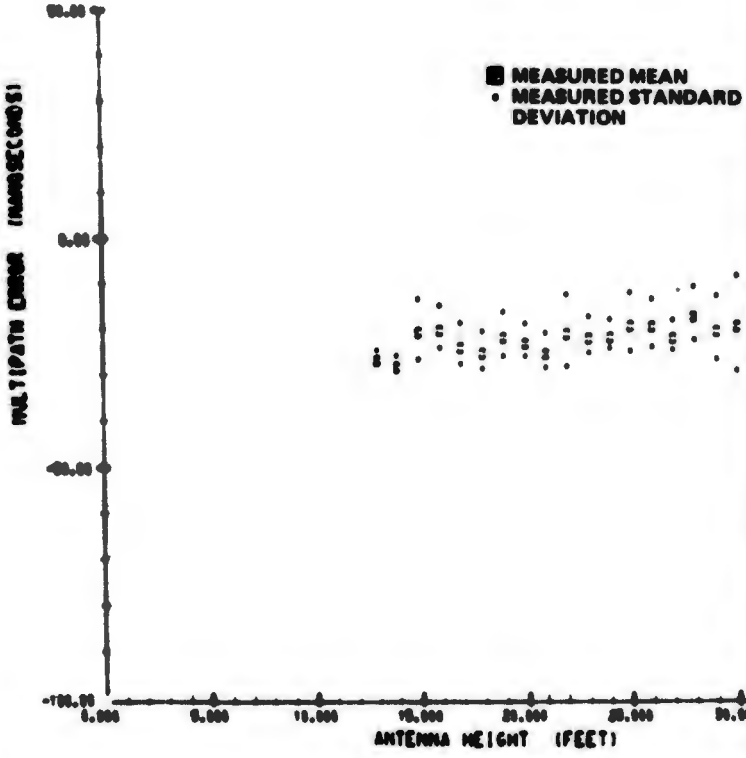

Figure 9-52 Northrop Strip Smooth Earth, Site No.

p Strip Smooth Earth, Site No. 3 Omni

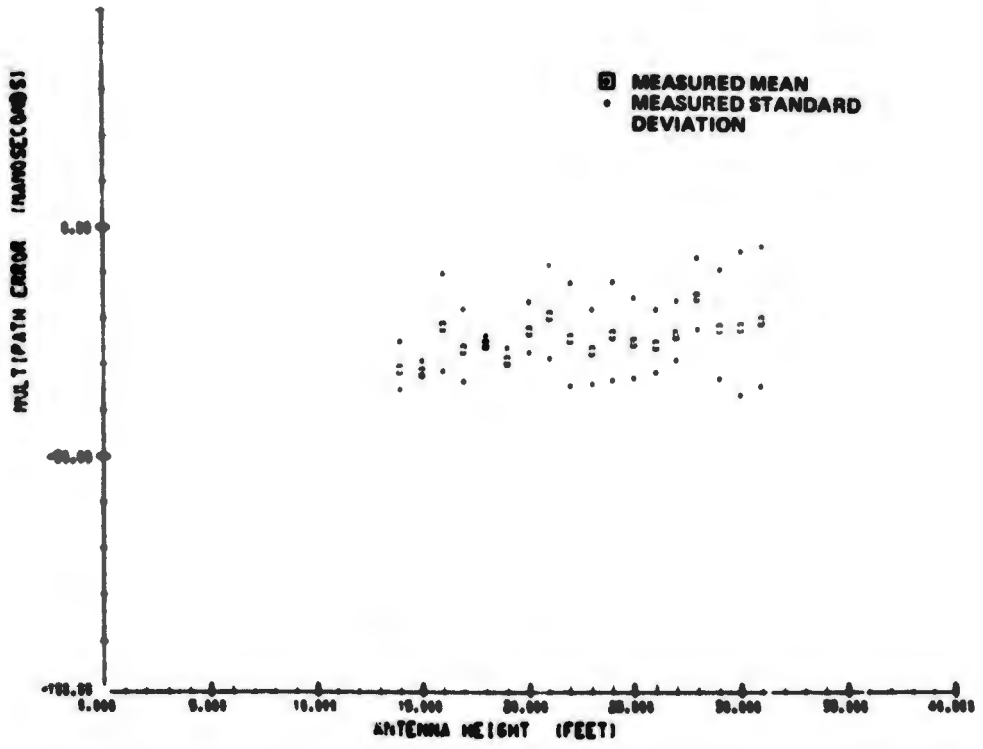

Figure 9-53 Northrop Strip Smooth Earth, Site No. 3 Horizontal Dipole

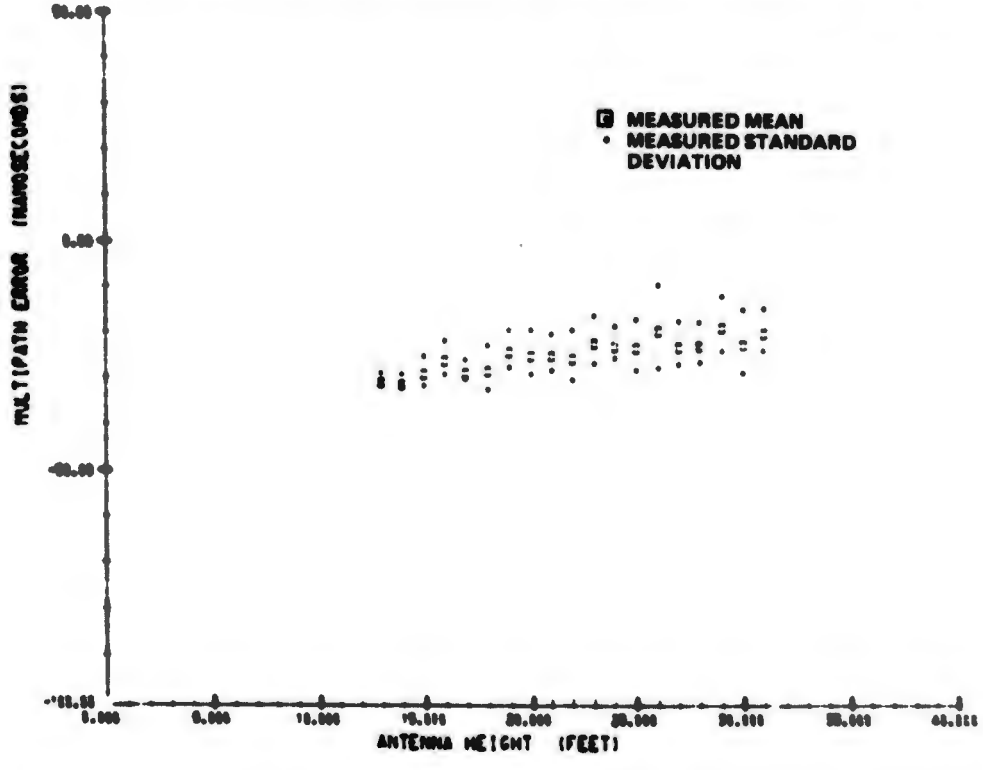

Figure 9-54 Northrop Strip Smooth Earth, Site No. 3 Vertical Dipole

2

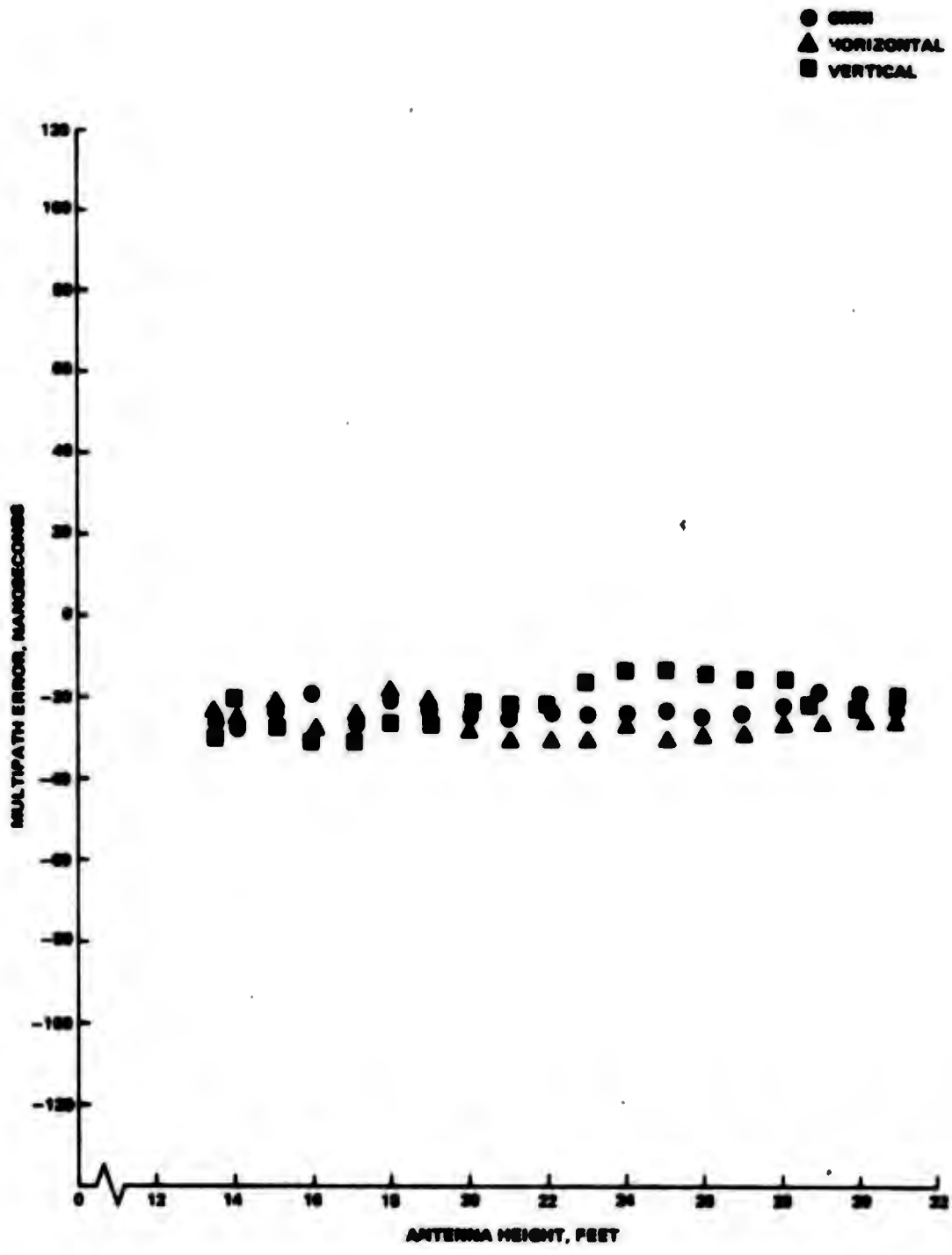

Figure 9-55 "Smooth Earth" Northrop Strip - Site No. 4

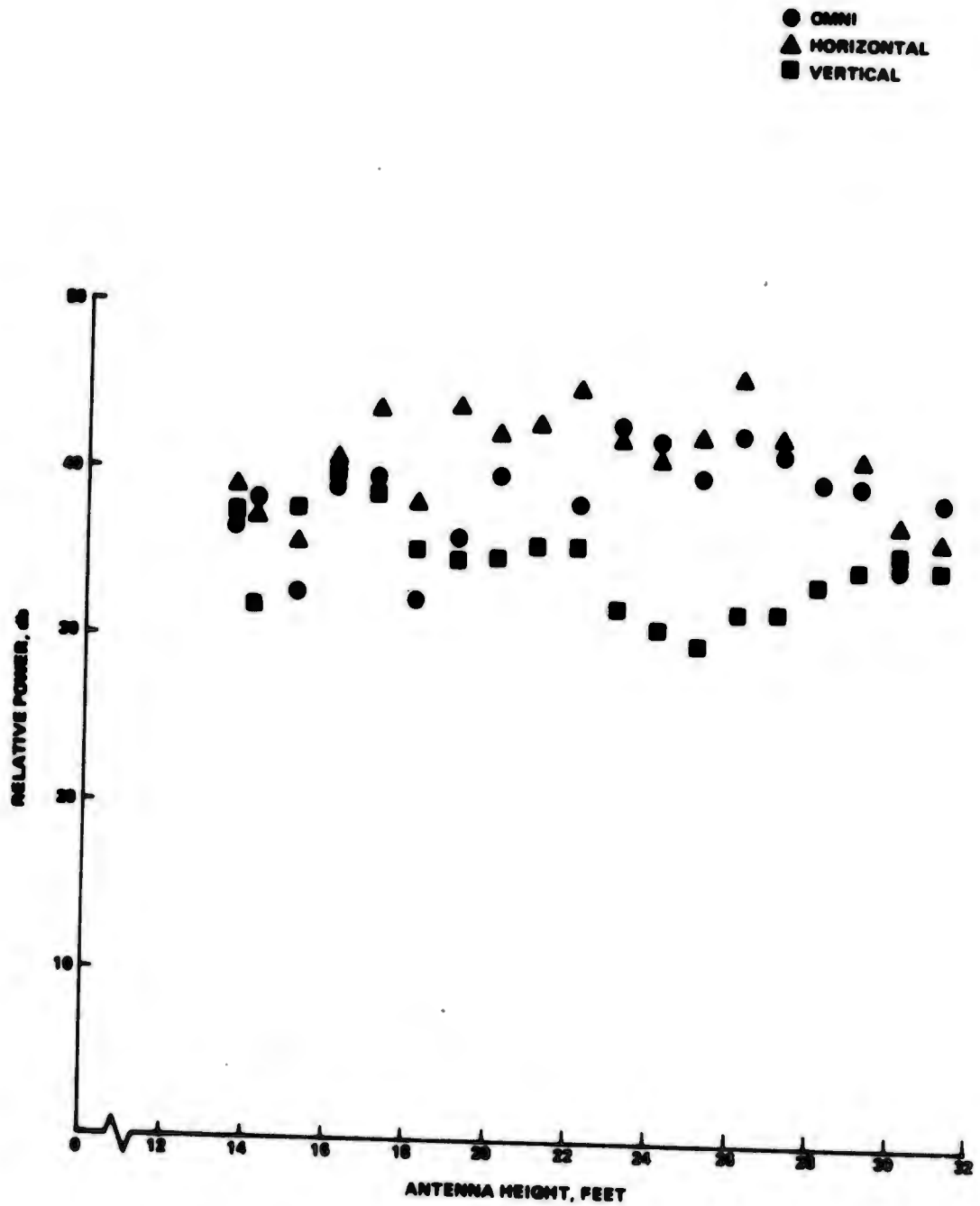

Figure 9-56 "Smooth Earth" Northrop Strip - Site No. 4

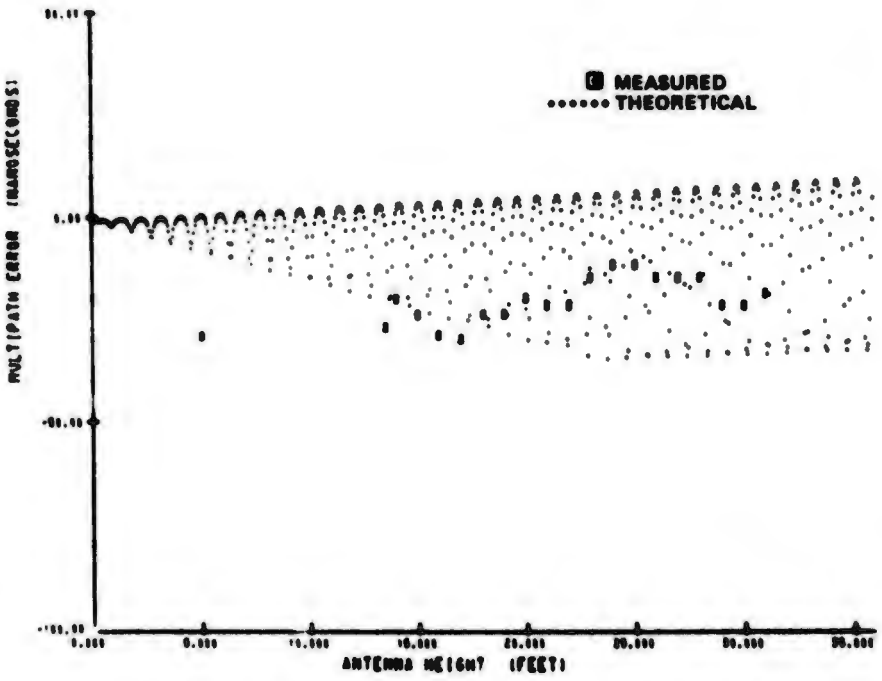

Figure 9-57 Northrop Strip Smooth Earth, Site No. 4, Vertical Dipole

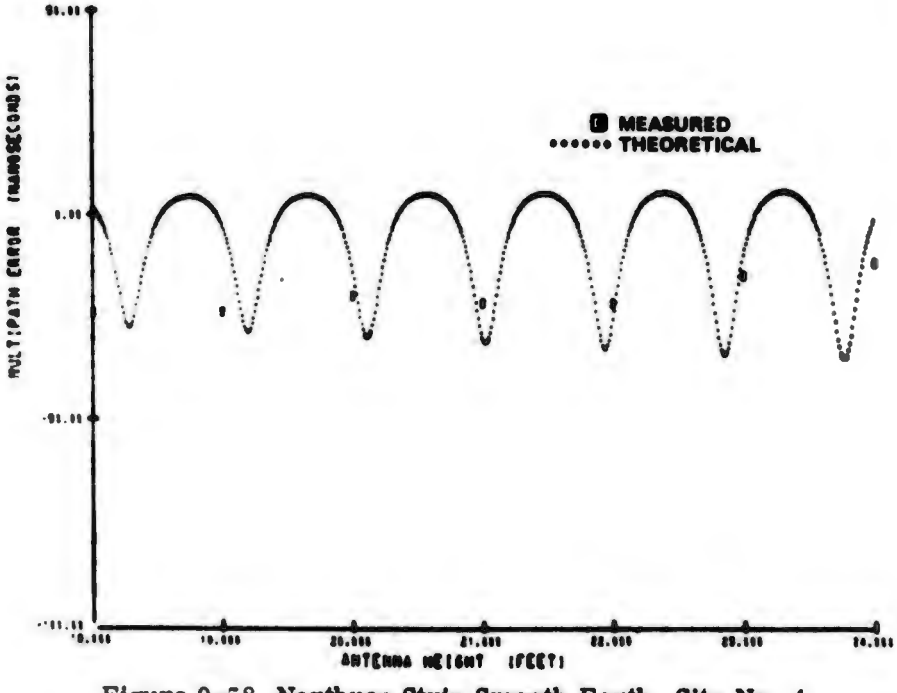

Figure 9-58 Northrop Strip Smooth Earth, Site No. 4, Vertical Dipole

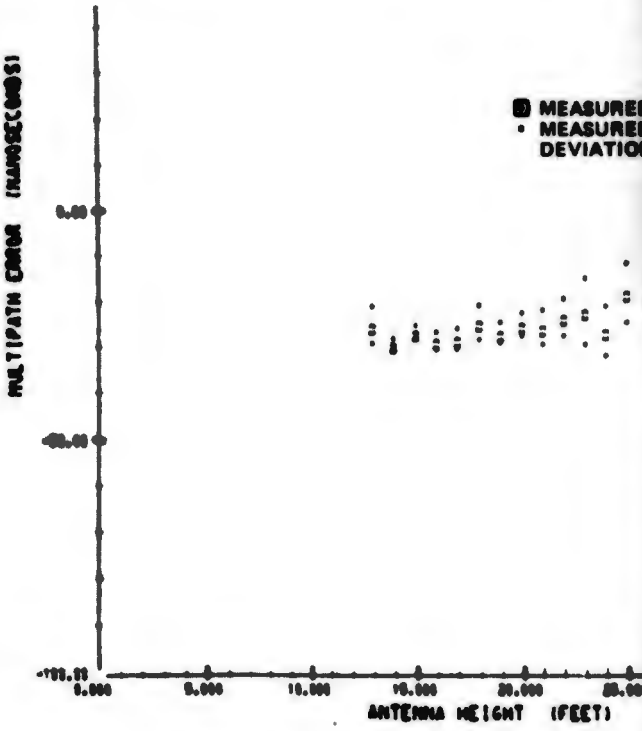

Figure 9-59 Northrop Strip Smooth
Site No. 4 Omni (Chan

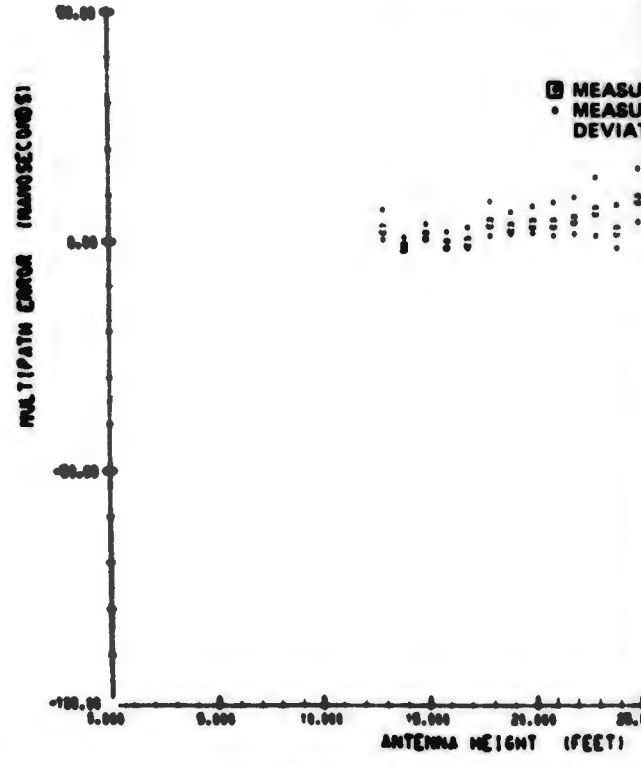

Figure 9-60 Northrop Strip Smoo
Site No. 4 Omni (Ch

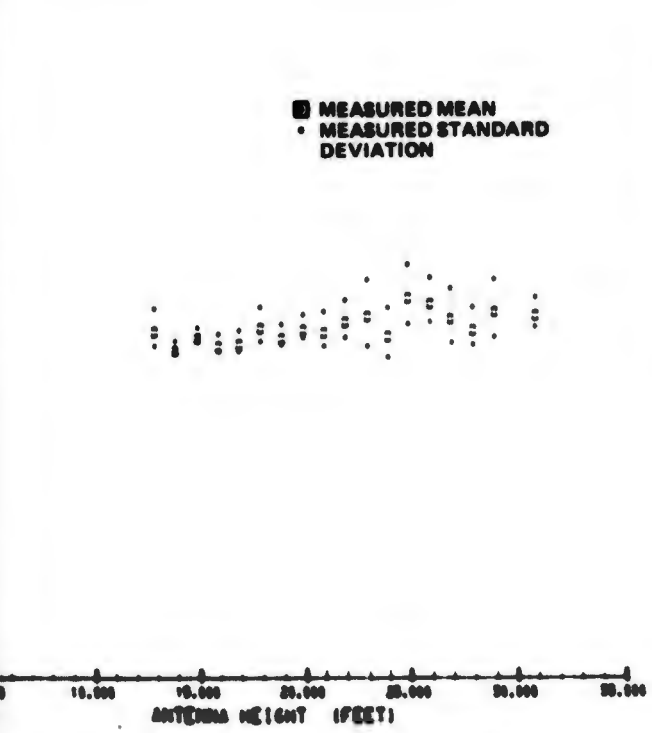

re 9-59 Northrop Strip Smooth Earth, Site No. 4 Omni (Channels 4-3)

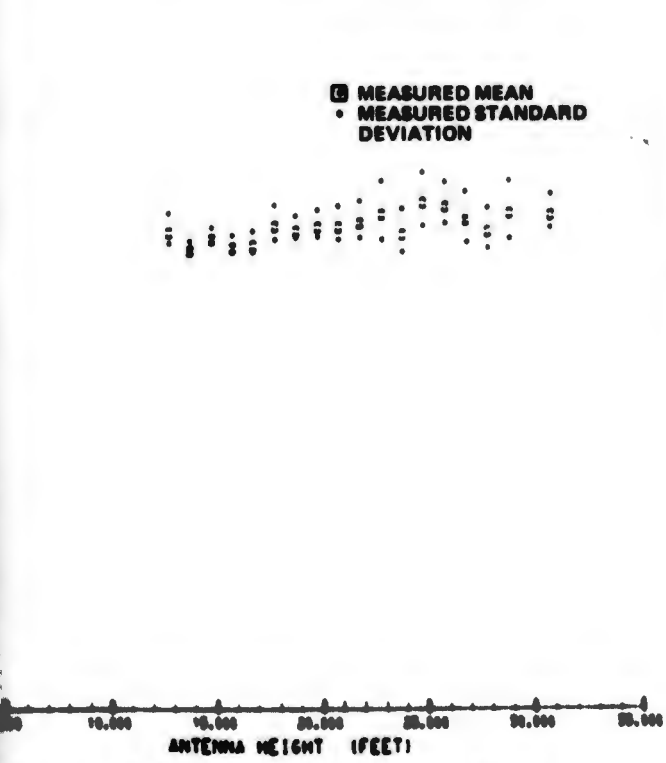

Figure 9-60 Northrop Strip Smooth Earth, Site No. 4 Omni (Channels 4-2)

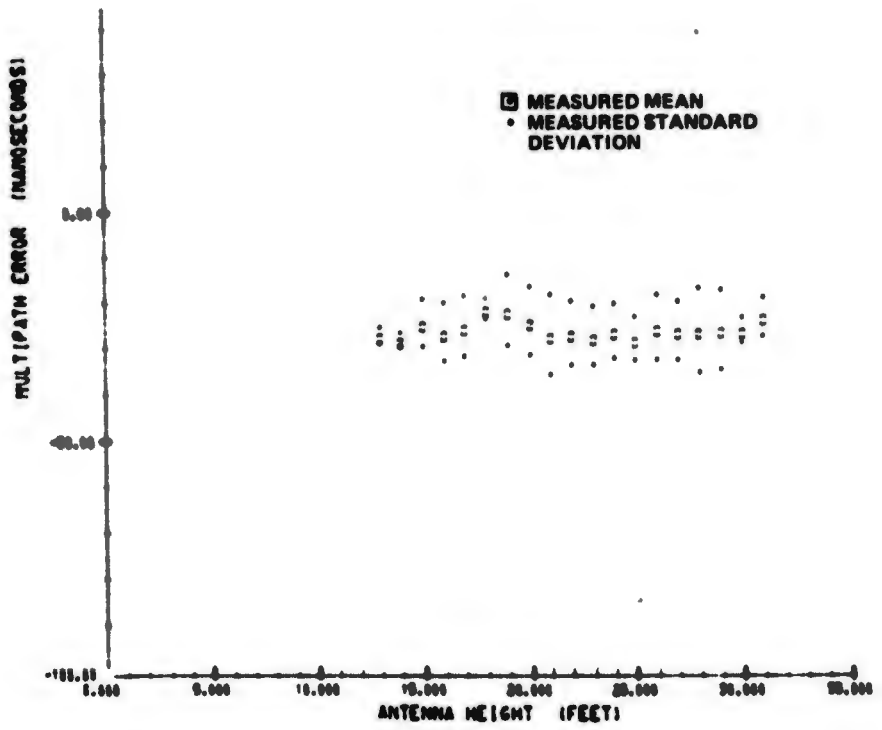

Figure 9-61 Northrop Strip Smooth Earth, Site No. 4 Horizontal Dipole

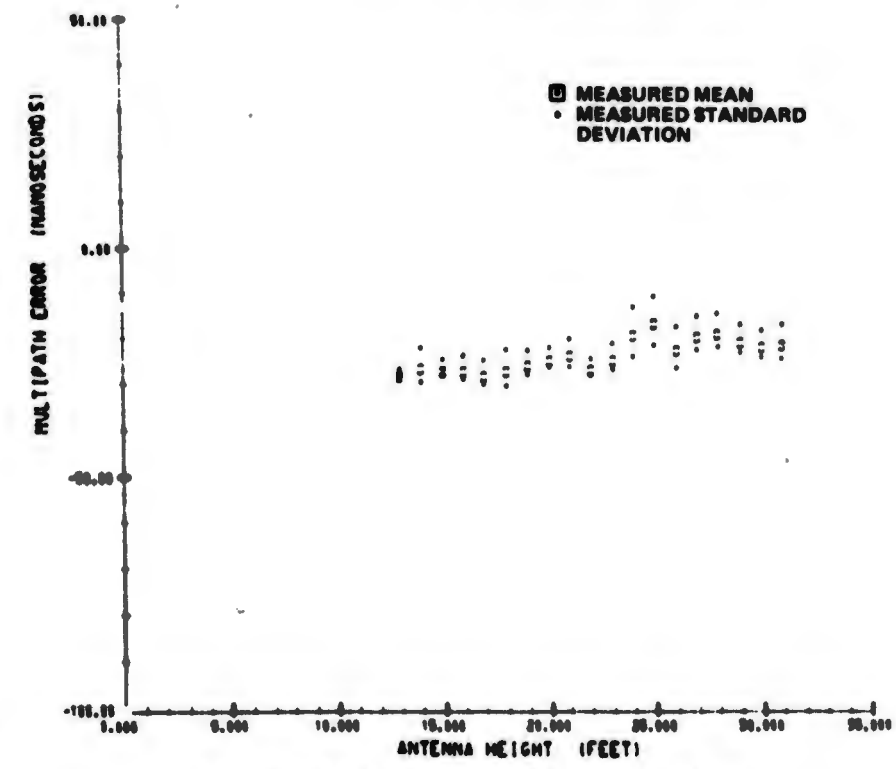

Figure 9-62 Northrop Strip Smooth Earth, Site No. 4 Vertical Dipole

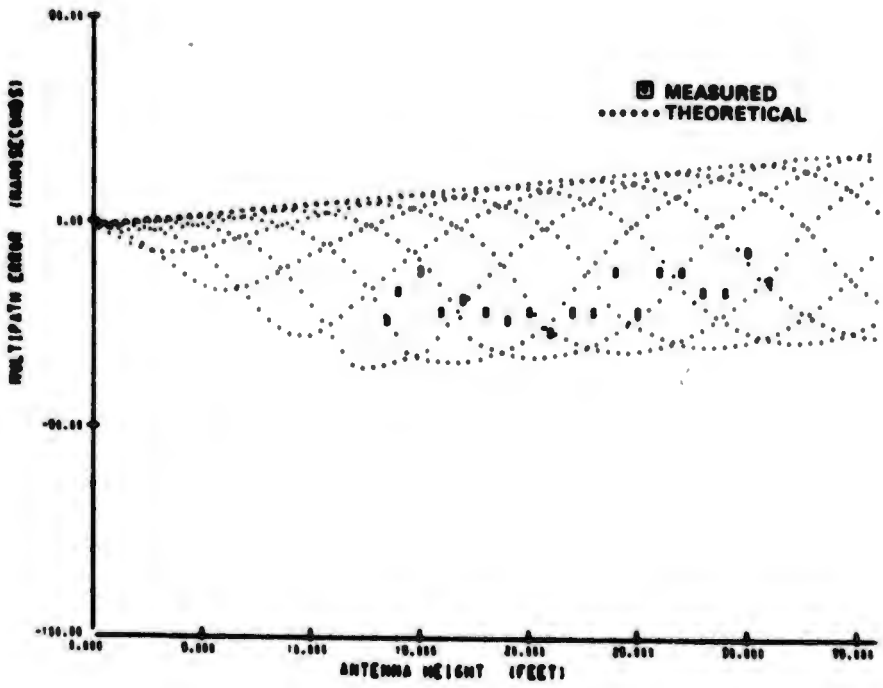

Figure 9-63 Northrop Strip Smooth Earth, Site No. 2, Vertical Dipole

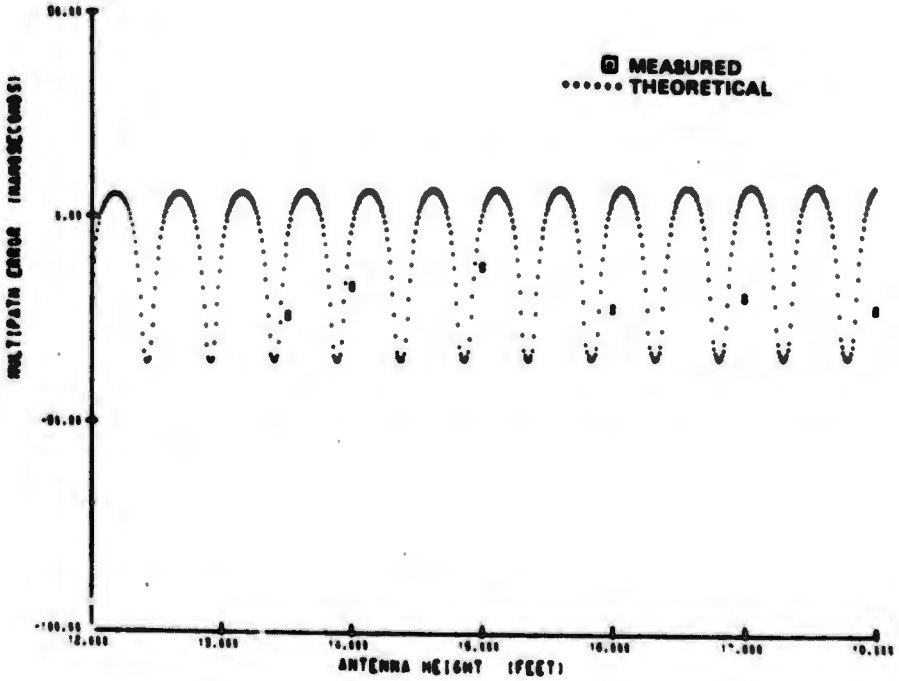

Figure 9-64 Northrop Strip Smooth Earth, Site No. 2, Vertical Dipole

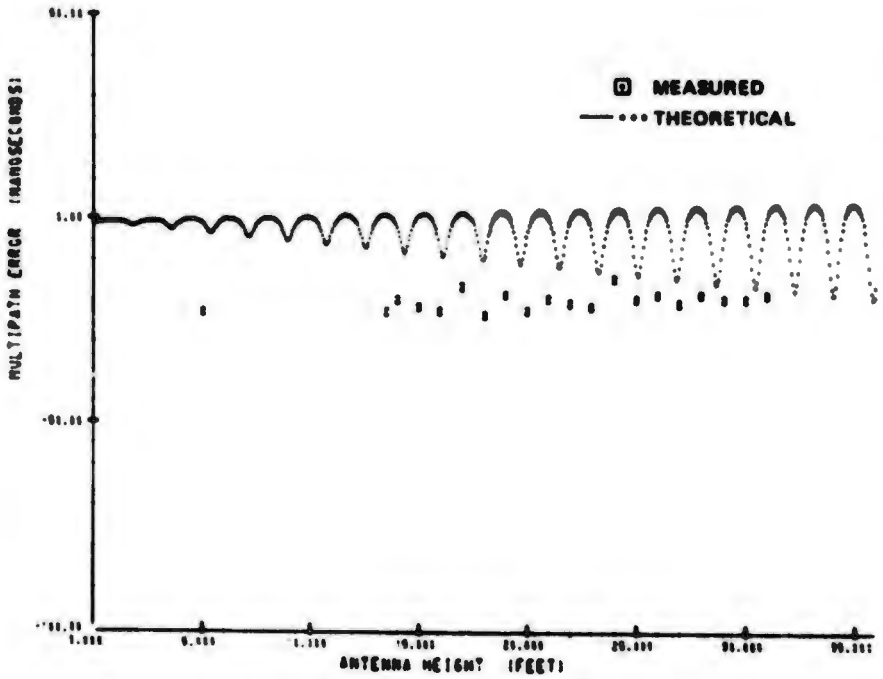

Figure 9-65 Northrop Strip Smooth Earth, Site No. 5, Vertical Dipole

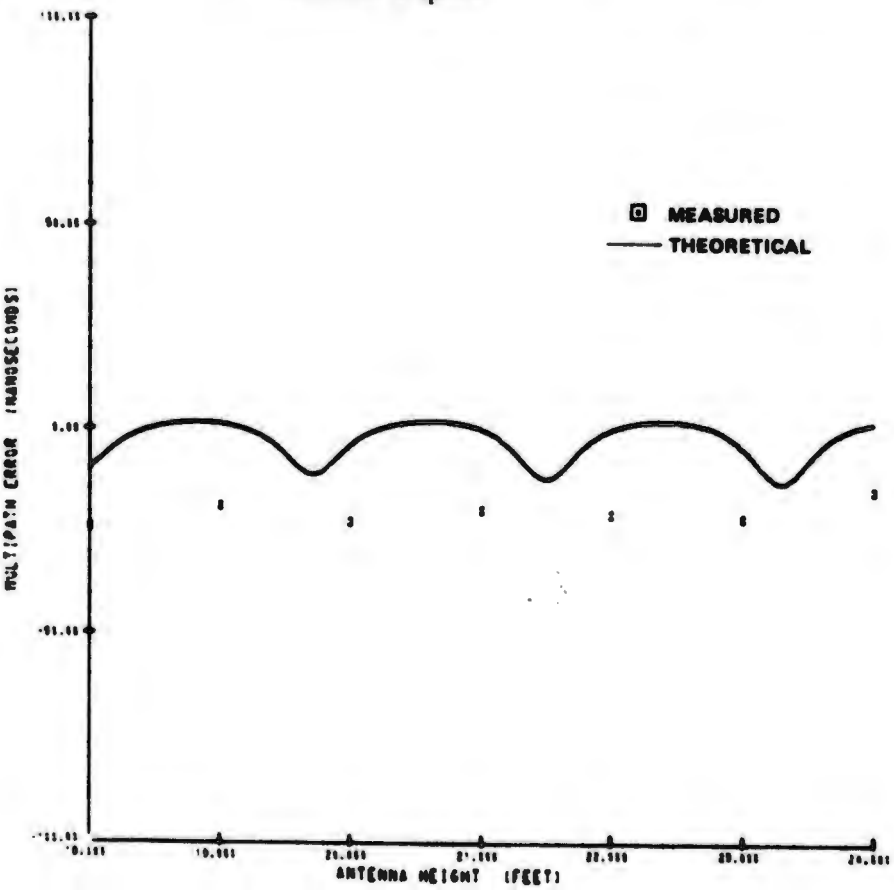

Figure 9-66 Northrop Strip Smooth Earth, Site No. 5, Vertical Dipole

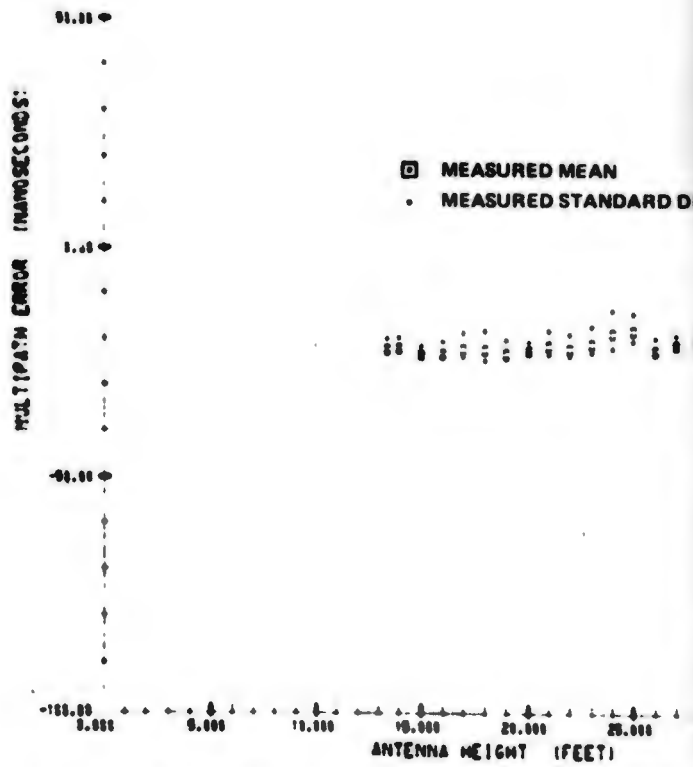

Figure 9-67 Northrop Strip Smooth Earth, Site

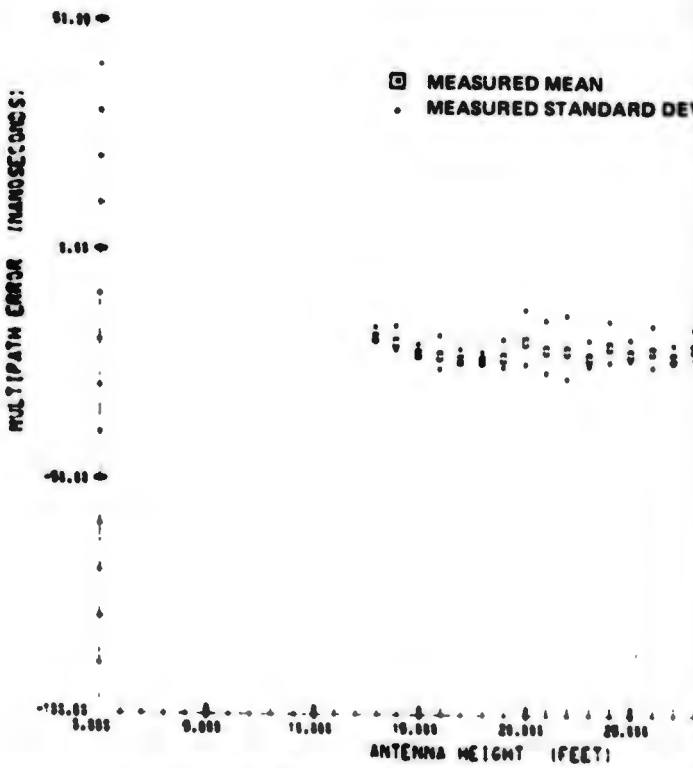

Figure 9-68 Northrop Strip Smooth Earth Site No. 5 Horizontal Dipole

Northrop Strip Smooth Earth, Site No. 5 Omni

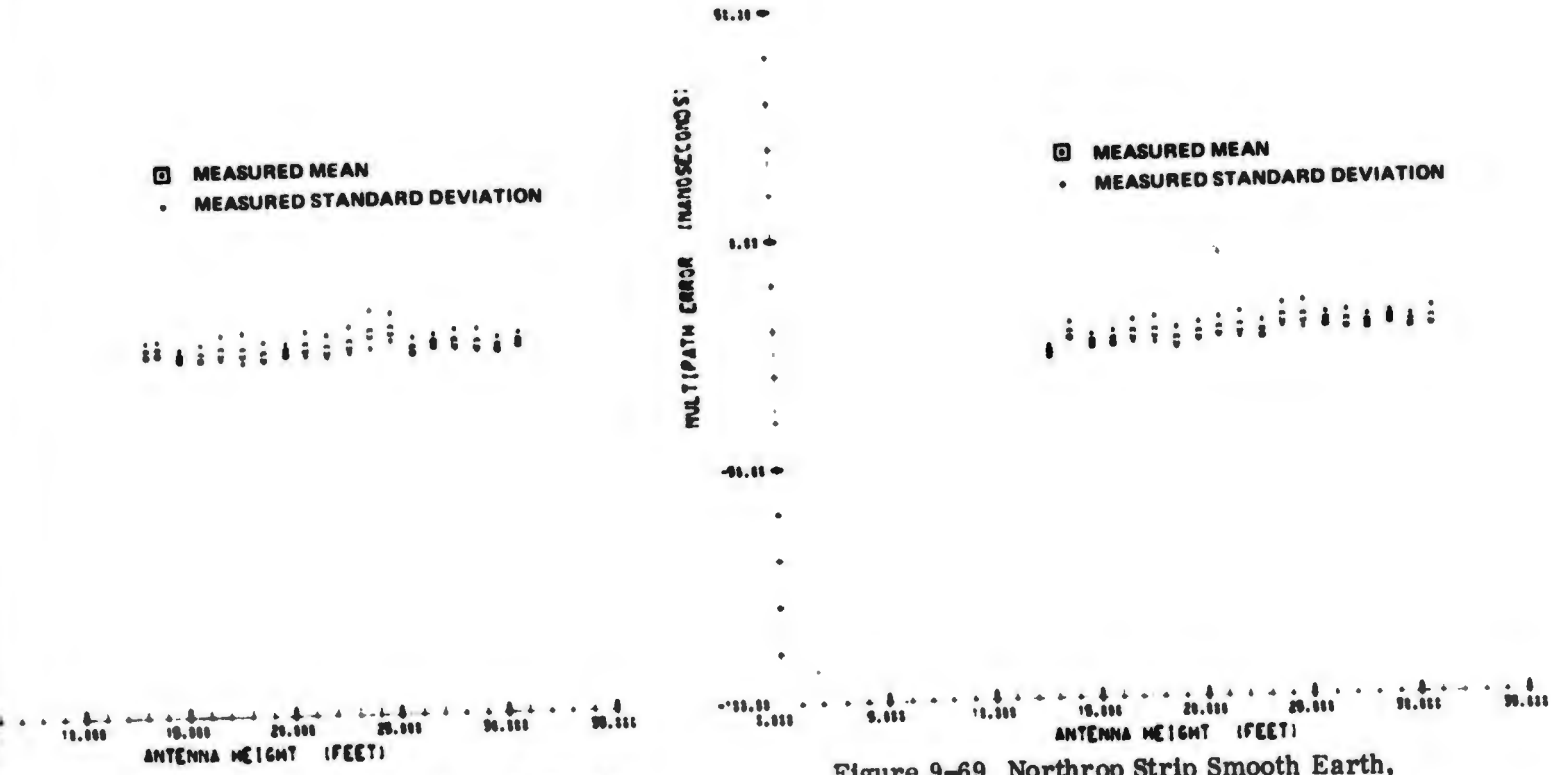

Figure 9-69 Northrop Strip Smooth Earth, Site No. 5 Vertical Dipole

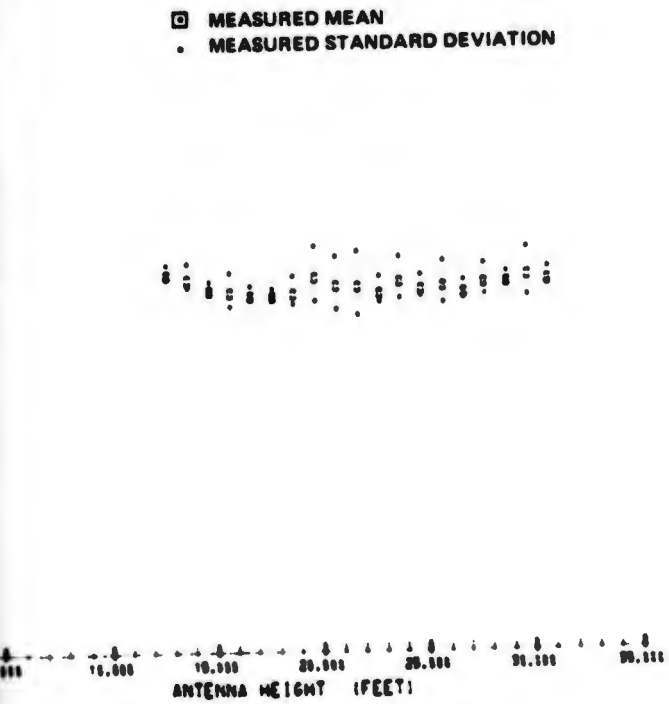

ure 9-68 Northrop Strip Smooth Earth, Site No. 5 Horizontal Dipole

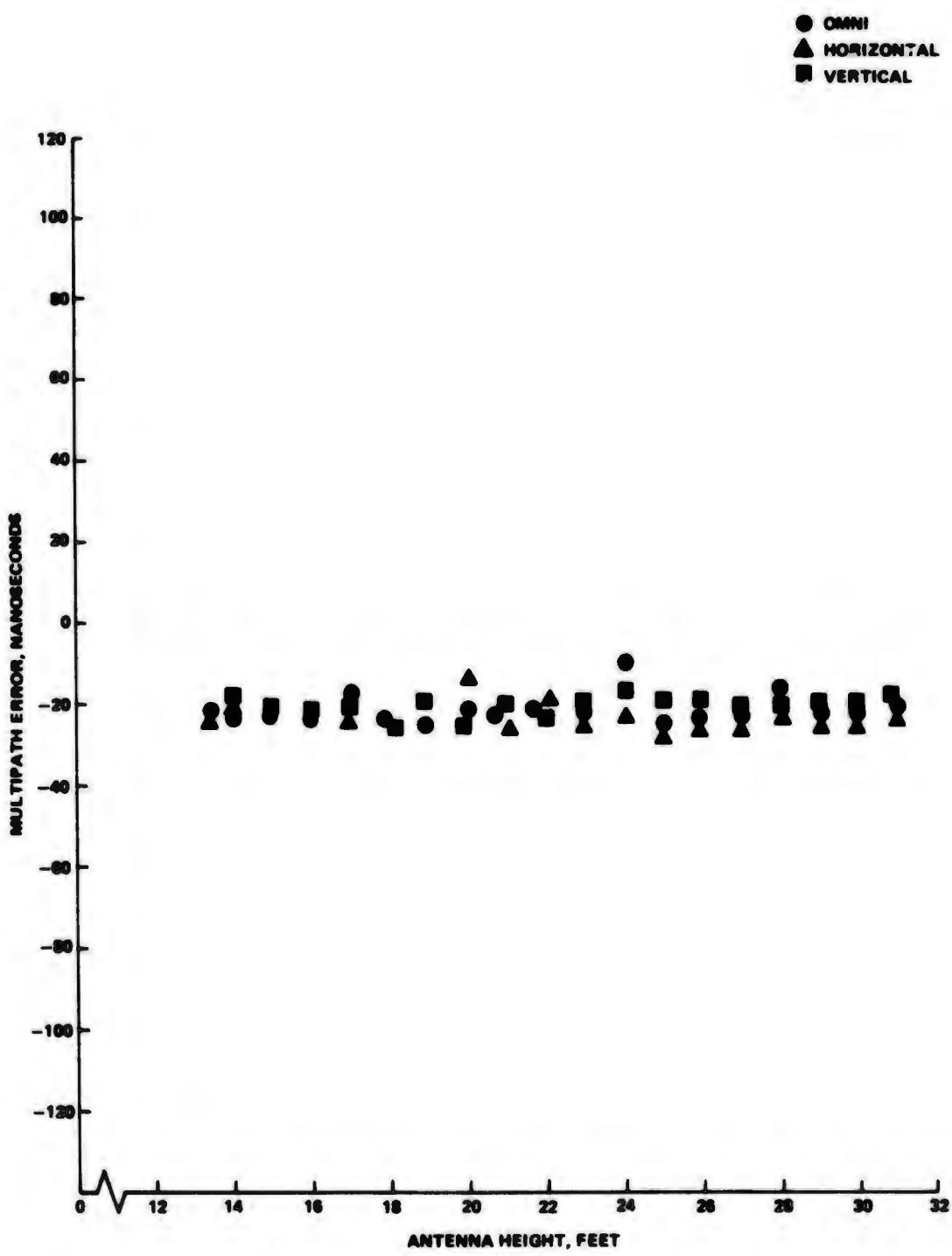

Figure 9-70 "Smooth Earth" Northrop Strip - Site No. 5

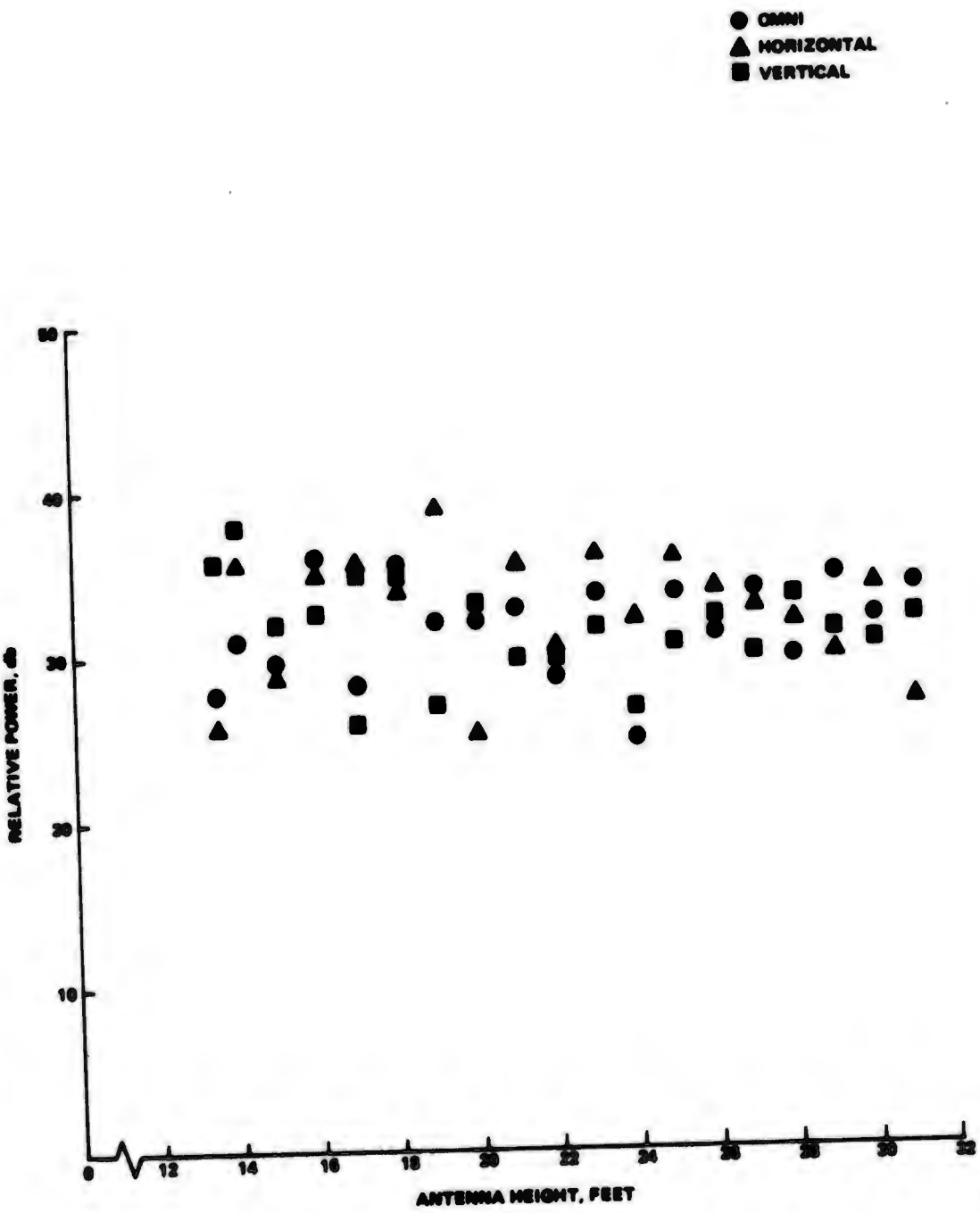

Figure 9-71 "Smooth Earth" Northrop Strip - Site No. 5

Figure 9-72 is a plot of antenna height vs multipath error for the first of the rough earth tests at test position six. Again all three polarizations were used, Figure 9-73 is a plot of antenna height vs signal level in db. An examination of the Rayleigh criterion in terms of the resultant combination of grazing angles, surface roughness and the transmission wavelength places the reflection in the "Partly Specular and Partly Diffused" to "Diffuse" regions. In the case of these tests, the slowly undulating random terrain with large correlation distance becomes essentially flat in the vicinity of the receiving antennas. Therefore, the test results are expected to follow theoretical curves of smooth terrain with large grazing incidence. Figures 9-74 and 9-75 demonstrate this fact. These plots of antenna height vs multipath error show the theoretical envelope with the measured data superimposed on the plot. Just about all the measured data falls within the envelope. Here one should notice again the moire patterns referred to earlier.

Figures 9-76 and 9-77 are plots of antenna height vs multipath error for test position seven, rough earth. As can be seen, the data show the presence of a deep fade condition or possibly the effects of tracking the reflected signal rather than the direct signal. In these cases the multipath error exceeds the theoretical maximum of 50 ft. Deep fade conditions, multiple specular reflections, diffraction or large bias errors caused by tracking the reflected signal has bot been modelled in the simulation program. Therefore, under these conditions the measured data points are expected to deviate from the theoretical simulation results. Figures 9-78 and 9-79 are multipath error and relative power level measurements for site seven highlighting the above findings.

Site eight data, the last of the rough earth tests, generally followed our expectations, and fell within the theoretical envelope, as shown in Figure 9-80 thru 9-83.

9.8 SIMULATION PROGRAM

9.8.1 Introduction

A summary of the parameters used to generate the theoretical curves of multipath vs antenna height is given in Table 9-1. A mathematical description and computer program functional flow diagram of the simulation is given in the following subsections and Table 9-2 respectively. The mathematical model used in the program includes the effect of ground roughness, terrain profile, physical constants of the reflecting surface on the Rayleigh criterion of reflection (diffuse or specular), Brewster's angle effects on the phase and magnitude of the reflected signal i.e. vertical polarization, antenna aperture illumination (both parabolic and uniform illumination is modelled), weighting of the reflected energy as a function of angle away from the antenna main beam center, transmission loss, space loss, and differential delay between antennas. The program computes the effective reflection coefficient for both the directional antenna and omni antenna channels as a function of antenna heights, antenna sizes and distance between transmitting and receiving antennas. Using the mathematical model for the early-late-gate discriminator in the computer program, the expected multipath errors are computed as a function of the effective reflection coefficient and differential delay in both receiving channels. The program also computes the total loss difference (transmission loss due to antenna proximity to ground and loss) between the transmitting and the two receiving antennas. This allows the comparison of the measurements with predicted performance. It also allows us to identify wild data points and to make reasonableness checks on the measurements.

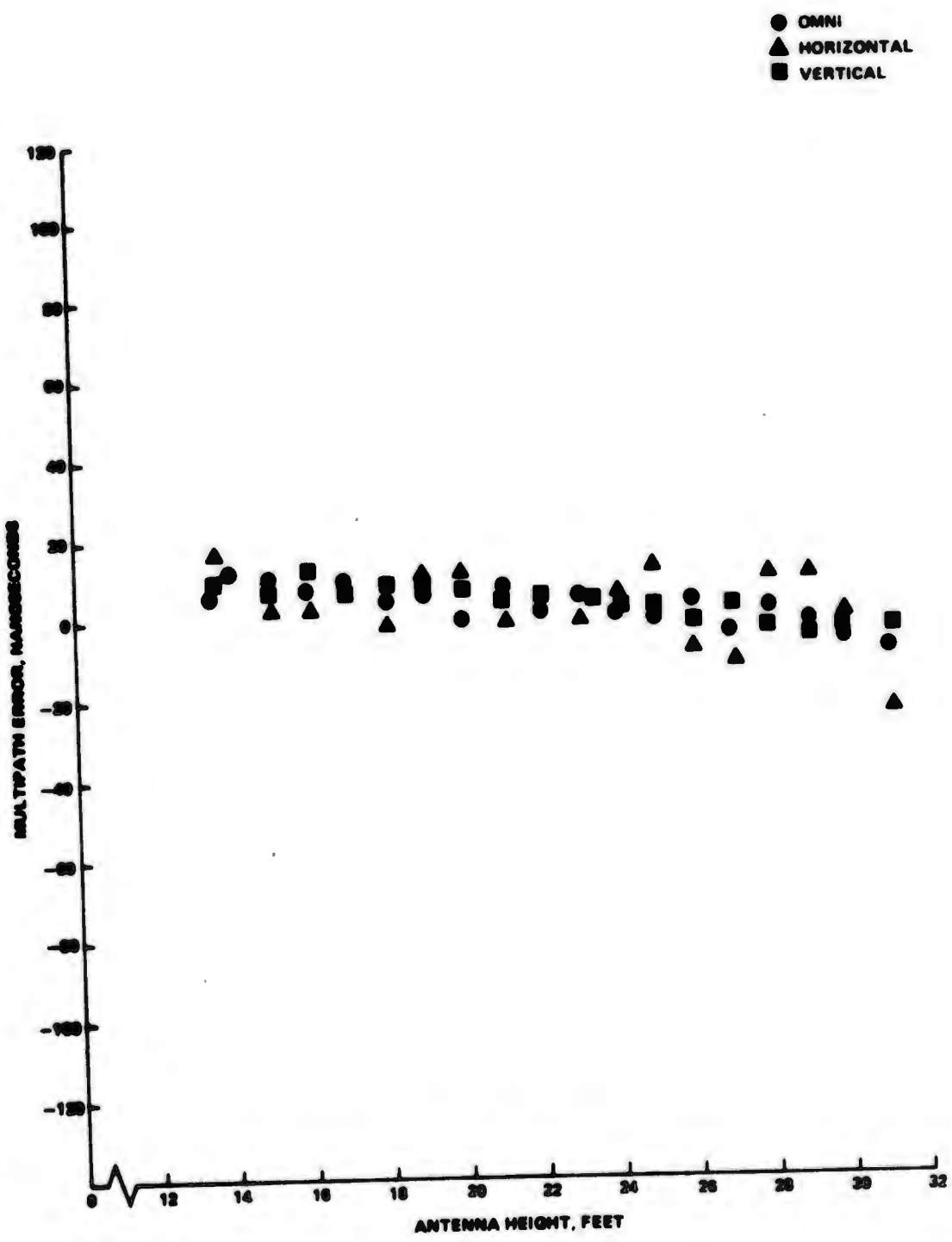

Figure 9-72 "Rough Earth" Site No. 6

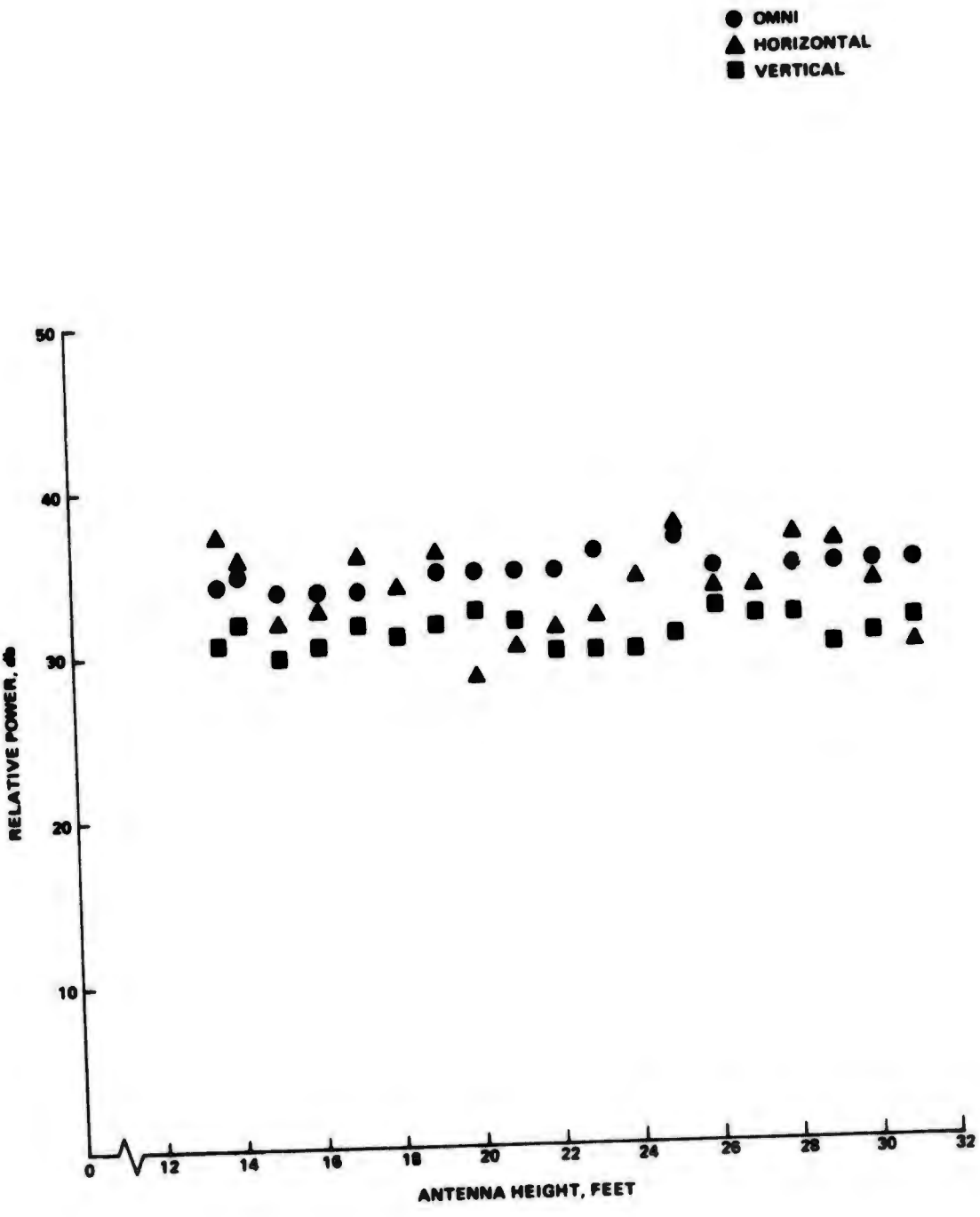

Figure 9-73 "Smooth Earth" Northrop Strip - Site No. 6

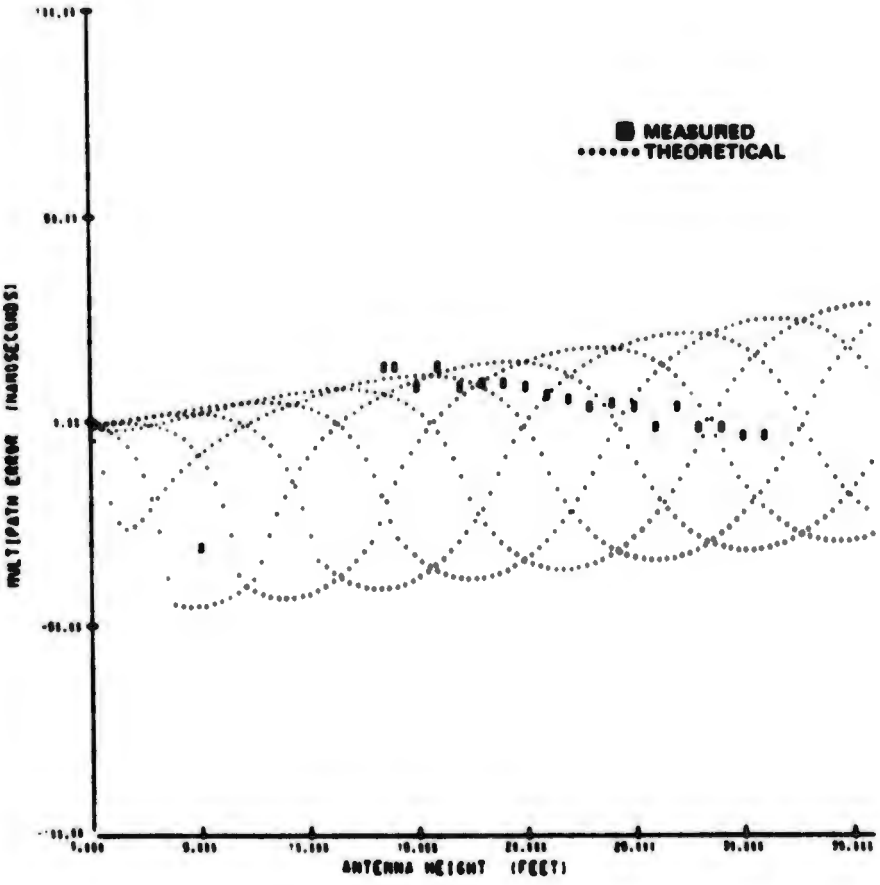

Figure 9-74 Northrop Strip Rought Earth, Site No. 6, Vertical Dipole

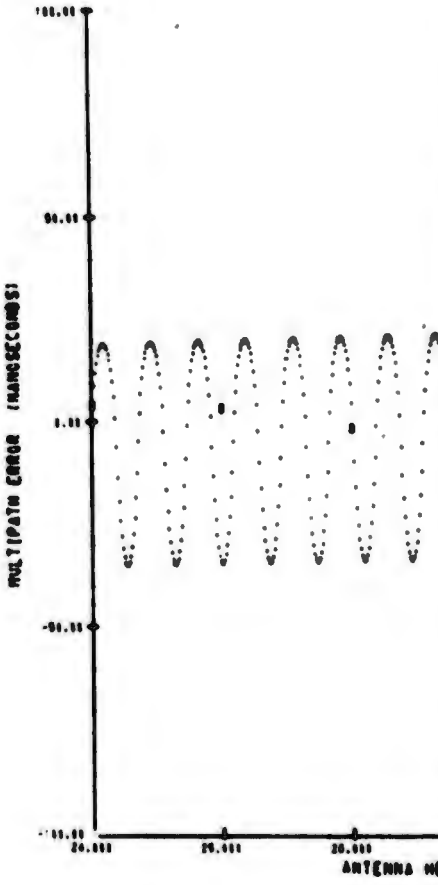

Figure 9-75 Northrop Strip Roug

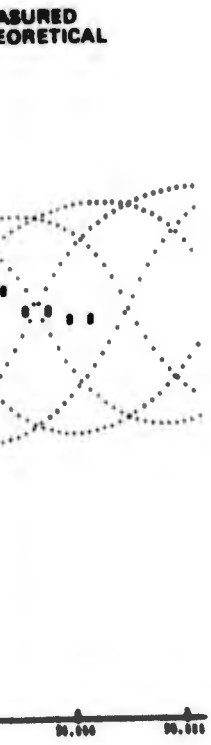

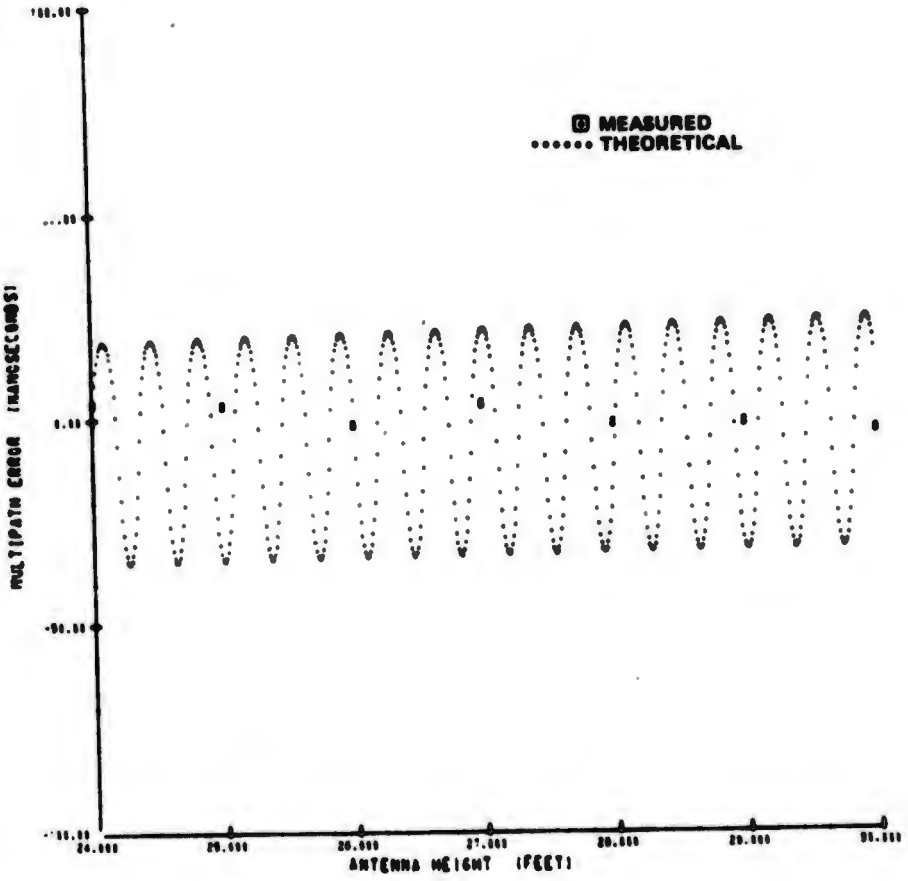

6, Vertical Dipole

Figure 9-75 Northrop Strip Rough Earth, Site No 6, Vertical Dipole

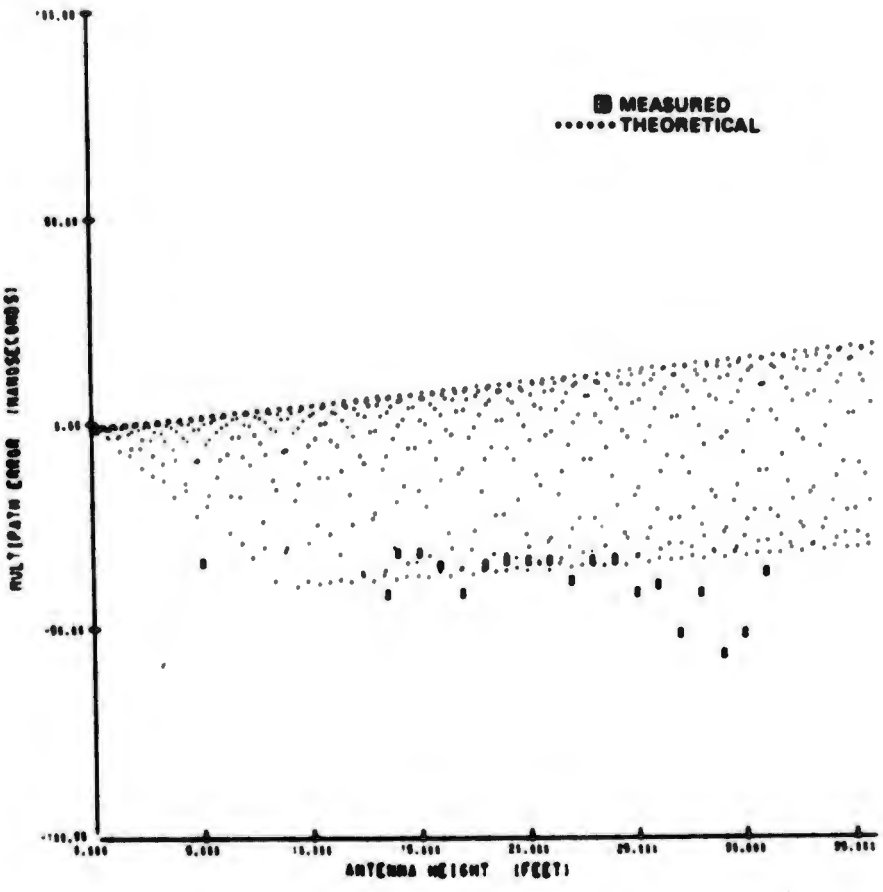

Figure 9-76 Northrop Strip Rough Earth, Site No. 7, Vertical Dipole

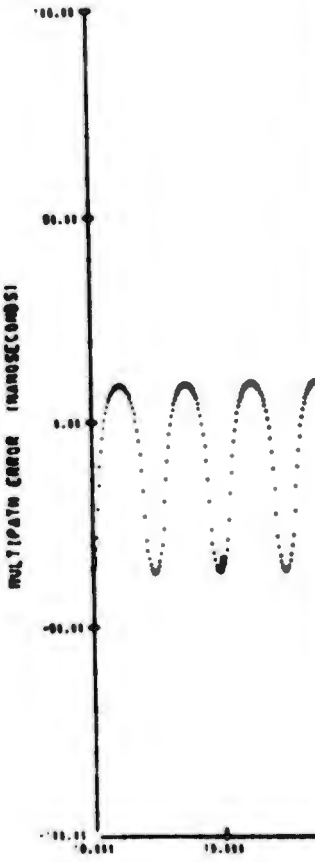

Figure 9-77 Northrop S

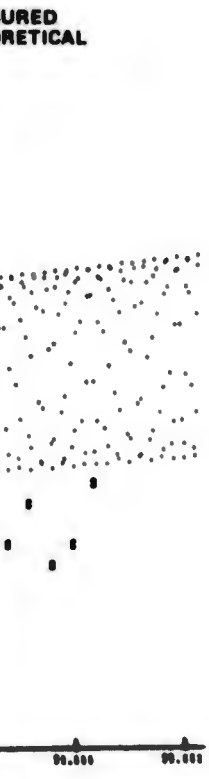

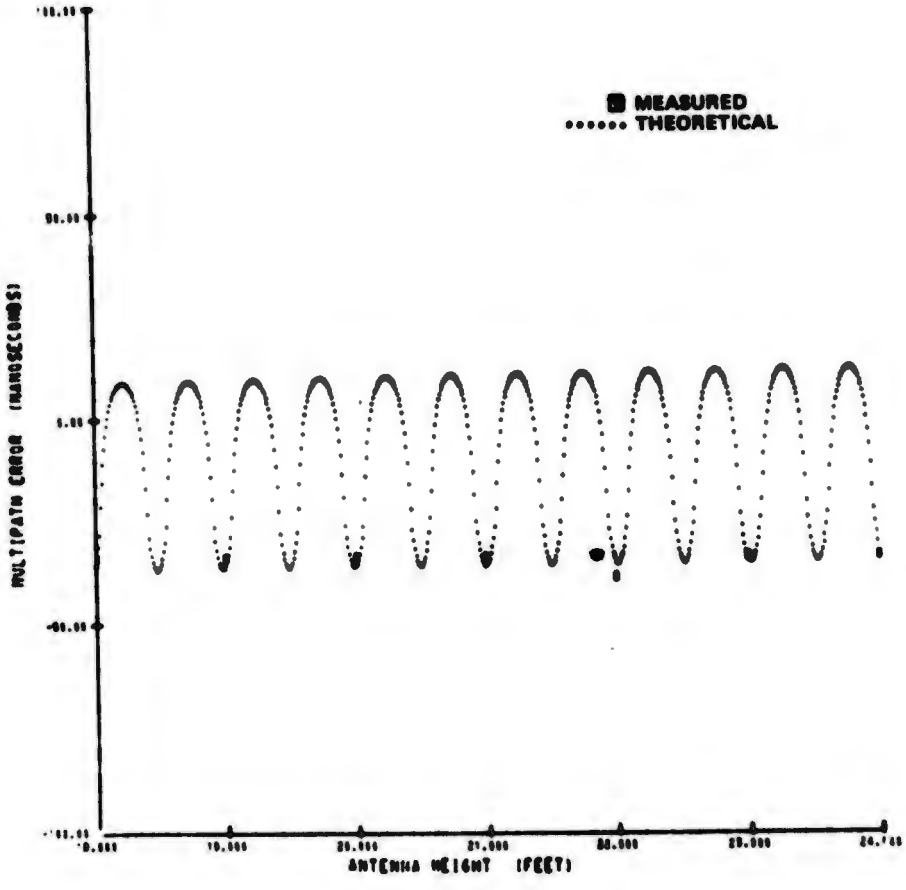

7, Vertical Dipole

Figure 9-77 Northrop Strip Rough Earth, Site No. 7, Vertical Dipole

2

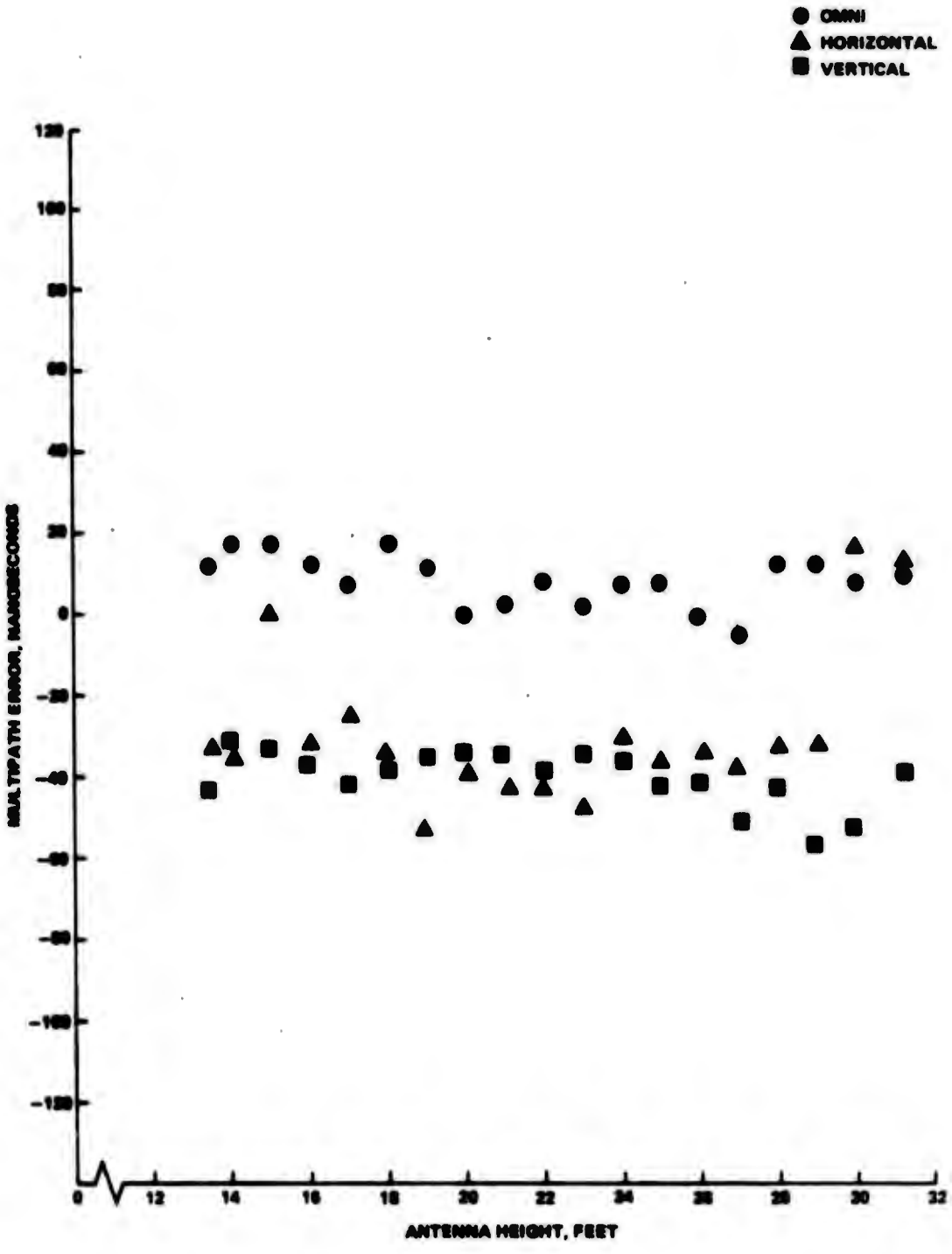

Figure 9-78 "Rough Earth" Northrop Strip - Site No. 7

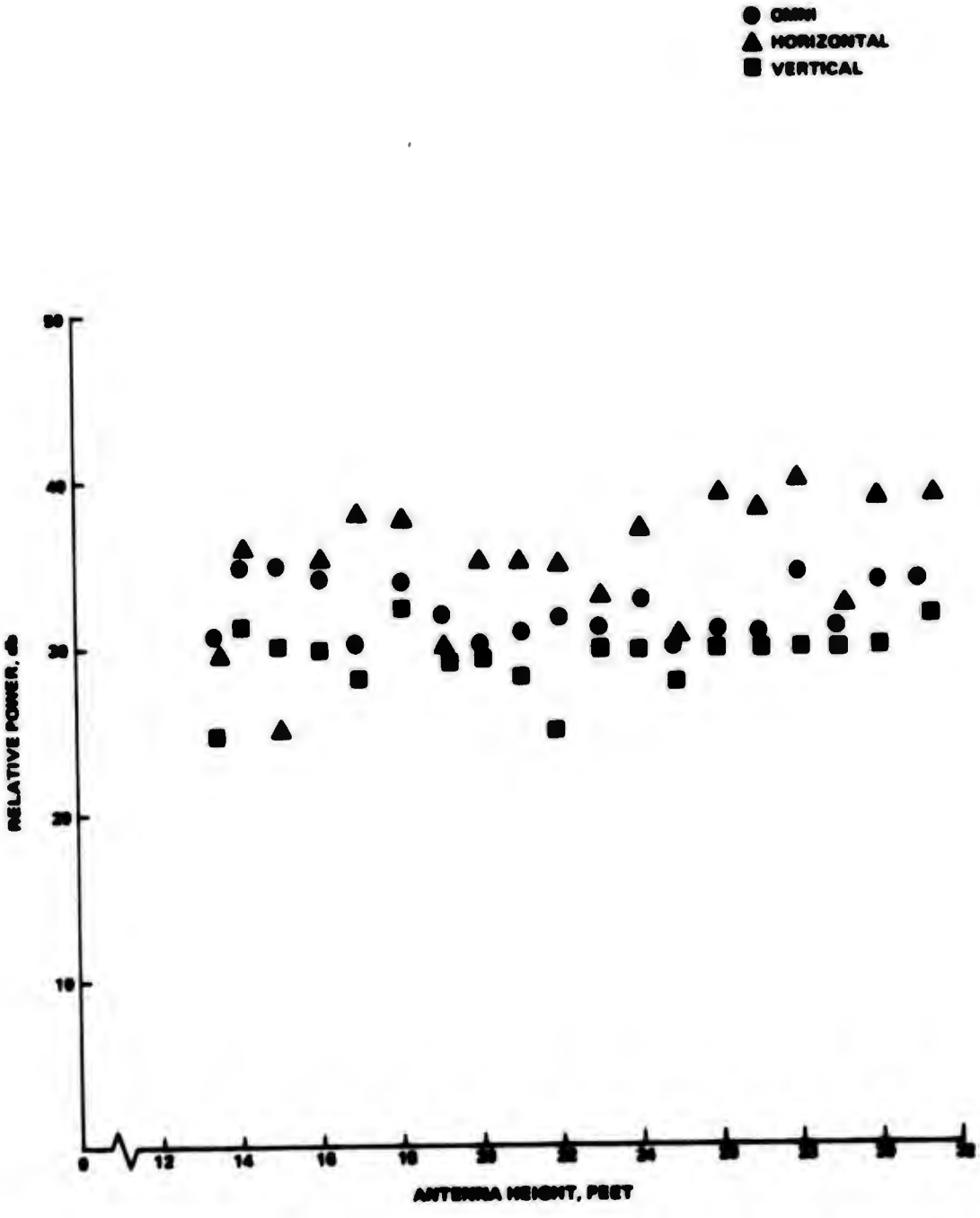

Figure 9-79 "Rough Earth" Northrop Strip - Site No. 7

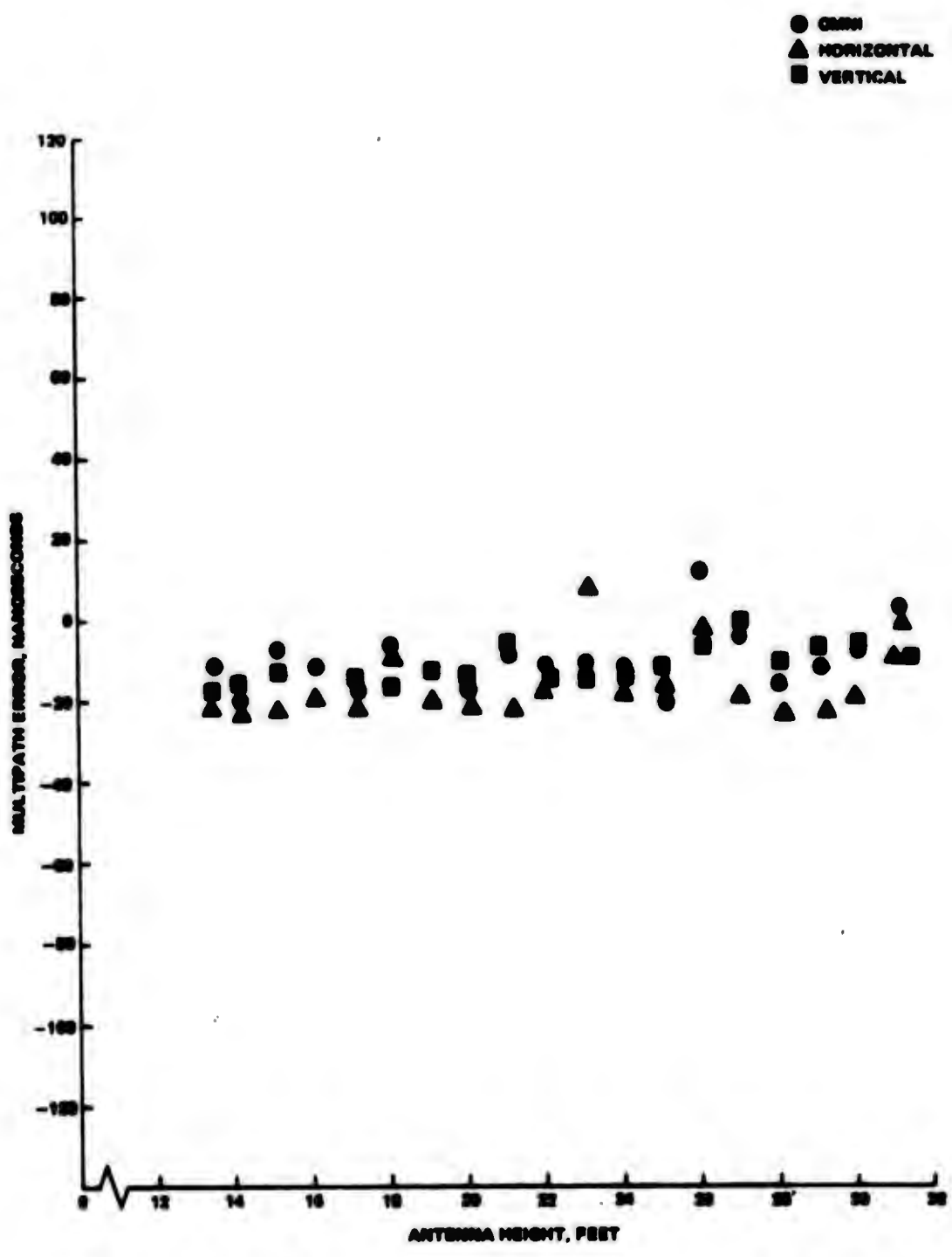

Figure 9-80 "Rough Earth" Site No. 8

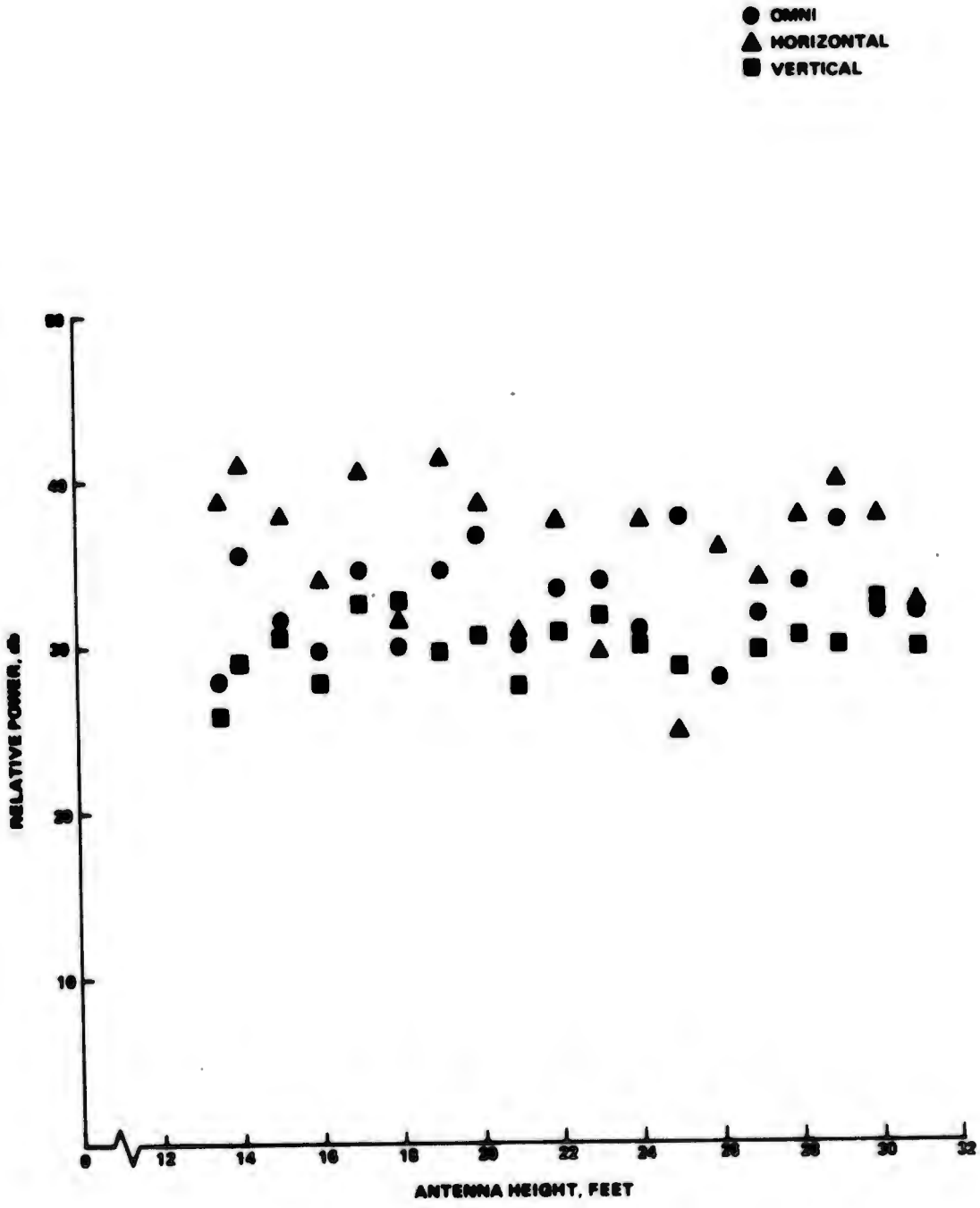

Figure 9-81 "Rough Earth" Site No. 8

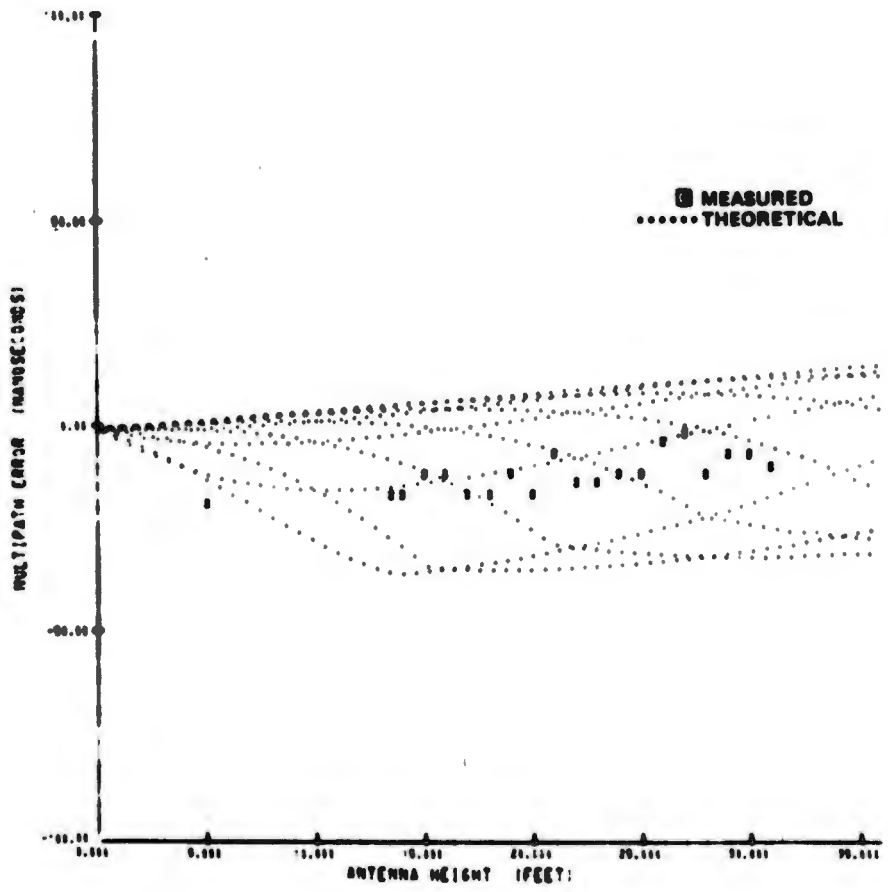

Figure 9-82 Northrop Strip Rough Earth, Site No. 8, Vertical Dipole

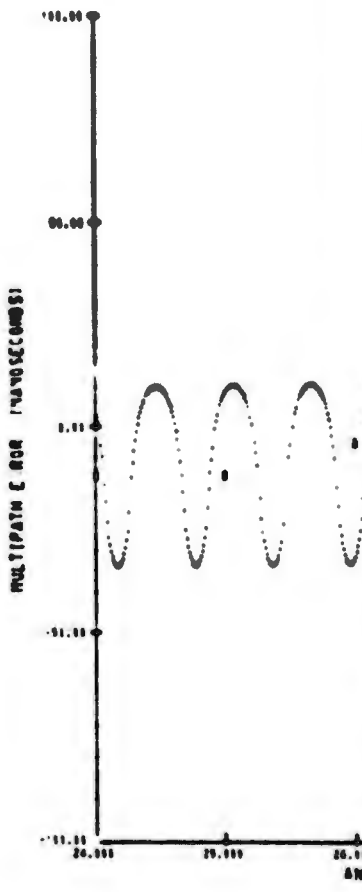

Figure 9-83 Northrop Strip

, Vertical Dipole

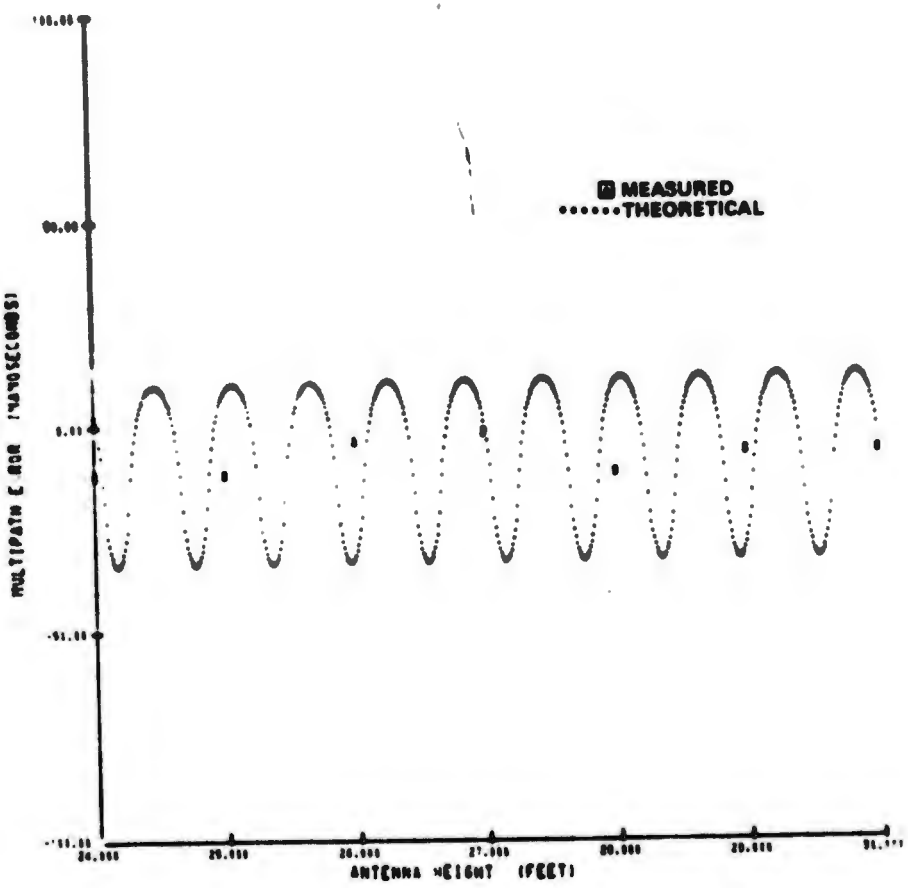

Figure 9-83 Northrop Strip Rough Earth, Site No. 8, Vertical Dipole

Table 9-1 Simulation Parameters

Test Description	Site No.	Trans. Antenna Height	Receiver Dish Antenna Height	Projected Dist. Between Antennas	Conduc-** tivity	Dielectric** Constant	Surface Rough-ness Coeff.	Dish Gain	Dish Dia.	Wave-length	Comments
Northrup Strip Site	1	2000	10	1109	40	20	0.1	24	6'	0.62449'	
(Smooth Earth)	2	↓	↓	2395	↓	↓	↓	↓	↓	↓	
	3			3471							
	4			5503							
	5			11301							
(Rough Earth)	6	1680		999	$1x10^{-2}$	3	10				
	7	2000		2551		↓	↓				
	8	2000		3258							
Dead Man's Canyon	1	11		979		10	5				Diffracted*
	2	71.7		754		↓	↓				Diffracted*
	3	20	20	974			1				
Tula Peak-Site	1	175	185	1566							
	2	75	85	1041	↓	↓		↓	↓	↓	

NOTE: * SIGNALS DIFFRACTED BY RIDGE OR OTHER OBSTACLES ARE NOT MODELLED. THEREFORE, SIMULATION RESULTS FOR THOSE CASES ARE EXPECTED TO BE POOR.

** DATA TAKEN FROM REF. (45).

Table 9-2 Functional Flow Diagram

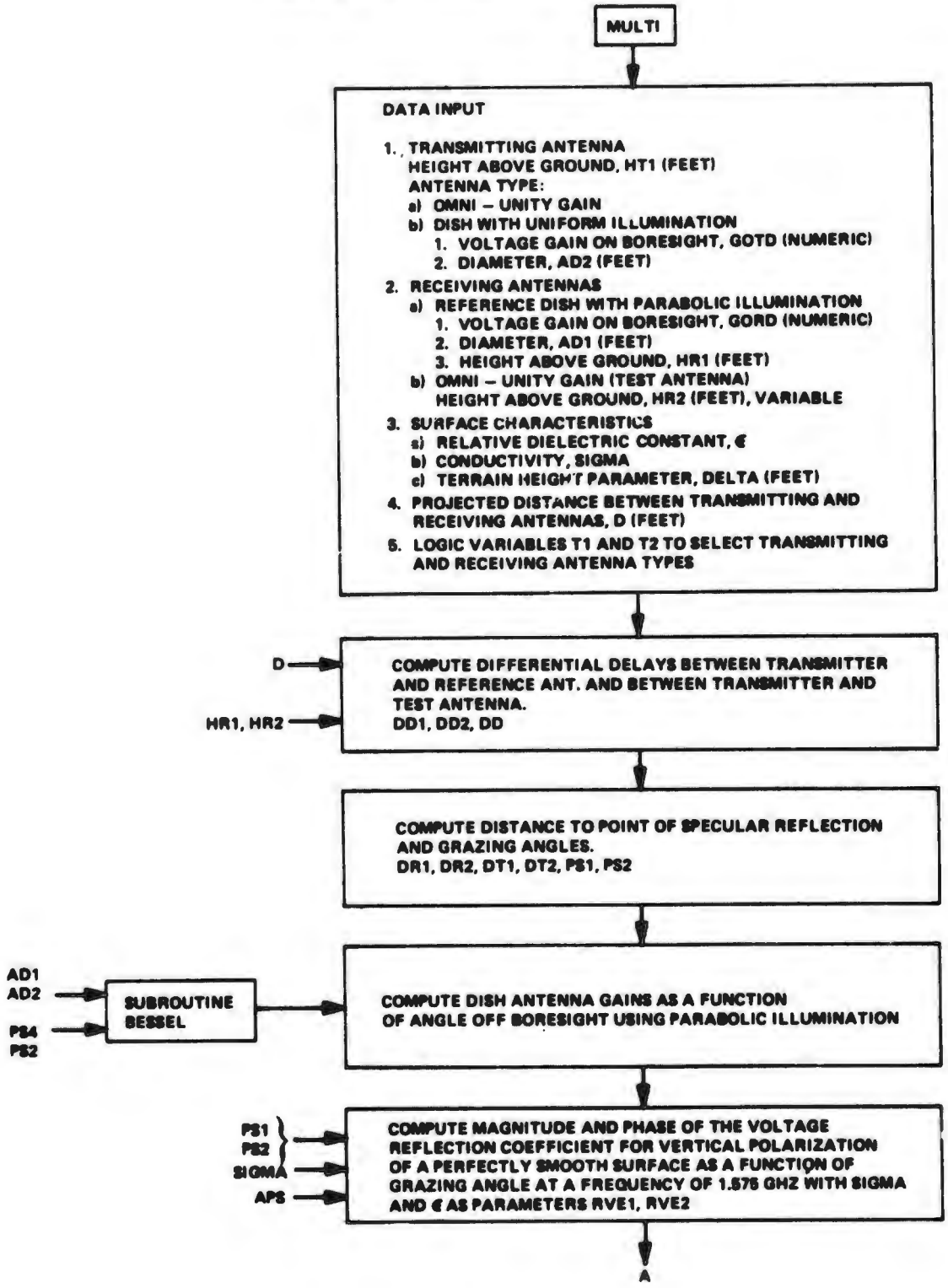

Table 9-2 Functional Flow Diagram (Concluded)

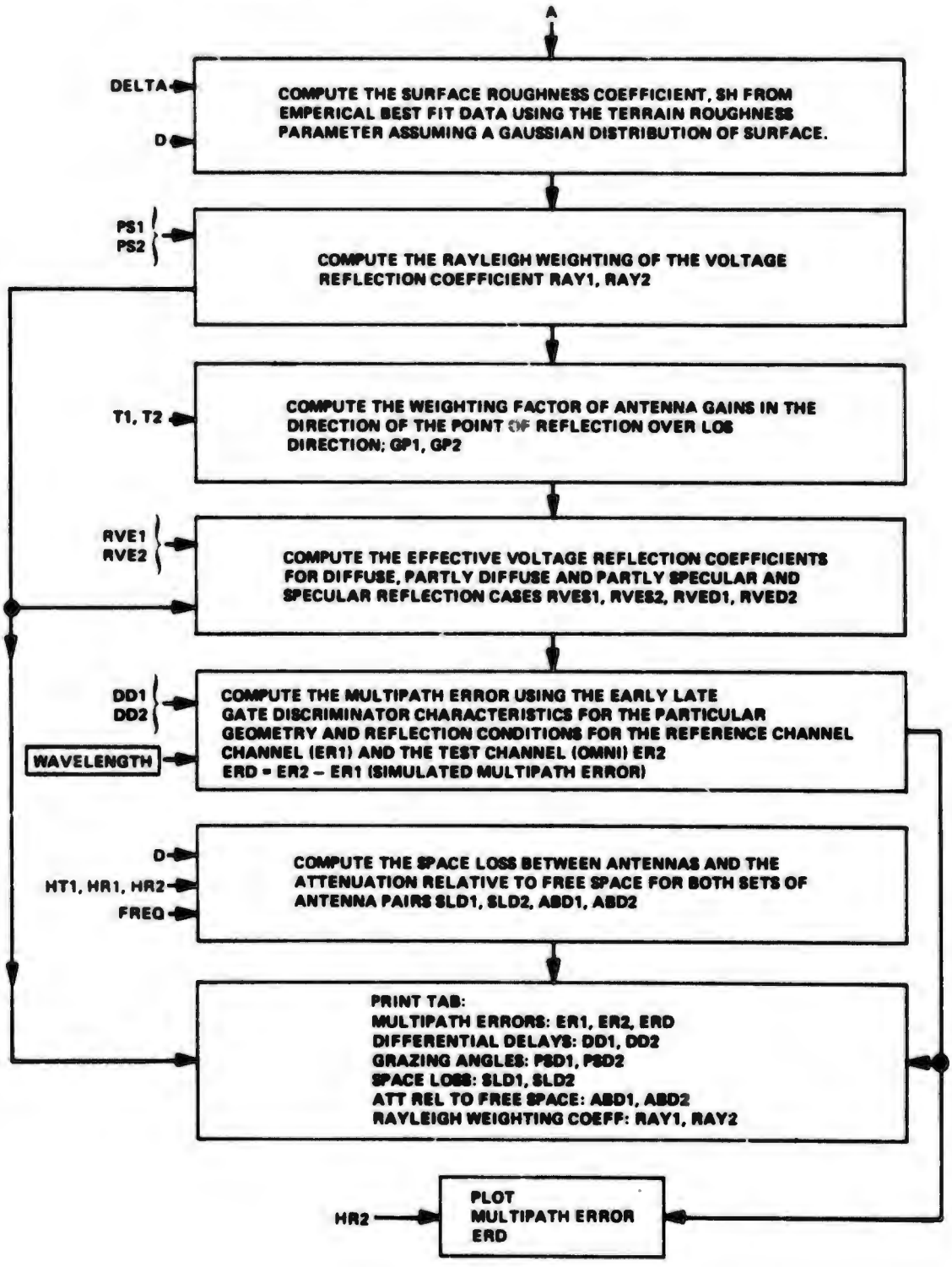

9.8.2 System Multipath Considerations - Simulation Model

9.8.2.1 Multipath System Model

The multipath system conceptual model used is assumed to consist of a cascade of two systems (refer to Figure 9-84) following the basic ideas of Kadar, Ref. (1). The geometry dependent system (with conceptual impulse response) $\underset{\sim}{h}(\underset{\sim}{s}, t)$ is a function of space and time. It describes the time varying channel created by both the user's (receiving antenna or system) relative motion with respect to the transmitters(s) or by the changes in the propagation medium (caused by ionospheric or tropospheric characteristics), the reflecting surface characteristics and the total electromagnetic environment. The second system, $h_r(t)$ describes the behavior of the receiver-demodulator performance for a given signal structure with the multipath interference present.

The impulse response of $\underset{\sim}{h}(\underset{\sim}{s}, t)$ is determined by consideration of the following parameters, Ref. (1).

- Frequency and polarization dependence of the reflection coefficient (Brewster's angle and phase changes)
- Polarization effects and antenna patterns
- Divergence factor, surface roughness and scattering coefficient
- Grazing angle bounds on above parameters for specular reflection
- Differential delay (geometry dependent)
- Differential doppler (geometry and aircraft speed dependent).
- Refraction index changes and fading phenomenon
- Free space attenuation.

The second system whose conceptual impulse response is $h_r(t)$, is dependent upon the following system parameters:

- Received signal power (direct and multipath)
- Carrier tracking loop noise bandwidth
- Code tracking loop discriminator transfer function (range errors)
- Doppler counting time (range code errors).

9.8.2.2 System Geometry

A typical flat earth geometry used in the simulation program model is shown in Figure 9-85. The path length difference between the direct and reflected paths is defined as

$$D = r_1 + r_2 - r_0 \text{ , ft} \qquad (1)$$

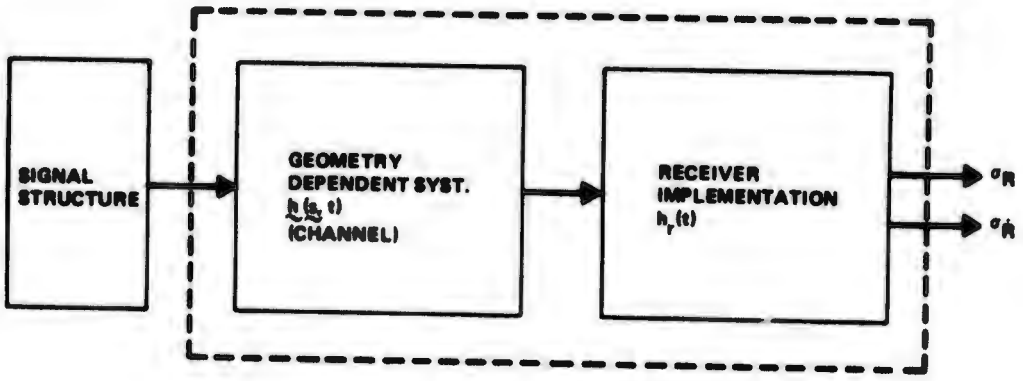

Figure 9-84 Conceptual Multipath System

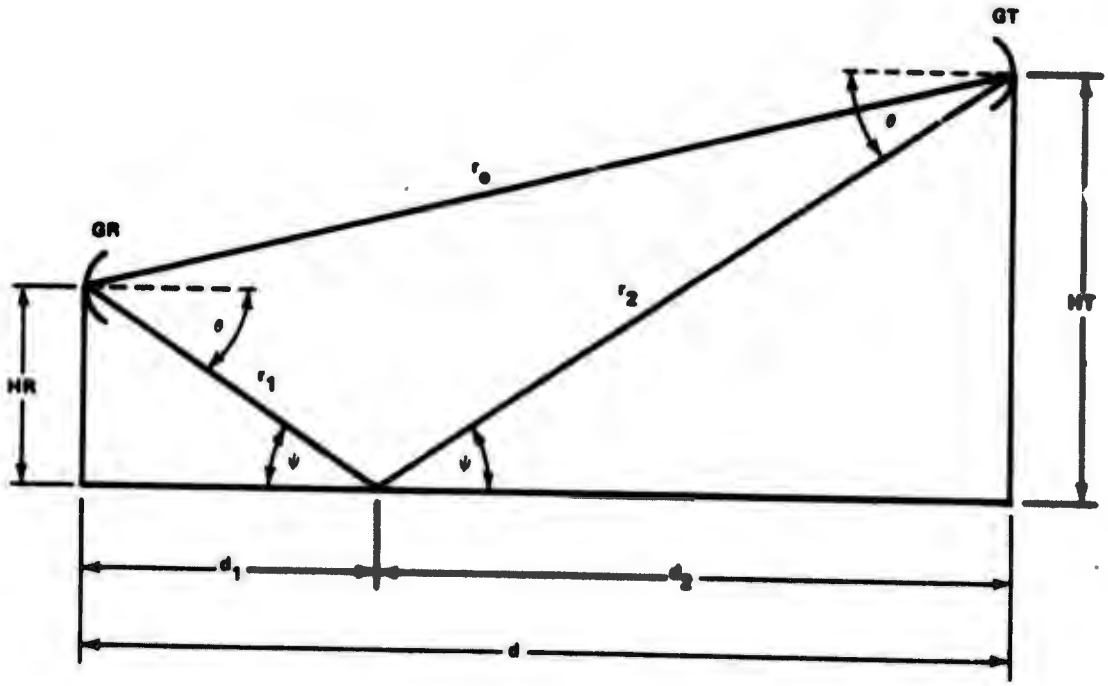

$$\text{TAN}\,\psi = \frac{HR}{d_1} = \frac{HT}{d_2} = \text{TAN}\,\theta$$

$$d = d_1 + d_2$$

Figure 9-85 Antenna Heights Above a Plane Tangent to the Earth at the Point of Reflection

also known as the differential delay. If the geometry* is time varying, one can define a fade frequency or differential doppler as

$$\Delta\omega = \frac{2\pi}{\lambda}\dot{D}\ ,\ \text{rad/sec} \tag{2}$$

where λ is the wavelength of the transmitted signal. In the simulation model the fade frequency term is not included since the ground test geometry is not moving with time.

The differential delay is readily computed from

$$D = \sqrt{d^2 + (HT + HR)^2} - \sqrt{d^2 + (HT - 1_iR)^2} \tag{3}$$

The distance to the point of specular reflection is determined by:

$$\left.\begin{aligned} d_1 &= d[1 + HT/HR]^{-1} \\ d_2 &= d[1 + Hr/HT]^{-1} \end{aligned}\right] \tag{4}$$

The grazing angle is computed directly

$$\psi = \tan^{-1}\left(\frac{HR}{d_1}\right) \tag{5}$$

9.8.2.3 Antenna Far Field Pattern

The far field radiation pattern of a circular aperture with parabolic illumination can be expressed in terms of the parameter $\pi D/\lambda \sin\psi$ as

$$G_p(\psi) = G_0 \frac{16 J_2^2\left(\frac{\pi D}{\lambda}\sin\psi\right)}{\left(\frac{\pi D}{\lambda}\sin\psi\right)^4} K(\psi) \tag{6}$$

where

η is the aperture efficiency.

$$K(\psi) = (1 + \cos\psi)^2\ ,\quad G_0 \simeq \left(\frac{\pi D}{\lambda}\right)^2 \eta$$

For a uniformly illuminated circular aperture the far field radiation pattern is given by

$$G_u(\psi) = G_0 \frac{J_1^2\left(\frac{\pi D}{\lambda}\sin\psi\right)}{\left(\frac{\pi D}{\lambda}\sin\psi\right)^2} K(\psi) \tag{7}$$

---

*NOTE: In all cases the simulation program models assume that the geometry and the distances involved are very short and the effects of surface refractivity are negligible in the computations.

9.8.2.4 Computation of Theoretical Plane Earth (Perfectly Smooth) Reflection Coefficients

The theoretical plane earth reflection coefficients for horizontal and vertical polarizations R_H R_v, and the phase angles C_H, C_v are functions of the carrier frequency f, the grazing angle ψ, and the ground constants σ (sigma) and ϵ. Their magnitudes are computed based upon the method of Ref. 43 as:

$$x = 1800\,\sigma/f, \quad q = x/(2p) \tag{8}$$

$$2p^2 = [(\epsilon - \cos^2\psi)^2 + x^2]^{1/2} + (\epsilon - \cos^2\psi) \tag{9}$$

$$b_v = \frac{\epsilon^2 + x^2}{p^2 + q^2}, \quad b_h = \frac{1}{p^2 + q^2} \text{ radians} \tag{10}$$

$$m_v = \frac{2(p\epsilon + qx)}{p^2 + q^2}, \quad m_h = \frac{2p}{p^2 + q^2}. \tag{11}$$

Then

$$R_v^2 = [1 + b_v \sin^2\psi - m_v \sin\psi]/[1 + b_v \sin^2\psi + m_v \sin\psi] \tag{12}$$

$$R_h^2 = [1 + b_h \sin^2\psi - m_h \sin\psi]/[1 + b_h \sin^2\psi + m_h \sin\psi] \tag{13}$$

The phase angle c is defined below for both horizontal and vertical polarization, c_h and c_v. The angle c_h defined as

$$c_h = \tan^{-1}\left(\frac{q}{p + \sin\psi}\right) - \tan^{-1}\left(\frac{q}{p - \sin\psi}\right) \text{ radians} \tag{14}$$

is always negative and ranges in value from $0 \geq c_h \leq -0.1$ radians. The angle c_v changes suddenly from near zero to $\pi/2$ at the pseudo-Brewster angle, $\sin^{-1}\sqrt{1/b_v}$. To define c_v, let

$$y_1 = (x \sin\psi + q)/(\epsilon \sin\psi + p), \quad y_2 = (x \sin\psi - q)/(\epsilon \sin\psi - p). \tag{15}$$

If $\epsilon \sin\psi \geq p$:

$$c_v = \tan^{-1} y_1 - \tan^{-1} y_2 + \pi \text{ radians}. \tag{16}$$

If $\epsilon \sin\psi < p$ and $p \sin\psi > 0.5$:

$$c_v = \tan^{-1} y_1 + \tan^{-1} y_2 \text{ radians}. \tag{17}$$

If $\epsilon \sin\psi \geq p$ and $p \sin\psi \leq 0.5$:

$$c_v = \tan^{-1} y_1 - \tan^{-1} y_2 \text{ radians}. \tag{18}$$

In the above formulas, $\tan^{-1} y$ is in the first quadrant if y is positive and in the fourth quadrant if y is negative.

9.8.2.5 Surface Characteristics

In the previous sections the characterization of the channel was introduced without the definition of the surface characteristics (i.e., other than perfectly smooth) and the electromagnetic environment. Clearly, the discussion of the channel implicitly contains the surface characteristics.

A surface may be described formally by giving its elevation $z = f(X, Y)$ at every point in the X-Y plane. The term z assumed to be a continuous random variable, which may be characterized by a joint probability density function and a correlation function. Ott (Ref. 47) derives the surface correlation function following the work of Beckmann defined as:

$$\rho(\tau) = \frac{1}{\sigma^2}\int_{-\infty}^{\infty}\int_{-\infty}^{\infty} Z_1 Z_2\, \rho(Z_2,\ Z_1;\ \tau)dZ_1 dZ_2 \tag{19}$$

where τ represents the distance between z_1 and z_2 and σ^2 is the mean square surface height.

The correlation function also depends upon the "correlation distance", T for which $\rho(\tau)$ will drop to the value σ^2/e. Large correlation distances represent large distance between the hills and valleys, i.e. the surface is gently rolling, whereas $T \longrightarrow o$ implies the surface has very densely packed irregularities Ref. (38).

In the description of the random surface one needs to consider for what values a wavelength, mean surface height, and angle of incidence does specular reflection change into diffuse scattering? The Rayleigh criterion answers the question, by defining surface roughness as Ref. (38).

$$\sqrt{g} = \frac{4\pi\sigma}{\lambda}\sin\psi \tag{20}$$

where ψ is the grazing angle measured from the horizontal, the λ is the wavelength in free space.

Rayleigh criterion may be best understood by considering a uniform wavefront impinging on a rough surface characterized by a step type discontinuity as shown in Figure 9-86. The path length difference (at a point far away from the surface) between the reflected specular ray at point A and the reflected ray at point B is, Δd, which may be expressed in terms of the grazing angle, and the surface roughness Δh as:

$$\Delta d = 2h\sin\psi \tag{21}$$

The corresponding phase difference is given by

$$\Delta\phi = \frac{2\pi}{\lambda}\Delta d = \frac{4\pi\Delta h}{\lambda}\sin\psi \tag{22}$$

Experiments have shown (Ref. 49) that if

$$\frac{\Delta h \sin\psi}{\lambda} \ll \frac{1}{8} \tag{23}$$

then the reflections are specular, and if

$$\frac{4\pi\Delta h \sin\psi}{\lambda} = \pi\ ,$$

then any energy reflected in the direction of the specular rays is diffuse, since the specular rays have cancelled by assumption.

An effective ground voltage reflection coefficient may be defined for a gaussian surface Ref. (38) as:

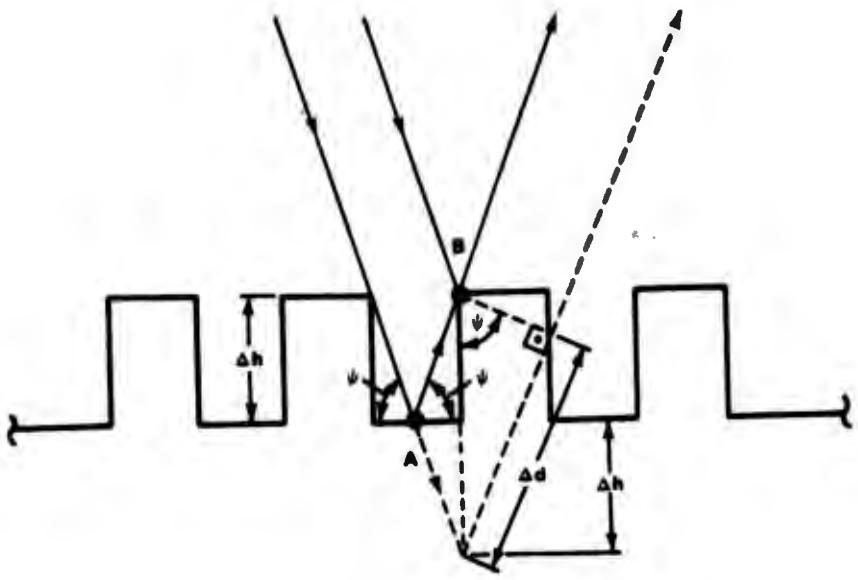

Figure 9-86 Surface Characterized by Step Type Discontinuity

$$R_e = DR_{V,H} G^{1/2}(\psi, h)\, e^{-4\pi\sigma \sin\psi/\lambda} \tag{24}$$

where: D, is the divergence factor allowing for the diverge of energy reflected from a curved surface, $R_{V,H}$ is the Fresnel reflection coefficient of a smooth surface (either for vertical or horizontal polarization), G (ψ, h) represents the weighting of the reflections by the antenna patterns and the reflected area, and the exponent is Rayleigh's criterion of roughness. For completely diffused reflections:

$$R_e = DR_{V,H} G^{1/2}(\psi, h) \tag{25}$$

where $G(\psi, h)$ is usually a very complex function of the surface and communication geometry Ref. (48).

In the simulation program it is assumed that the exact terrain profiles are not available and that the root-mean-square deviation of terrain profiles relative to a smooth curve within the first Fresnel zone projection can be determined based upon empirical data obtained from measurements on a large number of profiles, from Ref. 43.

The terrain roughness is modelled as

$$\sigma = \begin{cases} 0.78\ \Delta h(d) \exp\{-0.5[\Delta h(d)]^{1/4}\}, & \Delta h(d) > 4m \\ 0.39\ \Delta h(d), & \Delta h(d) \leq 4m \end{cases} \tag{26}$$

$$\Delta h(d) = \Delta h\,[1 - 0.08 \exp(-0.02d)],\ m \tag{27}$$

where $\Delta h(d)$ and Δh are in meters and distance d is in kilometers. In the computer simulation program all dimensions are converted to feet.

9.8.2.6 Weighting of the Reflected Energy

The Rayleigh coefficient of roughness for a Gaussian distributed surface $= e^{\frac{2\pi\sigma \sin\psi}{\lambda}}$ modifies the reflection coefficient for a perfectly smooth surface. If the antennas used are directional one needs to compute the weighting of the reflected energy, $G_w(\theta, \psi)$. In the simulation program using the principles of ray optics $G_w(\theta, \psi)$ becomes

$$G_w^{1/2}(\psi) = \left[\frac{GR(\psi_r) GT(\psi_r)}{GR(0) GT(0)}\right]^{1/2} \tag{28}$$

where $GR(\psi_r)$, $GT(\psi_r)$ represent the gains of each antenna in the direction of the point of ground reflections; GR(0), GT(0) are assumed to be the free space gains of each antenna in the direction of the other.

9.8.2 "Effective" Ground Voltage Reflection Coefficient

Experimental formulas combining the results of Beckmann (Ref. 38) with the Rayleigh criterion have been worked out by Longley and Rice (Ref. 43) and others (Ref. 49) for line of sight paths.

The reflections can be classified as:

Specular:

$$\text{If, } R_{V,H} e^{-(2\pi/\lambda)\sigma \sin\psi} > 0.5 \text{ and } > \sqrt{\sin\psi} \tag{29}$$

Partly Specular and Partly Diffused:

$$\text{If, } R_{V,H} e^{-(2\pi\sigma/\lambda)\sin\psi} > 0.244 \tag{30}$$

Diffuse:

$$\text{If, } R_{V,H} e^{-(2\pi\sigma/\lambda)\sin\psi} < 0.244 , \tag{31}$$

or if the specular criterion is not met and $\psi < 14^{o}$.

The simulation program for a given geometry categories the reflections according to the above equations and computes the effective ground reflection coefficients as:

$$Re = \begin{cases} R_{V,H} G_w^{1/2} e^{\frac{-2\pi\sigma\sin\psi}{\lambda}} & \text{for specular, partly specular and partly diffused reflection} \\ [G_w \sin\psi]^{1/2} & \text{for diffuse reflections} \end{cases} \tag{32}$$

9.8.2.8 Receiver Implementation

The correlation receiver implementation utilizes a code tracking loop with an interacting code-carrier tracking loops design. The code tracking loop discriminator (early-late-gate) characteristics govern the behavior of the receiver in the presence of interference within a code chip. This is the case of multipath.

The early late gate discriminator block diagram is shown in Figure 9-87. In reference to Figure 9-87 one can write

$$f_0(t) = \int C_i(t)\, C_r(t - \tau/2 + \tau)\, d\tau - \int C_i(t)\, C_r(t + \tau/2 + \tau)\, d\tau \tag{33}$$

where

T is the chip time

$C_i(t)$ is the received code

$C_r(t)$ is the locally generated code replica

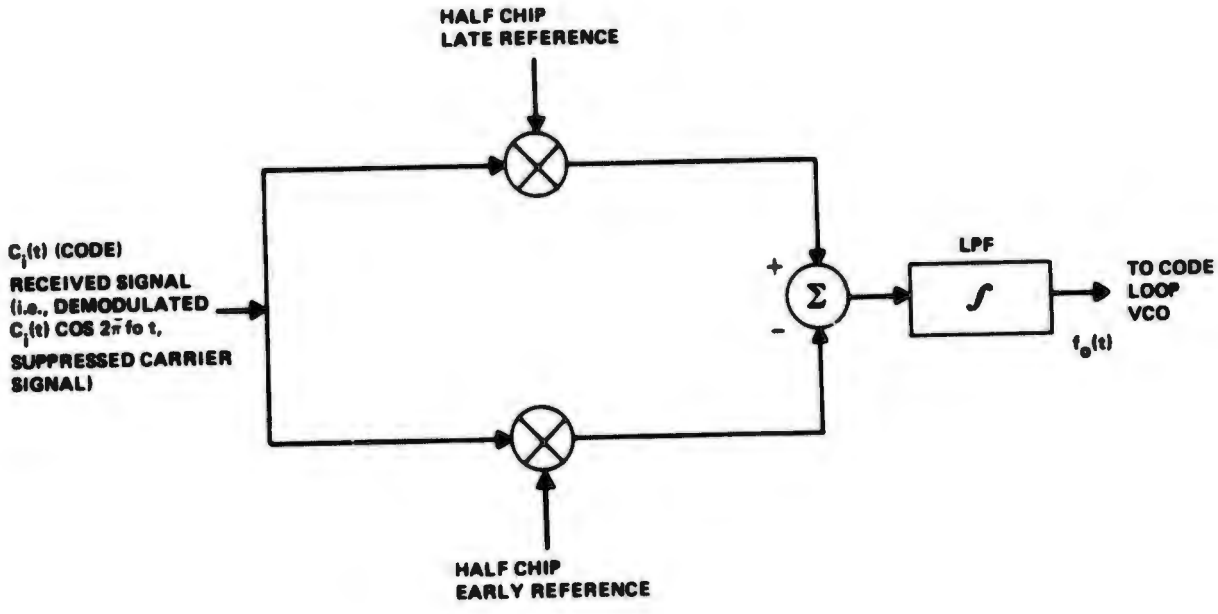

Figure 9-87 Early-Late-Gate Discriminator

The delay locked loop is assumed to be synchronized initially (with acquisition aide) within a chip. Therefore, the discriminator behavior is only relevant within a code chip. The correlation function is given by:

$$R(\tau) = \lim_{T\to\infty} \frac{1}{2T}\int_{-T}^{T} C_i(t)\, C_r(t+\tau)\, dt \tag{34}$$

where

$$Re(\tau) = \begin{cases} 1 - \dfrac{|\tau|}{T}, & |\tau| \le T \\ 0, & |\tau| > T \end{cases} \tag{35}$$

Therefore, $f_0(t)$ can be considered with change of variables equal to:

$$f_0(\tau) = -R(\tau - T/2) + R(\tau + T/2)$$

$$= R(\tau - T/c) - R(\tau + T/2) \tag{36}$$

as shown in Figure 9-88

If multipath signal is present with relative voltage reflection coefficient

$$R_e = R_{V,H}\cos\left(\frac{2\pi}{\lambda} D + \phi\right), \quad |R_e| \le 1 \tag{37}$$

where R_{V1H} is the magnitude of the effective voltage reflection coefficient for either vertical or horizontal polarization

λ = wavelength of the source (ft)

D = differential delay, (ft)

ϕ = phase angle (rad.) for either vertical or horizontal polarization

then

$$C_i^1(t) = C_{i_{desired}}(t) + R_e\, C_{multipath}\left(t - \frac{d}{V}\right) \tag{38}$$

where

$$V = \text{speed of light}, \quad \tau_0 = \frac{d}{V}$$

Since the delay-locked discriminator characteristics were assumed to be linear. superposition holds and the response to $C_i^1(t)$ is the sum of the responses due to C_i desired + C multipath.

Therefore,

$$S^1(\tau) = S(\tau) + R_e S(\tau - \tau_0) \tag{39}$$

The above equation describes the distorted discriminator characteristics in the presence of a delayed and amplitude weighted replica signal (multipath.)

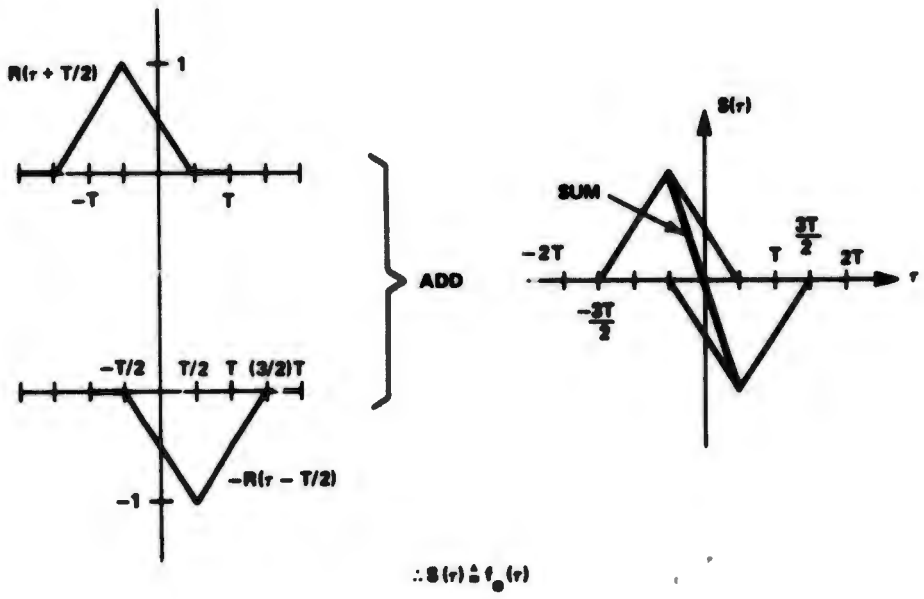

Figure 9-88 Shifted Correlation Functions and Discriminator Characteristics

The multipath error results from the linear combination of the direct signal and multipath signal characteristics, changing the crossover point on the τ - axis from zero to ϵ = (error) as shown in Figure 9-89 or

$$|\tau| < T/2$$

$$\begin{cases} S(\tau) = -\tau/(T/2) & \text{due to direct signal} \\ S^i(\tau) = -\dfrac{R_o(\tau - \tau_0)}{(T/2)} & \text{due to multipath} \end{cases} \tag{40}$$

The multipath error ϵ is given by

$$S(\epsilon) + S^i(\epsilon) = 0$$

$$\epsilon = \frac{R_o \tau_0}{R_o + 1}, \quad 0 \le \tau_0 < \frac{T}{2}(1 + R_o) \tag{41}$$

For

$$\tau_0 > T/2\,(1 + R_o)$$

$$S^i(\tau) = R_o\left(\tau + \frac{3}{2}T - \tau_0\right) \tag{42}$$

so

$$\epsilon = \frac{R_o}{2 - R_o}\left(\frac{3}{2}T - \tau_0\right) \quad \text{for} \tag{43}$$

$$\frac{T}{2}(1 + R_o) \le \tau_0 < \frac{3}{2}T$$

The total error characteristics is

$$\epsilon = \begin{cases} \dfrac{R_o \tau_0}{R_o + 1}, & 0 < \tau_0 < \dfrac{T}{2}(1 + R_o) \\ \dfrac{R_o}{2 - R_o}\left(\dfrac{3}{2}T - \tau_0\right), & \dfrac{T}{2}(1 + R_o) \le \tau_0 < \dfrac{3}{2}T \\ 0, & \tau_0 \ge \dfrac{3}{2}T \end{cases} \tag{44}$$

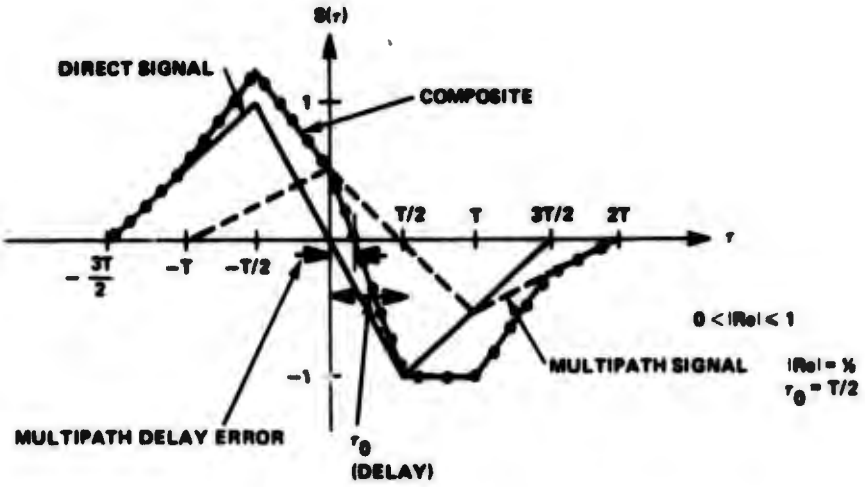

Figure 9-89 Discriminator Characteristics with Interference

A plot of the Tracking Loop Error as a function of differential delay is shown and in Figures 9-90, 91 and 92.

Note that when $D = n\tau$, $\cos(2\pi n + \phi) = \pm 1$, $n = 1, 2, \cdots$

$$\epsilon_{envelope} = \begin{cases} \dfrac{\pm R}{1 \pm R}, & D < \dfrac{T}{2}(1 + R) \\ \left(\dfrac{3T}{2} - D\right)\dfrac{\pm R}{2 \mp R}, & \dfrac{T}{2}(1 \pm R) \le D < \dfrac{3T}{2} \\ 0, & D \ge \dfrac{2T}{2} \end{cases} \qquad (45)$$

In other words, the focus of all points is on the envelope.

If $D = \dfrac{\lambda}{4} n$, $n = 1, 2, 3, \ldots$

$\epsilon = 0$

For $D = \dfrac{\lambda}{2} n$, there are two conditions.

If $n = 1, 3, 5, \ldots$ all points fall on the negative envelope.

If $n = 2, 4, 6, \ldots$ all points fall on the positive envelope.

9.8.2.9 Free Space Loss and Attenuation Relative to Free Space Between Antennas

The free space loss between two isotropic antennas may be expressed as:

$$L_{db} = 10 \log_{10}\left[\frac{\lambda}{4\pi d}\right]^2 \qquad (46)$$

where, d is the distance between antennas and λ is the free space wavelength. When the receiving and transmitting antennas are above ground, the attenuation relative to free space may be expressed as:

$$A = -10 \log_{10}\left\{(GR)(GT)\left[1 + R_e^2 - 2R_e \cos\left(\frac{2\pi}{\lambda} D - C\right)\right]\right\} \qquad (47)$$

where G_R and GT are the directive voltage gains for each antenna in the direction of the other for conditions of matched polarization, R_e is the effective ground voltage reflection coefficient and C is the phase angle. The computer simulation program incorporates the above equations to predict and/or estimate the received power variation.

ENVELOPE OF MULTIPATH ERROR VS. DIFF. DELAY
FOR, $0 \leq d \leq 150'$, $|R| = 0.99$, $\lambda = 0.62449'$

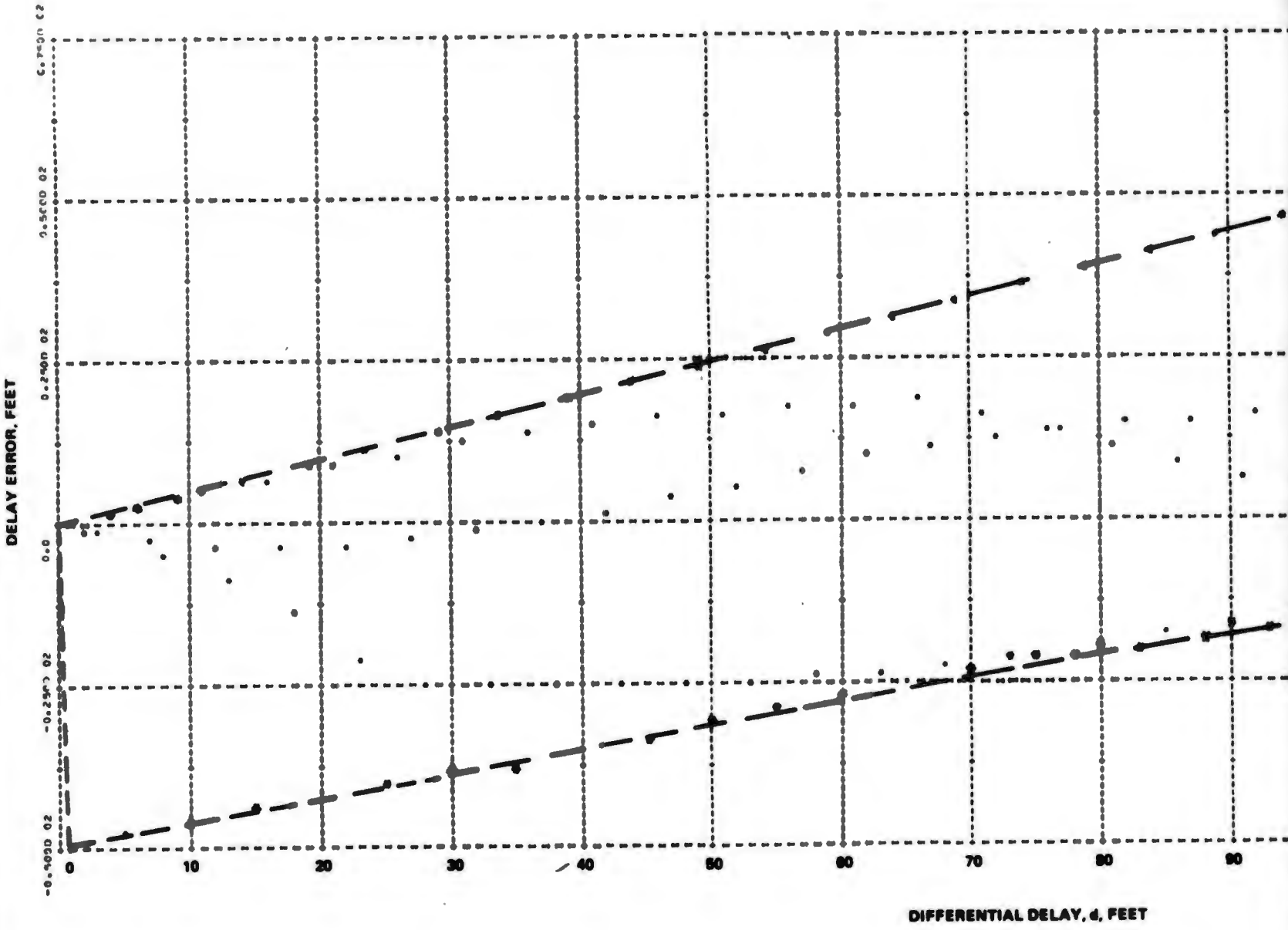

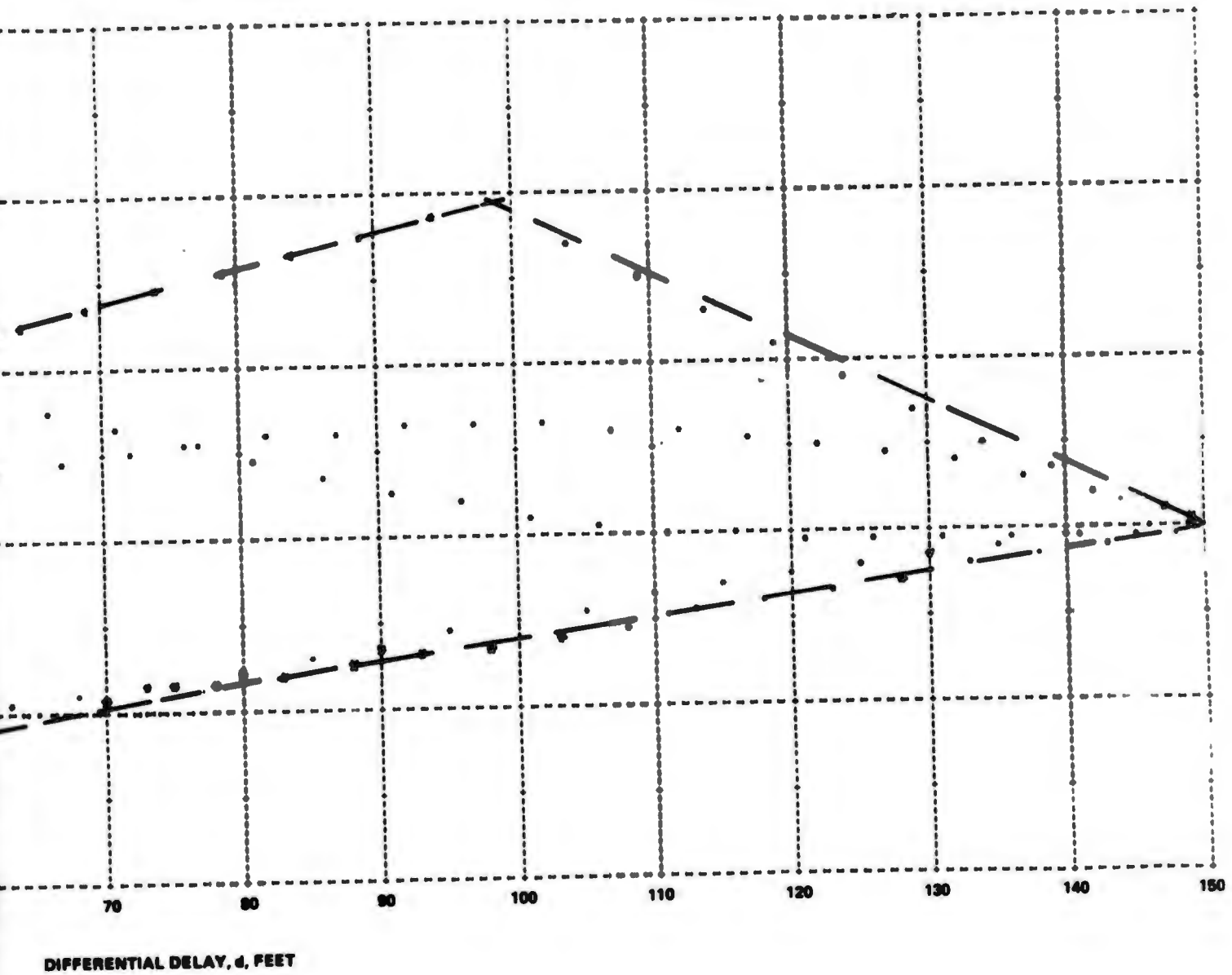

Figure 9-90 Multipath Error Envelope

$$\text{DELAY ERROR} = \begin{cases} \frac{1}{1+R'}\, d, & 0 \le d \le 50\,(1+R') \\ (150-d)\,\frac{R'}{2-R}, & 50\,(1+R') < d \le 150' \\ 0, & d > 150' \end{cases}$$

$$R' = 0.99 \cos\left(\frac{2\pi}{\lambda} d + \pi\right)$$

$$\lambda = 0.62449'$$

FINE STRUCTURE OF MU
FOR, $0 < d < 3.75'$, $|R'| =$

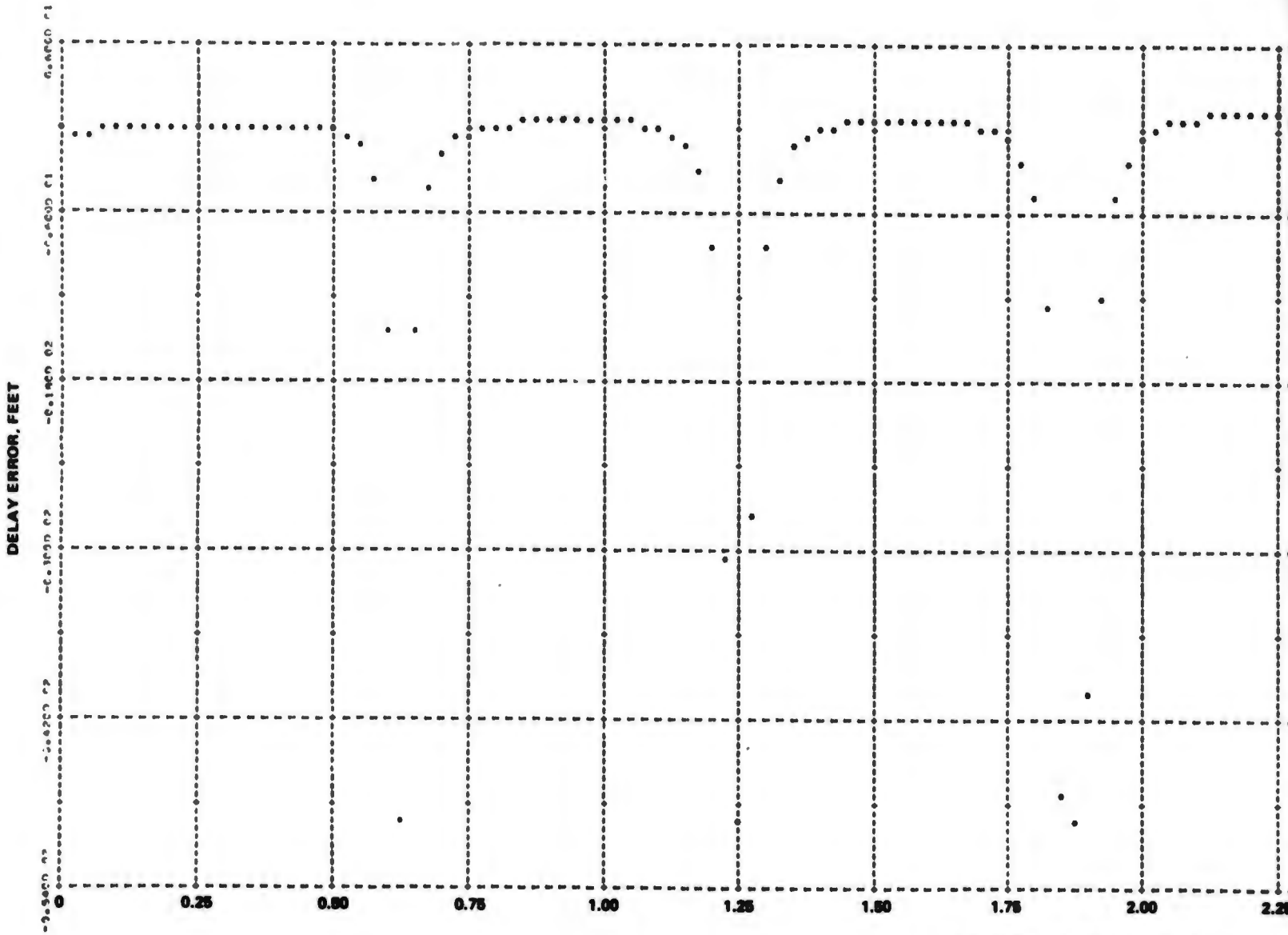

$\cos\left(\frac{4\pi}{\lambda} d + \pi\right)$

FINE STRUCTURE OF MULTIPATH ERROR VS. DIFF. DELAY
FOR, $0 < d < 3.75'$, $|R'| = -0.66$.

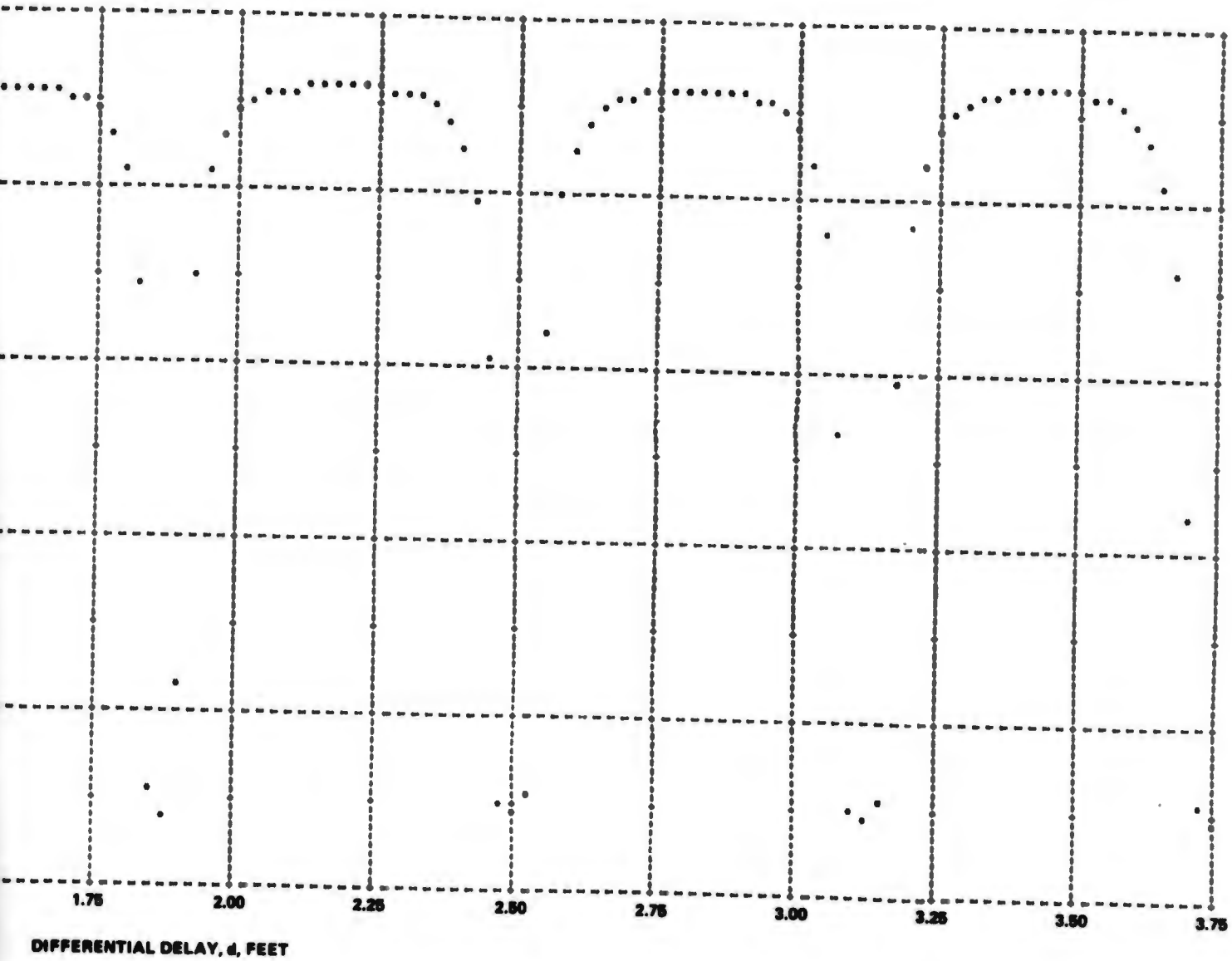

Figure 9-91 Multipath Fine Structure

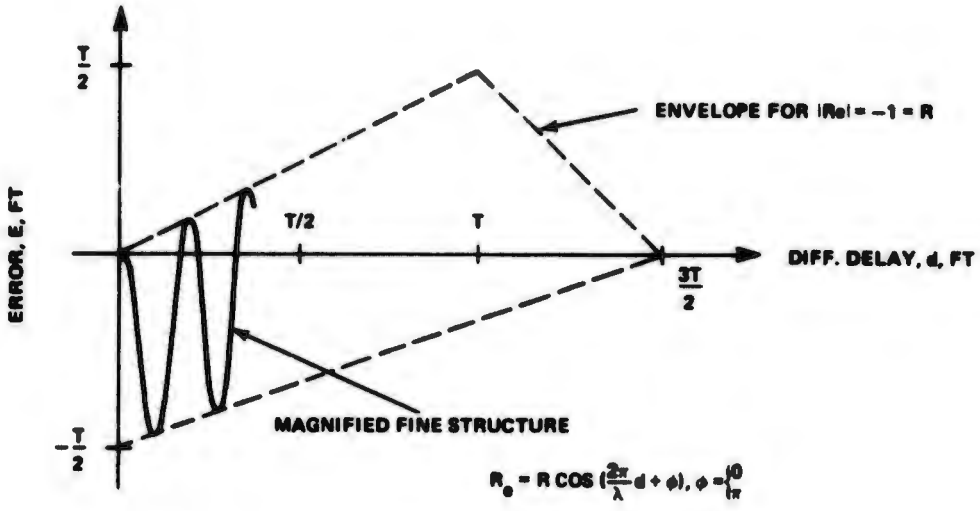

Figure 9-92 Multipath Error Envelope and Fine Structure

9.9 MULTIPATH CONCLUSIONS

The overall objective of the ground user multipath test was to establish the qualitative receiver performance in typical multipath environments. Multipath signals degrade the ranging accuracy of the receiver by creating a distortion of the modulation envelope of the total received signal. This develops an error in the receiver code tracking loop which affects the range accuracy. If the user is moving with respect to the transmitters the range rate accuracy is also affected. In this case the error in the carrier tracking loop is caused by the rate of change of phase of the resultant signal consisting of the direct and multipath reflected signals. This latter effect was not simulated in the ground multipath tests, since the tests were performed under static conditions.

The multipath tests conducted at WSMR consisted of a series of measurements using various transmitter-to-receiver antenna geometries at four separate multipath environments. These environments are characterized in Table 9-3. The overall results of these tests indicate that the theoretical understanding of multipath effects on range accuracy is verified by the experimental results. The theoretical envelope of range tracking error as a function of multipath expressed as the differential delay between the desired and interfering signals is shown in Figure 9-38.

Table 9-3 Ground User Multipath Test Environments

Test Locations	Multipath Characteristics	Multipath Geometries Used
Tula Peak	Specular reflections off a slightly rough surface containing desert sand, bushes, and rocks up to 3 feet in diameter.	• Low grazing angles: 8.5°, 12° • Short differential delay
Dead Man Canyon	Diffracted signals across a gravel pile and construction equipment. The test site was located in a gravel quarry area where excavations were in progress.	• Low grazing angles: $< 3°$ • Short differential delay
Northrop Strip	Diffuse, partly diffuse, and specular reflections from the flat surface of a dry alkalai salt flat.	• Grazing angles ranging from high, approximately 60° to low, approximately 10° • Long and short differential delay
White Sands Area	Diffuse and partly diffuse from the gypsum sand dunes in the White Sands National Monument.	• Grazing angles of 30°, 40° and 60° • Long differential delays

Receiver ranging errors can take on any value within this envelope depending upon the exact signal differential delay. The test data follows this prediction as shown in Figure 9-39. This figure shows all the data collected at the Northrop Strip location and is typical of the receiver performance at the other test sites. The theoretical envelope superimposed on this figure contains virtually all of the test data. The few points which fall outside of the envelope are a result of uncertainty in the true transmitter position and therefore, uncertainty in the value of differential delay determined from the transmitter-to-receiver geometry.

The test program has demonstrated that multipath effects on receiver performance are understood and are therefore predictable. A ground user on the average can experience as much as ±25 feet of multipath error depending on the exact system geometry. However, the differential delay sensitivity of the satellite-to-ground user geometry is only a function of the user antenna height above ground. This allows the ground user to determine the presence of multipath by changing his antenna height and then locate himself in low multipath error environments.

SECTION X

REFERENCE DATA

10.1 PURPOSE

The purpose of the best estimate trajectory (BET) supplied by WSMR was to serve as a position and velocity reference from which the accuracy of the navigation system under test could be determined. Since the accuracy of the navigation system was estimated to be ± 10 ft in position (1σ) ± 0.25 fps in velocity the BET should have been accurate to 5 ft (1σ) ft in position and 0.1 fps in velocity in order to serve as a valid reference. In general, the BET served as an adequate position reference.

10.2 FORMATION OF BET

The BET trajectory was developed from sensor information that have been calibrated and corrected for use on our test program. The sensors that provided input to the BET were:

- Doppler Velocity and Position (DOVAP)
- Cinetheodolite Cameras
- FPS-16 Radar
- LTN-51 Inertial Measuring Unit (IMU)

In the formation of a BET, the data from the above sensors were transformed to the coordinate system used on our program (see Volume II, Section 3.3), then time sequenced onto a MERGE tape. The MERGE tape was fed into a Kalman-type filter which generated the final trajectory. The data flow system on the BET is illustrated in Figure 10-1.

The quality of the BET is dependent on the quality and number of sensors used to track the aircraft. A minimum of two cinetheodolites are required to calculate a position in space but in order to guarantee that the geometry of each sensor (cine) is optimized, 9 cines were normally scheduled for each mission. As the aircraft passed through the field of cines, data from the particular cines that were optimally located, relative to the aircraft, were used to form the BET, normally 4 or 5 out of 9. The X, Y and Z position reported by the BET are sensitive to cine data. Figure 10-2 shows the geometry and data flow of a cinetheodolite. Similarly, the quality of DOVAP inputs affect the BET's velocity accuracy since the BET is dependent on DOVAP for accurate velocity data.

The BET for ILS is dependent only upon cinetheodolite data. No other sensors were used to develop the BET. The importance of maximum cine coverage and quality of data determines the quality of the BET to a greater degree in ILS than for the area navigation flights.

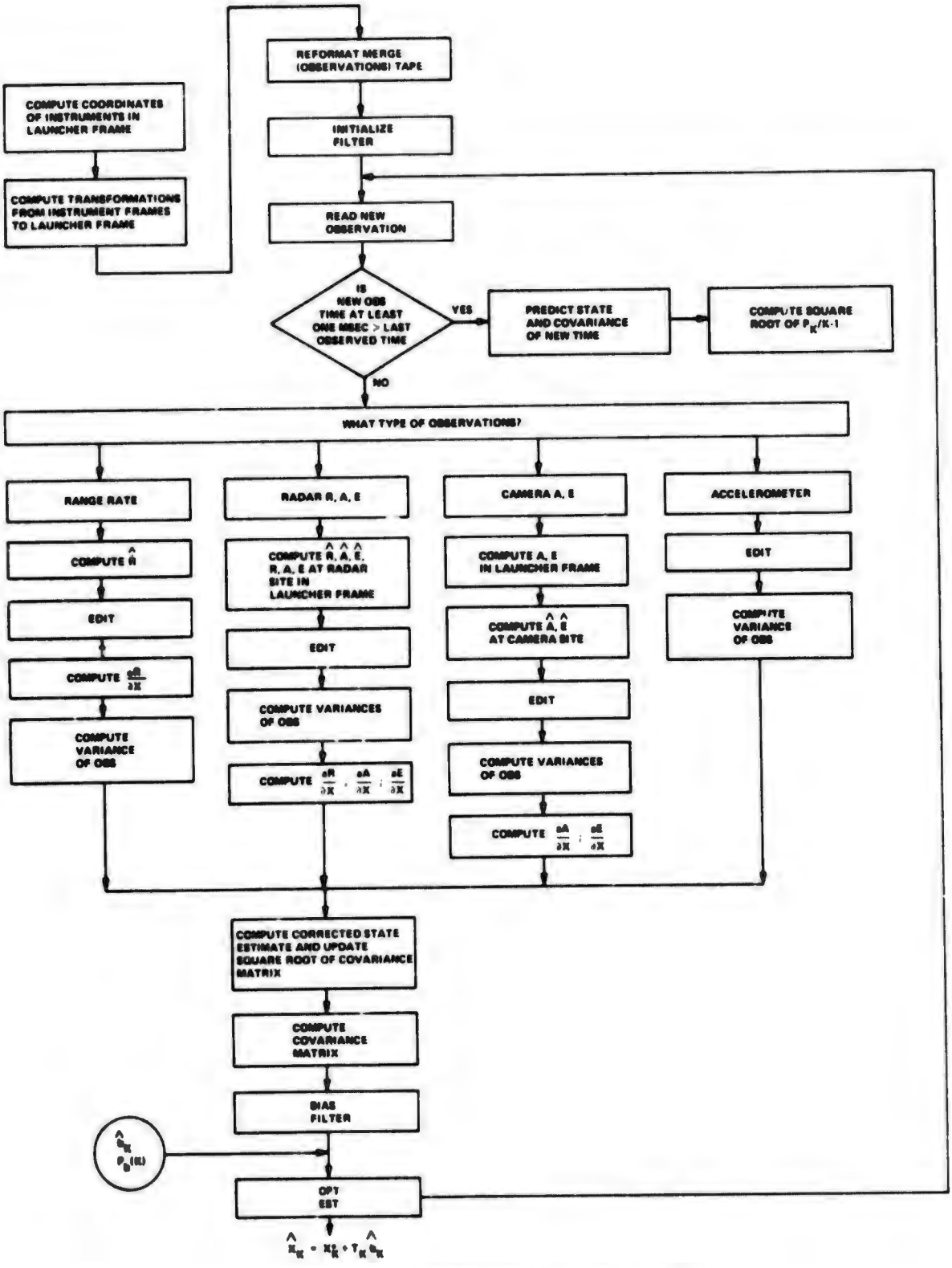

Figure 10-1 Functional Flow of WSMR BET

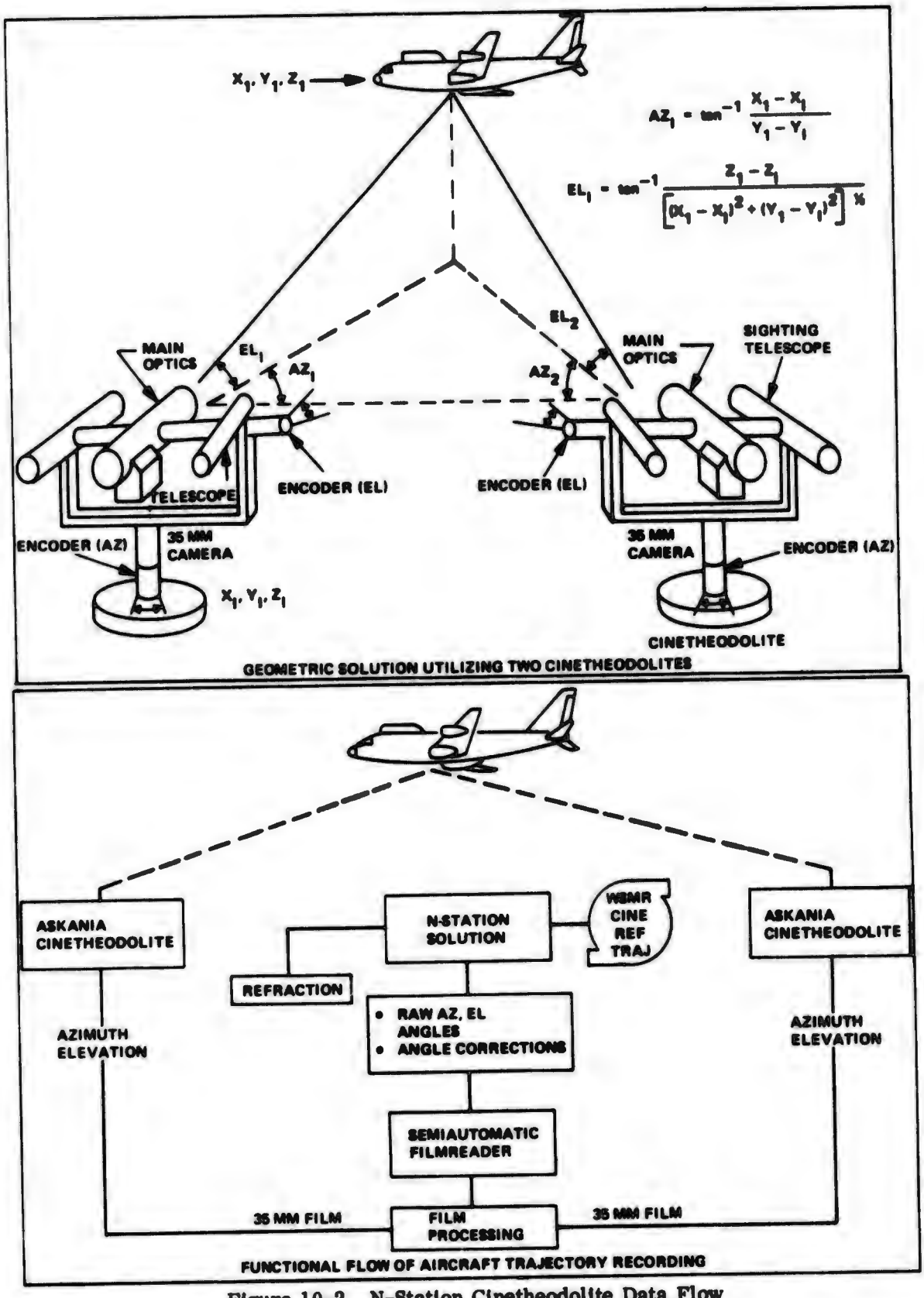

Figure 10-2 N-Station Cinetheodolite Data Flow

At the end of the flight test program, WSMR was asked to evaluate the quality of each BET on a flight-for-flight basis. Table 10-1 is a summary of WSMR comments.

Table 10-1 Qualitative Summary of Best Estimate Trajectory

Flight	Quality	Reason
3&4	Poor	Optical target on aircraft not visible to cine operators; therefore data from cine is questionable.
7,9&14	Fair	DOVAP and LTN-51 only sensors used to make solution
8,10,13,18, 19,&20	Best for 50-mi area	High quality optics, DOVAP and LTN-51 data
15	Fair	Good optics for 50% coverage, no DOVAP. Aircraft altitude was 24,000 AGL because of low cloud cover.
17	Fair	BET is primarily DOVAP and LTN-51 outputs. Pass 1 and 2 had "small" amount of optics but none on rest of flight
11&23	Poor	Aircraft 3,000 (D-Flight Path) altitude proved to be too low for effective DOVAP and line coverage
22	Poor	Poor optics coverage
25&31	Best for ILS	Good optics, both aircraft and balloon
27&29	Fair	Optics data "noisy"
30	Good	Good optics on both balloon and aircraft

10.3 BET TRAJECTORY VS TEST NAVIGATION TRAJECTORY

BET is in the form of a tape when we receive it. In order to compare the BET trajectory with the navigation solution trajectory both tapes are fed into a comparison program called MERGE. This program subtracts the numerical value of position and velocity as found on the navigation tape from its corresponding (in time) position and velocity on the BET tape. The result is presented in the form of a plot of residuals between both trajectories. Figures 10-3 and 10-4 show how the MERGE plots were derived for the Z position and Z velocity residuals of the HAZ receiver navigation solution on run 05, flight 19. The navigation solution position and velocity data on these figures is smoothed by a two-state filter.

It should be noted that the position and velocity plots show both the BET and the HAZ navigation solutions to have almost the same shape, but that the BET has less "noise" than the HAZ data. The residual plot, for position, is the numerical difference between

Z POSITION VS TIME FOR WSMR BET (BEST ESTIMATE TRAJECTORY)
AND HAZ NAVIGATION SOLUTION FLIGHT 19 RUN 05
PLOT START TIME 67522.167 SEC

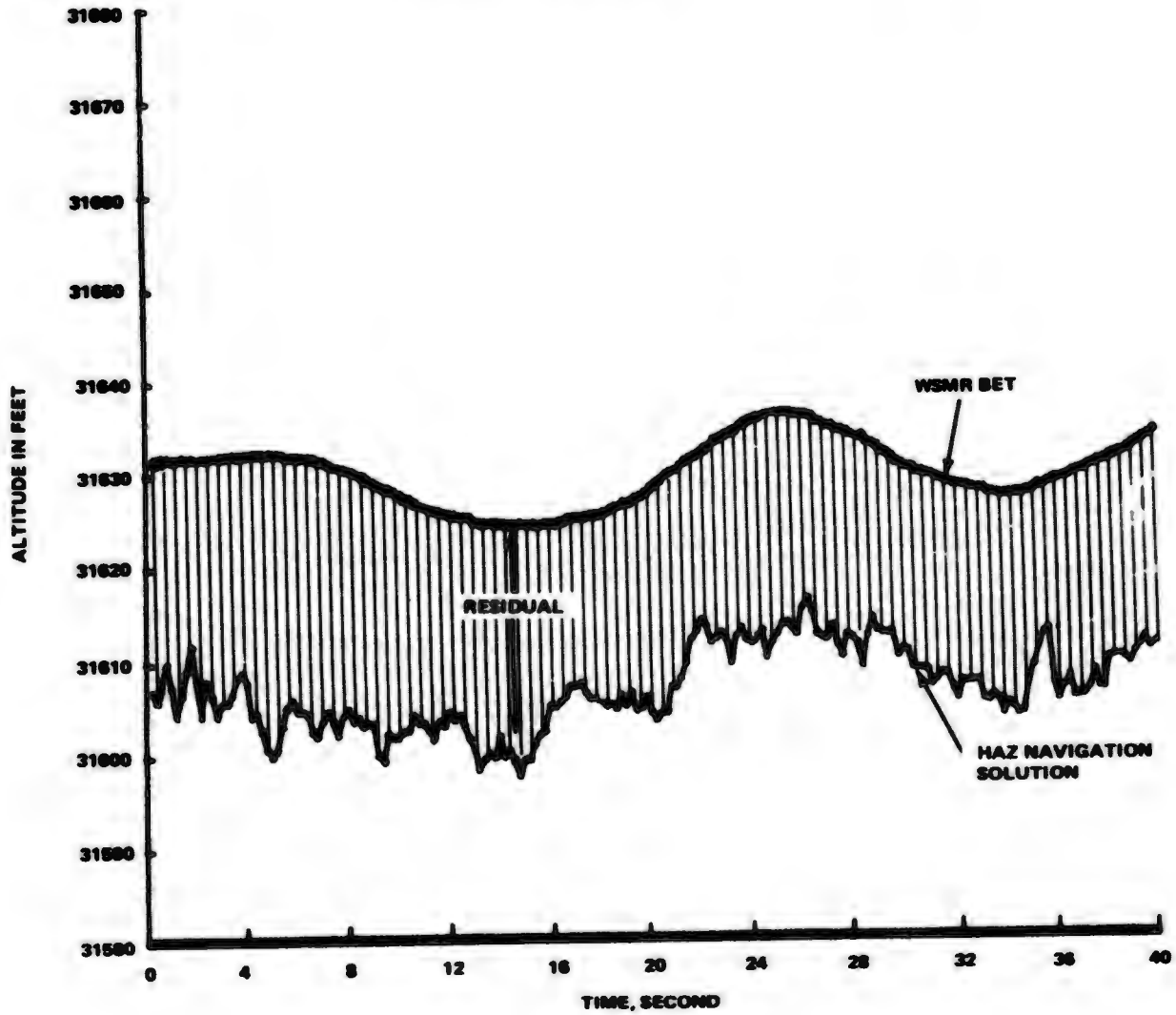

!!! MERGE PROGRAM !!!

Z POSITION RESIDUAL VS TIME FOR (HAZ NAVIGATION SOLUTION POSITION)
MINUS (BET POSITION SOLUTION) FLIGHT 19 RUN 05
PLOT START TIME 67522.167 SEC

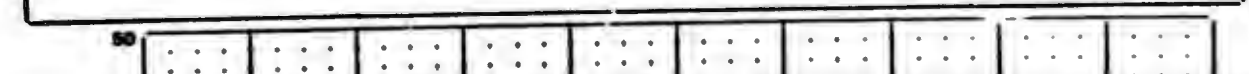

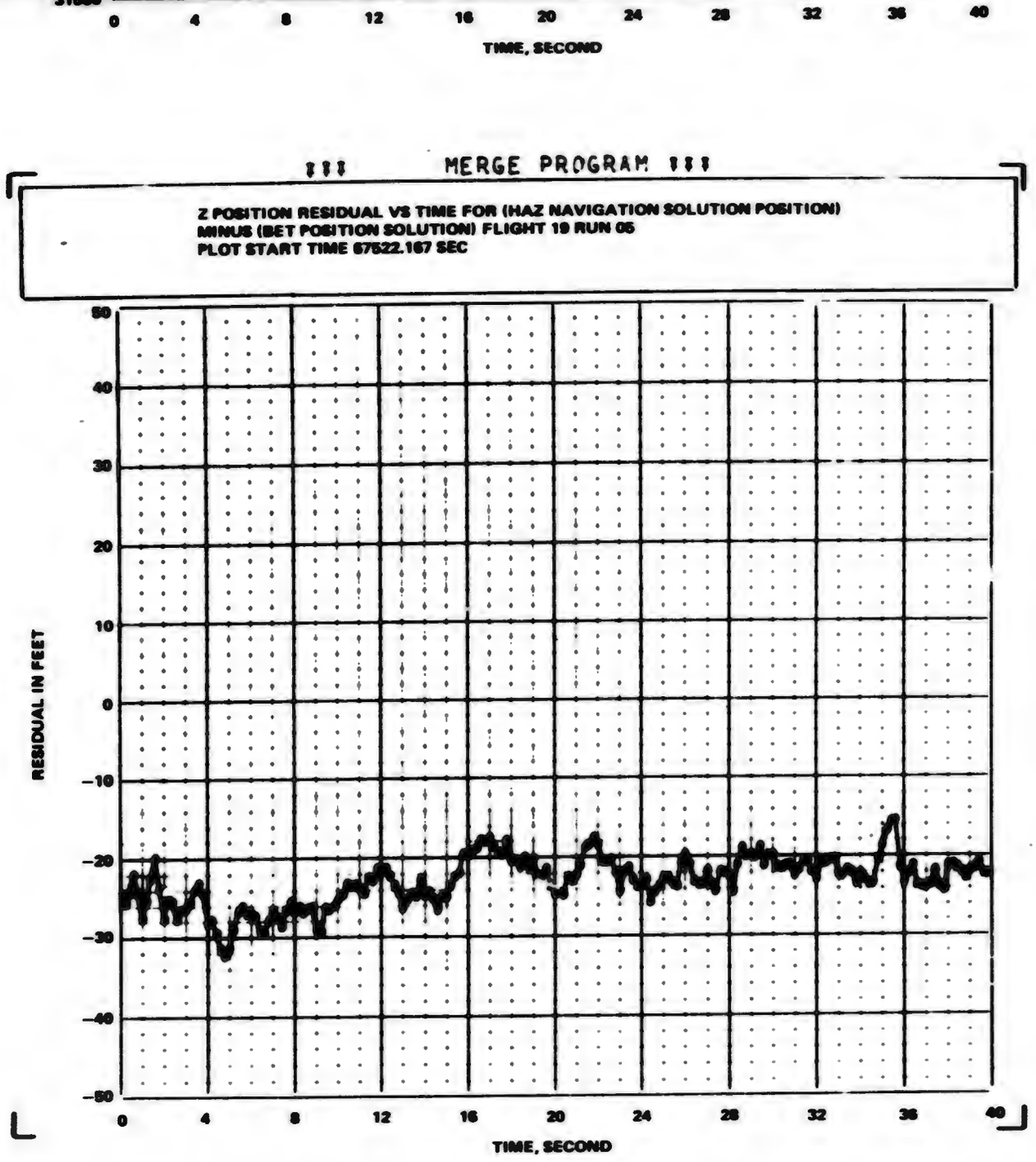

Figure 10-3 Formation of MERGE Analysis (Position)

Z VELOCITY VS TIME FOR BET SUPPLIED BY WSMR AND
HAZ NAVIGATION SOLUTION FLIGHT 19 RUN 05
PLOT START TIME 67522.167 SEC

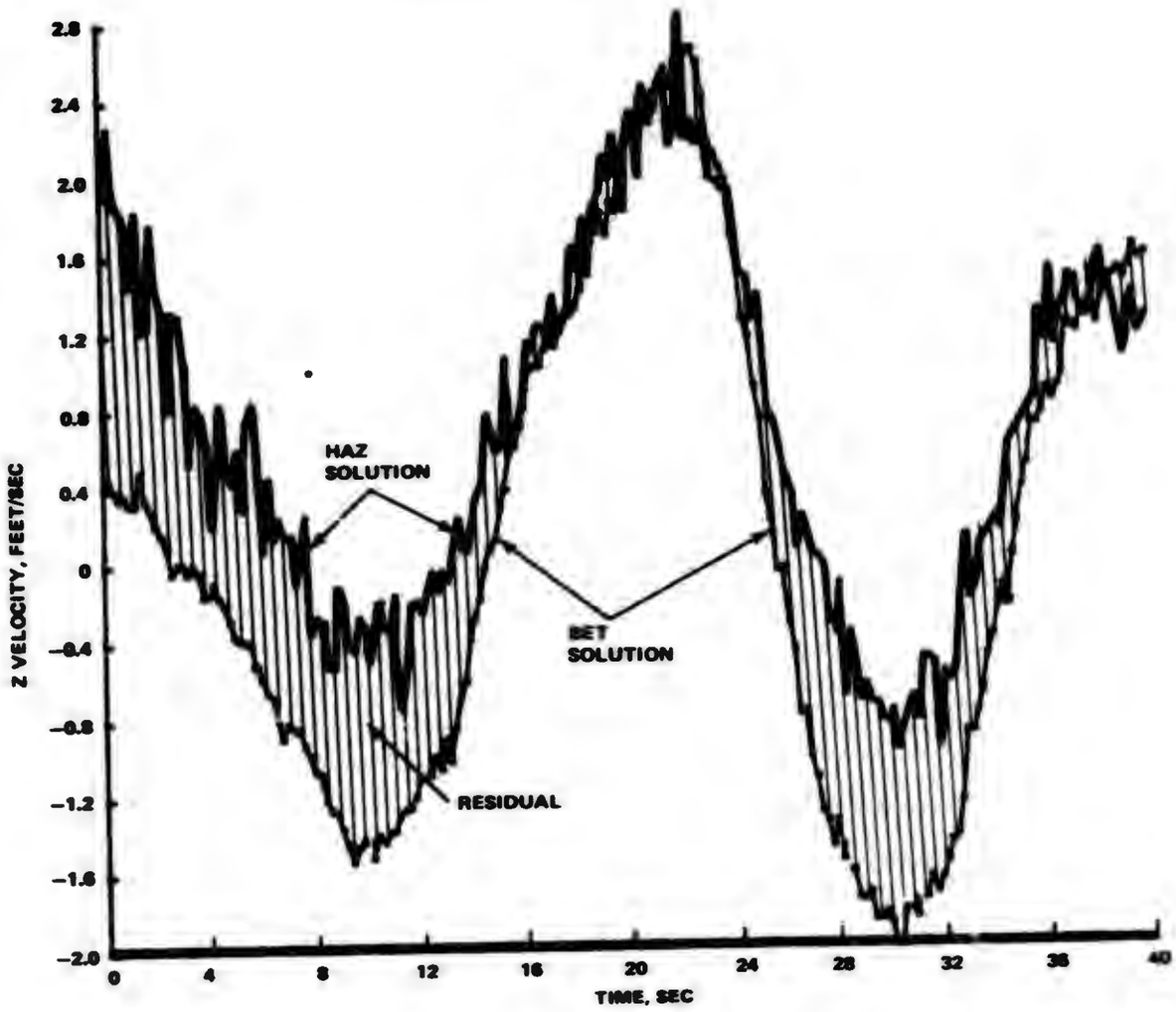

!!! MERGE PROGRAM !!!

Z VELOCITY VS TIME FOR (HAZ NAVIGATION SOLUTION)
MINUS (BET SOLUTION) FLIGHT 19 RUN 05
PLOT START TIME 67522.167 SEC

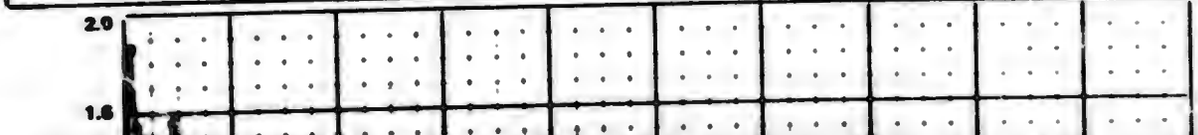

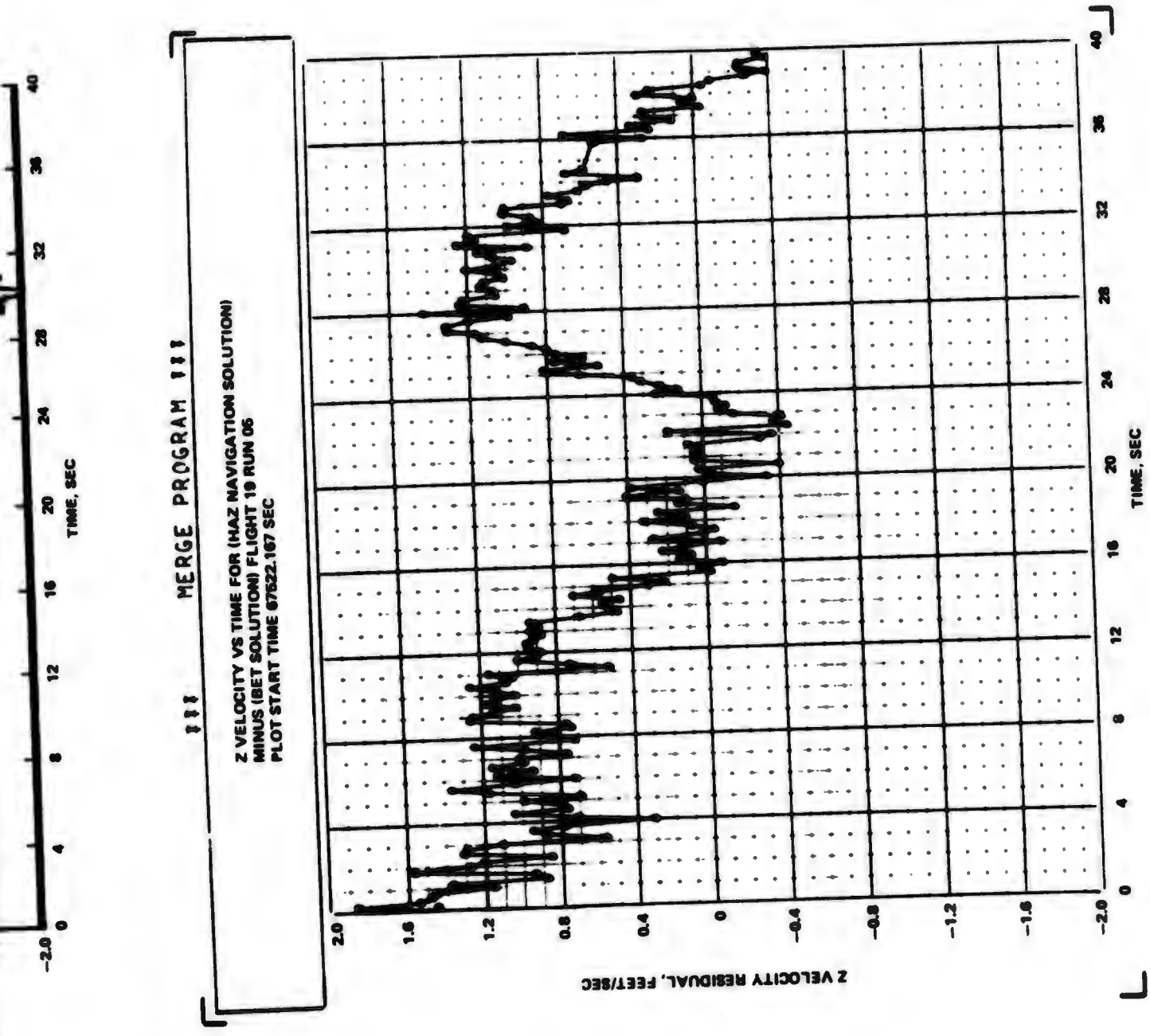

Figure 10-4 Formation of MERGE Analysis (Velocity)

BET and HAZ navigation solution; therefore its shape is not identical to, but does reflect the noise components of the HAZ navigation solution. For example, at a time of 34.5 seconds HAZ navigation solution shows an altitude increase of 9 ft in one second while the BET position curve is smooth. Therefore, the residual curve at that time reflects a decrease in the residual of 9 ft. Note that abscissa and ordinate are scaled identically for position and position residual plots.

An inspection of the velocity and velocity residual plots shows that the BET and navigation solution do not follow each other nearly as well as they did for position data. The velocity residual shows large average changes as a function of time. The large slowly varying changes in the velocity residual, Figure 10-4, appear to be related to a dynamic lag in the WSMR BET data and not to the test system.

In summary, one can conclude that the position residual data accurately reflects the performance of the navigation system and that the velocity residual reflects the noisiness of the navigation system velocity but also contains slowly varying trends which are introduced by the BET.

10.4 TOUCHDOWNS

The ILS test at Northrop Strip included two types of flight paths. On the first flight path, the aircraft flew down the 2.5^{0} glide slope to the flare point, flared, passed over the runway at a constant 100 ft AGL, then climbed back to 1100 ft AGL and repeated the "race track" pattern. This flight path was flown on flights number 24, 25, 26 and 27. The second flight path included the same approach, but the aircraft performed a touch and go instead of passing over the runway. This was done on flights 28, 29, 30 and 31.

Additional external instrumentation was used to record the position of the aircraft at the instant of touchdown. By knowing the position of the aircraft at a particular time during the flight profile, one could compare both the position as reported by the 621B navigation solution and the position as reported by the BET to the touchdown position. This third independent position was derived using the following instrumentation:

- A 250 frame per second high speed camera with a 46-in. focal length recorded the touchdown, together with IRIG B timing. The film was read by WSMR NR-A optics division to determine the instant (IRIG B time) of touchdown. We reread this film to verify time

- Five cinetheodolites tracked the aircraft on its approach, touchdown and roll out. The film from the theodolite in the area of the touchdown (G-278) was integrated by us to find position and time as a backup to the high speed camera results

- On board the aircraft, two accelerometers (one mounted within the Hazeltine receiver interface unit, the second mounted within the receiver itself) recorded changes in the "g" forces during the flight. The shock of touchdown and IRIG/B time documented the instant of touchdown

- The auto-pilot gyros recorded changes in aircraft attitude during the touchdown event. This was another check on time

- Position of the aircraft was found by observing each touchdown and making the tire tracks "footprint" of the landing gear at the instant of touchdown. After each mission, the footprint was surveyed by WSMR geodetics to within one foot accuracy (see Figure 10-5). WSMR NR-A rotated and translated the survey results into the 621B data reduction coordinate system. Once the footprint coordinate was known, the position of the 621B antenna on top of the NC-135 vertical/stabilizer was found by adjusting the surveyed position to the tail area.

The analysis flow used to make the position comparison between the BET, 621B receivers and external touchdown observations is shown below:

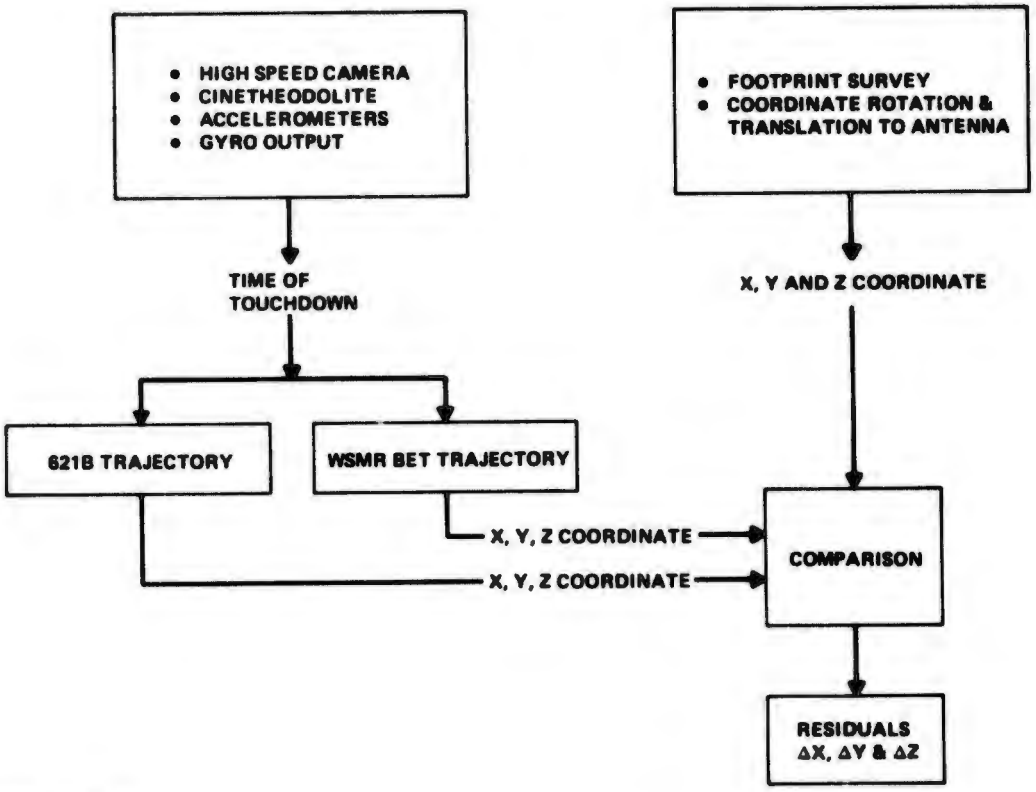

Example Case

Flight 31, flown on September 30, 1972, included seven touchdown runs on which this comparison was made. Run 2 was selected as an example for discussion.

1. The IRIG B time reported by WSMR NR-A optics branch, as a result of reviewing the high speed camera film - touchdown occurred at 16:08: 48.949. See Figure 10-6

2. We reviewed the cine film from cine station G-278 and concluded touchdown occurred between 16:08:48.80 and 16:08:49.00. See Figure 10-6. This result supports the conclusion of the high speed camera results.

3. Accelerometer and autopilot gyro outputs were examined which support the touchdown time of the high speed camera. The oscillograph traces recorded

Figure 10-5 621B Aircraft "Footprint" at Touchdown

changes in g forces and aircraft attitude at 16:49.540, approximately .600 second after the touchdown time reported by the high speed camera. The .600 second delay shows that the tire, landing gear, aircraft structure and equipment shock mounts work in series to delay the shock from being transmitted to the instrumentation. For the sake of verifying touchdown time in a general sense, the delayed recording serves its purpose. It is beyond the scope of this report to try to estimate if the .600 second delay is consistent with the theoretical dynamic characteristics of the shock transmittal train from tire to accelerometer. The gyro output shows that a change in the aircraft attitude or a pitching motion takes place after the aircraft physically touches the ground. This is consistent with the cine and high speed camera photos. The above results support the time reported by the high camera speed.

4. The surveyed position of the footprint was translated and rotated to the 621B Data Reduction Coordinate System (DRCS) by optics group of WSMR NR-A. For this case the resulting 621B DRCS coordinates were Y = - 1,879.50, X = +2.78, Z = -5.08.

5. The 621 DRCS system coordinates then had to be translated back to the aircraft tail antenna. To estimate what the Z and N corrections should be, the photo of touchdown from the high speed camera was used. The photo showed the aircraft nose wheel to be approximately 3.1 feet above ground level. This created a lever arm movement that had to be taken into account. Figures 10-7 and 10-8 illustrates the adjustments for this case. The adjusted coordinates to the 621 B antenna were Y = -1810.35, X = -9.87 and Z = +32.72 which could then be compared directly to the unfiltered 621B and BET trajectories.

6. The comparison of BET, 621B and the externally derived touchdown time and position is shown in Table 10-2.

Sources of Error

Each measurement tool used to derive the touchdown position had implicit errors. Three error sources can be estimated with reasonable assurance. They are: errors associated with use of a high speed camera to record the touchdown; inaccuracies of marking and surveying the aircraft's footprint, and errors of translation of the position given by survey to the aircraft's 621B antenna mounted on the vertical stabilizer.

The uncertainty in the determination of the time of aircraft touchdown causes an ambiguity in the comparison of touchdown survey coordinate data to 621B and WSMR BET trajectories. The ambiguity is caused by not being able to determine the "real" touchdown time to within .004 sec as originally anticipated. The camera and survey system was selected so that the aircraft's position could be calculated with an uncertainty of one foot to each of the three (x, y, and z) coordinates at one instant in time; that of touchdown. Both BET and 621B system navigation solution were estimated to have position uncertainties of 5 to 10 ft. The touchdown coordinates, therefore, could serve as an accurate position check on both the BET and the navigation solution trajectories. A high speed camera frame rate of 250 frames per second was selected so that for every foot of aircraft movement (260 fps velocity) at touchdown, we would have one frame of film. The intent was to isolate the single frame that captured the touchdown event, and therefore time tag the event with an uncertainty of .004 second, which is a Y position uncertainty of one foot. The problem with this system is that is is not possible to isolate the single frame of touchdown. This conclusion evolved when a trajectory

Cinethedolite Frame One Frame Prior to Touchdown Time: 16:08:48.800

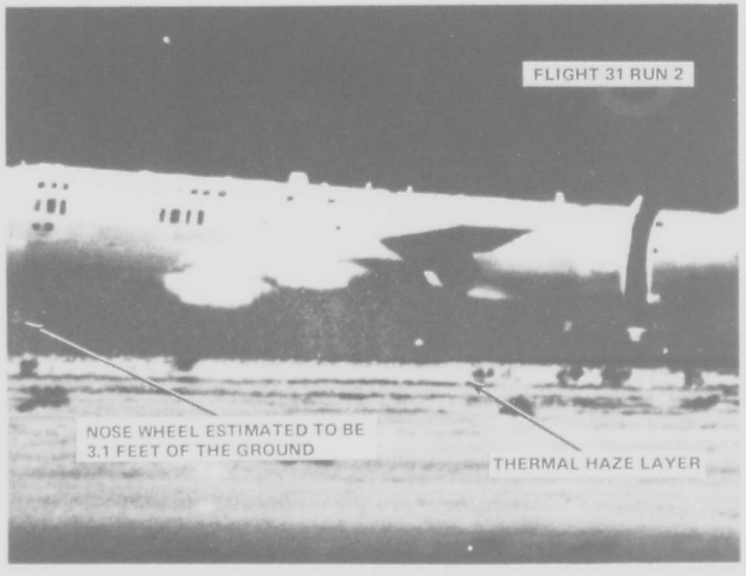

High Speed Camera Photograph of The Instant of Touchdown Time: 16:08:48.949

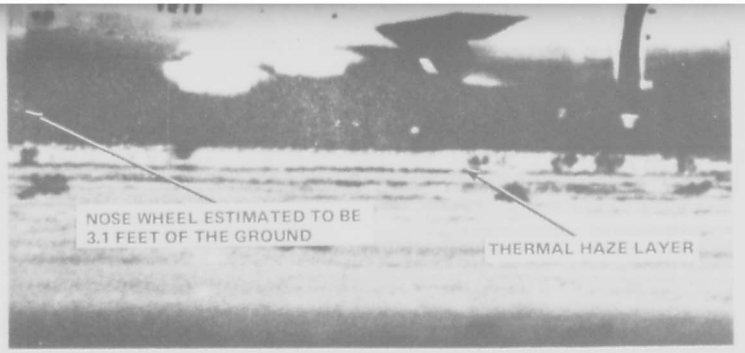

High Speed Camera Photograph of The Instant of Touchdown Time: 16:08:48.949

Cinethedolite Frame Showing Aircraft On The Runway Time: 16:08:49.00

Figure 10-6 NC-135 Touchdown at Northrop Strip

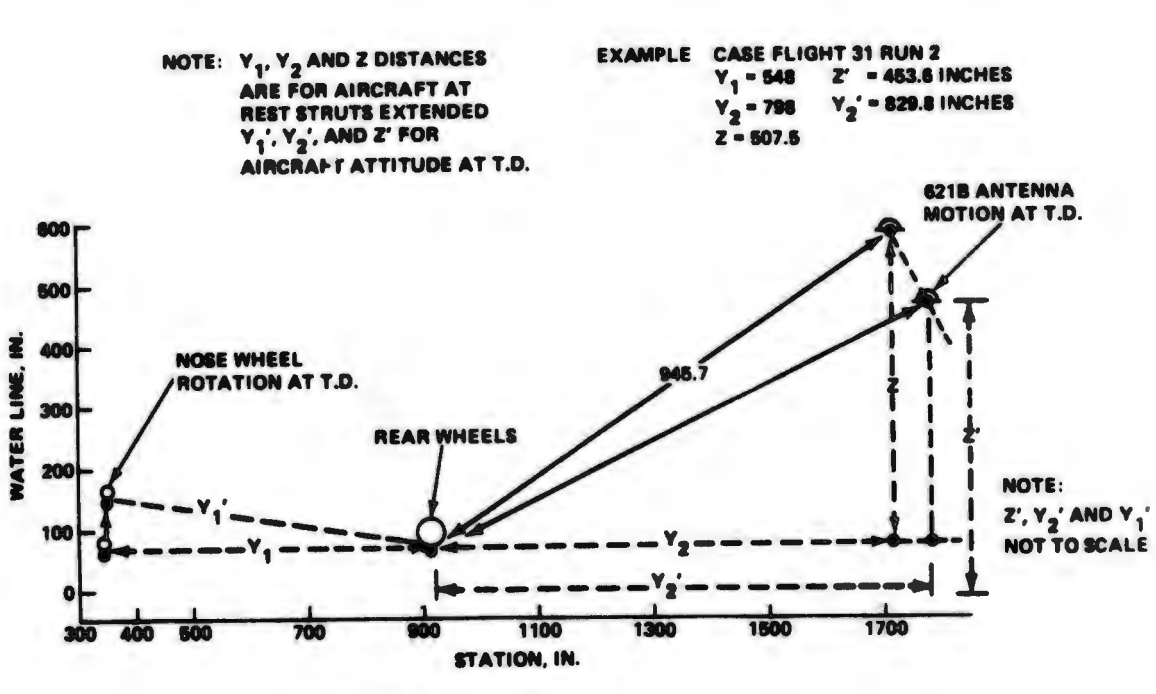

Figure 10-7 Touchdown Geometry

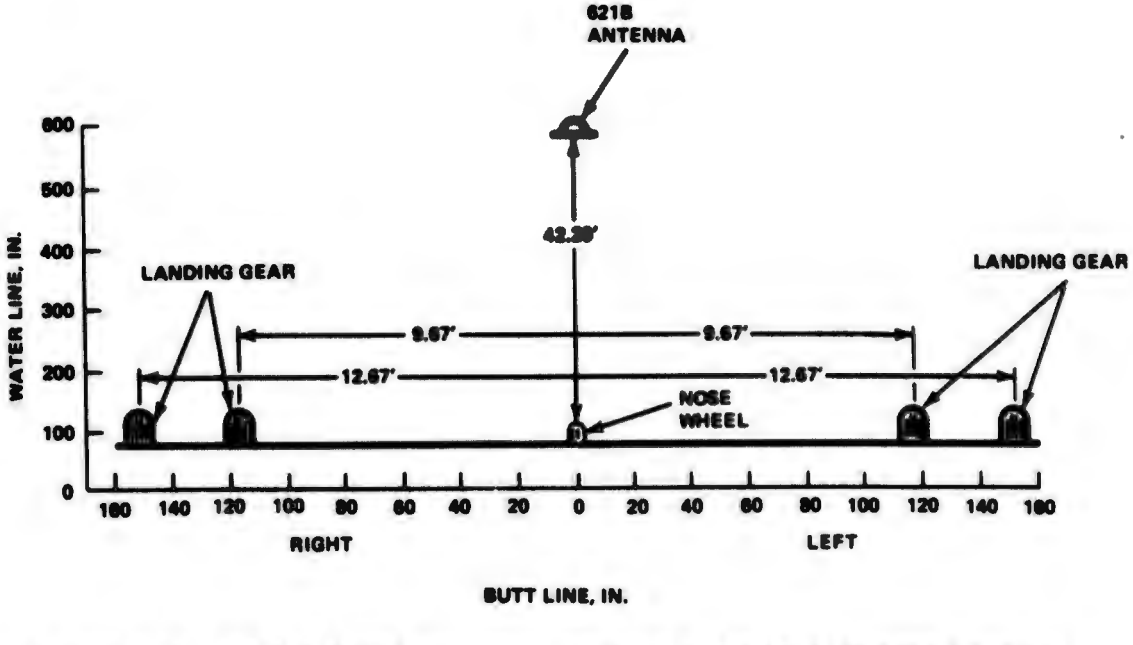

Figure 10-8 NC-135 Wheel Separation Relative to the 621B Antenna Location

Table 10-2 Coordinate of NC-135 Omni Antenna at Instant of Touchdown as Found by Survey Technique, 621 B Navigation Solution (MRL) and WSMR'S BE T

Flt/Run	Touchdown Time	Trajectories	X	Y	Z	Touchdown –MRL	Touchdown – BET	MRL–BET
Flt 29 Run 01	17:54:51.649 (64491.649	Touchdown	+ 0.15	–1500.27	+36.0	ΔX + .07	ΔX – .69	ΔX – .76
		MRL	+ 0.08	–1488.0	+35.8	ΔY – 12.3	ΔY – 14.3	ΔY – 2.0
		BET	+ 1.84	–1486.0	+36.6	ΔZ + 0.2	ΔZ – 0.6	ΔZ – 0.8
Flt 29 Run 02	18:04:23.705 (65063.705)	Touchdown	+ 5.72	–1665.86	+33.2	ΔX + .72	ΔX – 2.4	ΔX – 3.1
		MRL	+ 5.0	–1674.9	+36.0	ΔY + 9.0	ΔY – 40.9	ΔY – 49.9
		BET	+ 8.1	–1625.0	+36.4	ΔZ – 2.8	ΔZ – 3.2	ΔZ – 0.4
Flt 29 Run 03	18:13:35.732 (65613.732	Touchdown	–19.9	–1569.74	+31.81	ΔX – 0.6	ΔX + 1.4	ΔX + 2.0
		MRL	–19.3	–1591.1	+30.0	ΔY – 8.6	ΔY – 12.3	ΔY – 3.7
		BET	–21.3	–1567.4	+34.6	ΔZ + 1.8	ΔZ – 2.8	ΔZ – 4.6
Flt 29 Run 04	18:28:09:027 (66489.027)	Touchdown	–29.0	–1669.75	+31.5	ΔX + 42.5	ΔX + 1.9	ΔX – 40.6
		MRL	–71.5	–1677.9	+67.9	ΔY – 21.8	ΔY + 11.8	ΔY + 33.7
		BET	–30.9	–1711.6	+34.2	ΔZ – 36.4	ΔZ – 2.7	ΔZ + 33.7
Flt 29 Run 05	18:37:13.061 (67033.061)	Touchdown	+ 1.83	–1879.5	+32.6	ΔX – 0.2	ΔX – 0.7	ΔX – 0.5
		MRL	+ 2.0	–1840.	+29.7	ΔY – 39.5	ΔY – 21.5	ΔY + 18.0
		BET	+ 2.5	–1868.	+35.9	ΔZ + 2.9	ΔZ – 3.3	ΔZ – 6.2
Flt 29 Run 06	18:47:01.123 (67621.123)	Touchdown	– 2.92	–1779.01	+34.3	ΔX + 1.4	ΔX + 1.0	ΔX – 0.4
		MRL	– 4.3	–1763.4	+39.5	ΔY + 15.6	ΔY – 2.4	ΔY + 13.2
		BET	– 3.9	–1776.6	+37.2	ΔZ – 5.2	ΔZ – 2.9	ΔZ + 2.3
Flt 30 Run 01	15:47:55.783 (56875.783)	Touchdown	– 8.96	–1315.96	+34.6	ΔX + 0.44	ΔX + 0.14	ΔX – 0.3
		MRL	– 9.4	–1300.0	+36.9	ΔY – 15.96	ΔY – 11.56	ΔY + 4.4
		BET	– 9.1	–1304.4	+34.7	ΔZ – 2.3	ΔZ – 0.1	ΔZ + 2.2
Flt 31 Run 2	16:08:48.950 (58128.950)	Touchdown	– 9.9	–1810.4	+32.8	ΔX – 9.3	ΔX – 7.2	ΔX + 2.1
		MRL	– .6	–1802.5	+34.7	ΔY – 7.9	ΔY – 11.6	ΔY – 3.7
		BET	– 2.7	–1798.81	+36.8	ΔZ – 1.9	ΔZ – 4.0	ΔZ – 2.1

comparison was done using the touchdown times reported by WSMR. We found the difference in position at touchdown between both the navigation solution and BET as compared to the survey position was in the order of 100 ft in Y axis coordinate. We then reread the same high speed camera film that was read by WSMR and found a thermal distortion layer present on the surface of the airstrip that caused the film reader to misjudge the instant the landing gear touched the airstrip surface (see Figure 10-6). The correction for this problem was to measure the depth of the landing gear tire penetration into the haze layer when there was no question, that the aircraft was down on the surface of the runway, then go back to the point on the film where this measured depth first was noticed. We called this the point of touchdown. Flights 29 and 30 were corrected in this manner. (Flight 31 high speed camera film was not available). However, since the quality of the image on the high speed camera film was less than desired, we could identify ten frames that bracketed the touchdown event, but could not tell which of the ten frames was touchdown with any measure of confidence. The time uncertainty is not .004 second as anticipated but is .040 second, or 10 ft uncertainty in the Y axis comparison. X and Z are not affected measurably because of the low velocities in those axis.

A larger "human" error could develop if the film reader time-tagged the wrong set of landing gear touching the ground. This effect is diminished because both left and right landing gears were visible at touchdown based on the high speed cameras orientation to the touchdown area. Fortunately, the right or left gear but not both made contact with the airstrip at the instant of touchdown. Separation between right and left gear touchdown footprints ranged from 20 to 700 ft as determined by the tire impressions for most cases.

A check on gross errors of touchdown time as determined by the high speed camera was the cinetheodolite film from G-278 shooting at five frames per second. This allowed the touchdown to be bracketed to within .200 second. Cine film was not used to supply the absolute time of touchdown by itself, but only as a check on the high speed camera results. Thus it introduced no error into touchdown position determination.

In addition to the cine film, accelerometer and gyro output was reviewed. Since the purpose of this check was to support the touchdown time no effect on the accuracy of the touchdown coordinates was introduced.

A second error source was the marking and survey of the aircraft foot print. Each touchdown was marked between passes of the flight. After 20 touchdowns, it was difficult to determine which tire impression was which. Steps were taken to minimize this error, but the possibility still exists that the wrong tire impression was marked and surveyed. It is believed such a mistake would contribute greater errors than 20 ft in Y, because of the touchdown separations. It is impossible to accurately estimate such an error. The survey of each touchdown has uncertainties of plus or minus 6 in. in X, Y and Z because of the survey techniques used. This error could impact the final touch down results by ±.5 ft in X, Y and Z. The uncertainty of the marking method used by the ground observers to mark the touchdown point is ±.5 ft in X and Y, 0 in Z. The total error associated with the marking and survey is ±1.0 ft in X and Y, .5 ft in Z. See Figure 10-5.

A third error source comes from the fact that the coordinates of the 621B antenna mounted on the vertical stabilizer had to be calculated based on the aircraft attitude at touchdown. The aircraft antenna is the target that is tracked by the 621B system and

BET during ILS flights. The survey coordinates of the landing gear footprint had to be translated back to the aircraft antenna to make a valid comparison with 621B and BET position solution. The error was introduced when the aircraft attitude had to be estimated from the high speed camera photos. Nose wheel height above the ground was used as an estimate of the aircrafts attitude at the instant of touch down (see Figure 10-6). It is possible to be in error by approx. .75 ft in reading the nose wheel elevation based on numerous attempts at photo scaling. The .75 ft error at the nose wheel translates to an uncertainty of 1.1 ft in Z, .68 ft in Y and 0 ft in X for the aircraft antenna position.

In summary, three error sources can dilute the accuracy of the touch down position. The magnitude of the estimated error possibilities are as follows:

Source	Possible Error Magnitude, Ft	Coordinate
High Speed Camera Film Reading	± .5	X
	±5.0	Y
	±.5	Z
Marking and Survey of Foot Print	±1.0	X
	±1.0	Y
	±.5	Z
Coordinate Adjustments	± 0	X
	±.68	Y
	±1.1	Z

The root-sum-squares for the above error sources are:

RSS(X) = 1.12 ft

RSS(Y) = 5.17 ft

RSS(Z) = 1.31 ft

The uncertainty of the touch down coordinate can be assumed to be in the order of ±6 ft for Y and ±2 ft for X and Z assuming the aircraft did not roll or yaw during touchdown. This assumption is supported by review of touchdown films.

Results

A comparison of coordinates which resulted from this study is presented in Table 10-2 for Flights 29 and 30. A definition of the various parameters follows:

- Touchdown - The aircraft omni antenna coordinate as calculated from the surveyed landing gear tire impression presented in 621B data reduction coordinate system (621B DRCS, see Volume II, Section 3.3)

- MRL - The ILS unfiltered navigation solution trajectory resulting from Magnavox Research Lab's Airborne receiver data; the X, Y and Z coordinates are for touchdown time

- BET - WSMR BET of the NC-135 aircraft omni antenna. The X, Y and Z coordinates are for touchdown time.

An inspection of Table 10-2 shows that for Flight 29, runs 02, 04 and 05, the residuals are extremely large compared to the mean values. Flight 29, Run 02, for example, has Touchdown - MRL residuals of Y = 9.0 ft Touchdown - BET Y = 40.9 ft, MRL - BET Y = 49.9 ft which shows good agreement between MRL solution and touchdown pointing to the aircraft BET as being questionable for that portion of the run (around touchdown). A review of the WSMR BET shows that for Flight 29, Run 02, only two cinetheodolites were used to generate the BET and these were located on the same side of the runway. This makes for a poor geometry and supports the indication of the residuals that the BET is questionable at that point in the run.

A similar comparison can be done for Flight 29, Run 04. The residual for that run shows both Touchdown - MRL and MRL-BET to be relatively high, but Touchdown-BET residual is low indicating that the balloon position, or the MRL solution or both can be in error while the aircraft BET seems to be valid.

An investigation of the BET for the aircraft and balloon for Flight 29 Run 04 showed the probability is high that the BET on both aircraft and balloon is valid which support the assumption that the MRL solution is questionable for Flight 29, Run 02 near touchdown.

Below is a listing of the mean and standard deviation of the residuals in Table 10-2. "Wild" points such as described above have been omitted, since it is felt such large deviations with a small sample size would unfairly weight the mean.

Statistics of Residuals

	X (N)	Y (N)	Z (N)	$\hat{\sigma}_{\Delta X}$	$\hat{\sigma}_{\Delta Y}$	$\hat{\sigma}_{\Delta Z}$
Touchdown - MRL	+3.06 (6)	-3.35 (6)	-1.04 (7)	.71	12.6	2.8
Touchdown - BET	-.810 (8)	-6.73 (6)	-2.45 (8)	2.9	9.9	1.4
MRL-BET	-.709 (7)	+1.64 (5)	-1.37 (7)	1.6	7.2	3.2

N = number of data points used to determine mean and standard deviation.

Figures 10-9 and 10-10 are plots of the residuals shown in Table 10-2 with "wild" points omitted. From the data, two basic observations can be made:

- The MRL, BET and Touchdown data generally are within 10 ft of each other.

- Using the t distribution because of the small sample size and unknown standard deviation of the universe, we can estimate the confidence interval for the touchdown residual population means as follows:

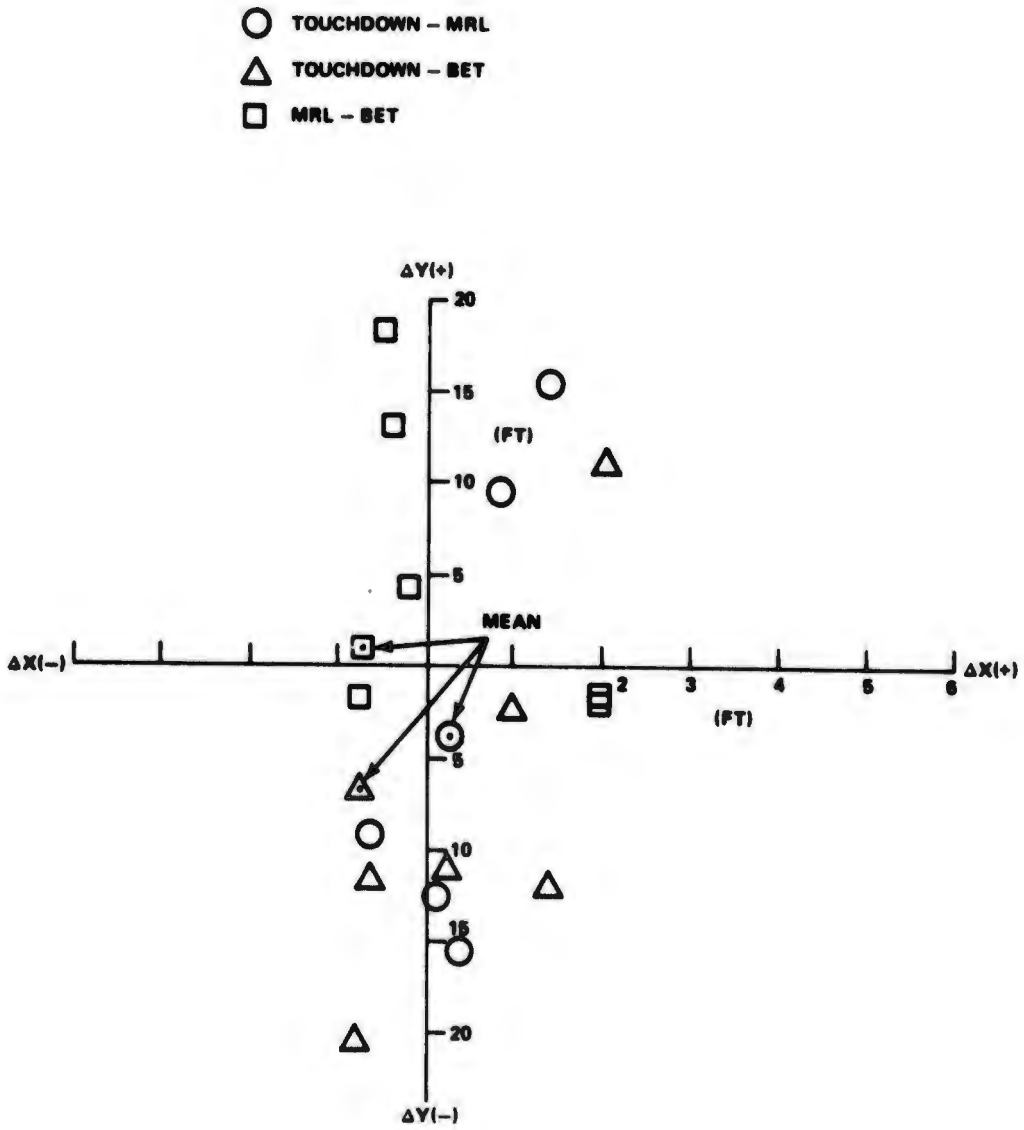

Figure 10-9 Residuals of Touchdown, BET and MRL Navigation Solution ΔY vs ΔX

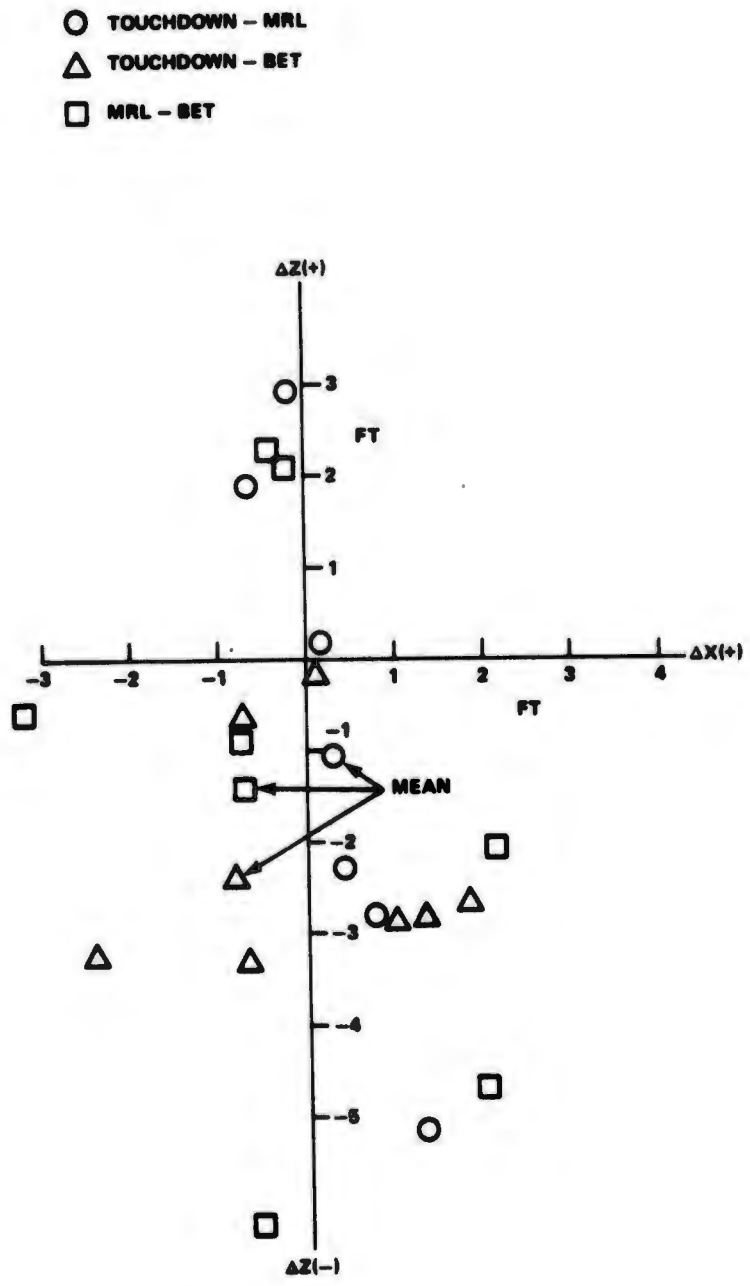

Figure 10-10 Residual of Touchdown, BET and MRL Navigation Solution ΔY vs ΔX

Prob. $(\Delta\bar{X} - t_{0.025}\hat{\sigma}_i/\sqrt{N} \leq \bar{X}' \leq \Delta\bar{X} + t_{0.025}\hat{\sigma}_i/\sqrt{N}) = 0.95$
where $\Delta\bar{X}'$ is the mean of the universe and $t_{0.025}$ is the 0.025 point of the t distribution for N-1 (degrees of freedom)

The confidence intervals are:

$2.571\ (\frac{0.71}{\sqrt{6}})$ for $\Delta\bar{X} \approx \pm 1.0$ ft (-.695, 1.305) for X

$2.571\ (\frac{12.6}{\sqrt{6}})$ for $\Delta\bar{Y} \approx \pm 14$ ft (-17.35, 10.65) for Y

$2.447\ (\frac{2.8}{\sqrt{7}})$ for $\Delta\bar{Z} \approx \pm 3$ ft (-4.04, 1.96) for Z

The extremely close agreement of the X coordinate values for the three solutions indicate a high degree of confidence (95%) that the data is in an interval of ±1.0 ft about the mean. The Z coordinates are in an interval of ±3 ft about the mean with the same confidence factor. The Y coordinate, however, shows more scatter which opens up the 95% confidence interval to ±14 ft about the mean.

The touchdown study has proven to be a useful tool in evaluating the navigation system performance and WSMR BET for the ILS testing.

SECTION XI

CONCLUSIONS AND RECOMMENDATIONS

11.1 GENERAI CONCLUSIONS

The test program successfully met the principal objective of evaluating a four channel receiver in typical flight and field environments, and confidence in the 621B concept was verified through the actual tests performance. Analysis of the error componerts indicates that a small average range measurement difference of about 2 ft still exists between the WSMR best estimate of trajectory (BET) and the 621B trajectory. The range rate measurement errors were less than one foot per second.

Several observations can be made about the system behavior. Perhaps the most important of these is that ranging bias errors (steady state errors) are extremely difficult to measure and control. Almost all of the error mechanisms have been determined through analysis of the data, and it has become clear that great care must be exercised during design and manufacturing to control signal delay variability throughout the system to the one or two nanoseconds required to achieve a 2 ft ranging accuracy. However the steady state bias errors proved to be the biggest problem.

The ILS testing conclusively demonstrated the suitability of the system in an aircraft landing environment. The mean error for vertical position was about 1.5 ft and for vertical velocity less than 0.5 fps. These are representative of absolute errors obtainable with a filtered solution. This quality of system performance is more than adequate for landing and the test results indicate that the signal environment (large changes in power and multipath effects) during this phase of aircraft operation do not appreciably degrade the navigation accuracy.

The test program confirmed that the performance of the receiver in the presence of multipath typical of ground user operation matches the theoretical predictions of the system behavior; hence the effect is well understood, can be predicted and will have little impact on a ground user.

11.2 AREA NAVIGATION CONCLUSIONS

The test system accuracy was demonstrated including the effects of user dynamics and multipath. The fast changing relative transmitter-to-user geometry in the limited flight test region simulated some of the effects of user dynamics (like accelerations of 0.5g and jerks of 0.3 ft/sec^3). In addition normal yaw maneuvers made by the pilot to maintain a straight and level flight trajectory resulted in user dynamics of the order of 0.5g and 3 ft/sec^3. On descent passes both yaw and pitch maneuvers were experienced resulting in dynamics of the same order of magnitude.

Most of the significant error sources we identified were associated with the ground system. For example, the results of flights 1-15 were degraded by uncontrollable variations in the calibration link delay (variations were nominally 15 nanosec).

During subsequent flights, i.e., 17-23 the calibration links shared the common shaped beam antennas driven by the uplink transmitter ports and the delay variation of the transmitters was eliminated.

With this large error source removed other error sources previously overshadowed were discovered. One such major discovery was the apparent signal delay variation with look-angle of the uplink antennas. This phenomenon was found to affect both the calibration and ground-to-user links. The remaining error sources in the calibration setup which were identified include cesium propagation delay measurement residual uncertainties, cable termination (VSWR) and rf leakage effects, tropospheric correction residuals, cable delay variation with temperature and delay variation in power dividers. All these error sources are discussed in Section 4.

Sources of bias errors identified in the flight system include receiver interchannel bias variation with power level, channel bias variation as a function of transmitted waveshape and specular multipath interference.

Table 11-1 summarizes the area navigation system performance as measured by the two receivers. It represents the errors that user equipment can be expected to contribute to the overall system performance in an operational environment, since all the identified errors associated solely with the ground test configuration have been removed.

Table 11-1 Summary of Contributions of User Receiver Performance to Navigation System Accuracy

	CASE 3			CASE 3	
	MEAN	1σ		MEAN	1σ
X, FT			$\dot{X}$, FPS		
HC	-1.0	5.8	HC	0.1	0.6
MRL	-2.3	6.1	MRL	0.1	0.5
Y, FT			$\dot{Y}$, FPS		
HC	0.4	10.3	HC	-0.1	0.6
MRL	1.3	8.2	MRL	0.2	0.7
Z, FT			$\dot{Z}$, FPS		
HC	-4.1	12.0	HC	0.3	0.6
MRL	1.6	8.5	MRL	-0.5	0.9

11.3 ILS CONCLUSIONS

This phase of the test program evaluated the landing navigation capabilities of the system. The ground calibration setup in the ILS flights utilized omni directional antennas which were common to both the calibration links and to the ground-to-aircraft links, and thus eliminated cable delays and other rf circuitry problems.

In order to keep the altitude GDOP at a minimum during touchdown, the GDOPS during the initial approach and rollout phases of the flight become quite large, which results in a substantial magnification of the measurement errors into the static solution domain. Thus, for purposes of determining 621B suitability for ILS, the region of primary interest corresponds to the span on the approach path from where the aircraft is approximately 300 ft above ground to the point where the aircraft is braking on the runway.

Table 11-2 summarizes the ILS system performance as measured by the two receivers. In general, we conclude that system performance is commensurate with ILS requirements.

Table 11-2 ILS Navigation Accuracy

	MEAN	1σ		MEAN	1σ
X, FT			$\dot{X}$, FPS		
HC	0.3	3.3	HC	0.2	1.1
MRL	−1.1	7.3	MRL	0.2	1.4
Y, FT			$\dot{Y}$, FPS		
HC	−2.7	11.4	HC	−0.5	1.7
MRL	2.2	12.3	MRL	−0.2	2.2
Z, FT			$\dot{Z}$, FPS		
HC	−1.3	13.3	HC	−0.2	2.3
MRL	−1.3	8.3	MRL	−0.4	2.0

11.4 MULTIPATH CONCLUSIONS

The overall objective of the multipath test was to evaluate the sensitivity of System 621B accuracy to multipath signals. Multipath signals degrade the ranging accuracy of the receiver by creating a distortion of the modulation envelope of the total received signal. This phenomenon develops an error in the receiver code tracking loop which affects the range accuracy. If the user is moving with respect to the transmitters the range rate accuracy is also affected. In this case the error in the carrier tracking loop is caused by the rate of change of phase of the resultant signal consisting of the direct and multipath reflected signals. This latter effect was not simulated in the ground multipath tests, since the tests were performed under static conditions.

The test sites selected encompassed a variety of terrain features representative of those that may be encountered by a typical ground based user.

The multipath tests conducted at WSMR consisted of a series of measurements using various transmitter-to-receiver antenna geometries at four separate multipath environments. The overall results of these tests indicate that the theoretical understanding of multipath effects on range accuracy is verified by the experimental results. The theoretical envelope of range tracking error as a function of multipath expressed as the differential delay between the desired and interfering signals is shown in Figure 11-1.

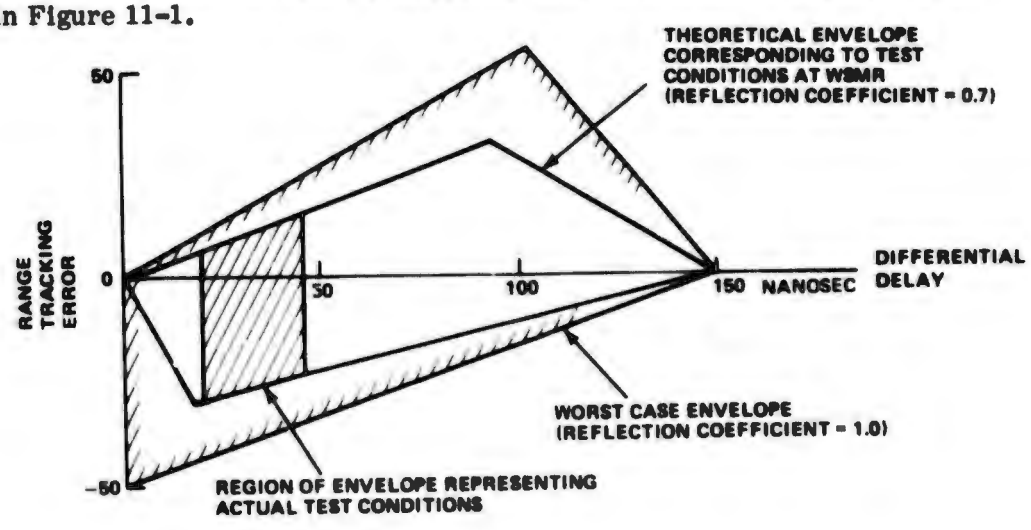

Figure 11-1 Theoretical Evnelope of Range Tracking Error Caused by Signal Multipath

Receiver ranging errors can take on any value within this envelope depending upon the exact signal differential delay. The test data follows this prediction as shown in Figure 11-2. This figure shows all the data collected at the Northrop Strip location and is typical of the receiver performance at the other test sites. The theoretical envelope superimposed on this figure contains virtually all of the test data. The few points which fall outside of the envelope are a result of uncertainty in the true transmitter position and therefore, uncertainty in the value of differential delay determined from the transmitter-to-receiver geometry.

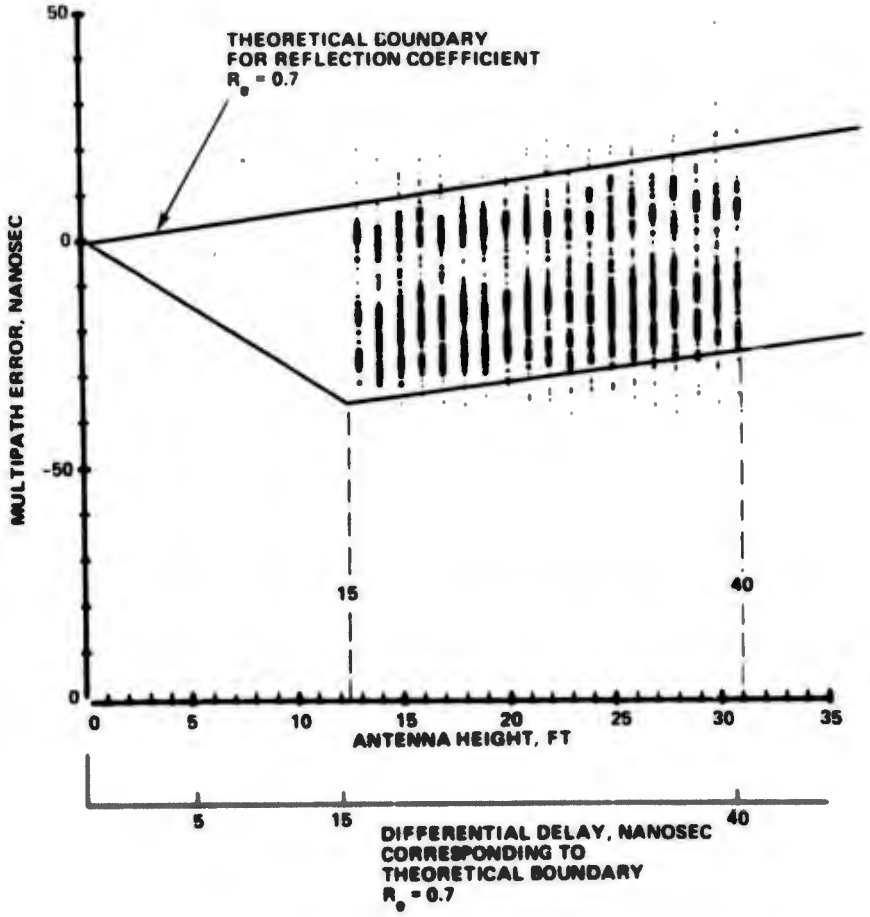

Figure 11-2 Multipath Measurement Results

The test program has demonstrated that multipath effects on receiver performance are understood and are therefore predictable. A ground user on the average can experience as much as ±25 feet of multipath error depending on the exact system geometry. However, the differential delay sensitivity of the satellite-to-ground user geometry is only a function of the user antenna height above ground. This allows the ground user to determine the presence of multipath by changing his antenna height and to then locate himself in low multipath error environments.

11.5 RECOMMENDATIONS

The following recommendations are based upon analysis of the flight test results, the practical and theoretical experience gained during the executions of the tests, and laboratory evaluation by Hazeltine of candidate equipment designs. They represent those considered most important in improving the pseudo-ranging navigation system performance.

Phase Lock Loop and AGC Design

In the equipment developed by Hazeltine, the PLL's (phase lock loops) are analog adaptive designs. The tracking circuits bandwidths widen as signal strength increases. This design automatically accommodates higher dynamics (second and higher order time derivatives of range) as the signal level increases above the designed performance threshold. In this way, the antijam margin is held fixed for a fixed level of jamming power.

An alternate approach is to fix the tracking circuit bandwidth at that required for the weakest signal specified.

We recommend the fixed-bandwidth approach because:

(a) it is not necessary to widen the tracking circuits bandwidths to accommodate dynamics

(b) jamming resistance intrinsically improves with increased signal level

(c) abrupt signal level changes (as due to short obscuration of a satellite, multipath, and pulse jamming signal suppression in gain modulated or saturated stages) should theoretically induce smaller tracking transients, than in a variable bandwidth receiver.

(d) averaging effects of scintillating multipath signals makes the receiver less sensitive to multipath.

It has been demonstrated by the flight tests at HAFB that stable third order PPL's can be designed for either variable or fixed bandwidth receivers. We would, however, recommend that future receivers be designed with digital loops and constant bandwidth.

Frequency Management Within the Receiver

Two points are made concerning the selection of frequencies inside the receiver. One, any IF signal should not be harmonically related to the code rate, as the reference code and related timing waveforms are rich in harmonics (and, often coherent with the signals). Second, processor designs generally require a wide band reference waveform to be multiplied by the wide band signal; the center frequencies of these must be sufficiently high and separated to prevent spectrum foldover or overlaps. If not, the output product is disturbed by undesired cross products which may be coherent (or conditionally coherent), leading to degraded ranging accuracy.

EMI Considerations Within the Receiver

In addition to correctly selecting frequencies within the receiver to minimize harmonic or cross product interference, special attention to control of conducted, coupled and radiated energy is essential in circuit areas where the desired "nulled" output (e.g., at the phase detector of a carrier PLL or early-late demodulator of a code PLL) can be contaminated by very low levels of interference; levels of 60 to 80 dB below the detector/demodulator reference signal input can cause a measurable error. Care must be exercised in this area, particularly as the area/volume allocated to such functions is reduced to meet miniaturization goals.

Range Digitizer

Two methods of digitizing may be employed in the receivers. One provides range and range rate outputs on demand while the other provides data updates only at specific intervals. The "on-demand" approach minimizes receiver/computer interface problems and is therefore recommended.

Recommended Follow-on Development

- Determine techniques which can be incorporated in the user equipment for detecting significant range tracking errors induced by multipath.

- Determine the effects on system performance of oscillators contained in user equipment subject to vibration and shock and develop techniques for maintaining adequate performance.

- It is suggested that the direct approach be applied to design of digital receivers rather than the digital-analog-equivalence approach. The benefits of the direct approach can be better performance per dollar, and, with the inevitable use of LSI and lessening distinction between receiver and computer, more sophisticated processing is practical than would be realized via the analog route.

- Our experience at the range leads us to recommend that in future test programs the links be calibrated by a two-way ranging system. Such a technique was considered early in this program, but was not implemented. One most interesting system proposal involves the use of two 621B receivers at different locations on the range. This concept not only has intrinsic merit, but also has the side benefit that once the links are calibrated, the system could be run continuously for a few days under varying ground conditions (reflection coefficients) to determine if there is multipath on the link, and more importantly, if it is varying.

- Recommend careful analysis of test equipment requirements so that better equipment can be developed to obviate the measurement problems encountered during this program.

SECTION XII

REFERENCES

1. Final Report, 621B User Equipment Definition and Experiment Program Phase I, Vol. IV, SAMSO TR 70-440, Dec. 1970.

2. Ackerman, R., Hraban, S., and Kadar, I., "An Annotated Description of the System 621B Navigation Algorithms and the Two State Kalman Filter", Grumman IOM Number 621B-181, Feb. 28, 1972.

3. Technical Report, SAMSO-TR-72-213, Dec. 1972.

4. Operating and Maintenance Manuals for 621B Experimental Equipment, Vol. II, III and IV.

5. Operating and Maintenance Manuals for 621B Experimental Equipment, Vol. V and VI.

6. Introduction to White Sands Missile Range, White Sands Missile Range, New Mexico 88002, Apr. 1, 1968.

7. California Bearing Ratio Tests, Conducted at Northrop Strip, 1972, and Report No. AFWL-TR-66-148, Landing Site Evaluations, Appendix 1, Site 81, White Sands, N.M., L.M Womack and J.T. Lewis, Feb. 1967.

8. Operation Requirement 621B User Equipment Tests and Demonstrations 49201 through 49208.

9. 621B Ground Transmitter Site Survey Requirements for System Demonstration Tests, 621B-158, M. Neglia.

10. 621B Program Antenna Points for Salt Site, Survey No. 189-72, Mr. Beckett/ SY/3718, Feb. 24, 1972.

11. 621B Program Antenna Points for EC-50 Site, Survey No. 116-72, Mr. Beckett/ SY/3718, Feb. 24, 1972.

12. 621B Program Antenna Points for Bomb Site, Survey No. 190-72, Mr. Beckett/ SY/3718, Feb. 24, 1972.

13. 621B Program Antenna Points for WC-50 Site, Survey No. 185-72, Mr. Beckett/ SY/3718, March 6, 1972.

14. 621B Program Antenna Points for Corner Site, Survey No. 184-72, Mr. Beckett/ SY/3718, Feb. 24, 1972.

15. Coordinate Systems Related to WSMR, Data Reduction Division, WSMR New Mexico, July 1964.

16. Comprehensive Survey Report for 621B, No. 700-72, Mr. Beckett/SY 3718, September 15, 1972.

17. Survey Data for 621B Program, Survey No. 829-72, Mr. Beckett/SY/3718, Oct. 20, 1972.

18. Re-Survey of 621B Program Antenna Points, Survey No. 610-72, Mr. Beckett/SY/3718, August 15, 1972.

19. Antenna Height Selection for the Calibration Links, GAC IOM - 621B-73 Apr. 20, 1971 Kadar, I.

20. General Test Plan, 621B, June 11, 1971.

21. Cox, James M. Dayton Municipal Airport ILS RWY6L CAT II Approach Plate Dayton, Ohio.

22. Fried, W.R. and Kayton, M., "Avionics Navigation Systems", Chapter 14, 1969 John Wiley & Sons Inc.

23. 621B Utilization of an Optical Landing System for Repeatable Glide Slope Trajectories, 621B-61 March 23 1971, M.S. Moore.

24. The WSMR Best Estimate of Trajectory - An Overview, Internal Memorandum No. 129, January 1972, prepared by Data Reduction Division, Math Services Branch, White Sands Missile Range, New Mexico, 88002.

25. 621B Software Documentation Library, Grumman IOM Number FAD-07-711-IOM-72-12, April 26, 1972, Richards, P. et al.

26. Richards, P., "The Variate Difference Method of Variance Estimation with Application to 621B Trajectory Data", Grumman Systems Flight Test Technical Report Number SFT-TCR-71-4, October 8 1971.

27. "Richards, P., "Two State Bias Filter Implementation for 621B Flight Test Program", Grumman Systems Flight Test Technical Report Number SFT-TCR-72-2.

28. Agee, Wm. S., "Matrix Square Root Formulation of the Kalman Filter Covariance Equations", The Office of the Chief of Research and Development, Durham, N.C., ARO-D Report 70-1.

29. Fridland, Bernard "Treatment of Bias in Recursive Equations", IEEE Transactions on Control, Oct. 68.

30. Agee, Wm. S., "Exponentially Weighted Variate Differences (A Technique for Real Time Variance Estimator)", WSMR, NM, STEWS-NR-AM, 27 Aug. 70. Technical Report No. 16.

31. Martinez, R. S., Peters, G., Wilkinson, J. H., "Symmetric Decomposition of Positive Definite Matrix", Numerische Mathematik, Bund 7, p. 362-383, 1965.

32. Kadar, I. and Richards P. "621B Best Estimate Trajectory Errors", Grumman Inter-Office Memorandum Number 621B-188 dated June 7, 1972.

33. P. Richards, "Deterministic Navigation Software for System 621B Field Tests", FAD-SFT-TN-71-1, 29 February 1972.

34. I. Kadar, "A Note on the 621B Navigation Algorithm", GAC IOM 621B-176, 2 February 1972.

35. I. Kadar, "Bias Shift Sensitivity of Navigator Position", GAC IOM 621B-184, 20 April 1972.

36. Theory and Applications of Kalman Filtering, AGARDograph 139, Edited by C. T. Leondes, February 1970.

37. I. Kadar, "General Signal Design and Systems Considerations for Navigation Satellites and Links", RFR, 1972.

38. P. Beckmann and A. Spizzichino, The Scattering of Electromagnetic Waves from Rough Surfaces, Pergamon Press 1963.

39. Christensen, R., Capt USAF (Staff Met.), "Index of Refraction Variability at White Sands Missile Range, New Mexico, in Support of Project 621B", 6585th Test Group, Holloman Air Force Base, N. M. July 1, 1972.

40. U. S. Army Manual, CCTM 105-50, Part 3.

41. K. Bullington, "Radio Propagation Fundamentals", Bell Laboratories Report, 1956.

42. A. Papoulis, Systems and Transforms With Applications in Optics, McGraw Hill, 1965.

43. A. G. Longley and P. L. Rice, "Prediction of Tropospheric Radio Transmission Loss Over Irregular Terrain", ESSA, ERL 79-ITS67, July 1968.

44. I. Kadar, "Ground User Multipath Test Procedure for 621B Experiment Program", GAC Report 621B-TP-5, July 1971.

45. J. R. Lundien, "Terrain Analysis by Electromagnetic Means", Technical Report No. 3-693, U. S. Army Material Command, Sept. 1966.

46. Final Report - System 621B User Equipment Definition and Equipment Program, Phase I, Vols. I, II, III, & IV, SAMSO TR70-440, Dec. 1970.

47. R. H. Ott and G. A. Schiak, "Backscattering from Rough Terrain", ESSA RL 60-ITS 57, Sept. 1967.

48. S. H. Durrain and H. Staras, "Multipath Problems in Communications Between Low Altitude Spacecraft and Stationary Satellites", RCA Review, May 1968.

49. A. B. Glenn, "Fading From Irregular Surfaces for Line-Of-Sight Communications", IEE Trans. on AES, Vol. AES 4, Mar. 1968.

APPENDIX A

SENSITIVITY CONTOURS FOR UNITY MEASUREMENT ERRORS

APPENDIX A

SENSITIVITY CONTOURS FOR UNITY MEASUREMENT ERRORS

This appendix contains contour maps of the navigation solution sensitivity to steady-state measurement errors in the individual channels for both the Area Navigation and ILS test geometries. The maps are generated by introducing a 1 ft error into a pseudo-range measurement channel and performing a perturbation analysis similar to that discussed in Section 4.2 for planar regions at selected heights above ground level for both test geometries. To use the contour maps the following procedure applies:

1. Find the effect of a 4 ft steady-state error in channel 1 on the aircraft Y position in the Area Navigation test. The aircraft is at 30,000 ft AGL and located 40,000 ft south of Salt Site.
2. Referring to Figure A-1, the aircraft is located in a region of -H (the dots indicate the region is negative). Therefore, the user Y error is $4 \times (-12) = -48$ ft.
3. A similar error in channel 3, Figure A-5, results in a user Y position error of $4 \times (+5) = +20$ ft.

The ILS contours, Figures A-9 to A-12, are used the same way. In the ILS case, although an entire planar region has been mapped, the aircraft flight path was essentially a straight line along $X = 0$, and the geometry was optimized only for a small region around $X = 0$, $Y = 0$.

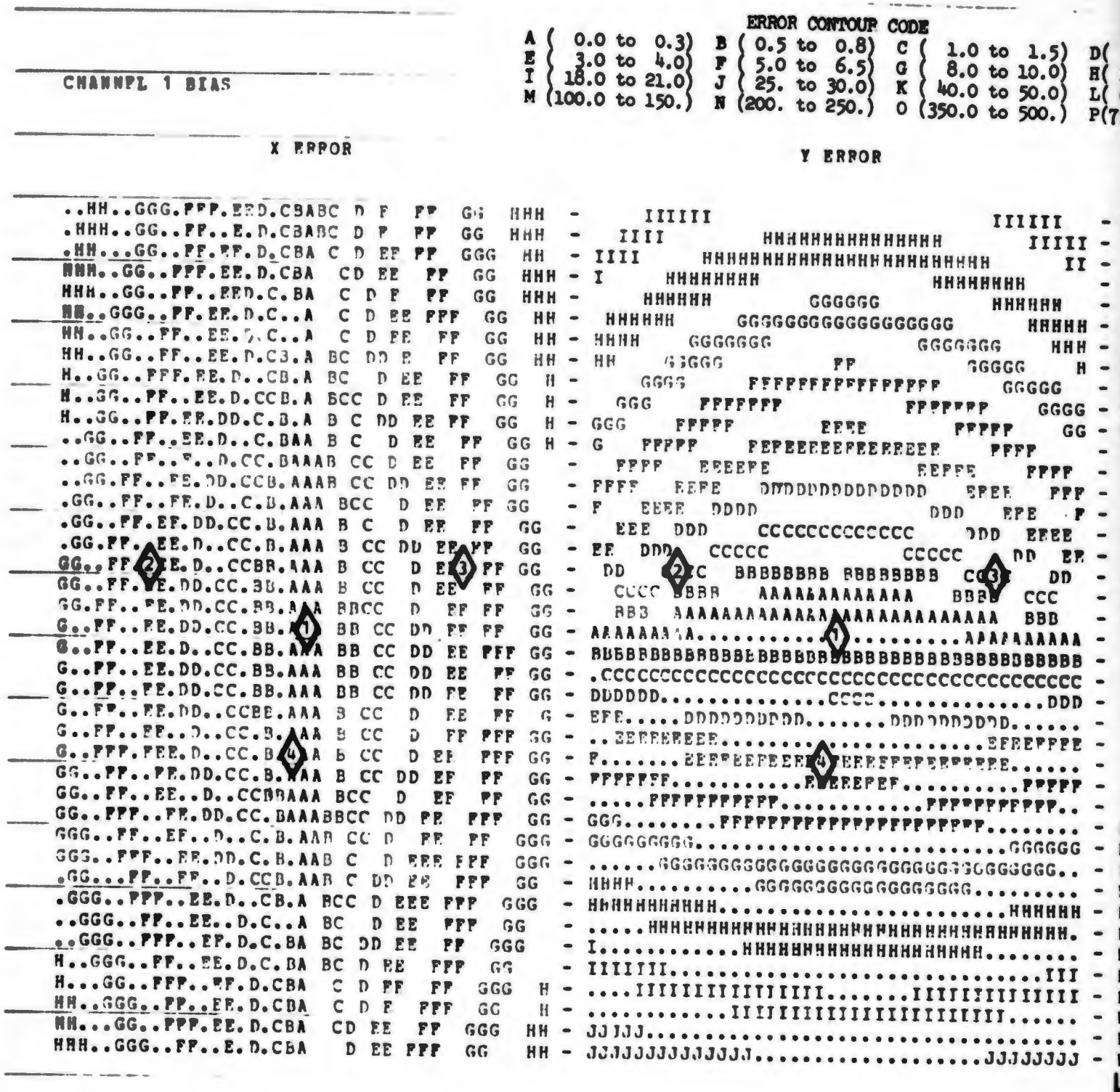

Figure A-1 Ch
Ge

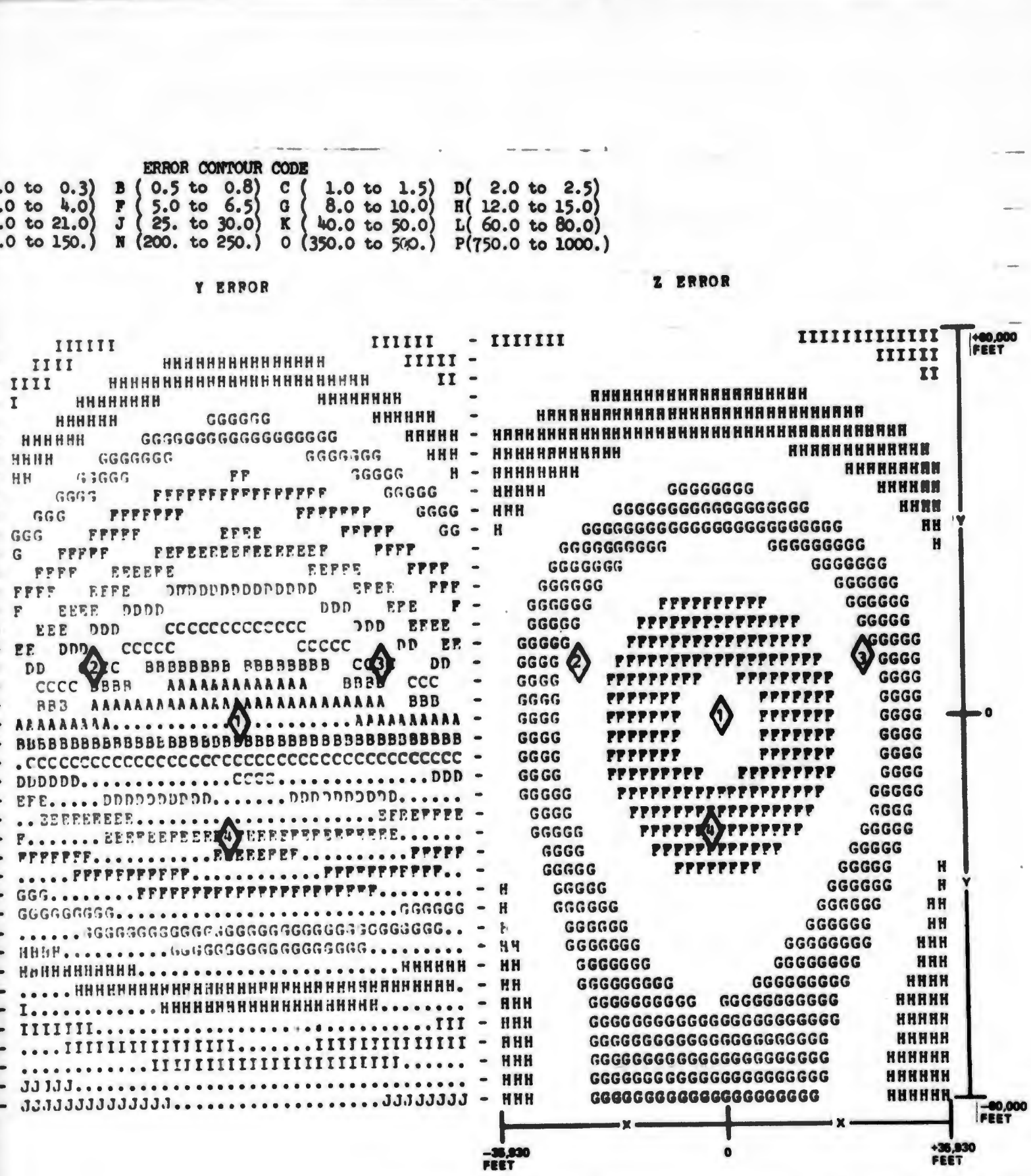

Figure A-1 Channel 1 Bias Sensitivity Contour for the Area Navigation Test Geometry in the X, Y Plane at 30,000 Feet Above Ground Level

ERROR CONTOUR CODE

A (0.0 to 0.3)	B (0.5 to 0.8)	C (1.0 to 1.5)	D(2.
E (3.0 to 4.0)	F (5.0 to 6.5)	G (8.0 to 10.0)	H(12.
I (18.0 to 21.0)	J (25. to 30.0)	K (40.0 to 50.0)	L(60.
M (100.0 to 150.)	N (200. to 250.)	O (350.0 to 500.)	P(750.

CHANNEL 1 BIAS

CLOCK ERROR

HORIZONTAL ERROR

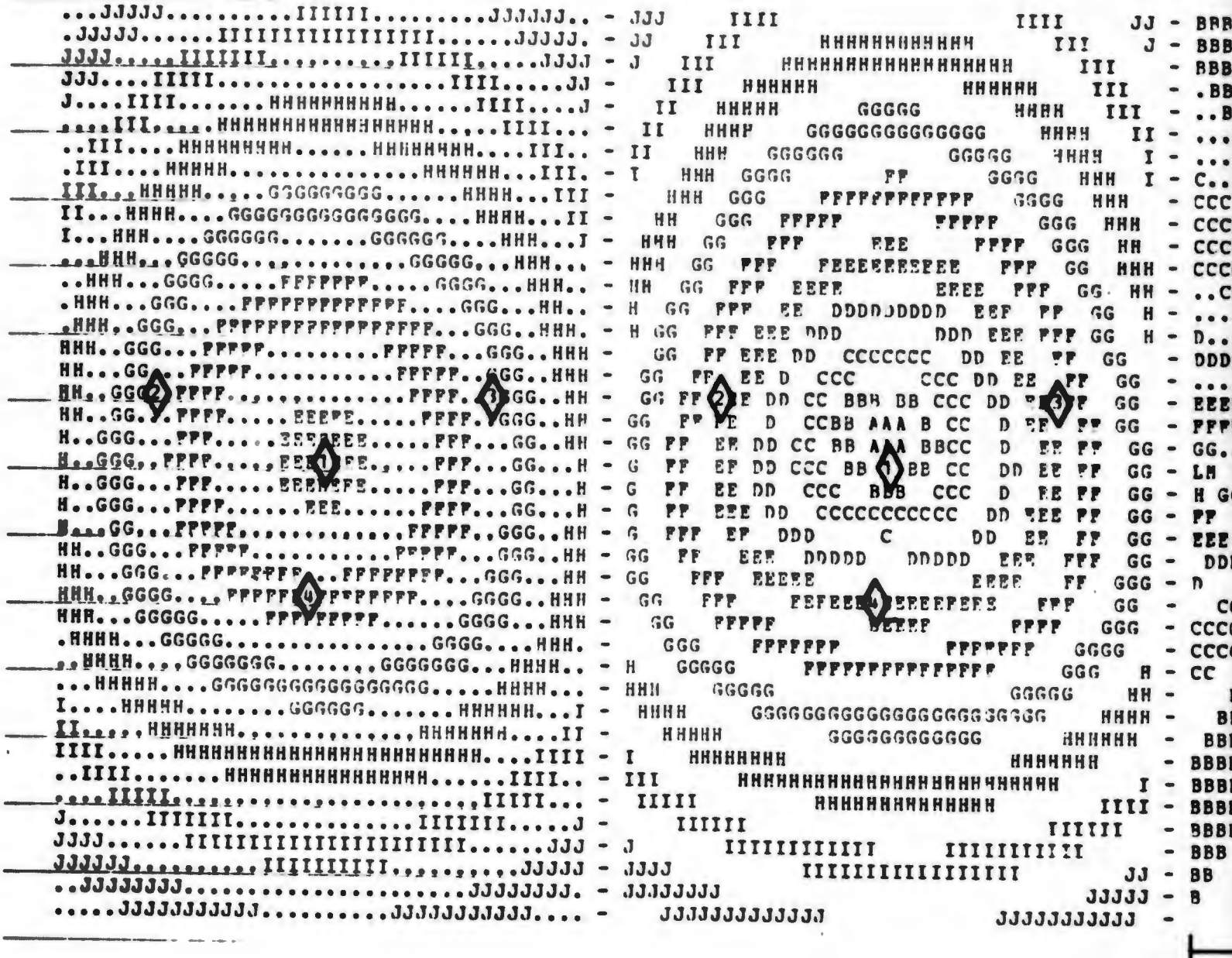

-36,930 FEET

Figure A-2 Channe
Geome

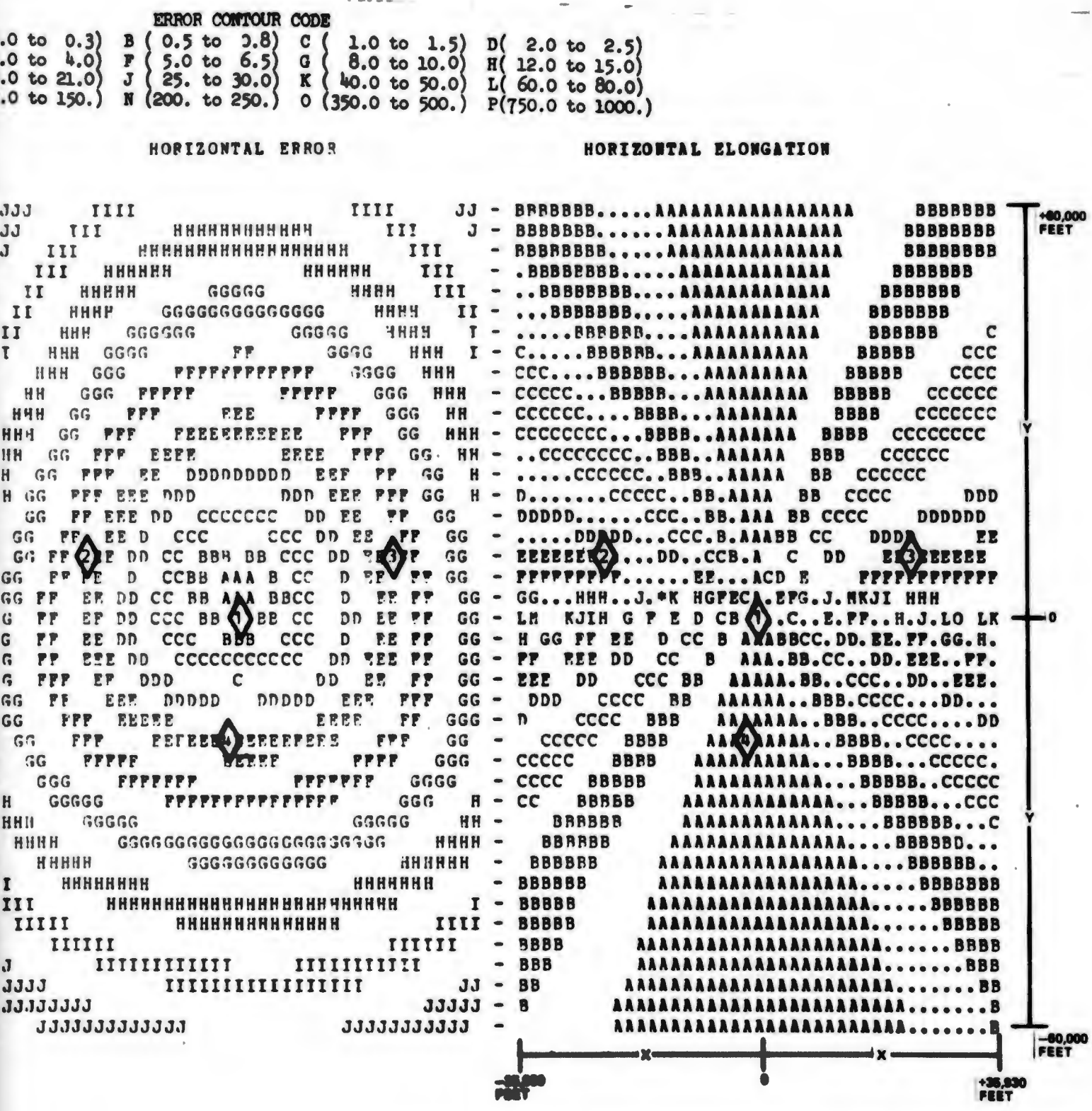

Figure A-2 Channel 1 Bias Sensitivity Contour for the Area Navigation Test Geometry in the X, Y Plane at 30,000 Ft Above Ground Level

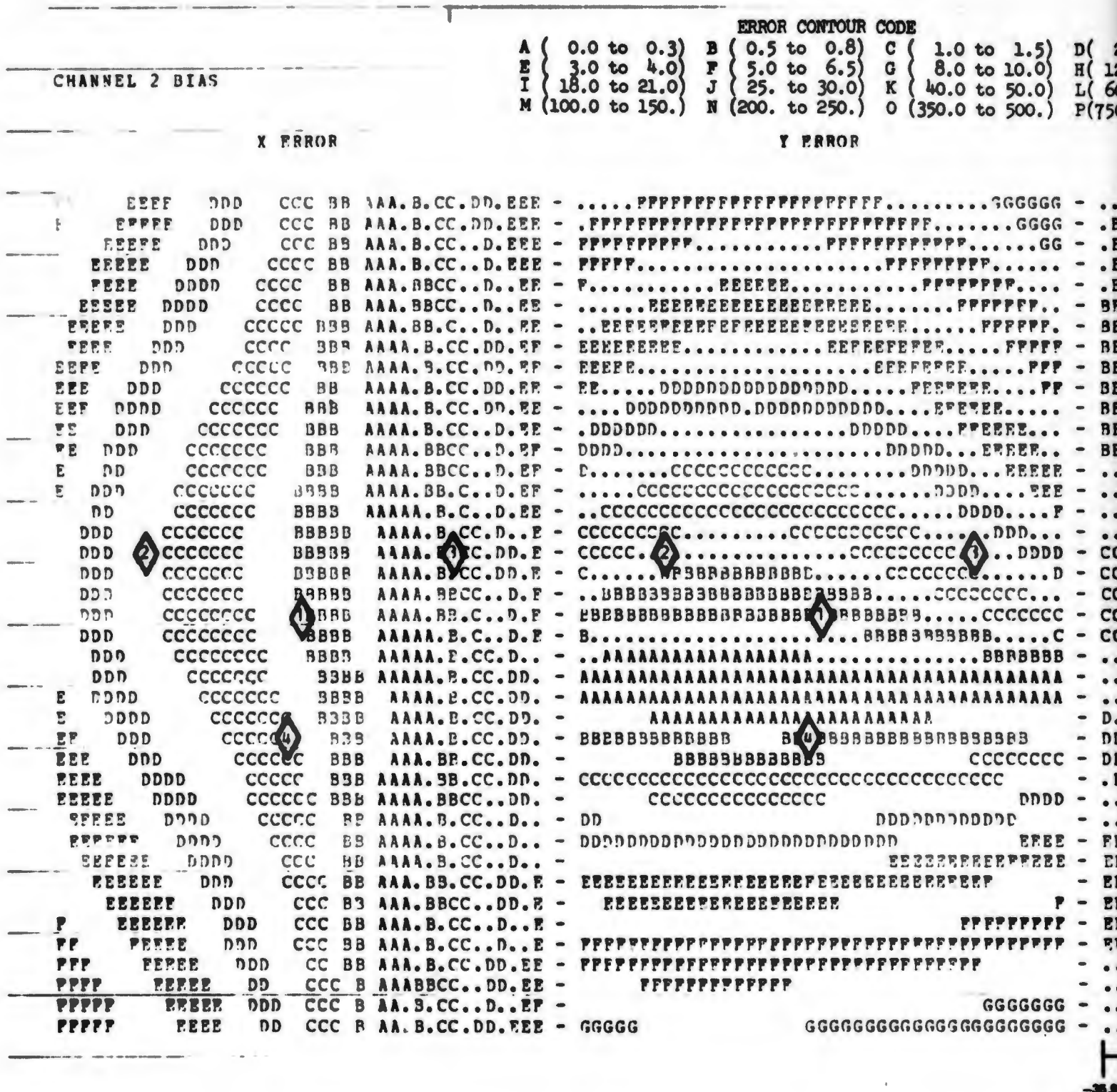

Figure A-3 Ch
Ge

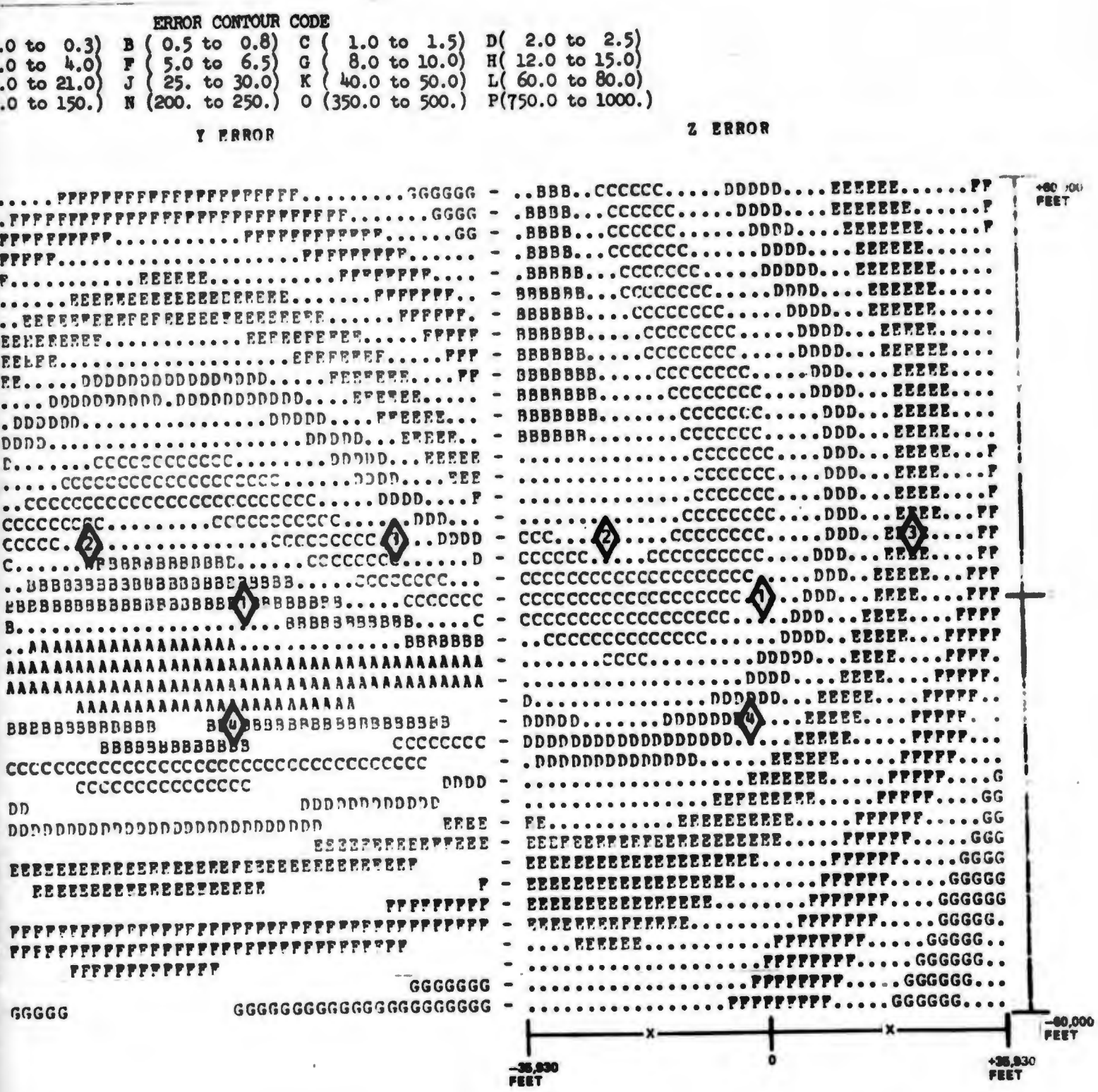

Figure A-3 Channel 2 Bias Sensitivity Contour for Area Navigation Test Geometry in the X, Y Plane at 30,000 Feet Above Ground Level

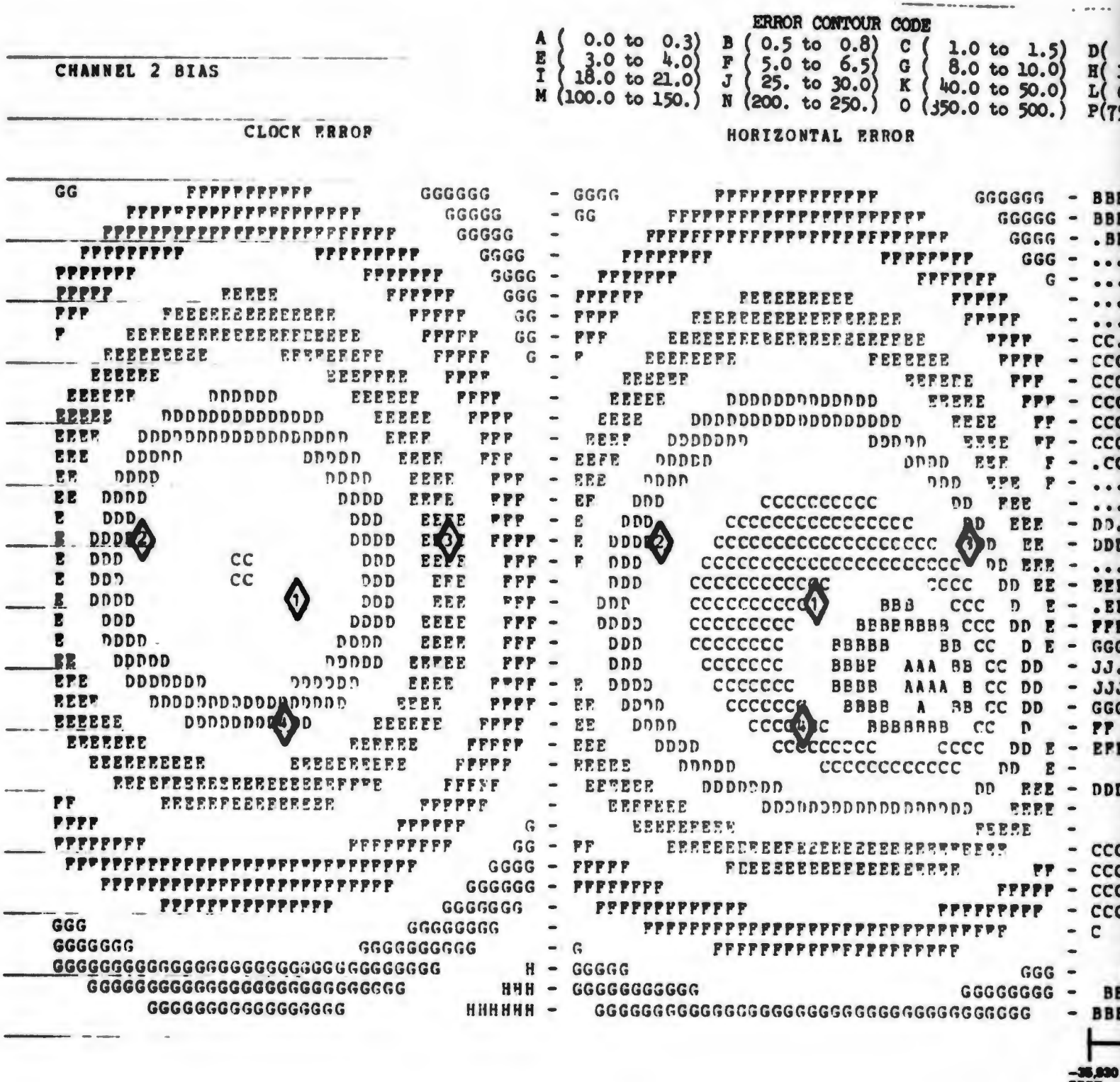

Figure A-4 Char
Geor

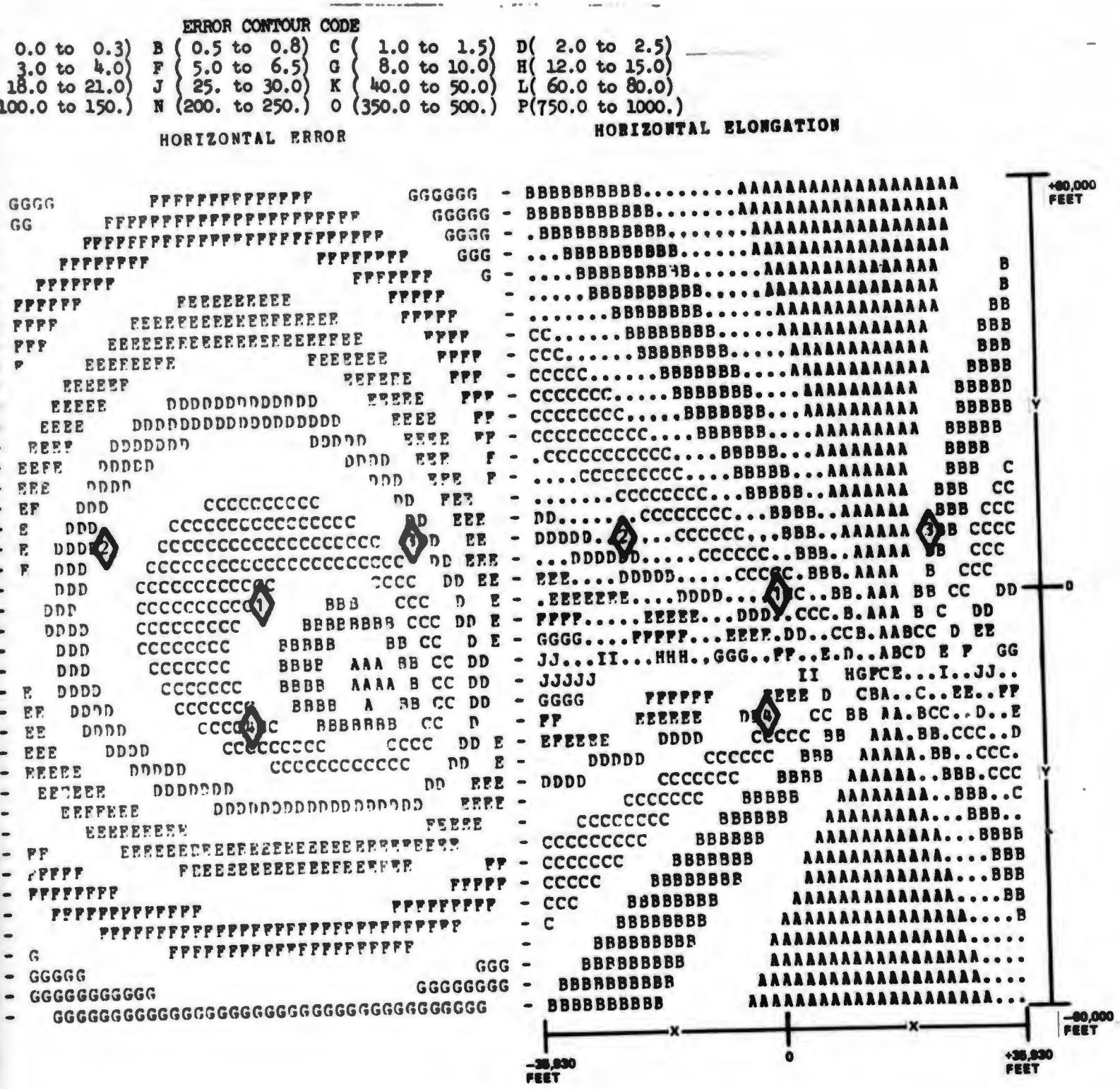

Figure A-4 Channel 2 Bias Sensitivity Contour for Area Navigation Test Geometry in the X, Y Plane at 30,000 Feet Above Ground Level

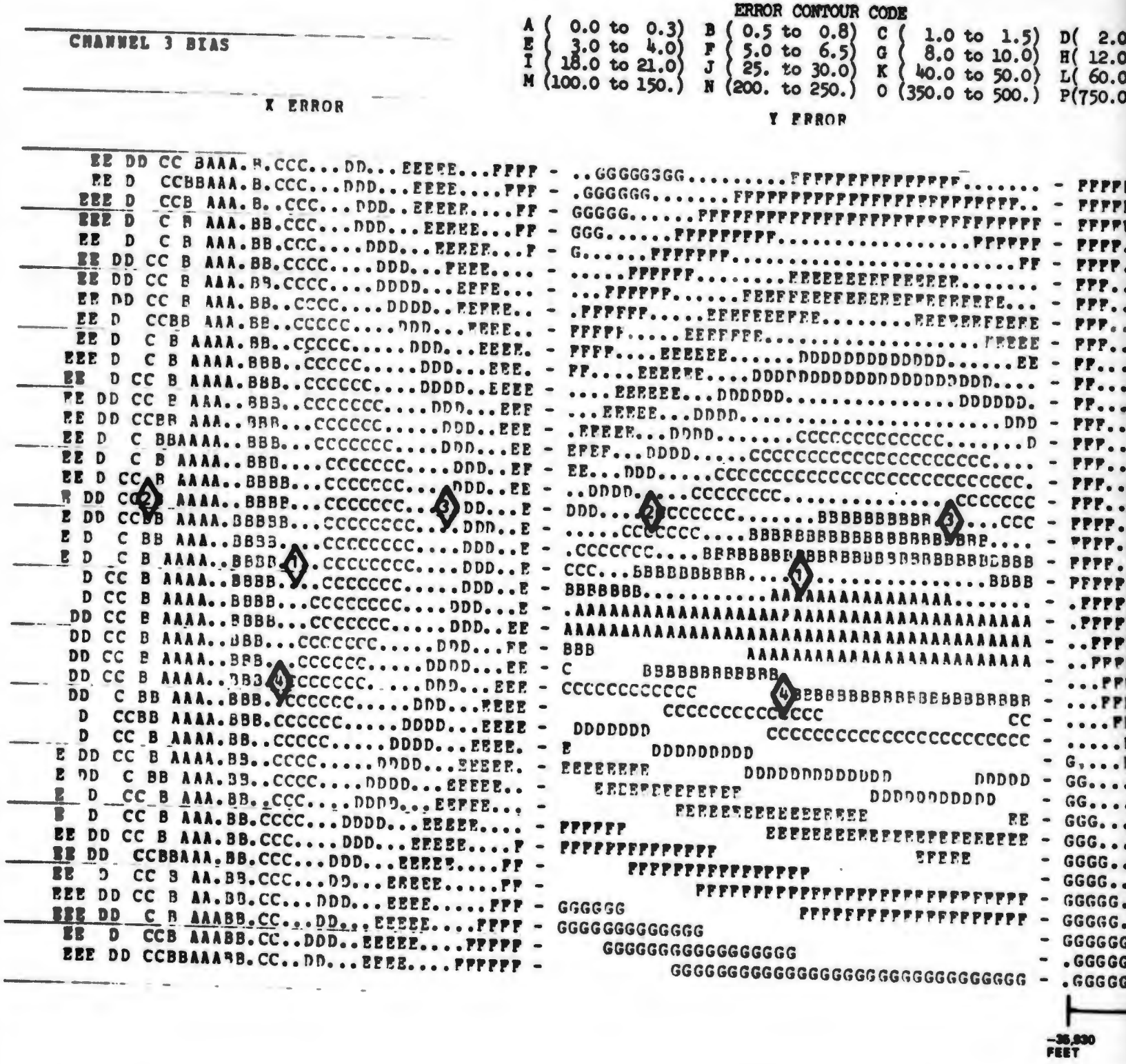

Figure A-5 Channel 3
Geometry

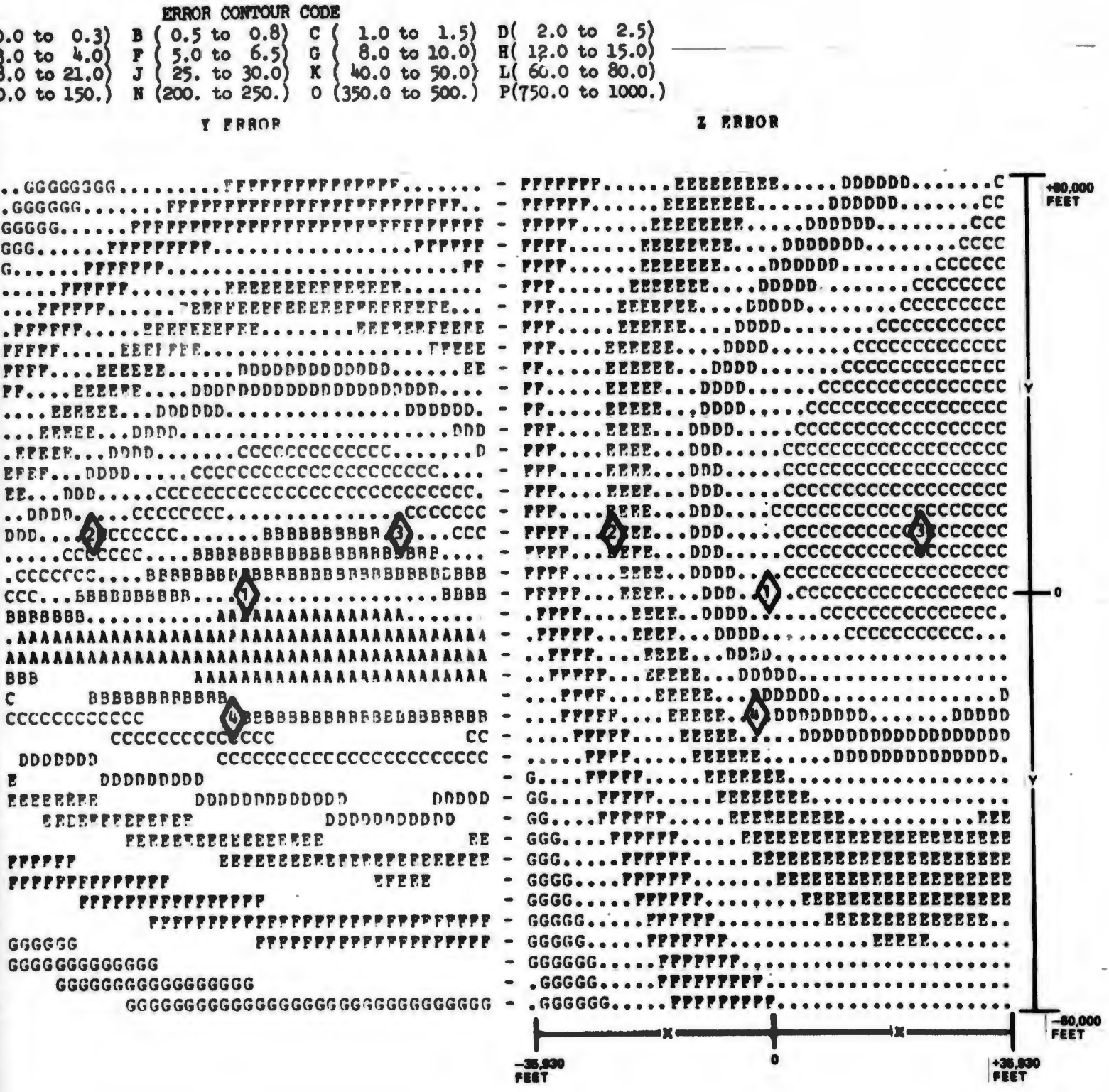

Figure A-5 Channel 3 Bias Sensitivity Contour for the Area Navigation Test Geometry in the X, Y Plane at 30,000 Feet Above Ground Level

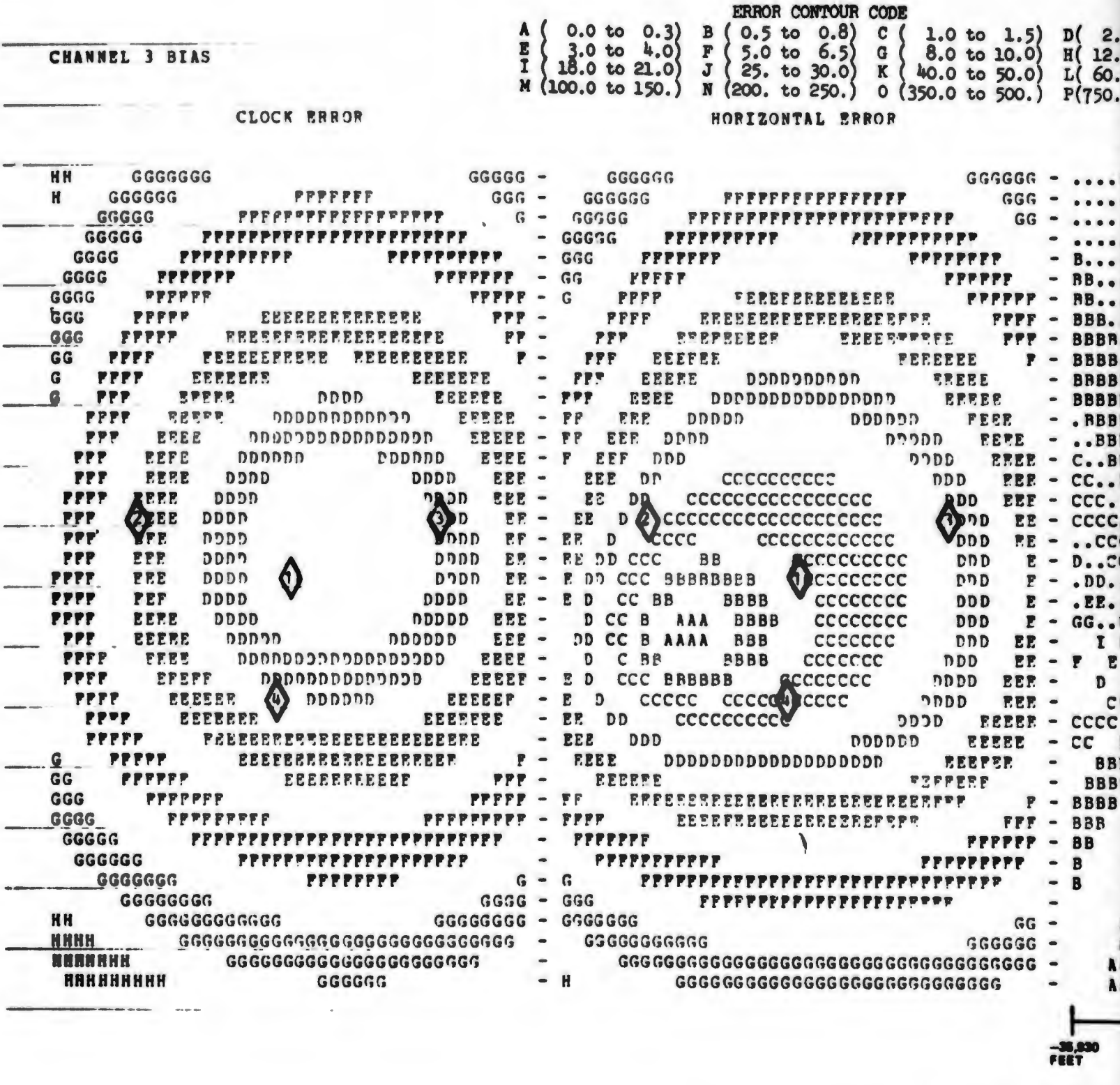

Figure A-6 Channel Geometr

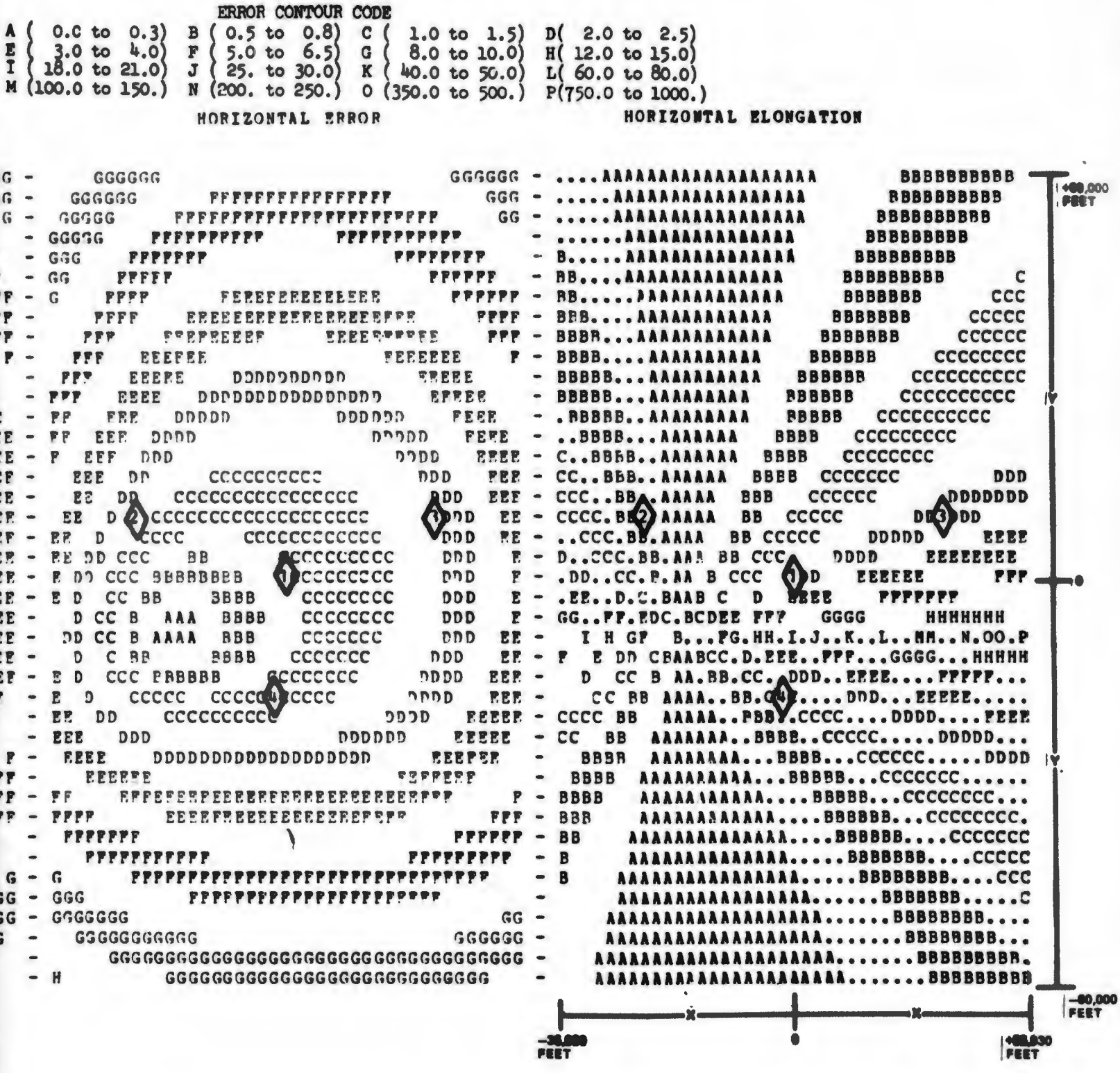

Figure A-6 Channel 3 Bias Sensitivity Contour for the Area Navigation Test Geometry in the X, Y Plane at 30,000 Ft Above Ground Level

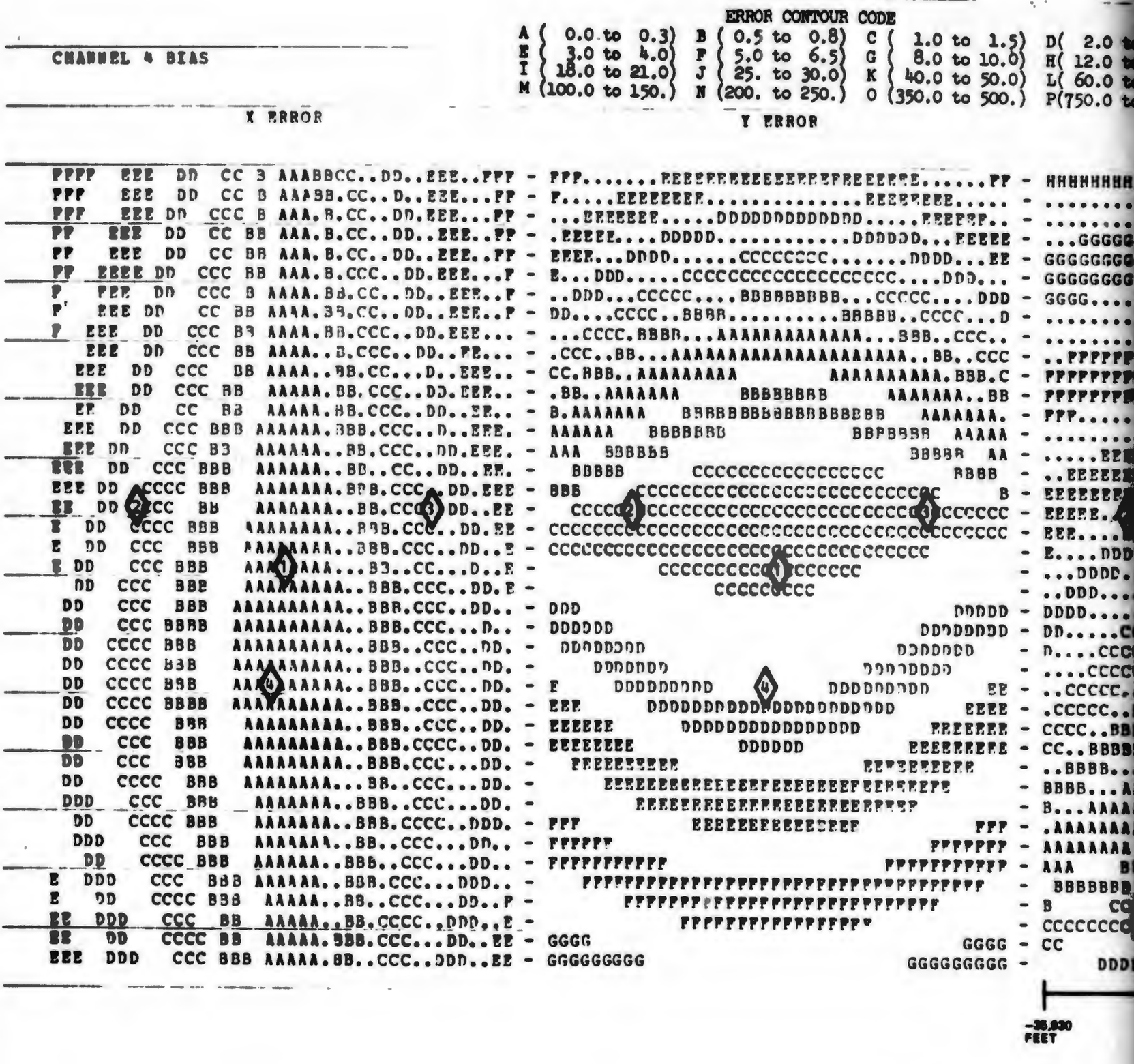

Figure A-7 Channel 4 Bia
Geometry in t

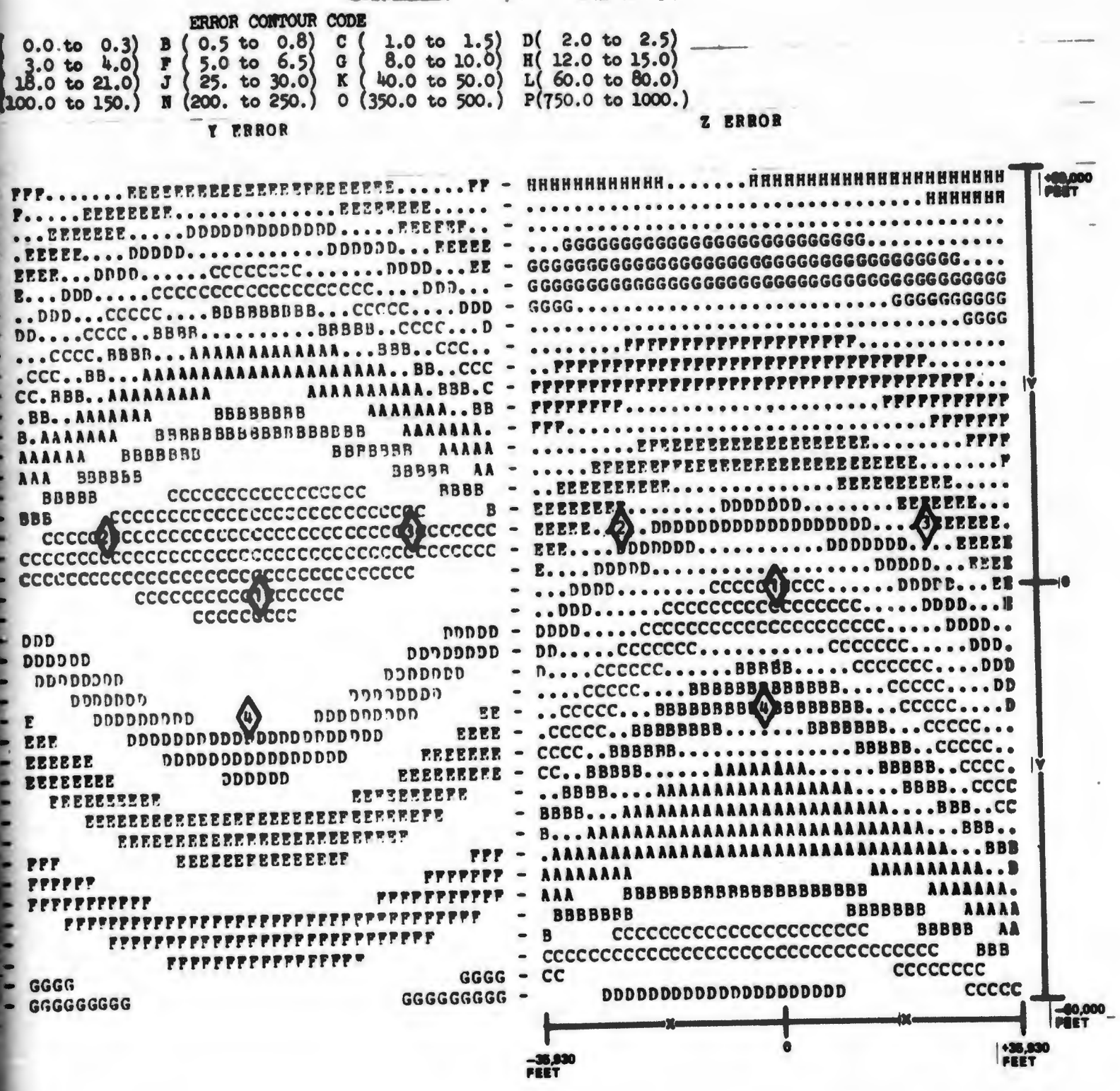

Figure A-7 Channel 4 Bias Sensitivity Contours for the Area Navigation Test Geometry in the X, Y Plane at 30,000 Feet Above Ground Level

ERROR CONTOUR CODE

A	(0.0 to 0.3)	B	(0.5 to 0.8)	C	(1.0 to 1.5)	D	(2.0 t
E	(3.0 to 4.0)	F	(5.0 to 6.5)	G	(8.0 to 10.0)	H	(12.0 t
I	(18.0 to 21.0)	J	(25. to 30.0)	K	(40.0 to 50.0)	L	(60.0 t
M	(100.0 to 150.)	N	(200. to 250.)	O	(350.0 to 500.)	P	(750.0 t

CHANNEL 4 BIAS

CLOCK ERROR

HORIZONTAL ERROR

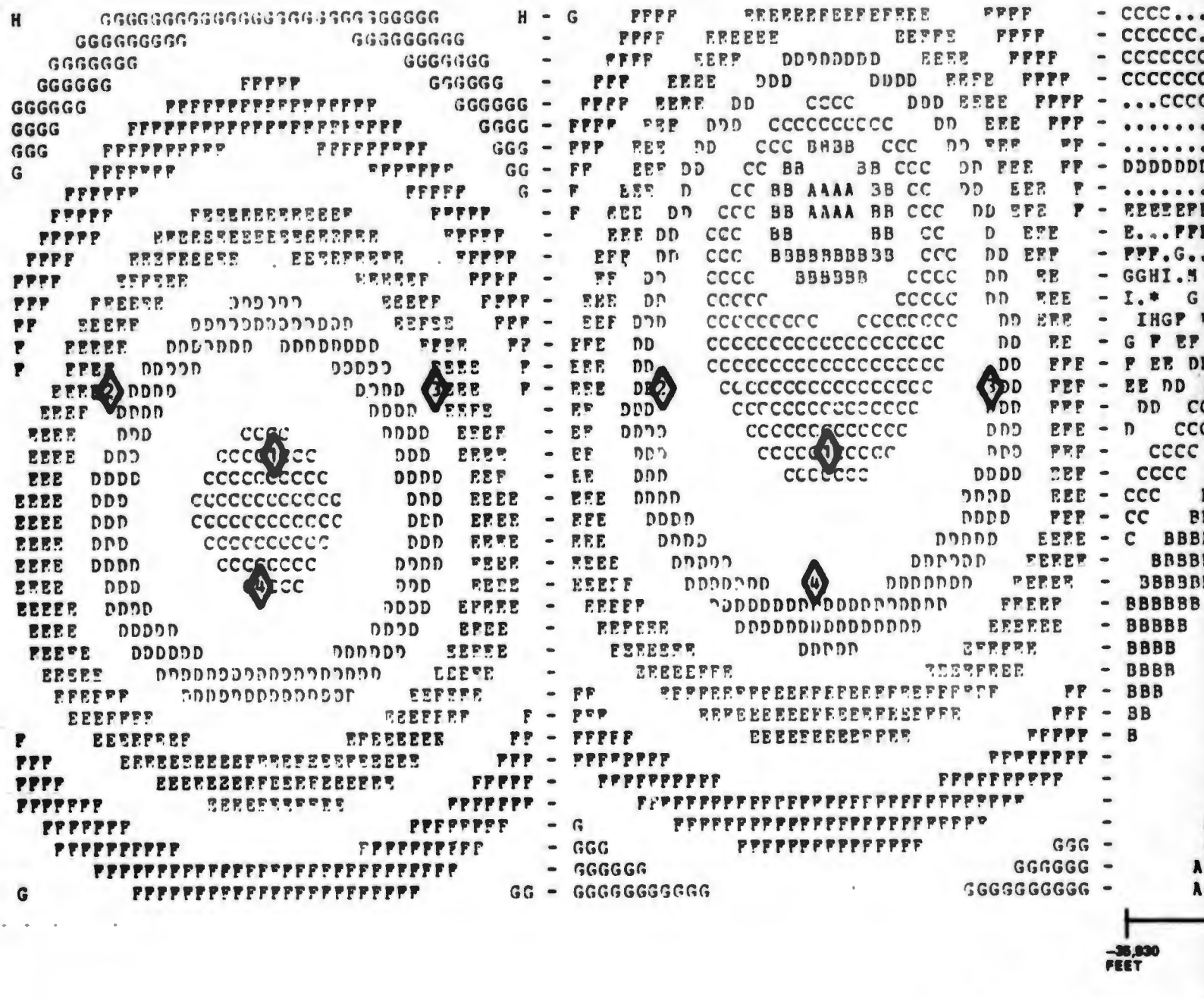

Figure A-8 Channel 4 B
Geometry in

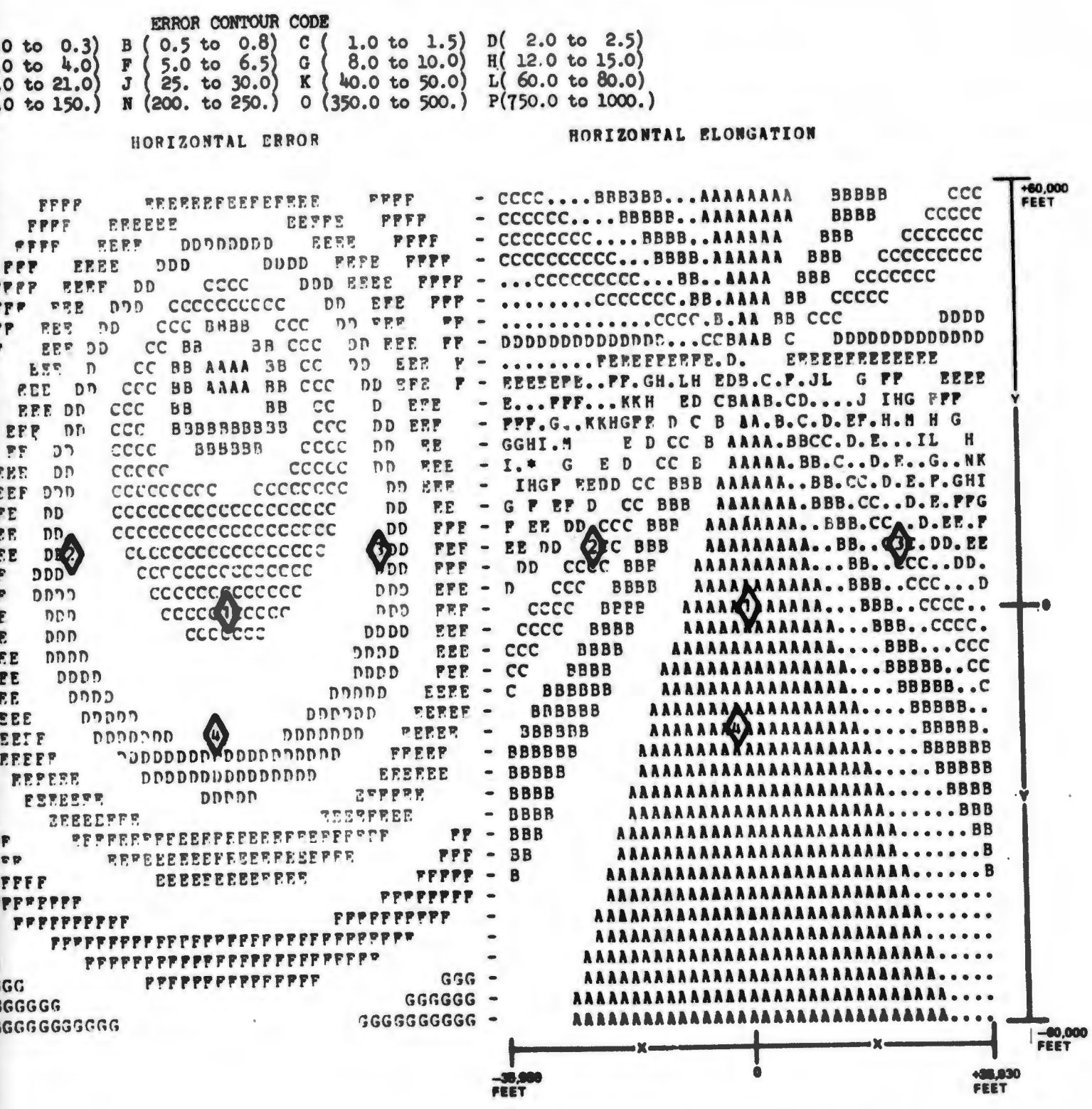

Figure A-8 Channel 4 Bias Sensitivity Contour for the Area Navigation Test Geometry in the X, Y Plane at 30,000 Feet Above Ground Level

ERROR CONTOUR CODE

A (0.0 to 0.3)	B (0.5 to 0.8)	C (1.0 to 1.5)	D(2
E (3.0 to 4.0)	F (5.0 to 6.5)	G (8.0 to 10.0)	H(12
I (18.0 to 21.0)	J (25. to 30.0)	K (40.0 to 50.0)	L(60
M (100.0 to 150.)	N (200. to 250.)	O (350.0 to 500.)	P(750

CHANNEL 1 BIAS

X ERROR

Y ERROR

Figure A-9

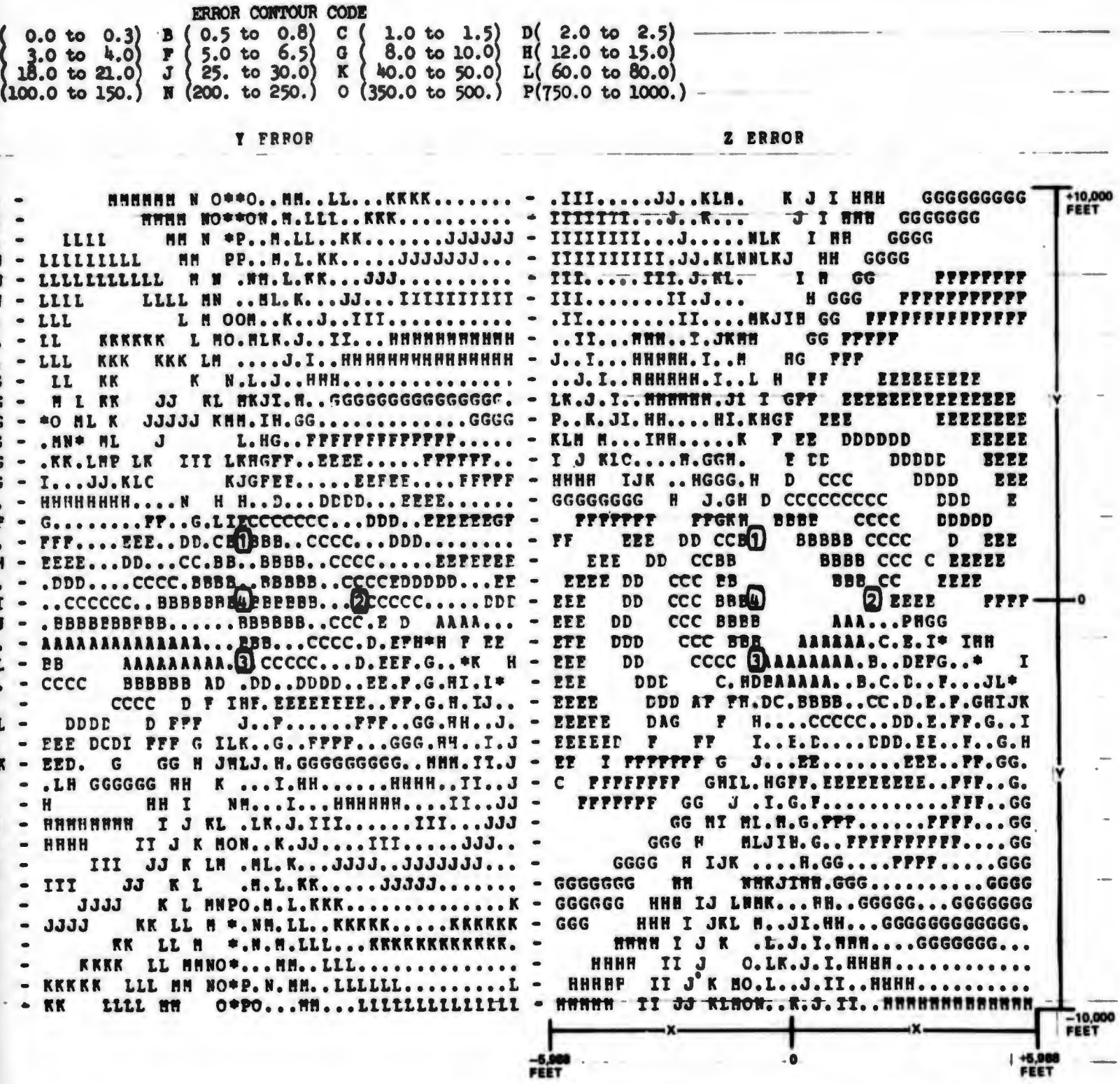

Figure A-9 Channel 1 Bias Sensitivity Contours for ILS Test Geometry, in the X, Y Plane at 50 Feet Above Ground Level

ERROR CONTOUR CODE

A (0.0 to 0.3)	B (0.5 to 0.8)	C (1.0 to 1.5)	D(2.0 to
E (3.0 to 4.0)	F (5.0 to 6.5)	G (8.0 to 10.0)	H(12.0 to
I (18.0 to 21.0)	J (25. to 30.0)	K (40.0 to 50.0)	L(60.0 to
M (100.0 to 150.)	N (200. to 250.)	O (350.0 to 500.)	P(750.0 to

CHANNEL 2 BIAS

X ERROR

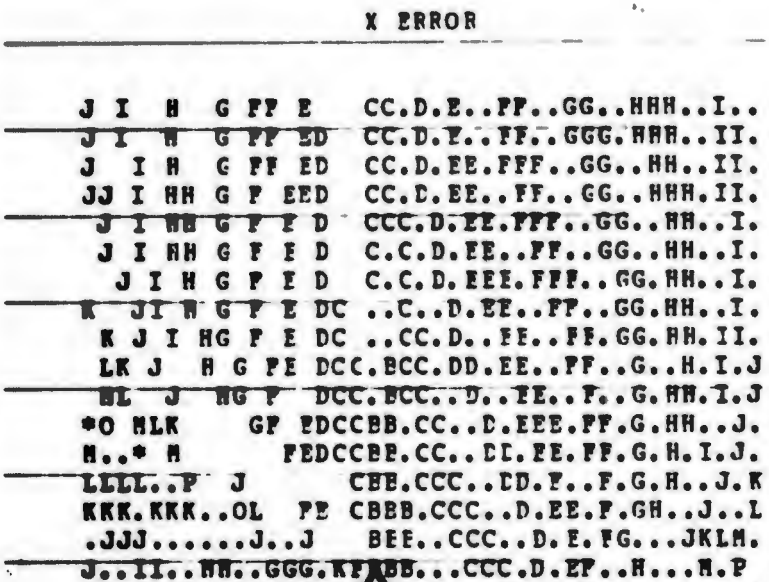

Y ERROR

-5,988 FEET

Figure A-10 Chenna
the X, Y

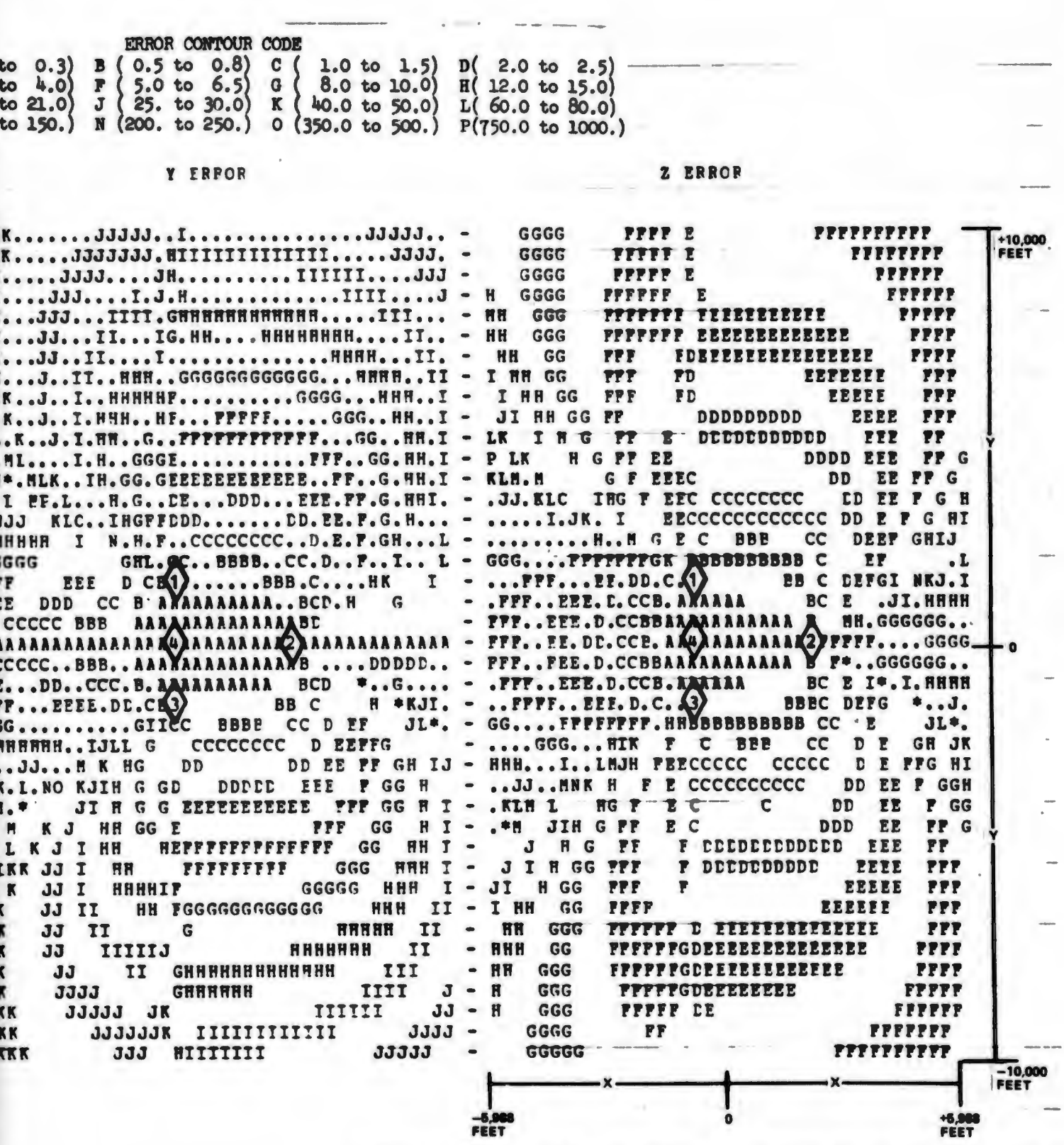

Figure A-10 Chennal 2 Bias Sensitivity Contours for ILS Test Geometry in the X, Y Plane at 50 Feet Above Ground Level

2

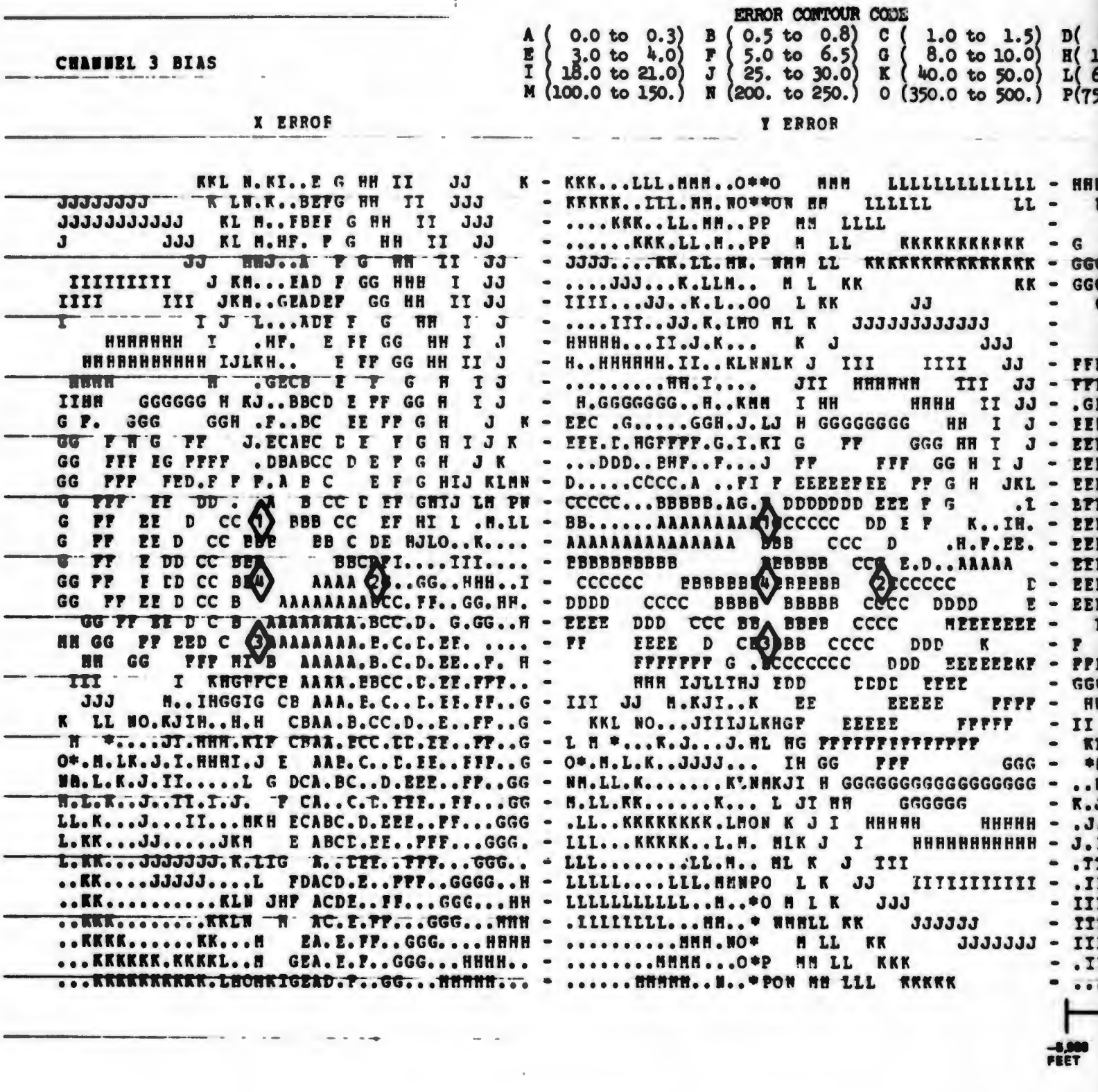

Figure A-11 Ch
the

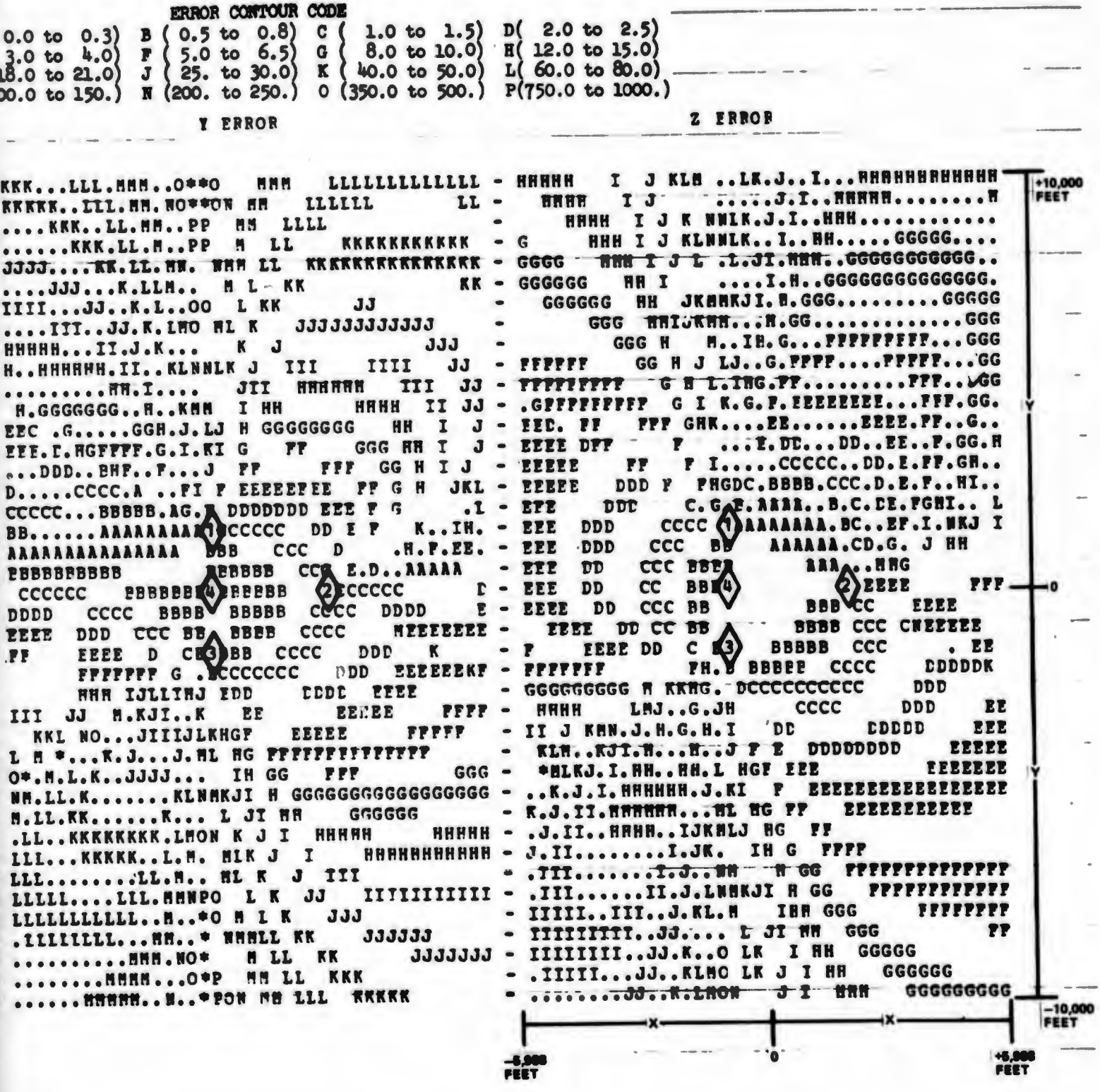

Figure A-11 Channel 3 Bias Sensitivity Contours for ILS Test Geometry in the X,Y Plane at 50 Feet Above Ground Level

CHANNEL 4 BIAS

ERROR CONTOUR CODE

A	0.0 to 0.3	B	0.5 to 0.8	C	1.0 to 1.5	D	2.
E	3.0 to 4.0	F	5.0 to 6.5	G	8.0 to 10.0	H	12.
I	18.0 to 21.0	J	25. to 30.0	K	40.0 to 50.0	L	60.
M	100.0 to 150.	N	200. to 250.	O	350.0 to 500.	P	750.

X ERROR

Y ERROR

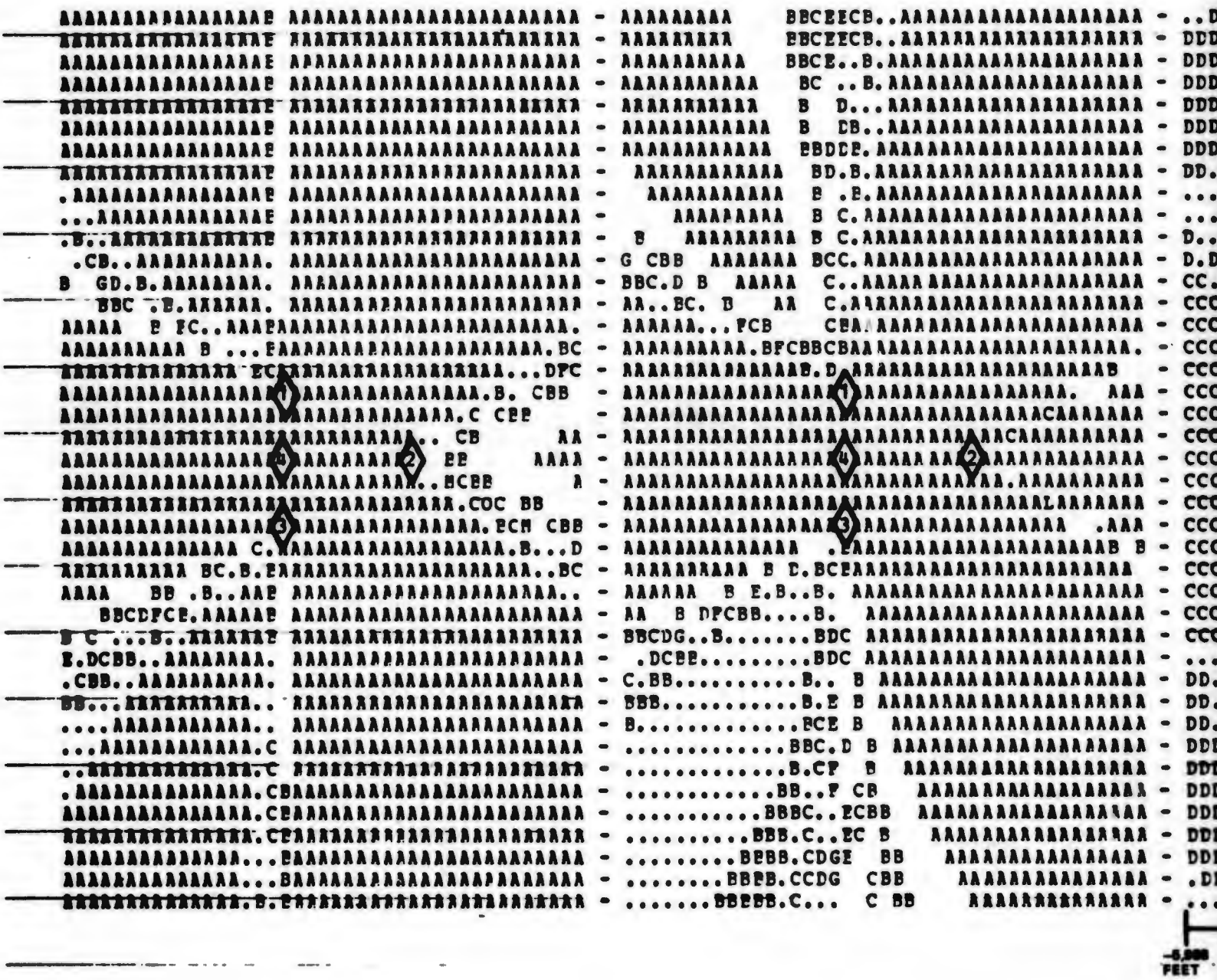

Figure A-12 Channe
X,Y Pl

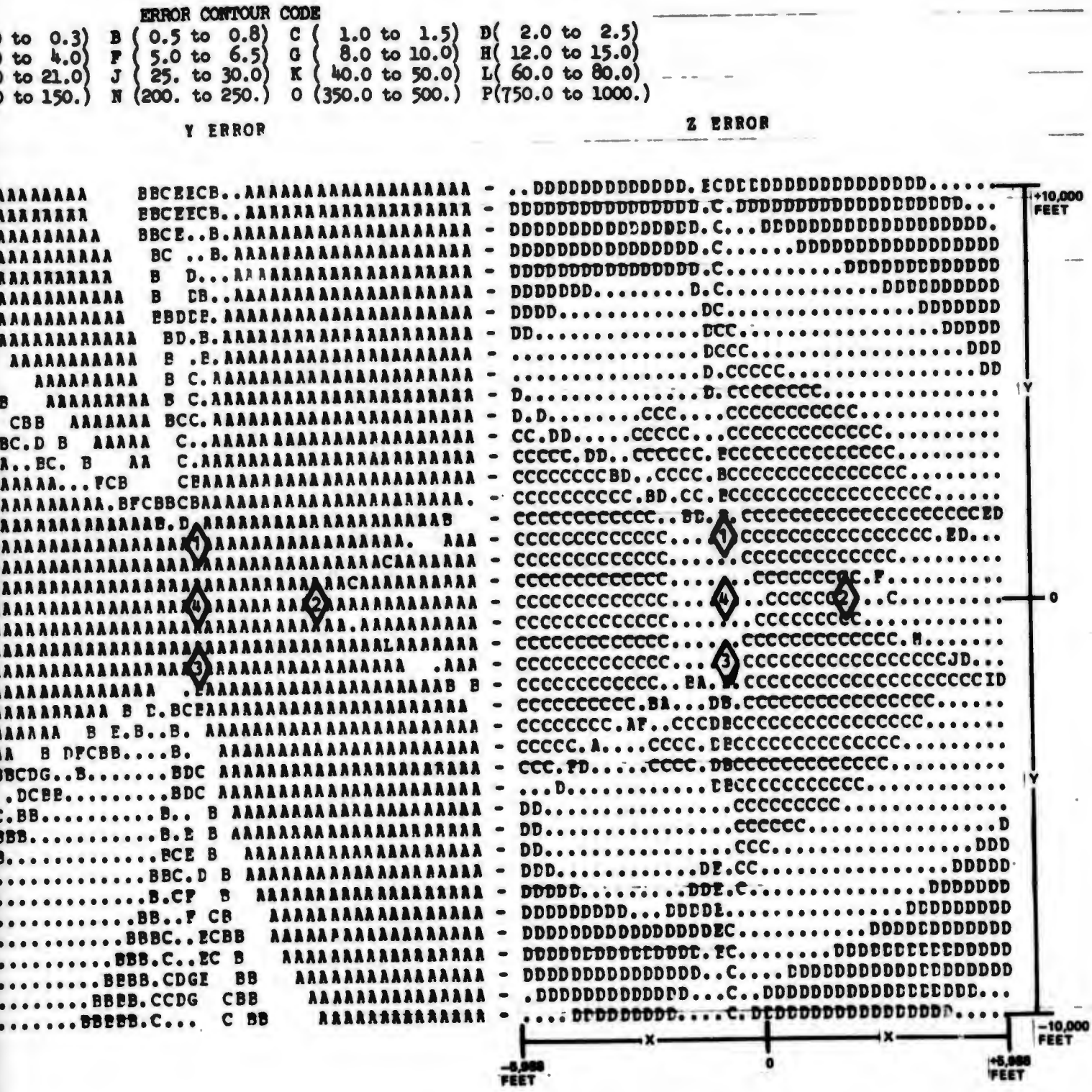

Figure A-12 Channel 4 Bias Sensitivity Contours for ILS Test Geometry in the X, Y Plane at 50 Feet Above Ground Level

APPENDIX B

TABULATION OF MULTIPATH WEATHER DATA

Significant Weather Data Recorded During Ground Multipath Tests

Site: NW 30 Alt: 4015.85 Ft MSL

Date	Time MST (Hrs)	Press. (Millibars)	Temp °C	Dewpoint	Rel Hum. %	Density gm/m³	Speed of Sound (Knots)	Wind Direction From TN	Wind Speed (Knots)	Index of Refraction	
Aug 11, 1972	0400	882.0	20.9	16.6	76.0	1036.7	670.4	170.3	3.9	1.000	313
	0500	882.4	19.8	14.7	72.0	1042.0	668.8	270.0	2.9		306
	0600	883.0	20.5	14.9	70.0	1040.1	669.7	.0	.0		306
	0700	883.4	20.7	14.7	68.0	1040.0	669.9	.0	.0		305
	0800	883.6	24.0	15.3	58.0	1028.4	673.7	.0	.0		304
	0900	993.6	25.5	15.3	53.0	1023.2	675.4	.0	.0		302
Aug 17, 1972	0600	881.0	20.1	18.0	87.0	1037.5	669.7	.0	.0		322
	0700	881.4	20.2	17.5	84.0	1037.9	669.8	.0	.0		319
	0800	881.5	21.4	17.7	79.0	1033.7	671.2	.0	.0		318
	0900	881.6	23.7	16.9	65.0	1026.3	673.6	.0	.0		311
	1000	881.4	25.0	17.1	61.0	1021.5	675.1	.0	.0		310
	1100	881.0	27.4	16.8	52.0	1013.0	677.8	.0	.0		306
Aug 18, 1972	0500	880.0	17.5	15.2	86.0	1047.1	666.3	.0	.0		311
	0600	879.4	18.0	15.7	86.0	1044.3	666.9	.0	.0		312
	0700	878.0	19.5	16.3	81.0	1037.0	668.8	.0	.0		312
	0800	880.5	21.0	16.3	74.0	1034.7	670.5	20.0	2.9		311
	0900	880.5	22.6	15.6	64.0	1029.5	672.2	30.0	2.9		306
	1000	880.4	25.0	16.0	57.0	1020.9	676.0	130.0	2.9		305
	1100	879.8	29.4	16.0	44.0	1006.3	679.9	160.0	6.8		299
Aug 21, 1972	0600	882.6	19.0	17.4	90.0	1043.7	668.4	.0	.0		321
	0700	883.1	20.5	18.0	86.0	1038.6	670.2	340.0	1.9		322
Aug 23, 1972	0500	875.4	20.2	16.4	78.0	1031.4	669.6	.0	.0		311
	0600	875.7	19.9	15.7	76.0	1033.2	669.1	.0	.0		308
	0700	875.9	23.3	14.7	58.0	1022.1	672.8	.0	.0		299
	0800	876.4	22.2	15.7	66.0	1026.0	671.7	.0	.0		306
	0900	876.7	24.2	17.3	65.0	1018.6	674.3	160.0	1.9		311
	1100	876.8	27.6	13.6	42.0	1009.0	677.5	150.0	15.0		290
Aug 24, 1972	0500	872.3	22.0	12.4	54.0	1023.4	671.0	.0	.0		290
	0600	872.3	24.8	8.8	36.0	1015.1	673.8	250.0	14.8		274
	0700	872.4	26.9	9.3	33.0	1007.9	676.2	250.0	14.8		274
	0800	872.8	26.4	14.3	47.0	1008.1	676.3	240.0	15.9		293
	0900	873.4	27.2	15.3	48.0	1005.6	677.4	140.0	2.9		297
	1000	873.6	29.7	10.4	30.0	999.6	679.5	330.0	1.9		275
	1100	873.3	22.9	12.1	22.0	1025.0	670.9	360.0	5.9		255
Aug 25, 1972	0500	876.3	21.4	10.6	50.0	1030.9	670.1	350.0	9.9		285
	0600	877.2	20.7	10.3	51.0	1034.5	669.3	320.0	7.4		285
	0700	877.9	22.4	8.9	42.0	1029.9	671.0	340.0	8.9		279
	0800	878.2	24.5	11.2	43.0	1022.1	673.7	345.0	3.1		284
	0900	878.6	25.1	12.4	45.0	1020.1	674.5	290.0	1.9		288
	1000	878.7	30.0	14.2	38.0	1002.9	680.3	160.0	11.9		290
	1100	878.6	30.2	13.1	35.0	1002.6	680.4	180.0	8.9	1.000	285

Significant Weather Data Record During Ground Multipath Tests (Cont)

Site: NW 30 Alt: 4015.85 Ft MSL

Date	Time MST (Hrs)	Press. (Millibars)	Temp °C	Dewpoint	Rel Hum %	Density gm/m3	Speed of Sound (Knots)	Wind Direction From TN	Wind Speed (Knots)	Index of Refraction
Oct 2, 1972	0500	876.4	12.8	5.7	62.0	1063.6	659.7	20.0	1.4	1.000 279
	0600	876.8	11.4	4.9	64.0	1069.6	658.0	.0	.0	279
Balloon Multi	0700	877.5	13.7	4.6	54.0	1062.0	660.7	330.0	2.9	276
	0800	877.7	18.0	6.6	47.0	1046.0	665.8	350.0	6.8	276
	0900	877.9	21.0	7.7	42.0	1035.2	669.3	360.0	4.1	276
	1000	877.9	25.0	6.8	31.0	1021.6	673.8	350.0	4.9	270
	1100	877.6	26.8	12.2	40.0	1013.2	676.4	.0	.0	285
	1200	877.2	28.8	9.6	30.0	1007.0	678.3	90.0	2.9	274
	1300	876.5	29.3	7.3	25.0	1005.3	678.7	130.0	4.9	266
Oct 3, 1972	0500	879.2	13.5	4.1	53.0	1064.9	660.4	320.0	2.9	275
	0600	879.5	14.2	4.8	53.0	1062.5	661.3	330.0	2.9	276
Balloon Multi	0700	880.0	15.5	7.1	57.0	1057.6	663.0	330.0	4.9	281
	0800	880.4	20.3	12.4	60.0	1038.9	669.1	330.0	2.9	294
	0900	880.6	21.3	8.3	43.0	1037.1	669.7	30.0	1.9	279
	1000	881.0	25.0	13.6	49.0	1022.7	674.6	360.0	8.7	294
	1100	880.4	28.2	14.9	44.0	1010.6	678.4	345.0	1.9	296
	1200	879.6	28.3	11.5	35.0	1010.8	678.0	.0	.0	281
	1300	879.5	28.0	16.7	50.0	1009.3	678.5	120.0	3.9	304
	1400	878.6	29.8	19.9	55.0	1000.4	681.1	130.0	1.9	318
Oct 4, 1972	0800	881.7	18.0	14.8	81.0	1047.6	666.8	340.0	1.0	308
	0900	882.3	20.8	14.8	69 0	1038.3	670.0	360.0	5.1	305
Balloon Multi	1000	881.9	23.5	16.9	66.0	1027.3	673.4	.0	.0	311
	1100	881.2	27.2	19.9	64.0	1012.1	678.2	150.0	19.4	323
	1200	880.6	29.1	21.2	62.0	1004.2	680.6	140.0	4.1	328
	1300	879.5	29.5	16.8	46.0	1004.2	680.2	150.0	5.1	302
	1400	878.7	29.2	19.1	54.0	1003.1	680.3	150.0	6.0	314
	1500	878.4	28.2	17.8	53.0	1006.7	678.9	160.0	4.1	309
Oct 5, 1972	0745	881.2	20.3	16.9	80.0	1037.7	669.8	.0	.0	315
	0800	881.6	22.7	15.2	62.0	1030.6	672.2	100.0	4.1	304
Balloon Multi	1000	881.5	26.3	19.9	64.0	1016.0	677.0	130.0	1.9	319
	1100	881.1	26.2	17.4	58.0	1016.0	676.6	.0	.0	310
	1200	880.4	27.0	16.7	53.0	1013.7	677.3	30.0	2.1	306
	1300	879.4	27.5	14.6	45.0	1011.9	677.6	60.0	2.1	295
	1400	878.7	27.8	13.1	40.0	1010.8	677.7	90.0	2.1	288
	1500	878.8	29.5	12.1	34.0	1005.6	679.4	.0	.0	262
Oct 6, 1972	0800	884.2	17.0	4.0	42.0	1058.1	664.4	330.0	9.9	272
	0900	884.2	18.3	13.5	73 0	1050.1	666.9	360.0	9.9	303
Balloon Multi	1000	884.2	19.1	14.5	74.0	1046.8	668.0	340.0	9.9	306
	1100	883.5	20.6	14.4	67.0	1040.6	669.7	360.0	9.9	303
	1200	883.3	21.4	14.9	66.0	1037.3	670.7	10.0	6.0	305
	1300	882.8	22.3	14.3	60.0	1033.9	671.6	360.0	6.0	301
	1400	881.8	22.4	14.6	61.0	1032.2	671.8	330.0	2.1	302
	1500	880.5	25.5	15.6	54.0	1019.5	675.5	90.0	2.9	1.000 302

APPENDIX C

CESIUM CALIBRATION RESULTS FROM GROUND SYSTEM AT WSMR

APPENDIX C

GROUND CALIBRATION LINK DATA

This appendix contains calibration link data from cesium measurements shown in Table C-1 for the 50-mile area, and Table C-2 for Northrop Strip, cable length data shown in Table C-3 and C-4, and data used to generate the 3 navigation solution cases discussed in this volume shown in Table C-5.

DISH-TO-DISH DELAYS

The dish-to-dish delay numbers are based on averaging simple differences instead of drift corrected measurements because the simple differences represent the most accurate values available from these field data. These early data (March and April 1972) were taken using 30 and 60 minute averaging times for each reading, but these extended averaging times were later found to introduce additional errors. This evaluation led to the improved measuring technique with drift correction.

Examination of the simple differences revealed that some data were outside of the range expected for data from the same population. These values were excluded from the averages.

UPLINK A-TO-DISH DELAYS

The tabulated delays were obtained by the mean of the high and low measured values along with a plus and minus value that is one-half the difference between the high and low value. The substantial uncertainty is due to the bias between measurements made with different cable configurations. This was discussed in Section 4.

UPLINK B-TO-DISH DELAYS

The values listed for EC-50 and WC-50 are the result of cesium measurements made on July 20 and July 21, 1972 respectively. The tolerance is unspecified because only one set of measurements was made, and, the accuracy is suspect because of the observed uncertainty with cable configuration changes for A calibration link measurements.

The value for Salt is based on October 1972 cesium measurements of A and B links, and February 1973 measurements of the Salt uplink antenna at Bethpage, N.Y. The A and B cesium measurements were made on consecutive days with the same cable configuration. Thus, the measured difference of 3 nanosec is expected to be reasonably accurate. The difference obtained from antenna measurements is 1.5 nanosec. It is estimated that the antenna measurements are more accurate than the difference in the cesium measurements. Thus, the value of 2 nanosec listed in Table C-1 was obtained by weighting the antenna measurements by a factor of 2.

The value for SC-50 is based on the February 1973 antenna measurements at Bethpage which indicate the B calibration link delay is 18 nanosec less than that for the A link. Other less accurate measurements indicated values of 9 and 14 nanosec. It is expected that the February antenna measurements are the most accurate measurements.

Table C-1 50-Mile Area Calibration Link Delays

	Dish-to-Dish	A-to-Dish	B-to-Dish	D-to-Dish
Salt	7316	7334 ±4	① A-2	7334 ±4
WC-50	32384	32383 ±5	32367	32373
EC-50	18166	18158 ±1	① 18149	18142
SC-50	22406	22425 ±8	A-18	22425 ±8

NOTES:

- All numbers in nanosec
- The delay includes transmitter and receiver Spiroline cables, and antenna flex cables as appropriate

① (A - X) means the B calibration link delay is X nanosec less than the A calibration link delay.

Table C-2 Northrop Strip Calibration Link Delays from Cesium Measurements

	Without Receive Cable	With Receive Cable
Alpha	2666.7 ±1.5	2759.2 ±1.5
Charlie	2674.7 ±1.5	2768.3 ±0.9
Delta	1027.5 ±1.5	1119.9 ±2.0

NOTES:

- All numbers in nanosec
- ± Value identifies the 95% confidence range

UPLINK D-TO-DISH

The values listed for Salt and SC-50 are the same as the A-to-Dish values since the identical antenna configuration is employed for both A and D.

The values listed for EC-50 and WC-50 are the result of cesium measurements made on July 20 and July 21, 1972 respectively. The tolerance is unspecified because only one set of measurements was made, and, the accuracy is suspect because of the observed uncertainty with cable configuration changes for A calibration link measurements.

NORTHROP STRIP

The measured data are presented in Table C-2. The two sets differ by the cable used to connect the receive antenna to the receiver. All of the data appear to be valid. The data do not contain a bias between with-cable and without-cable measurements. The cable delay obtained by averaging the difference between data sets is 92.8 nanosec which translates to 59.9 ft of RG-214 cable (divide by the cable factor of 1.55 nanosec/ft). This is very close to 60.2 ft, the measured length of the cable.

CABLE DELAYS

The cable delay measurements are tabulated in Tables C-3 and C-4. Figure C-1 shows the cable configurations.

TOTAL GROUND DELAYS USED IN THE NAVIGATION SOLUTION

The total ground calibration delay values used to generate the three area navigation solutions, Cases 1,2, and 3 which were discussed in Section 6 are given in Table C-5. These delays include all elements from the MCS receiver to the uplink transmitting antenna as discussed in Section 3 and represent the value ℓ_1 on page 3-3. The table also provides the mean error in the navigation solution with respect to the WSMR trajectory resulting from the use of these ground calibration delays. The solution errors are referred to channel 4 to provide continuity with the ground error analysis given in Subsection 4.2.1.

Table C-3 50-Mile Area, Measured Cable Delays

	All Uplink	A Uplink				B Uplink			
	Xmtr Flex	RF Switch	Flex	Spiro-line	Ant. Flex	RF Switch	Flex	Spiro-line	Ant. Flex
Salt	9.3	0	0	(1-7) 43.2 (8-15) 45.3 (17-21) 46.3	6.7	0	0	(1-7) 43.2 (8-15) 45.3 (22) 46.3	6.7
WC-50	9.5	(1-7)0 (8-23)2.6	(1-7)0 (8-23)6.5	(1-15) 47.4 (17-21) 47.8	6.5	(1-7)0 (8-23)3.1	(1-7)0 (8-23)6.4	(1-15) 40.3 (22) 40.2	6.5
EC-50	9.3	(1-7)0 (8-23)3.0	(1-7)0 (8.23)6.5	(1-15) 48.2 (17-21) 48.2	6.5	(1-7)0 (8-23)3.0	(1-7)0 (8-23)6.3	(1-15) 42.9 (22) 42.9	6.5
SC-50	9.6	0	0	(1-15) 48.4 (17-21) 48.8	6.6	0	0	(1-15) 48.4 (22) 48.8	6.6

NOTES:

- All delays in nanosec
- Numbers in parentheses identify applicable flight numbers

Table C-4 50-Mile Area, Measured Cable Delays

	All Uplink	D Uplink				Xmtr Dish		MCS	
	Xmtr Flex	RF Switch	Flex	Spiro-line	Ant. Flex	Xmtr Flex	Spiro-Line	Flex	Spiro-line
Salt	9.3	0	0	(1-7) 43.2 (8-15) 45.3 (23) 46.3	6.7	9.3	(1-15) 31.9	17.0	(1-15) 112 (17-23) 110
WC-50	9.5	(1-7)0 (8-23)3.0	(1-7)0 (8-23)6.5	(1-15) 41.3 (23) 42.8	6.5	9.5	(1-15) 32.8	15.5	(1-15) 135.7 (17-23) 106.4
EC-50	9.3	(1-7)0 (8-23)3.1	(1-7)0 (8-23)6.5	(1-15) 39.6 (23) 41.2	6.5	7.7	(1-15) 35.1	15.0	(1-15) 141.4 (17-23) 108.0
SC-50	9.6	0	0	(1-15) 48.4 (23) 48.8	6.6	9.6	(1-15) 32.8	16.5	(1-15) 99 (17-23) 98.9

NOTES:

- All delays in nanosec
- Numbers in parentheses identify applicable flight numbers

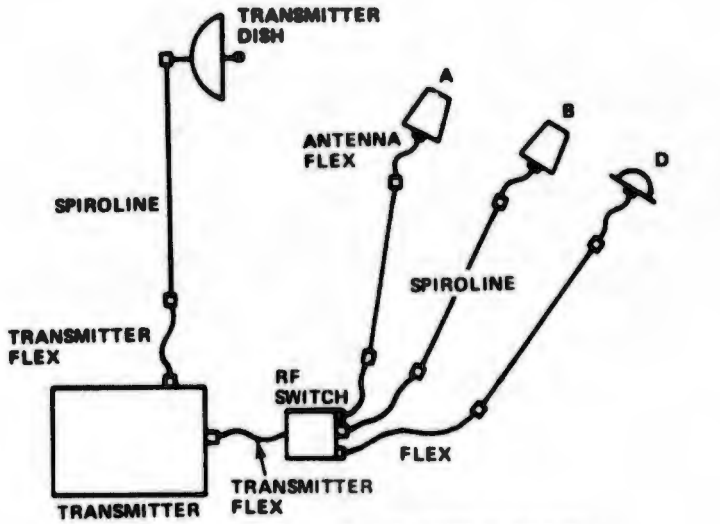

WC–50 AND EC–50 HAVE ABOVE CONFIGURATION

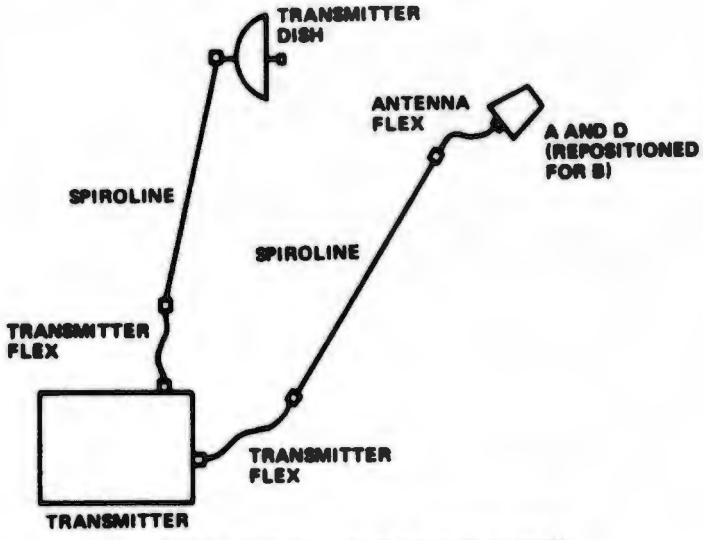

SALT AND SC–50 HAVE ABOVE CONFIGURATION

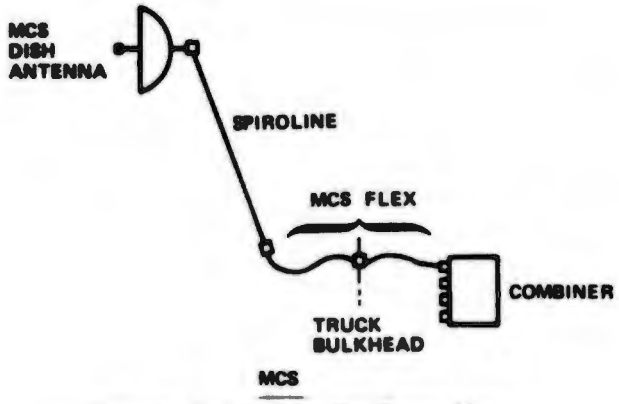

Figure C-1 Cable Configuration

Table C-5 Total Ground Delays used in the Navigation Solution

	Total Ground Delay, nanosec	Mean Nav Solution Error ωrt WSMR, Ft
Case 1	7298.2 32346.8 18117.7 22392.5	R_{1-4} = -14.0 R_{2-4} = -14.2 R_{3-4} = -14.4
Case 2	7292.1 32348.4 18116.5 22376.4	R_{1-4} = -5.8 R_{2-4} = 3.09 R_{3-4} = -5.25
Case 3	7286.9 32334.4 18110.9 22365.5	R_{1-4} = 0 R_{2-4} = 0 R_{3-4} = 0

- Total Ground Delay includes all elements from the MCS receiver to the transmitting antenna.

APPENDIX D

PSEUDO RANGE NAVIGATION SOLUTION

APPENDIX D

PSEUDO RANGE NAVIGATION SOLUTION

The reference coordinate system utilized with Field Tests is given in Figure .

$$(\bar{Y}-\bar{X}_1)\cdot(\bar{Y}-\bar{X}_1) = (R_1-B)^2$$

$$\bar{Y}\cdot\bar{Y}+\bar{X}_1\cdot\bar{X}_1-2\bar{Y}\cdot\bar{X}_1 = R_1^2+B^2-2R_1B$$

Now take these differences

$$(\bar{Y}-\bar{X}_J)\cdot(\bar{Y}-\bar{X}_J) = (R_J-B)^2$$

$$\underline{-(\bar{Y}-\bar{X}_1)\cdot(\bar{X}-\bar{X}_1) = (R_1-B)^2} \qquad J = 2,3,4$$

$$\bar{Y}\cdot(\bar{X}_1-\bar{X}_2)+B(R_2-R_1) = (R_2^2-R_1^2+\bar{X}_1\cdot\bar{X}_1-\bar{X}_2\cdot\bar{X}_2)/2$$

$$\bar{Y}\cdot(\bar{X}_1-\bar{X}_3)+B(R_3-R_1) = (R_3^2-R_1^2+\bar{X}_1\cdot\bar{X}_1-\bar{X}_3\cdot\bar{X}_3)/2$$

$$\bar{Y}\cdot(\bar{X}_1-\bar{X}_4)+B(R_4-R_1) = (R_4^2-R_1^2+\bar{X}_1\cdot\bar{X}_1-\bar{X}_4\cdot\bar{X}_4)/2$$

we can rewrite these as

$$\begin{bmatrix} X_{11}-X_{21} & X_{12}-X_{22} & X_{13}-X_{23} \\ X_{11}-X_{31} & X_{12}-X_{32} & X_{13}-X_{33} \\ X_{11}-X_{41} & X_{12}-X_{42} & X_{13}-X_{43} \end{bmatrix} \begin{bmatrix} Y_1 \\ Y_2 \\ Y_3 \end{bmatrix} + \begin{bmatrix} (R_2-R_1)B \\ (R_3-R_1)B \\ (R_4-R_1)B \end{bmatrix} = \begin{bmatrix} C_1 \\ C_2 \\ C_3 \end{bmatrix}$$

where

$$C_i = (R_{i+1}^2-R_1^2+\bar{X}_1\cdot\bar{X}_1-\bar{X}_{i+1}\cdot\bar{X}_{i+1})/2$$

$$\begin{bmatrix} X_{11}-X_{21} & X_{12}-X_{22} & X_{13}-X_{23} & R_2-R_1 \\ X_{11}-X_{31} & X_{12}-X_{32} & X_{13}-X_{33} & R_3-R_1 \\ X_{11}-X_{41} & X_{12}-X_{42} & X_{13}-X_{43} & R_4-R_1 \end{bmatrix} \begin{bmatrix} Y_1 \\ Y_2 \\ Y_3 \\ B \end{bmatrix} = [C]$$

$$\underbrace{\begin{bmatrix} X_{11}-X_{21} & X_{12}-X_{22} & R_2-R_1 \\ X_{11}-X_{31} & X_{12}-X_{32} & R_3-R_1 \\ X_{11}-X_{41} & X_{12}-X_{42} & R_4-R_1 \end{bmatrix}}_{A} \underbrace{\begin{bmatrix} Y_1 \\ Y_2 \\ B \end{bmatrix}}_{Z} = \underbrace{[C]}_{C} - \underbrace{\begin{bmatrix} X_{13}-X_{23} \\ X_{13}-X_{33} \\ X_{13}-X_{43} \end{bmatrix}}_{E} [Y_3]$$

$$[A]\,[Z] = [C] - [E]\,[Y_3]$$

$$[Z] = [A]^{-1}\,[C] - [A]^{-1}\,[E]\,Y_3$$

therefore,

$$Y_1 = A^{-1}(1)C \quad -A^{-1}(1)EY_3 \quad = K_1+K_2Y_3$$

$$Y_2 = A^{-1}(2)C \quad -A^{-1}(2)EY_3 \quad = K_3+K_4Y_3$$

$$B = A^{-1}(3)C \quad -A^{-1}(3)EY_3 \quad = K_5+K_6Y_3$$

now from the original equation

$$\bar{Y}\cdot\bar{Y}+\bar{X}_1\cdot\bar{X}_1-2\bar{Y}\cdot\bar{X}_1=(R_1-B)^2$$

$$Y_1^2+Y_2^2+Y_3^2+\bar{X}_1\cdot\bar{X}_1-2Y_1X_{11}-2Y_2X_{12}-2X_3X_{13}=R_1^2+B^2-2R_1B$$

we can now substitute and solve for Y_3:

$$K_1^2+K_2^2Y_3^2+K_3^2+K_4^2Y_3^2+Y_3^2+\bar{X}_1\cdot\bar{X}_1-2X_{11}K_1-2X_{11}K_2Y_3$$

$$-2X_{12}K_3-2X_{12}K_4Y_3-2X_{13}Y_3-R_1^2-K_5^2-K_6^2Y_3^2+2R_1K_5+2R_1K_6Y_3=0$$

Now let:

$$\alpha=K_2^2+K_4^2-K_6^2+1$$

$$2\beta=-2X_{11}K_2-2X_{12}K_4-2X_{13}+2R_1K_6$$

$$\gamma=K_1^2+K_3^2+\bar{X}_1\cdot\bar{X}_1-2X_{11}K_1-2X_{12}K_3-R_1^2-K_5^2+2R_1K_5$$

$$Y_3=\frac{-2\beta\pm\sqrt{4\beta^2-4\alpha\gamma}}{2\alpha}=\frac{-\beta\pm\sqrt{\beta^2-\alpha\gamma}}{\alpha}$$

and

$$Y_1=K_1+K_2Y_3$$

$$Y_2=K_3+K_4Y_3$$

$$B=K_5+K_6Y_3$$

PSEUDO RANGE VELOCITY SOLUTION

$$(\bar{Y}-\bar{X}_1)\cdot(\bar{Y}-\bar{X}_1)=(R_1-B)^2$$

Take time derivative

$$(\bar{Y}-\bar{X}_1)\cdot(\bar{V}-\dot{\bar{X}}_1)=(R_1-B)(\dot{R}_1-\dot{B})$$

$$\underbrace{\frac{(\bar{Y}-\bar{X}_1)}{(R_1-B)}}_{\bar{\gamma}}\cdot(\bar{V}-\dot{\bar{X}}_1)=\dot{R}_1-\dot{B}$$

$$\underbrace{\begin{bmatrix}\gamma_{11}&\gamma_{12}&\gamma_{13}&1\\ \gamma_{21}&\gamma_{22}&\gamma_{23}&1\\ \gamma_{31}&\gamma_{32}&\gamma_{33}&1\\ \gamma_{41}&\gamma_{42}&\gamma_{43}&1\end{bmatrix}}_{\bar{M}}\begin{bmatrix}V_1\\V_2\\V_3\\\dot{B}\end{bmatrix}=\begin{bmatrix}\dot{R}_1\\\dot{R}_2\\\dot{R}_3\\\dot{R}_4\end{bmatrix}+\begin{bmatrix}\bar{\gamma}_1^T\cdot\dot{\bar{X}}_1\\\bar{\gamma}_2^T\cdot\dot{\bar{X}}_2\\\bar{\gamma}_3^T\cdot\dot{\bar{X}}_3\\\bar{\gamma}_4^T\cdot\dot{\bar{X}}_4\end{bmatrix}$$

$$\begin{bmatrix} \dot{V}_1 \\ \dot{V}_2 \\ \dot{V}_3 \\ \dot{B} \end{bmatrix} = M^{-1} \begin{bmatrix} \dot{R}_1 \\ \dot{R}_2 \\ \dot{R}_3 \\ \dot{R}_4 \end{bmatrix} + M^{-1} \begin{bmatrix} \bar{\gamma}_1^T \cdot \ddot{\bar{X}}_1 \\ \bar{\gamma}_2^T \cdot \ddot{\bar{X}}_2 \\ \bar{\gamma}_3^T \cdot \ddot{\bar{X}}_3 \\ \bar{\gamma}_4^T \cdot \ddot{\bar{X}}_4 \end{bmatrix}$$

APPENDIX E

FLOW DIAGRAM OF TWO STATE BIAS FILTER EXECUTIVE PROGRAM

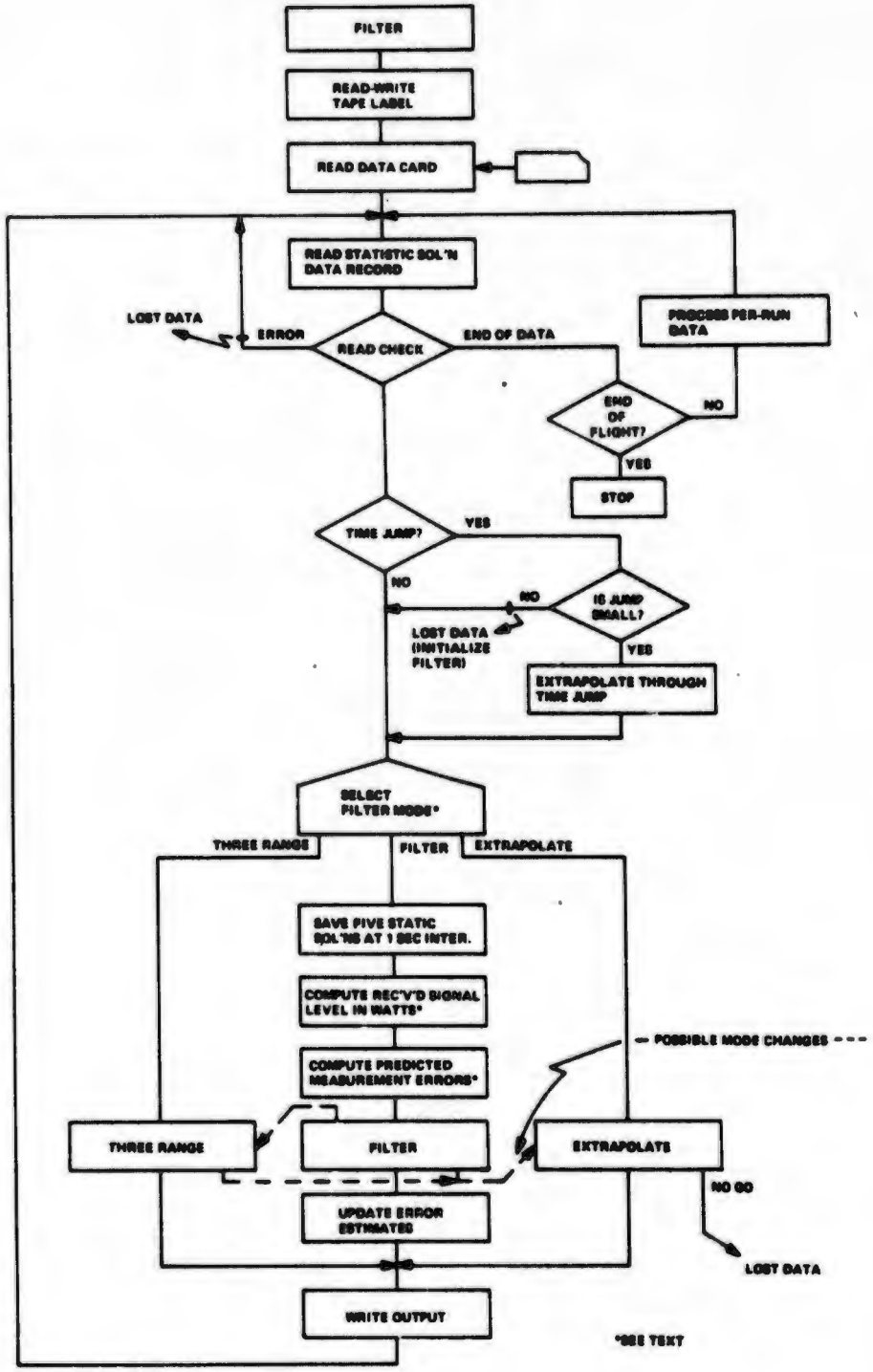

Figure E-1 Two-State Bias Filter Implementation, Excutive Flow

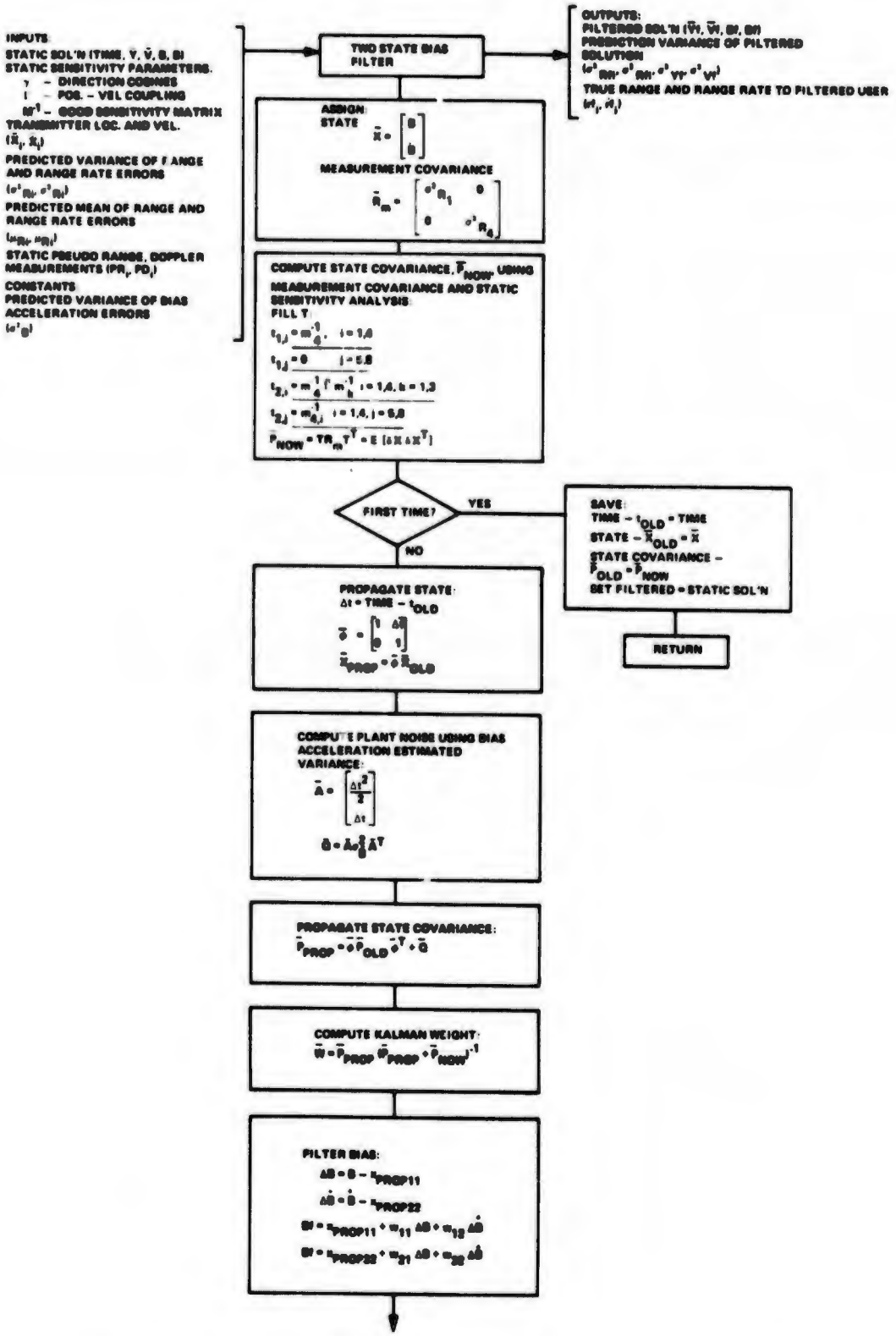

Figure E-1 Two-State Filter Flow, Filter Algorithms (Continued)

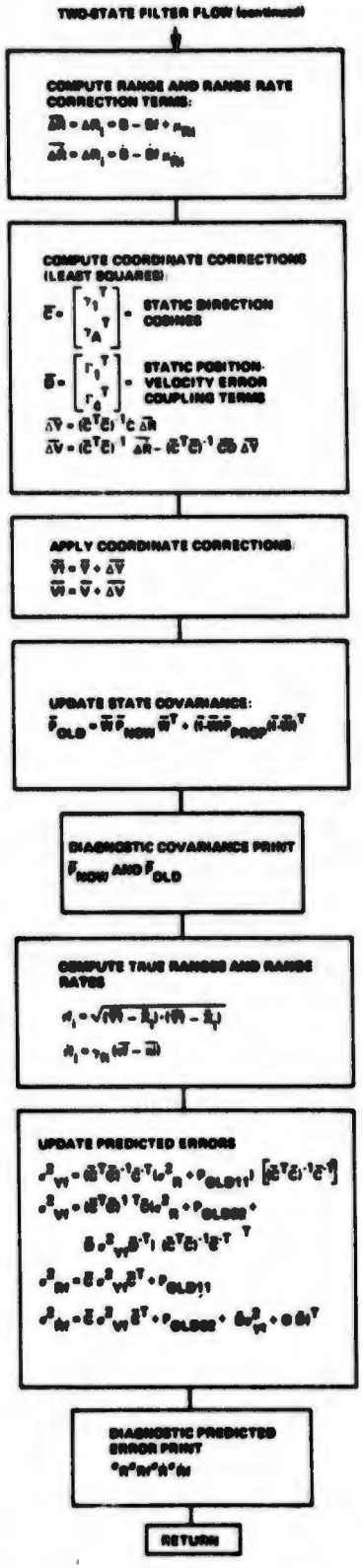

Figure E-1 Two-State Bias Filter Data Flow, Filter Algorithms (Continued)

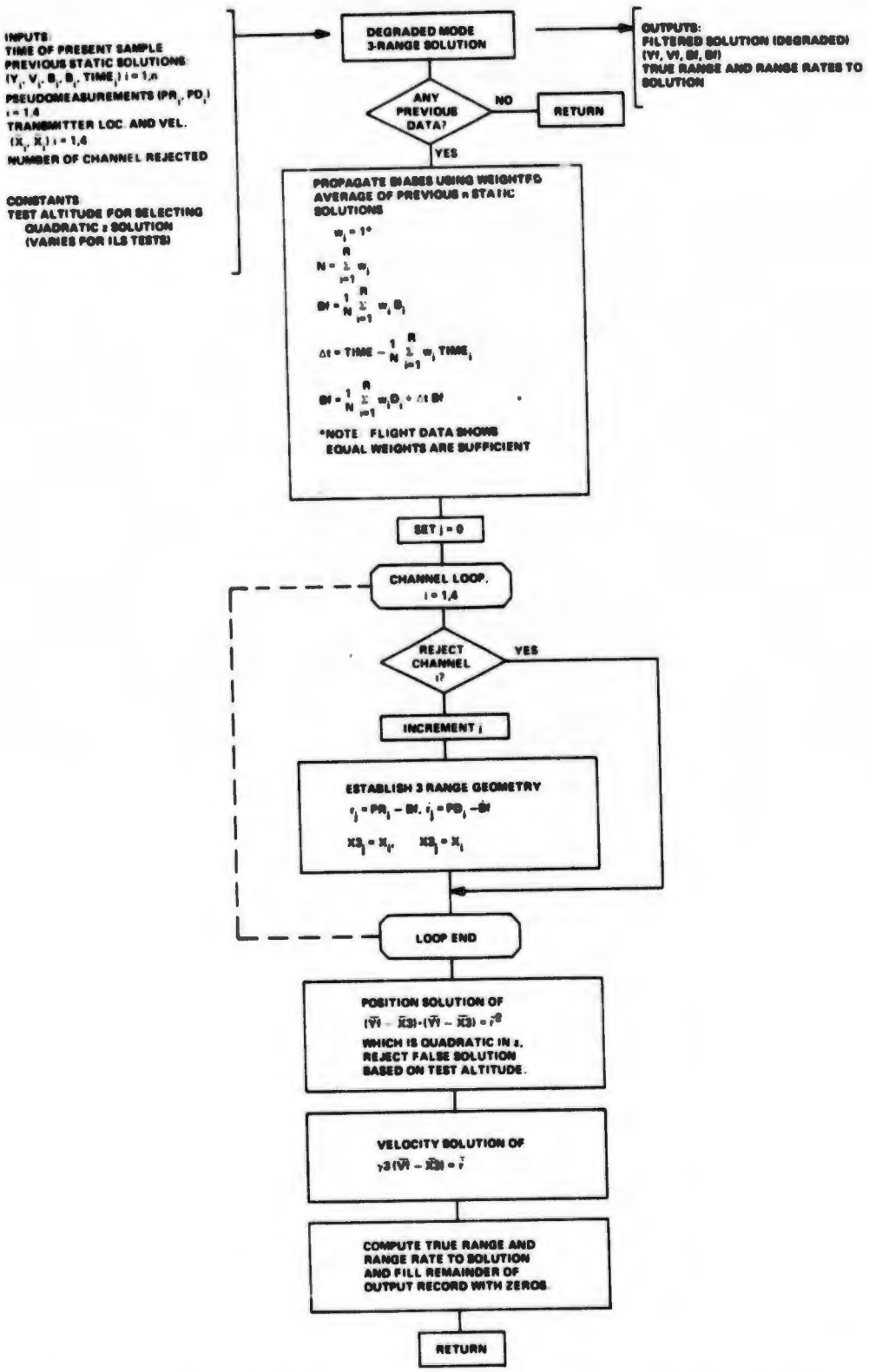

Figure E-1 Two-State Bias Filter Data Flow, 3-Range Navigation (Continued)

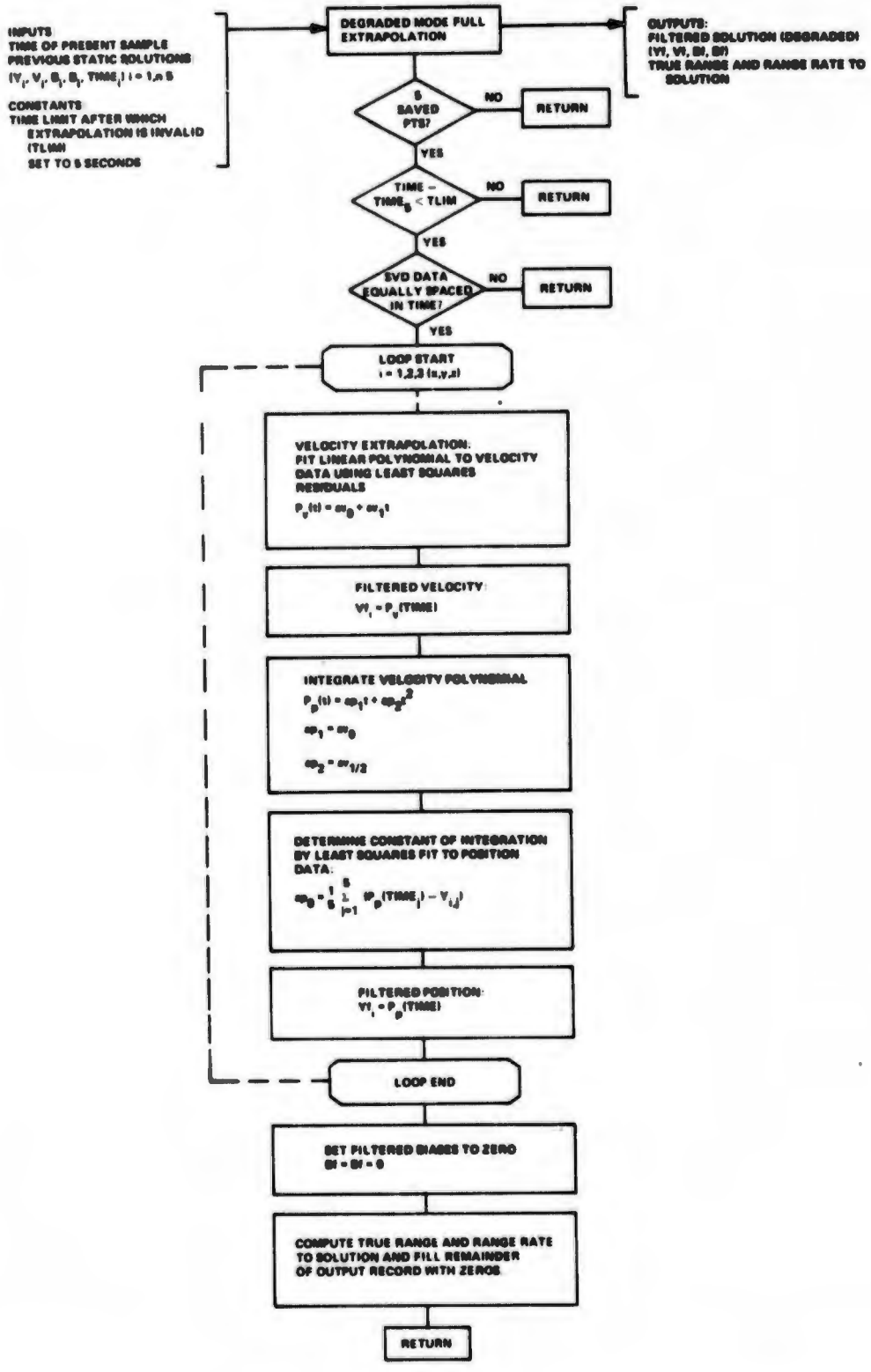

Figure E-1 Two-State Filter Flow, Dead-Reckon Navigation (Concluded)

APPENDIX F

FLOW DIAGRAM OF 11-STATE BIAS FILTER PROGRAM

APPENDIX F

FLOW DIAGRAM OF 11-STATE BIAS FILTER PROGRAM

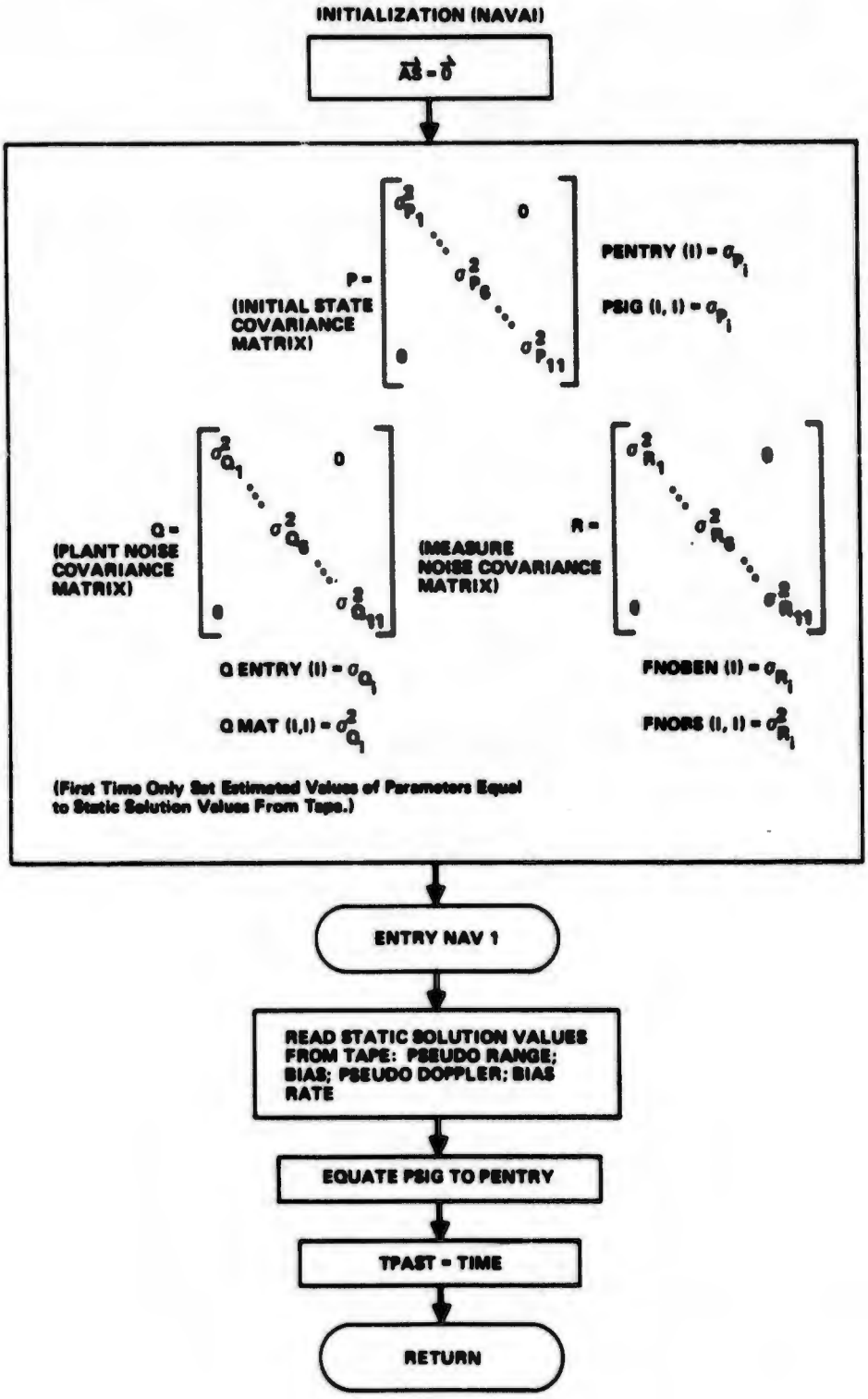

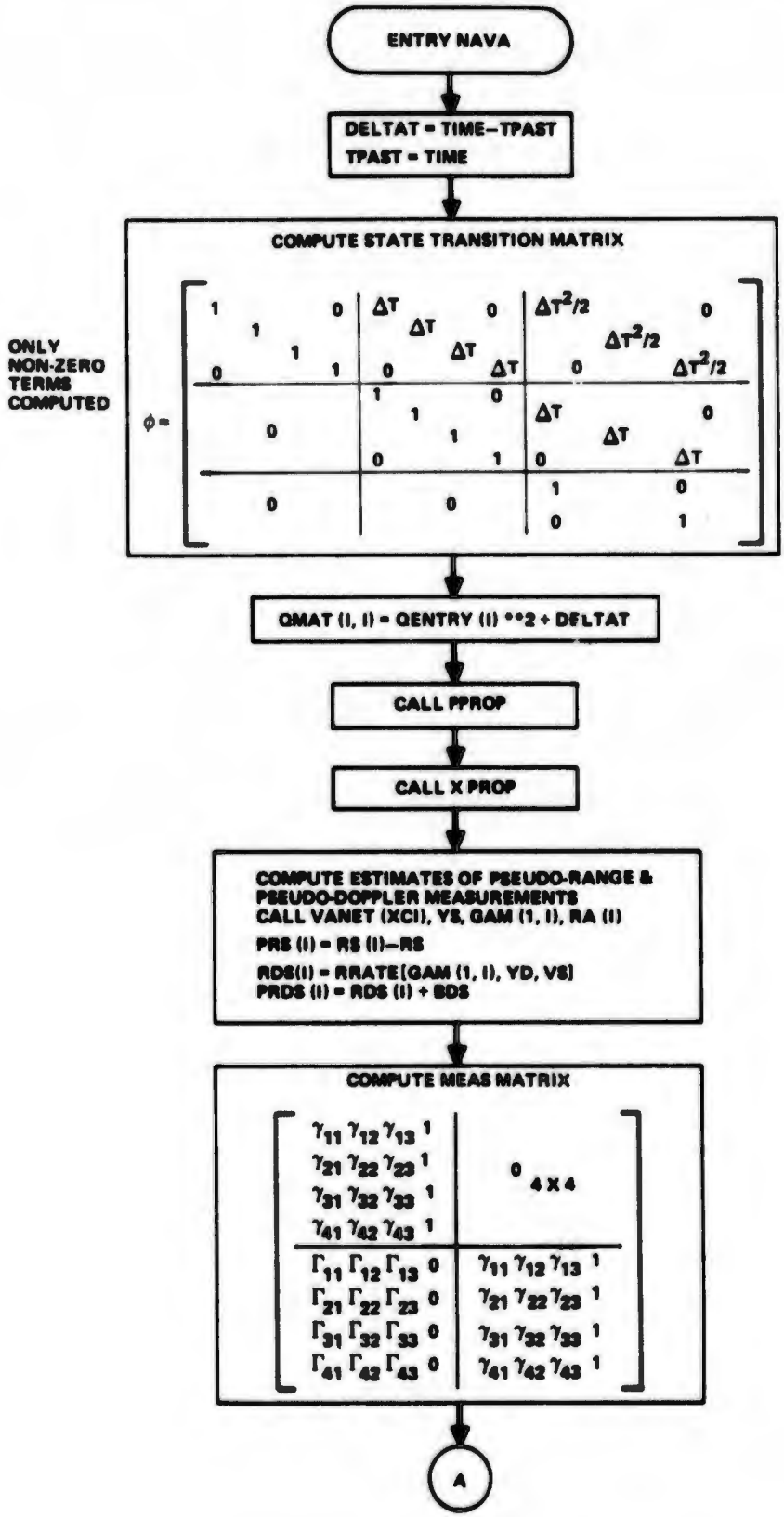
ENTRY NAVA
DELTAT = TIME–TPAST
TPAST = TIME
COMPUTE STATE TRANSITION MATRIX
ONLY NON-ZERO TERMS COMPUTED
Φ =
QMAT (I, I) = QENTRY (I) **2 ÷ DELTAT
CALL PPROP
CALL X PROP
COMPUTE ESTIMATES OF PSEUDO-RANGE & PSEUDO-DOPPLER MEASUREMENTS
CALL VANET (XCI), VS, GAM (1, I), RA (I)
PRS (I) = RS (I)–RS
RDS(I) = RRATE[GAM (1, I), VD, VS]
PRDS (I) = RDS (I) + BDS
COMPUTE MEAS MATRIX
4 X 4
A

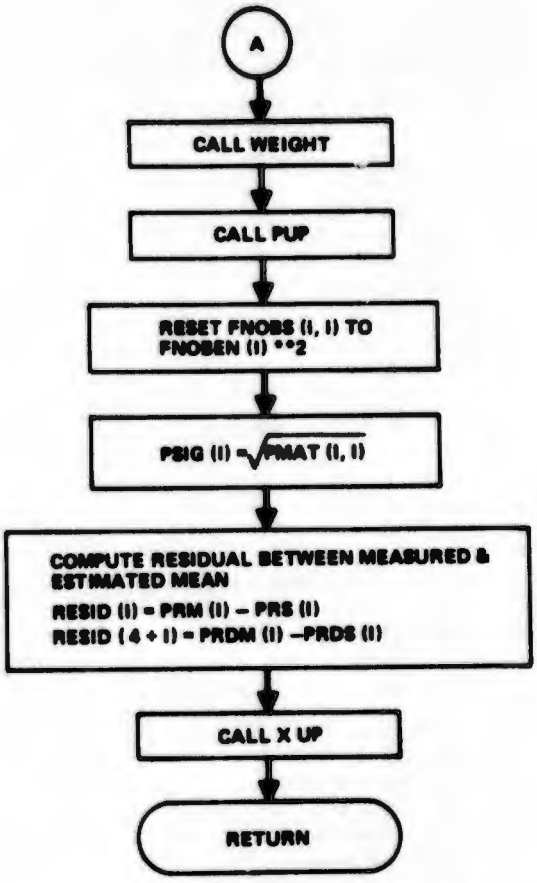
A
CALL WEIGHT
CALL PUP
RESET FNOBS (I, I) TO FNOBEN (I) **2
PSIG (I) = √PMAT (I, I)
COMPUTE RESIDUAL BETWEEN MEASURED & ESTIMATED MEAN
RESID (I) = PRM (I) – PRS (I)
RESID (4 + I) = PRDM (I) –PRDS (I)
CALL X UP
RETURN

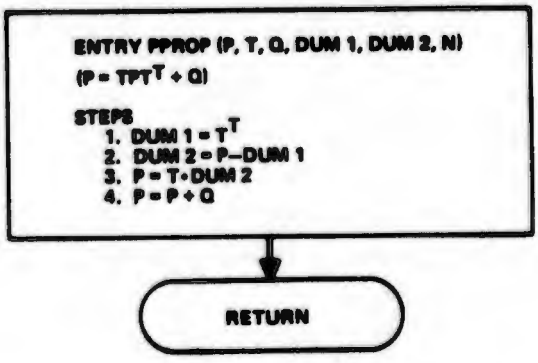
ENTRY PPROP (P, T, Q, DUM 1, DUM 2, N)
(P = TPT^T + Q)
STEPS
1. DUM 1 = T^T
2. DUM 2 = P–DUM 1
3. P = T•DUM 2
4. P = P + Q
RETURN

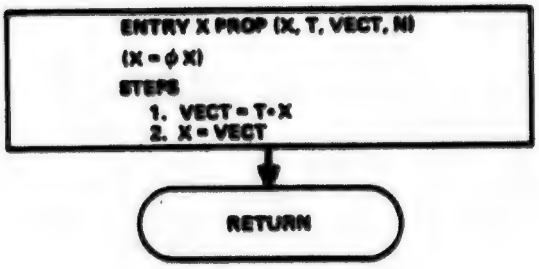
ENTRY X PROP (X, T, VECT, N)
(X = ϕ X)
STEPS
1. VECT = T•X
2. X = VECT
RETURN

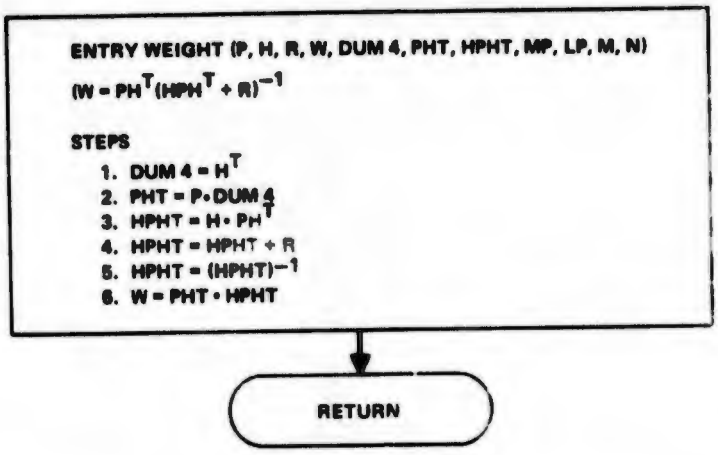
ENTRY WEIGHT (P, H, R, W, DUM 4, PHT, HPHT, MP, LP, M, N)
(W = PH^T(HPH^T + R)^-1
STEPS
1. DUM 4 = H^T
2. PHT = P•DUM 4
3. HPHT = H• PH^T
4. HPHT = HPHT + R
5. HPHT = (HPHT)^-1
6. W = PHT • HPHT
RETURN

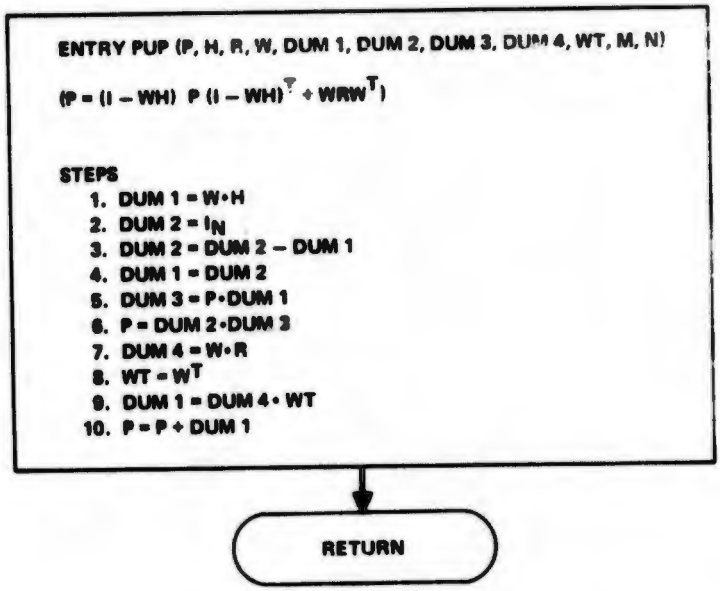
ENTRY PUP (P, H, R, W, DUM 1, DUM 2, DUM 3, DUM 4, WT, M, N)
(P = (I – WH) P (I – WH)^T + WRW^T)
STEPS
1. DUM 1 = W•H
2. DUM 2 = I_N
3. DUM 2 = DUM 2 – DUM 1
4. DUM 1 = DUM 2
5. DUM 3 = P•DUM 1
6. P = DUM 2•DUM 3
7. DUM 4 = W•R
8. WT = W^T
9. DUM 1 = DUM 4 • WT
10. P = P + DUM 1
RETURN

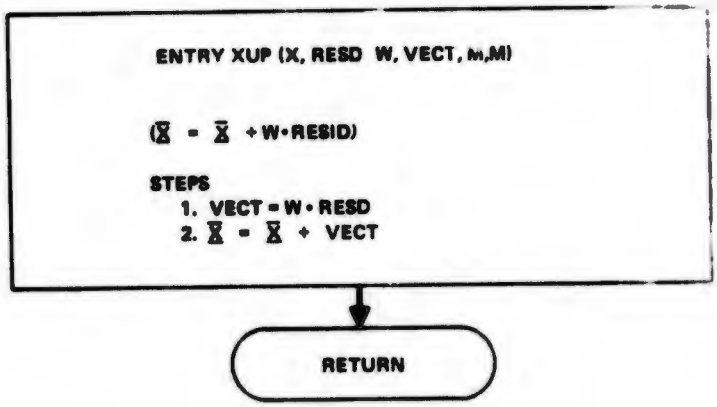
ENTRY XUP (X, RESD W, VECT, M,MI)
(X̄ = X̄ + W•RESID)
STEPS
1. VECT = W • RESD
2. X̄ = X̄ + VECT
RETURN

APPENDIX G

FLIGHT 19 TRAJECTORY RESIDUAL DATA

APPENDIX G

FLIGHT 19 TRAJECTORY RESIDUAL DATA

This appendix presents the data from all passes of Flight 19, and is typical of the data collected from flights 17-23. Data from the other flights are available and may be obtained by contacting Lt. Col. Valentine L. Denninger of the Defense Navigation Satellite Development Program Office at SAMSO.

The data presented are for Case 2A. An explanation of Cases 1, 2 and 3 can be found on pages 2-5 of this volume, together with some measurement details contained in Section 4 of this volume.

An explanation of Case 2A requires a brief recapitulation of Cases 1 and 2. Case 1 solutions were those obtained by using the total ground rf link delays which we thought at the time of flights 17-23 were the proper ones based on our measurements. Further analyses of the data and our measurements revealed two significant errors. One was a 15 nanosec change to channel 4 due to a cable mismatch problem; the other was a variation in the apparent signal delay of the uplink antennas as a function of the aspect angle to the aircraft from the uplink antennas. Case 2 solutions were generated by taking into account these two errors and making the proper corrections.

Further analyses of the data and our measurements indicated that a 6 nanosec error was present in channel 1 which was finally traced to the coiled cable at Salt Site. (See page 4-49 of this volume). Appropriate corrections were made for this effect, and the solutions were rerun. These solutions represent Case 2a.

The data presented are the time history residuals between the 621B solution and the WSMR BET. An explanation of the notation used on these computer-generated plots is included to assist in identifying the pertinent source (i.e., HC or MRL) and test configuration for each plot. Note that some of the notation does not apply to these plots and should be disregarded.

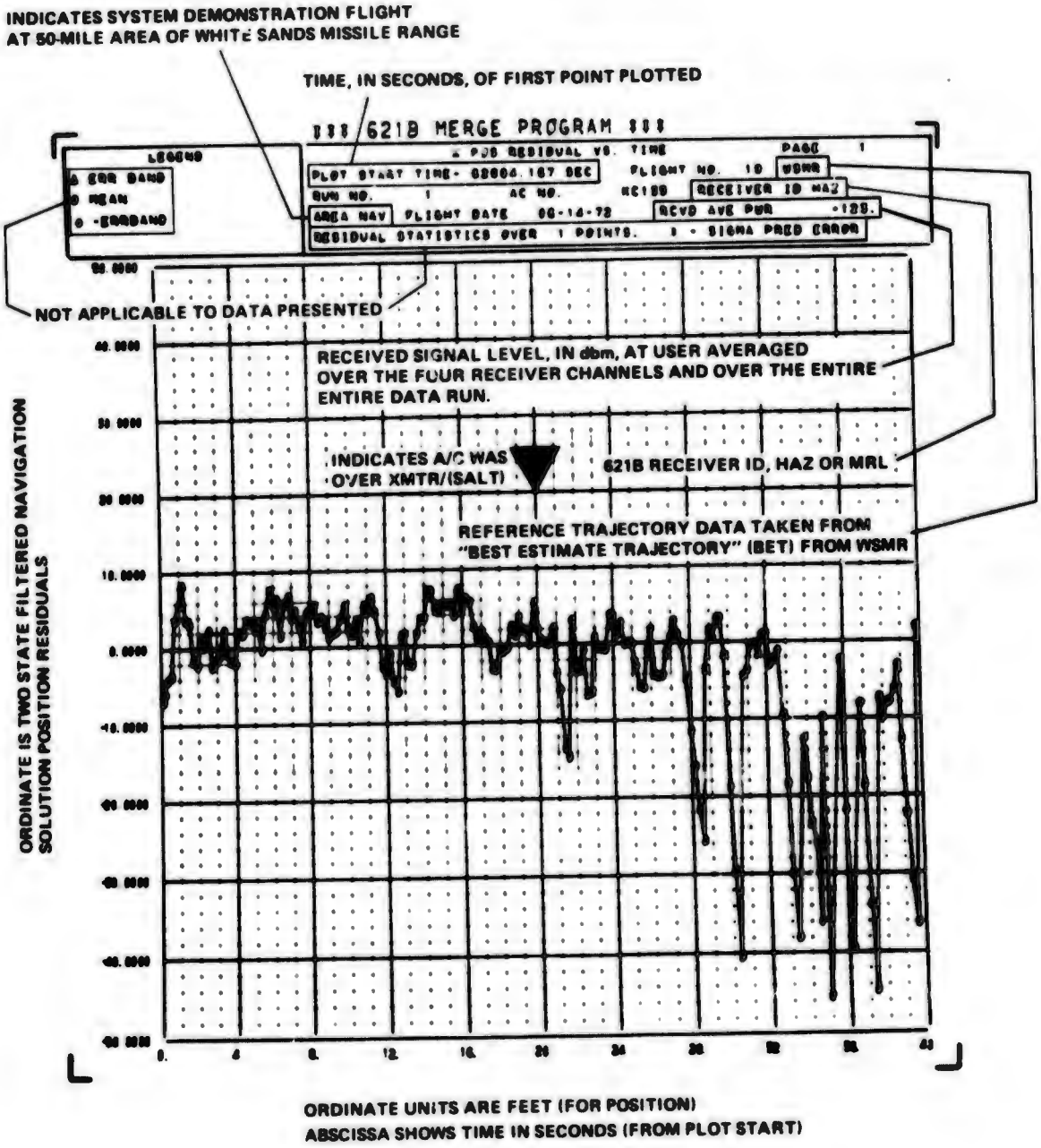
INDICATES SYSTEM DEMONSTRATION FLIGHT
AT 50-MILE AREA OF WHITE SANDS MISSILE RANGE
TIME, IN SECONDS, OF FIRST POINT PLOTTED
NOT APPLICABLE TO DATA PRESENTED
RECEIVED SIGNAL LEVEL, IN dbm, AT USER AVERAGED OVER THE FOUR RECEIVER CHANNELS AND OVER THE ENTIRE ENTIRE DATA RUN.
INDICATES A/C WAS OVER XMTR/(SALT)
621B RECEIVER ID, HAZ OR MRL
REFERENCE TRAJECTORY DATA TAKEN FROM "BEST ESTIMATE TRAJECTORY" (BET) FROM WSMR
ORDINATE IS TWO STATE FILTERED NAVIGATION SOLUTION POSITION RESIDUALS
ORDINATE UNITS ARE FEET (FOR POSITION)
ABSCISSA SHOWS TIME IN SECONDS (FROM PLOT START)

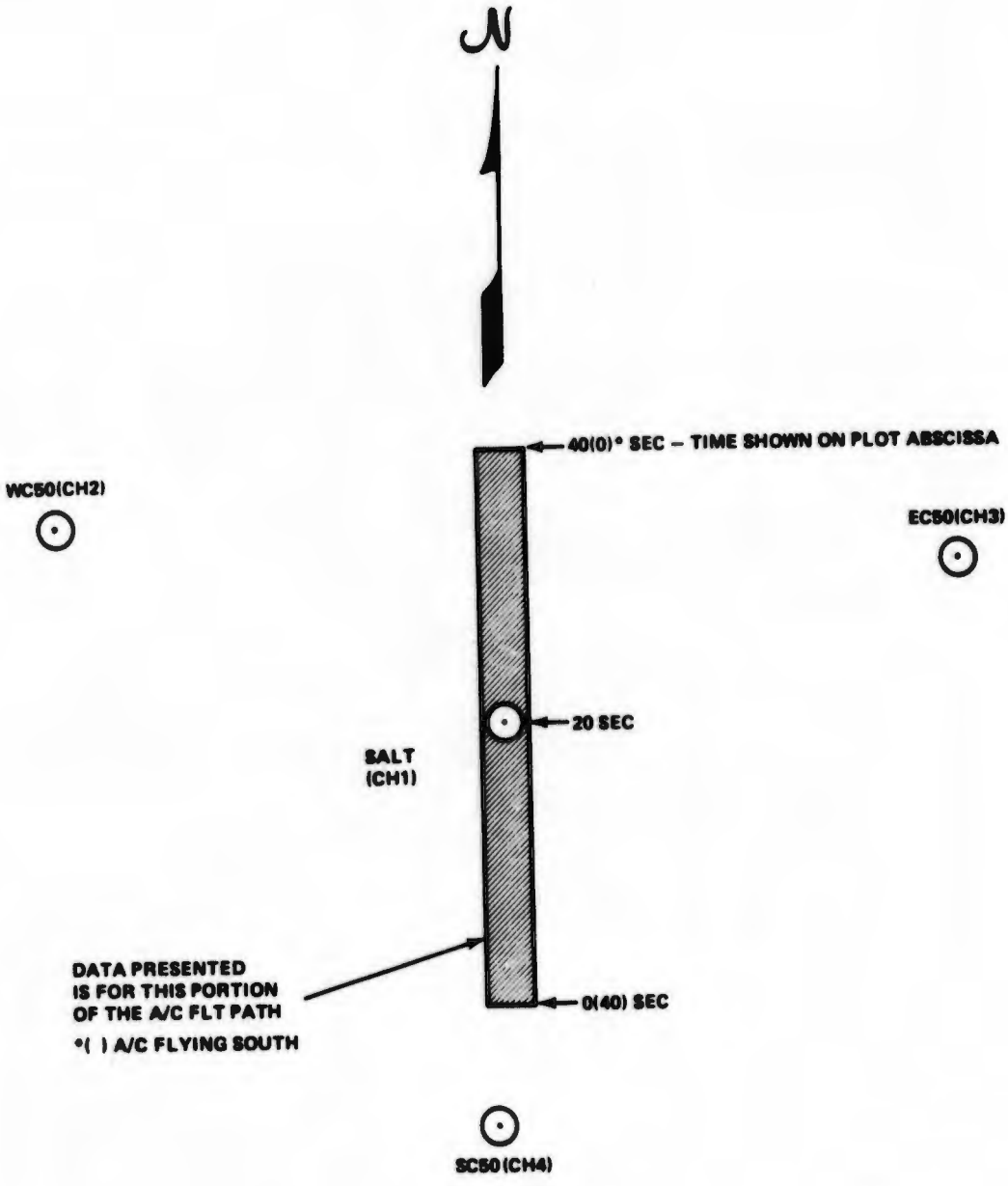

Plan View of Ground Transmitters and
Portion of Flight Path Shown In Appendix G Plots

Flight Path Characteristics for Flight 19

FLT 19

RUN	FLT PATH, TYPE	ALTITUDE, K FT	TIME OVER CENTER XMTR, SEC	A/C SPEED, FPS	DIRECTION
1	A	34	62804	681	SOUTH
2	A	34	63408	723	NORTH
3	A	34	63878	687	SOUTH
4	A	34	67698	740	NORTH
5	A	34	67842	684	SOUTH
6	A	34	67980	741	NORTH
7	A	34 ↓ 22	68439	681	SOUTH
8	C	22	68875	742	NORTH

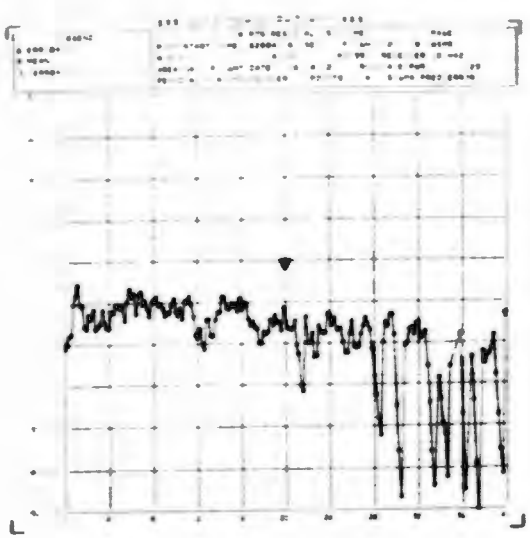

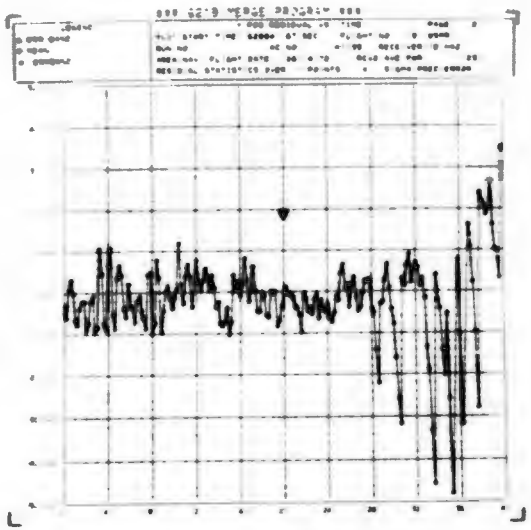

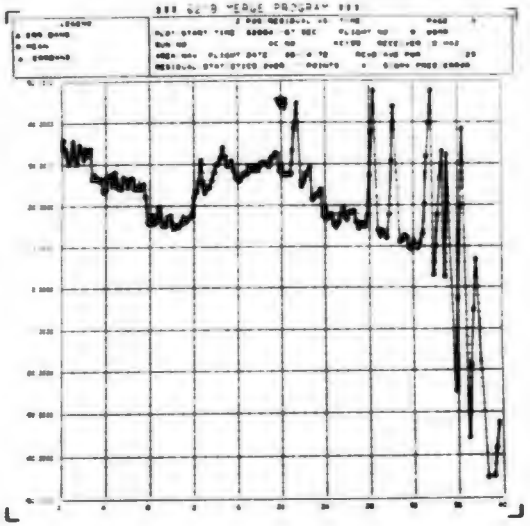

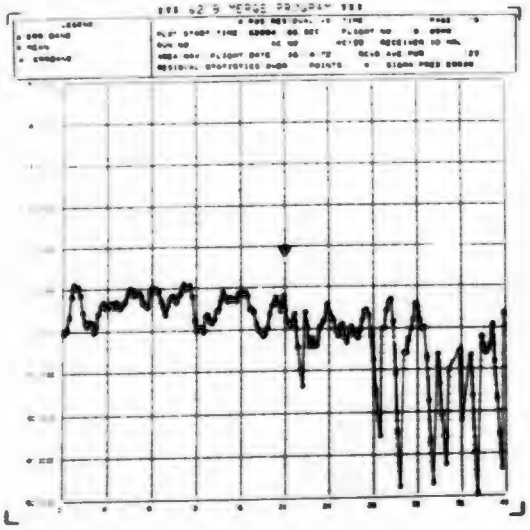

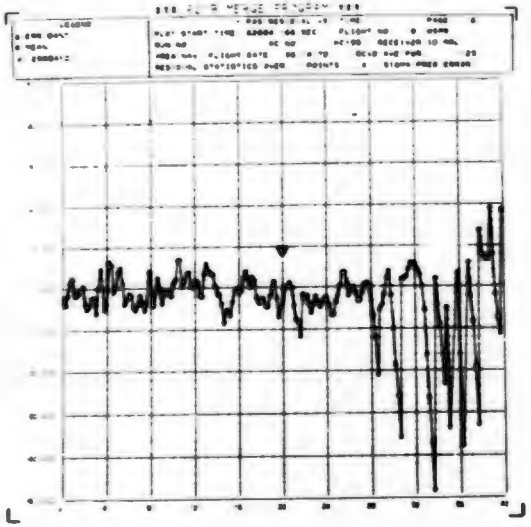

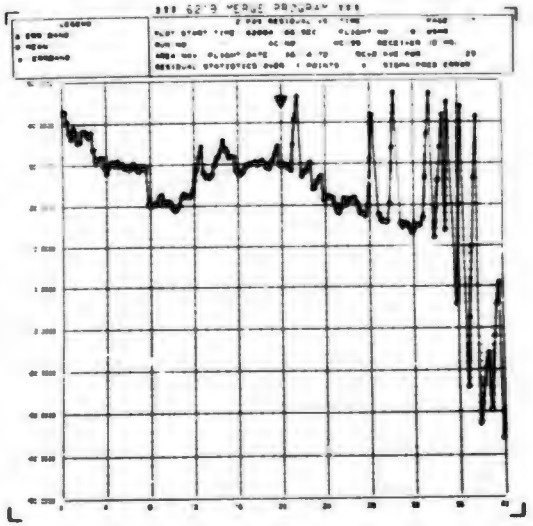

C-4

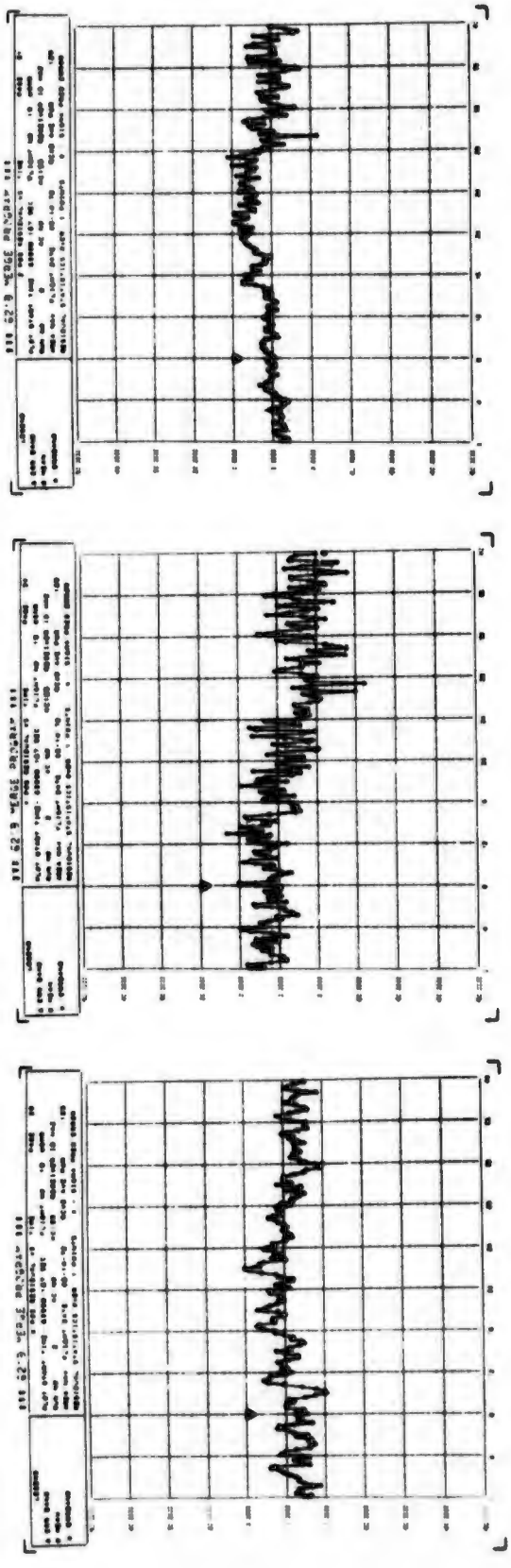

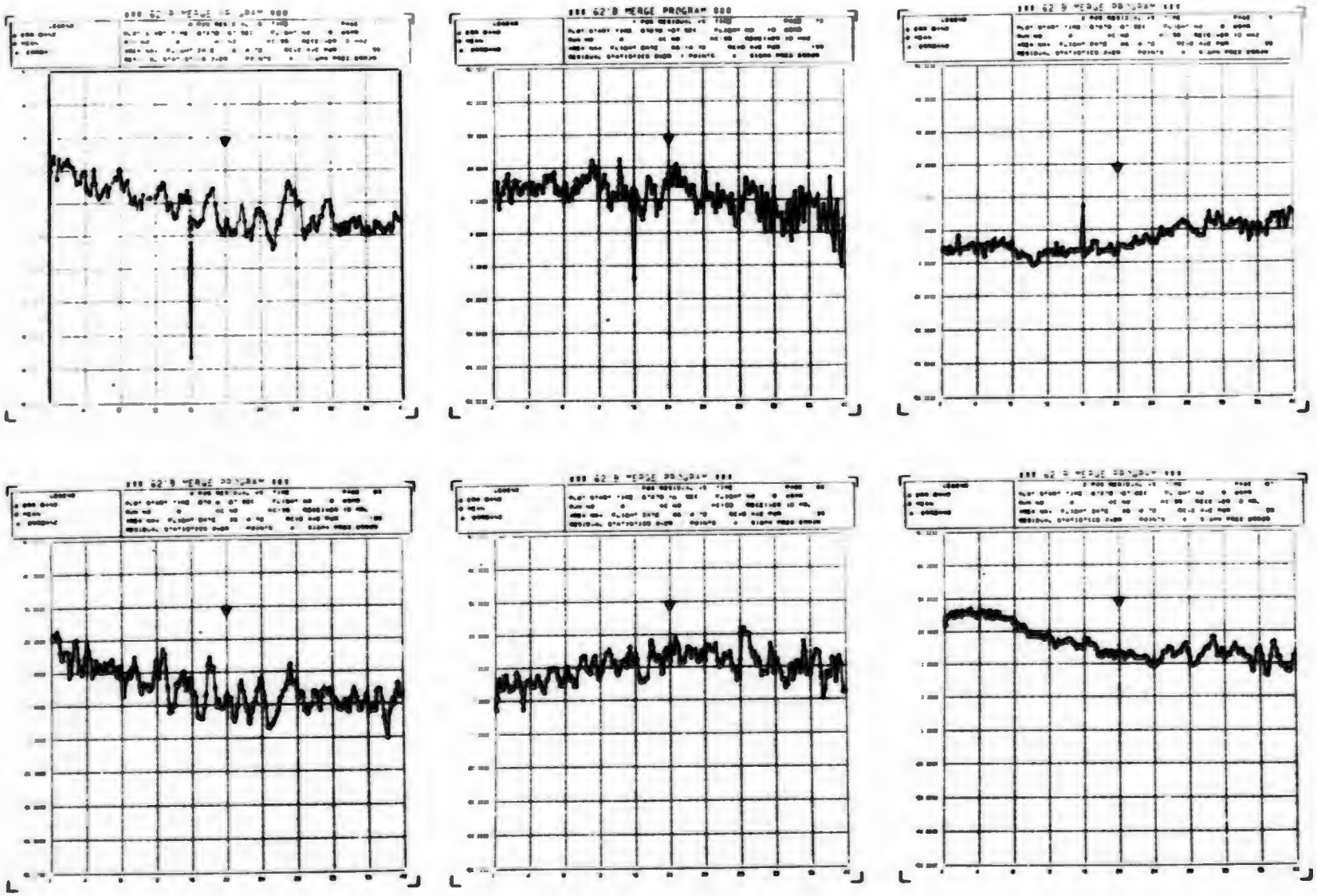

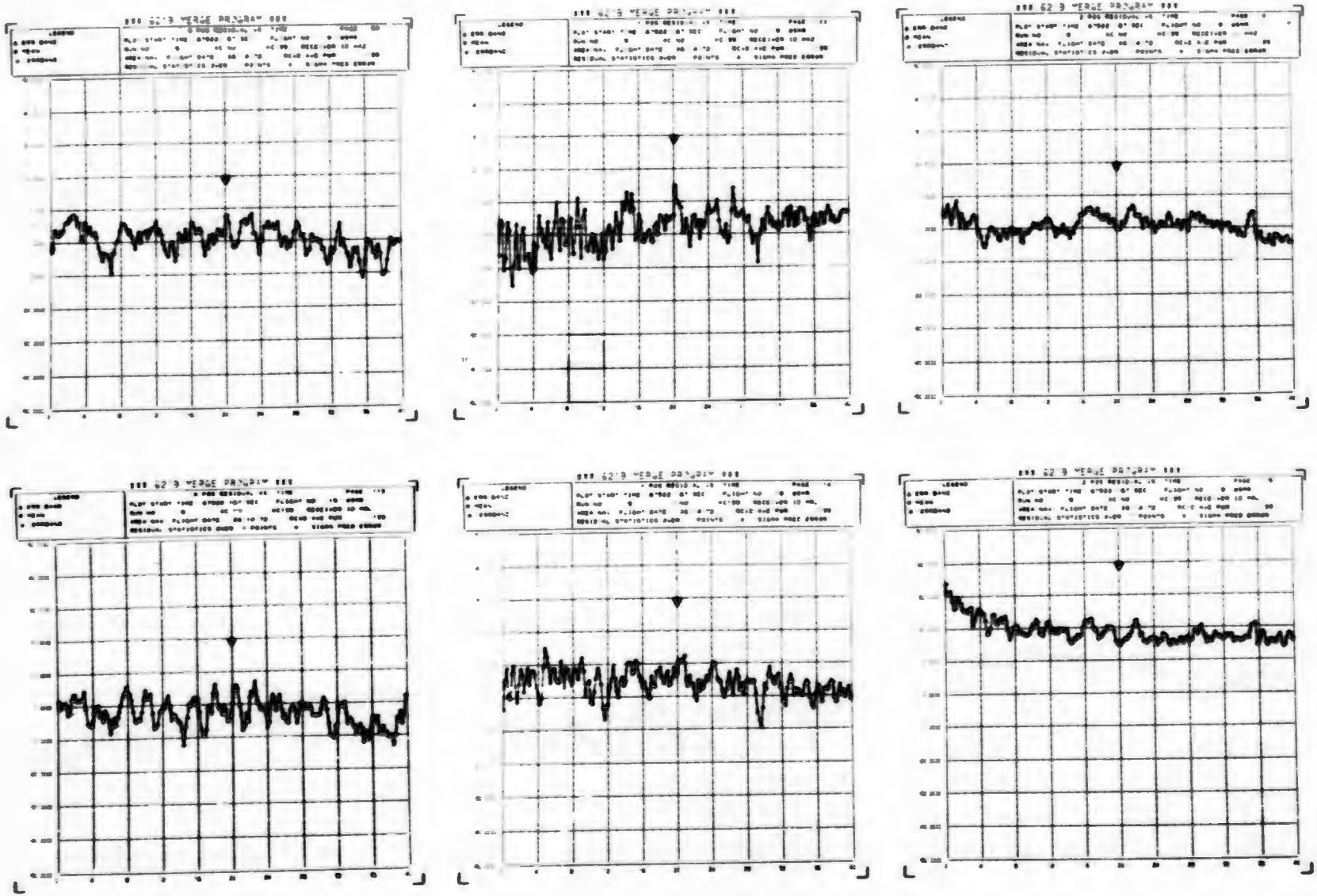

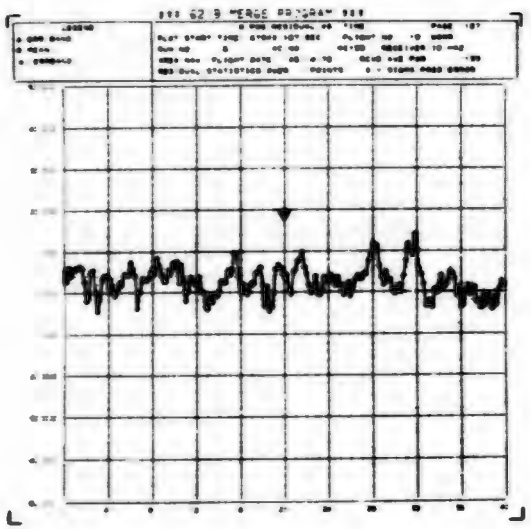

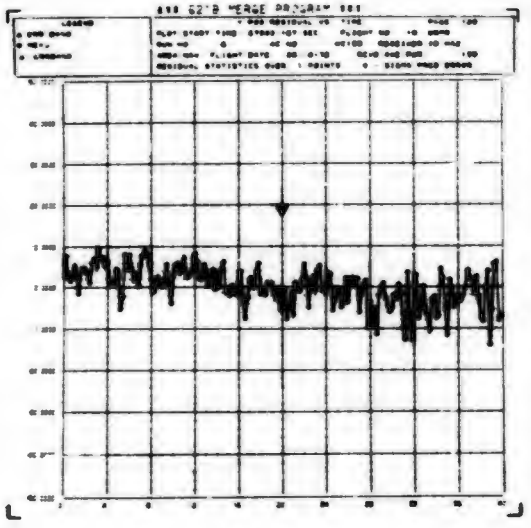

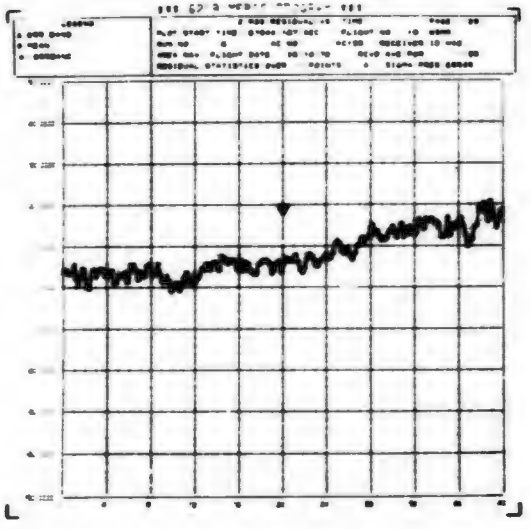

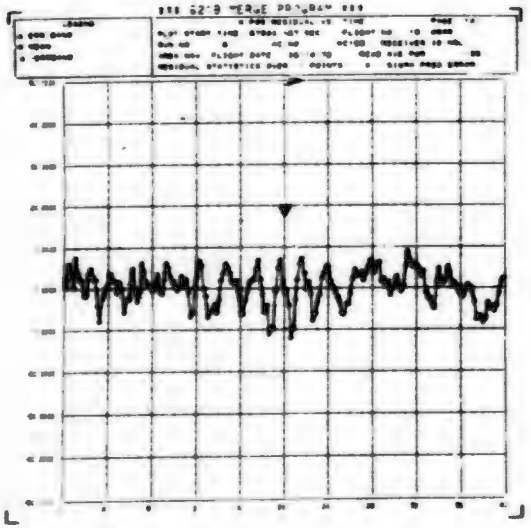

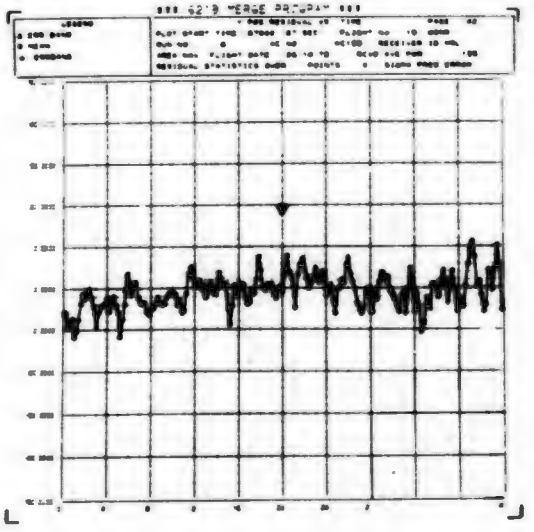

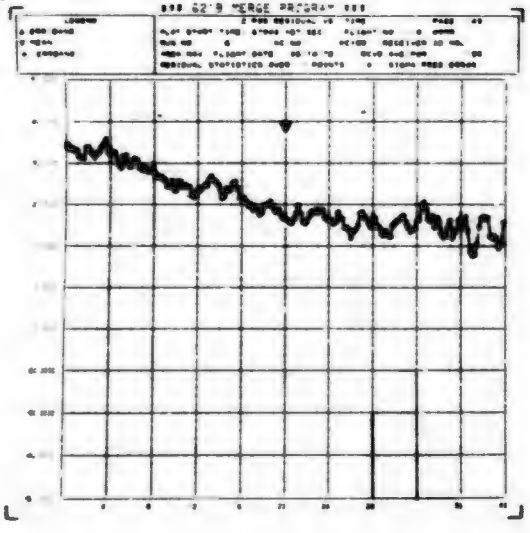

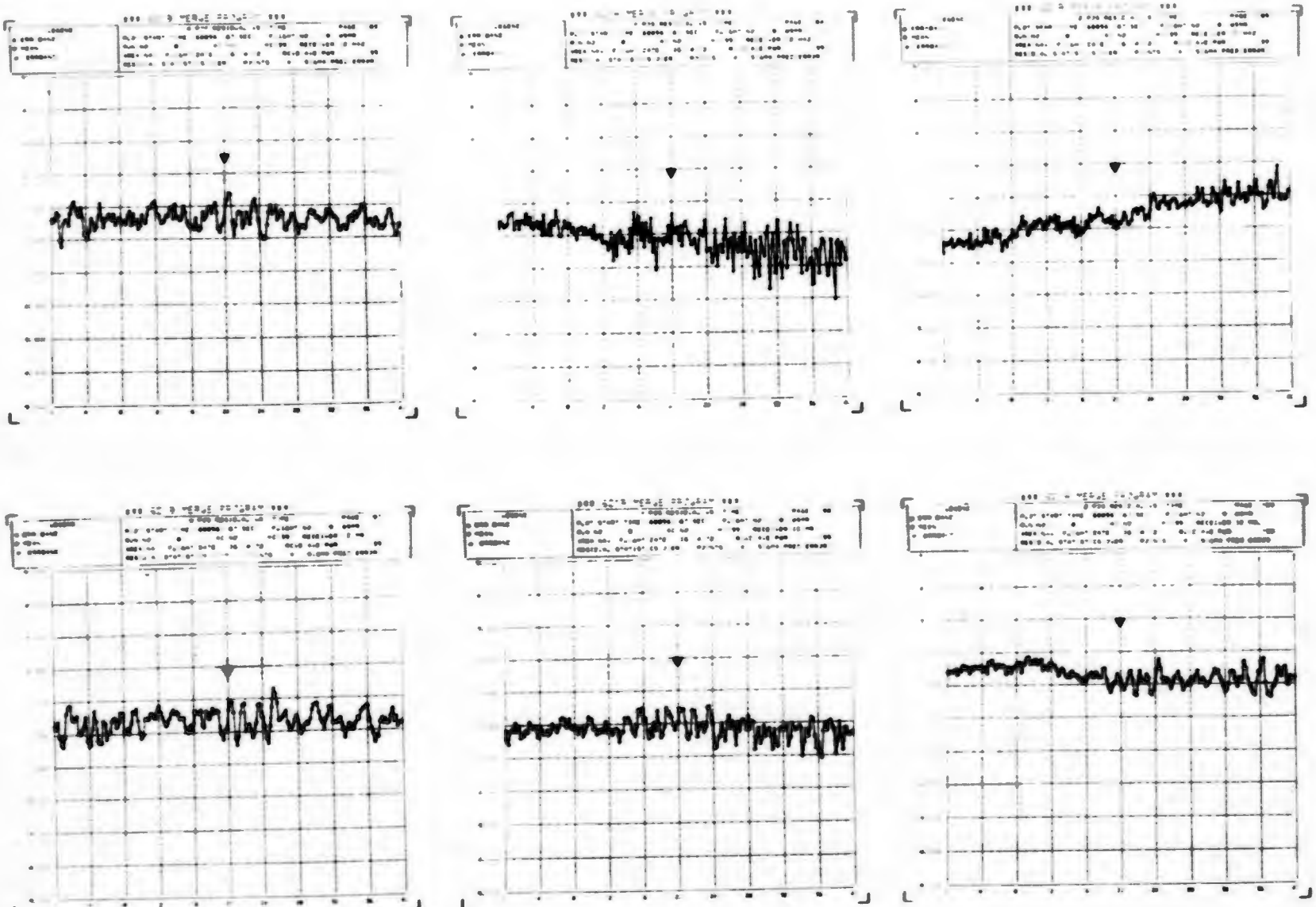

Security Classification

DOCUMENT CONTROL DATA - R & D

(Security classification of title, body of abstract and indexing annotation must be entered when the overall report is classified)

1. ORIGINATING ACTIVITY *(Corporate author)*

Grumman Aerospace Corporation
Bethpage, New York, 11714

2a. REPORT SECURITY CLASSIFICATION

UNCLASSIFIED

2b. GROUP

3. REPORT TITLE

FINAL REPORT, SYSTEM 621B USER EQUIPMENT DEFINITION AND EXPERIMENTS PROGRAM, PHASE II FIELD TESTS.

4. DESCRIPTIVE NOTES *(Type of report and inclusive dates)*

FINAL REPORT 11 Jan 1971 to 11 April 1973

5. AUTHOR(S) *(First name, middle initial, last name)*

John J. Courtney, Jr. — Paul Richards — Robert Regis (HC)
Ralph Laho — Michael Moore — Bert Glazer (MRL)
Ivan Kadar — Michael Neglia

6. REPORT DATE

11 April 1973

7a. TOTAL NO. OF PAGES

7b. NO. OF REFS

8a. CONTRACT OR GRANT NO.

FO 4701-71-C0176

b. PROJECT NO.

SYSTEM 621B

c.

d.

9a. ORIGINATOR'S REPORT NUMBER(S)

Vol. I. - None
Vol. II. - None
Vol. III. - None

9b. OTHER REPORT NO(S) *(Any other numbers that may be assigned this report)*

SAMSO TR 73-65

10. DISTRIBUTION STATEMENT

Distribution limited to U. S. Government Agencies only; Test and Evaluation, February 1973. Other requests for this document must be referred to HQ SAMSO/XRN.

11. SUPPLEMENTARY NOTES The distribution of this report is limited because it contains technology requiring disclosure only within the Department of Defense.

12. SPONSORING MILITARY ACTIVITY

Space and Missile System Organization (XRLO)
P.O. Box 92960, Worldway Postal Center
Los Angeles, California, 90009

13. ABSTRACT

System 621B is a concept for a global satellite - based precision navigation system designed to meet the requirements of land, sea and air military forces in an advantageous cost effective manner. One of the most important elements in this system is the user receiver. This report summarizes a series of flight and ground tests conducted at the White Sands Missile Range to evaluate the performance of a four-channel receiver in typical flight and field environments in order to solidify confidence in the predicted performance of System 621B receivers.

DD FORM 1 NOV 68 1473

Security Classification

14. KEY WORDS	LINK A		LINK B		LINK C	
	ROLE	WT	ROLE	WT	ROLE	WT
Receiver Test						
Flight Test of Navigation Receiver						
Ground Equipment for Receiver Test						
Flight Test Data Processing						
Airborne Installation						
Antenna Design and Installation						
Flight Test Data Analysis						
Multipath Testing						